

D I S S E R T A T I O N

Topography Simulation of Novel Processing Techniques

ausgeführt zum Zwecke der Erlangung des akademischen Grades
eines Doktors der technischen Wissenschaften

eingereicht an der Technischen Universität Wien
Fakultät für Elektrotechnik und Informationstechnik
von

Lado Filipovic

Neustiftgasse 67-69/17
A-1070 Wien, Österreich

geboren am 12. Februar 1983 in Sarajevo, Jugoslawien

Wien, im December 2012

Abstract

Topography simulations allow for a visualization of semiconductor surfaces as well as the interfaces between various material regions after a given processing step. Topography modeling of well-established processing techniques, such as material etching and deposition, has been studied for decades and very sophisticated models exist which envision the semiconductor surfaces and interfaces using the Level Set method. However, as the technology node shrinks along the predicted path of Moore's law, novel processing techniques are constantly introduced in order to enable miniaturization and to ease the financial burden of processing at these reduced nodes.

The ability to simulate semiconductor wafer topographies after the application of newly-introduced process technologies can go a long way in understanding their potential. The local anodic oxidation of silicon surfaces with an atomic force microscope (AFM) is a method which produces nanosized patterns on a silicon wafer using a localized charged needle. The technology has been developed in order to tackle the limited miniaturization potential of current photolithographic techniques. In the scope of this work, a technique which models the changing silicon topography as the silicon dioxide pattern is applied to the wafer is introduced. The topography motion is simulated using a Monte Carlo technique, whereby a particle distribution follows the surface charge density distribution. The charge density arises from the application of a strong electric field between the AFM needle tip and the silicon wafer surface.

Similarly, EEPROM memory cells can not be miniaturized further with the current processing techniques. Therefore, three-dimensional structures are being introduced in order to increase the number of available memory cells without increasing the area required. In the scope of this work, a model for Bit Cost Scalable (BiCS) memory hole etching is implemented in a Level Set framework as a combination of silicon and silicon dioxide etching steps.

A spray pyrolysis deposition model is also developed and implemented within the Level Set framework. This processing technique enables the deposition of thin films for applications such as gas sensors and solar cells. Two models for the topography modification due to spray pyrolysis deposition are presented, with an electric and a pressure atomizing nozzle. The resulting film growth is modeled as a layer by layer deposition of the individual droplets which reach the wafer surface or as a CVD-like process, depending on whether the droplets form a vapor near the interface or if they deposit a film only after surface collision.

Kurzfassung

Topographiesimulationen ermöglichen eine Visualisierung der Waferoberfläche und der Materialschichten eines Bauelements nachdem ein oder mehrere Prozesse durchlaufen worden sind. Weit verbreitete Prozesstechniken, wie Ätzen oder Abscheiden neuer Materialschichten, wurden jahrzehntelang erforscht und hoch komplexe Modelle existieren bereits. Durch die Level Set-Methode ist es möglich die Veränderung der Topographie darzustellen. Um dem Mooreschen Gesetz gerecht zu werden, werden ständig neue Prozesstechniken entwickelt, die eine Miniaturisierung möglich machen und gleichzeitig die Produktionskosten niedrig halten.

Das Verständnis von neuen Prozesstechnologien wird durch die Anwendung von Topographiesimulationen verbessert. Die lokale anodische Oxidation von Siliziumoberflächen mit Hilfe eines Rasterkraftmikroskops ist eine Methode zur Erzeugung nanometergroßer Muster mit einer geladenen Nadel. Diese Technologie wurde entwickelt, um die Grenzen der Fotolithographie bei der fortschreitenden Miniaturisierung zu überwinden. Im Rahmen dieser Arbeit wurde ein Modell entwickelt, das die Simulation von Topographieänderung bei der Anwendung der lokalen anodischen Oxidation ermöglicht. Die Topographieänderung wurde unter Verwendung der Monte Carlo-Methode modelliert, wobei die Partikelverteilung der Oberflächenladungsdichteverteilung folgt. Die Ladungsverteilung entsteht durch ein starkes elektrisches Feld zwischen der Rasterkraftmikroskopnadel und dem Siliziumwafer.

Eine ähnliche Situation findet man auch bei EEPROM Speicherzellen, die nach derzeitigem Stand der Prozesstechnik nicht weiter miniaturisiert werden können. Aus diesem Grund werden dreidimensionale Strukturen eingeführt, die eine Erhöhung der Anzahl der verfügbaren Speicherzellen ermöglicht ohne dabei mehr Oberfläche zu beanspruchen. Für die Herstellung eines Ätzprofils hierzu wurde, im Rahmen dieser Arbeit, ein Ätzmodell für Bit Cost Scalable (BiCS) Speicherzellen im Level Set-Framework entwickelt.

Weiters wurde ein Sprühpyrolyse-Abscheidungsmodell entwickelt und in das Level Set-Framework integriert. Diese Prozessmethode ermöglicht eine Abscheidung dünner Schichten, die unter anderem bei Solarzellen und Gassensoren Verwendung finden. Es wurden zwei Modelle für die Topographieänderung infolge des Sprühpyrolyse-Prozesses präsentiert, davon eines mit einem Elektro- und eines mit einem Druckzerstäuber. Das erste Modell beschreibt eine schichtweise Abscheidung einzelner Tröpfchen beim Aufprall auf den Wafer. Beim zweiten Modell verdampfen die Tröpfchen kurz vor dem Aufprall und ein CVD-ähnlicher Schichtzuwachs erfolgt.

Acknowledgement

First and foremost, I would like to thank my advisor Prof. Siegfried Selberherr for providing me with a supportive working environment, where I was able to pursue my ideas and attend numerous international conferences, where I was able to collaborate and exchange ideas with the world's leading experts.

I would also like to thank Dr. Hajdin Ceric for positively responding to my initial interest in coming to the Institute for Microelectronics and for the opportunities provided through the Christian Doppler Laboratory for Reliability Issues in Microelectronics.

Additional thanks go to Giorgio Mutinati, Elise Brunet, Stephan Steinhauer, and Dr. Anton Köck from the Austrian Institute of Technology (AIT) for sharing with me their expertise and insights into the spray pyrolysis deposition process.

I am grateful to Dr. Otmar Ertl for introducing me to topography simulations and the Level Set framework, which is simultaneously a joy and challenge to work with. Additional thanks go to Ines Anzenbacher, Dr. Ceric, and Dr. Thomas Windbacher for their assistance with the abstract translation to German.

I am very grateful to all my colleagues for making me feel like a part of a big collective and making it a pleasure to come to work every day.

To Ines Anzenbacher, I am grateful for showing me that an exceptional work environment is not the only reason to fall in love with Austria.

To my parents, who have sacrificed very much in their lives in order to provide me with a life where I feel that every goal is within my reach, I am and forever remain grateful.

Lastly, many thanks go to my sister, Lidija Filipovic, for her many helpful comments regarding the technical aspects of this work. In addition, her constant support and belief in my abilities have shown me what it is like to go through life with my biggest fan always by my side, cheering me on.

Contents

| | |
|-------------------------------------------------------------------------|-------------|
| Abstract | ii |
| Kurzfassung | iii |
| Acknowledgement | iv |
| Contents | v |
| List of Figures | viii |
| List of Tables | xiii |
| List of Abbreviations | xiv |
| List of Symbols | xvi |
| 1. Introduction | 1 |
| 1.1. Traditional Semiconductor Process Technologies | 1 |
| 1.1.1. Lithography | 1 |
| 1.1.2. Etching | 1 |
| 1.1.3. Deposition | 2 |
| 1.1.4. Chemical Mechanical Planarization | 2 |
| 1.1.5. Oxidation | 2 |
| 1.1.6. Ion Implantation | 3 |
| 1.1.7. Diffusion | 3 |
| 1.2. Approaches to Semiconductor Modeling | 3 |
| 1.2.1. Atomistic Approach | 4 |
| 1.2.2. Continuum Approach | 5 |
| 1.3. Motivation for Novel Processing Techniques | 6 |
| 1.4. Simulator Implementation | 8 |
| 1.4.1. Fast Level Set Framework | 9 |
| 1.4.2. Surface Rate Calculation | 11 |
| 1.5. Outline of the Thesis | 15 |
| 2. Silicon Oxidation Techniques | 17 |
| 2.1. Silicon Dioxide Properties | 18 |
| 2.1.1. Molecular Structure of the Silicon-Silicon Dioxide Interface . . | 21 |

| | | |
|-----------|--------------------------------------------------------------------|------------|
| 2.2. | Thermal Oxidation of Silicon | 22 |
| 2.2.1. | Kinetics and Growth of Silicon Dioxide | 24 |
| 2.3. | Linear Parabolic Description of Thermal Oxidation Growth | 29 |
| 2.3.1. | Deal-Grove Model | 30 |
| 2.3.2. | Limitations of the Deal-Grove Model | 37 |
| 2.3.3. | Massoud Model | 37 |
| 2.3.4. | Other One-Dimensional Oxide Growth Models | 40 |
| 2.4. | Local Oxidation Nanolithography | 41 |
| 2.4.1. | Technology Background | 43 |
| 2.4.2. | Scanning Tunneling Microscope Lithography | 44 |
| 2.4.3. | Atomic Force Microscope Lithography | 46 |
| 3. | Simulating Silicon Oxidation | 50 |
| 3.1. | Thermal Oxidation Simulators | 50 |
| 3.1.1. | History of Oxidation Simulators | 50 |
| 3.1.2. | Visco-Elastic model using FEM | 52 |
| 3.1.3. | Simulating Oxide Growth using Volume Expansion | 53 |
| 3.2. | Oxidation Modeling using Linear Parabolic Equations | 55 |
| 3.2.1. | Multiple moving interfaces | 55 |
| 3.2.2. | Separating Material Interfaces | 58 |
| 3.2.3. | LS Surface Vector Motion | 58 |
| 3.3. | Nitric Acid Oxidation | 61 |
| 3.3.1. | NAOS Modeling | 62 |
| 3.4. | Local Oxidation Nanolithography | 65 |
| 3.4.1. | AFM Oxidation Mechanism and Kinetics | 65 |
| 3.4.2. | Empirical Models for LON | 67 |
| 3.4.3. | Nanodot Modeling Using the MC Method | 76 |
| 4. | Novel Deposition and Etch Techniques | 87 |
| 4.1. | Spray Pyrolysis Deposition | 87 |
| 4.1.1. | Technology Background | 88 |
| 4.1.2. | Atomization Procedure | 89 |
| 4.1.3. | Aerosol Transport of Droplets | 91 |
| 4.1.4. | Precursor Decomposition | 94 |
| 4.2. | Bit Cost Scalable Memory Holes | 96 |
| 4.2.1. | Technology Background | 96 |
| 4.2.2. | Etching of Silicon Dioxide | 98 |
| 4.2.3. | Etching of Silicon | 99 |
| 5. | Simulating Deposition and Etch Processes | 100 |
| 5.1. | Spray Pyrolysis Deposition Modeling | 100 |
| 5.1.1. | Modeling Droplet Atomization | 101 |
| 5.1.2. | Modeling Droplet Transport | 102 |
| 5.1.3. | Modeling Interaction between Droplet and Wafer Surface | 111 |

| | |
|--------------------------------------------------------------------------|------------|
| 5.2. Modeling BiCS Memory Hole Etching | 112 |
| 5.2.1. Carbon Fluorides for Silicon Dioxide Etching | 112 |
| 5.2.2. Halogen Gas for Silicon Etching | 115 |
| 6. Applications | 118 |
| 6.1. Silicon Oxidation | 118 |
| 6.1.1. Oxide Growth without Native Oxide | 118 |
| 6.1.2. Oxide Growth with Native Oxide Present | 119 |
| 6.1.3. Oxidation with Orientation effects | 121 |
| 6.1.4. Oxidation with LOCOS | 121 |
| 6.2. Nitric Acid Oxidation | 124 |
| 6.3. Atomic Force Microscope Lithography | 124 |
| 6.3.1. AFM Nanodot Generation | 125 |
| 6.3.2. AFM Nanowire Generation | 126 |
| 6.3.3. High Density Data Storage using AFM | 127 |
| 6.3.4. Silicon Nanowire Transistor | 131 |
| 6.4. Spray Pyrolysis Deposition | 132 |
| 6.4.1. YSZ Deposition using ESD Pyrolysis | 135 |
| 6.4.2. Tin Oxide Deposition using PSD Pyrolysis | 138 |
| 6.5. BiCS Memory Hole Etching | 141 |
| 7. Summary and Outlook | 143 |
| A. Droplet Transport Equations for Spray Pyrolysis Modeling | 145 |
| A.1. Transport under a Velocity-Dependent Acceleration | 145 |
| A.2. Transport under a Velocity- and Displacement-Dependent Acceleration | 147 |
| B. Generating a Distribution for the Droplet Radius | 151 |
| Bibliography | 154 |
| List of Publications | 173 |
| Curriculum Vitae | 175 |

List of Figures

| | |
|----------------------------------------------------------------------------------------------------------------------------------------------------------------------------------------------|----|
| 1.1. Comparison of sizes of semiconductor manufacturing process nodes since the early 1970s. | 7 |
| 1.2. Numbering of material regions in (a) leads to the Level Set description in (b). | 11 |
| 1.3. The simulation of particle transport, which is divided into the reactor-scale and feature-scale regions. | 12 |
| 2.1. Difference in uses of thermally grown versus deposited silicon dioxide in silicon technology. | 18 |
| 2.2. (a) Structure of fused silica glass along with (b) a six-membered ring structure of SiO_2 | 20 |
| 2.3. Moving interfaces and volume expansion after silicon oxidation. | 21 |
| 2.4. Atomistic configurations of the Si- SiO_2 interface. | 22 |
| 2.5. LOCOS processing steps | 23 |
| 2.6. STI processing steps | 24 |
| 2.7. Oxide thickness versus oxidation time for dry (O_2) oxidation of a (100) oriented silicon wafer under various temperatures. | 25 |
| 2.8. Oxide thickness versus oxidation time for wet (H_2O) oxidation of a (100) oriented silicon wafer under various temperatures. | 26 |
| 2.9. Oxide thickness versus process temperature for wet (H_2O) and dry (O_2) oxidation of a (100) oriented silicon wafer at 1000°C | 27 |
| 2.10. Effects of hydrostatic pressure on thermally grown oxide thickness for a (100) oriented silicon wafer in a) dry (O_2) and b) wet (H_2O) ambients. | 28 |
| 2.11. Oxide thickness versus oxidation time for (100) and (111) oriented silicon by wet oxidation at various temperatures. | 29 |
| 2.12. One-dimensional Deal-Grove model for the oxidation of silicon. | 30 |
| 2.13. Comparison between the Deal Grove and Massoud models for the oxide thickness during the first hour of oxidation in a dry ambient on (100) oriented silicon. | 40 |
| 2.14. Typical STM schematic for surface imaging. | 44 |
| 2.15. Typical AFM schematic for surface imaging. | 45 |
| 2.16. Generation of a water meniscus between the AFM tip and silicon substrate after a negative voltage is applied. | 46 |

| | |
|----------------------------------------------------------------------------------------------------------------------------------------------------------------------------------------------------------------------------------------------------------|----|
| 3.1. Modeling approach when a single LS interface is split into two interfaces, which move in opposite directions for a 500×500 geometry moving at velocities 0.25 and -0.75 for the top and bottom surfaces, respectively. | 56 |
| 3.2. Modeling approach when the initial LS geometry contains two interfaces which need to be moved in opposite directions, for a 500×500 geometry at velocities 0.25 and -0.75 for the top and bottom surfaces, respectively. | 57 |
| 3.3. Modeling approach when the initial LS geometry contains two interfaces, one a mask and one a surface to be grown. A $15 \times 15 \times 5$ geometry is used. | 58 |
| 3.4. Geometry of a mask and its LS labeling when the mask is used for a material growth or deposition process. | 59 |
| 3.5. The initial and final geometry after surface evolution of Φ_{down} downward and Φ_{up} upward at rates of -0.25 and 0.75, respectively. | 60 |
| 3.6. Simulation of the translation of a sphere under vector motion. The sphere has a radius of 50 grid points and is moving downward at a rate of 1 grid point per time unit for 250 time units. | 60 |
| 3.7. Phase diagram of the Nitric acid ($\text{HNO}_3/\text{H}_2\text{O}$) system. | 62 |
| 3.8. The dependence of immersion time and temperature on the growth of NAOS oxide submersed in a 61wt% HNO_3 solution. | 63 |
| 3.9. Plots of the SiO_2 thickness with respect to the oxidation time at different temperatures when the vapor NAOS method is used. Dots are experimental results from [103] and lines are the results of the presented empirical model. | 65 |
| 3.10. Oxidation driven by oxyions, which are generated due to the presence of the strong electric field, interacting with the silicon surface. | 66 |
| 3.11. Modeling approach for a hemispherical AFM needle tip versus a rough AFM needle tip. (a) Dot charge used to model AFM with a hemispherical needle tip and (b) Ring of charges used to model AFM with a rough needle tip. | 67 |
| 3.12. The width of the oxide lines on a silicon substrate as a function of the applied bias, from [109]. | 70 |
| 3.13. Height of the oxide as a function of the applied voltage, as presented in [192] and implemented in the presented simulator. | 72 |
| 3.14. FWHM of the oxide as a function of the applied voltage. Measurements are from [192], while the simulations are from (3.44). | 73 |
| 3.15. Height and width of the oxide nanodot as a function of the applied voltage and pulse time. | 74 |
| 3.16. Effects of humidity on the nanodot height and width, as presented in [53]. | 74 |
| 3.17. Effects of time, voltage, humidity, and orientation on the nanowire height and width. Experimental (dots) and model (lines) values are shown. | 76 |

| | |
|---------------------------------------------------------------------------------------------------------------------------------------------------------------------------------------------------------------------------------------------------------------------------------------------------------------------|-----|
| 3.18. Effects of wire orientation on the nanowire height and width, with $t=0.1\text{ms}$, $V_b=7\text{V}$, and $h=55\%$. The vertical axis is scaled by 100 for better visualization. The top surface represents the oxide-ambient interface, while the lower surface represents the oxide-silicon interface. . | 77 |
| 3.19. Image representation of the MC method of “imprinting” a desired particle distribution onto the silicon surface in order to generate an oxide growth. The particles are accelerated using ray tracing techniques within the LS simulator environment. | 78 |
| 3.20. Flow chart of the simulation process implementing the Monte Carlo method with ray tracing in a LS environment. | 79 |
| 3.21. Nanodot generated using Gaussian particle distribution. The vertical dimension has been scaled by 20 for better visualization. (a) NCM nanodot generated using a Gaussian distribution of particles and (b) Diagonal cross-section of the nanodot from Figure 6.13a | 80 |
| 3.22. (a) Comparison between the Gaussian distribution and the surface charge density and (b) comparison between the Lorentzian distribution and the surface charge density. | 80 |
| 3.23. Cross-sectional nanodot height generated using a Lorentzian distribution. | 82 |
| 3.24. The vertical dimension has been scaled by 20 for better visualization. (a) NCM nanodot generated using a Lorentzian distribution of particles and (b) Diagonal cross-section of the nanodot from Figure 3.24a. | 83 |
| 3.25. Normalized effective nanodot cross section height and the normalized SCD function. | 86 |
| 3.26. The effective diagonal cross-section height of a nanodot when using a rough AFM needle tip versus a hemispherical AFM needle tip. | 86 |
| 4.1. Summary of chemical thin film deposition technologies. | 87 |
| 4.2. General schematic of a spray pyrolysis deposition process. | 88 |
| 4.3. Single jet and multi jet modes of electrostatic spray deposition. | 90 |
| 4.4. Spray pyrolysis droplets modifying as they are transported from the atomizing nozzle to the substrate. Whether the temperature [216] or the initial droplet size [187] are varied, there are four potential paths which the droplet can take as it moves towards the substrate (A-D). . | 91 |
| 4.5. Air temperature above a heated plate for substrate temperatures 210°C , 250°C , 310°C , and 400°C during a pressurized spray process. | 94 |
| 4.6. Technology scaling for FLASH memory. | 97 |
| 4.7. Image of a typical BiCS structure with memory holes. | 98 |
| 5.1. The droplet transport in the space above the substrate surface and the accelerations which are considered in the transport model. T_{th} is the height of the thermal zone ($\sim 10\text{mm}$ for ESD, $\sim 5\text{mm}$ for PSD), and H is the distance between the substrate and atomizer. | 103 |

| | | |
|------|------------------------------------------------------------------------------------------------------------------------------------------------------------------------------------------------------------------------------------------------------------------------------------------------------------------------------------------------------------------------------------------------------------------------------------|-----|
| 5.2. | The effects of varying the atomizing nozzle's outer radius on the strength of the electric field with and without the inclusion of the K_V effects. . | 108 |
| 5.3. | Magnitude of the normalized electric potential Φ/Φ_0 during ESD processing. The distance between needle and deposition plate as well as the radial distance from the center are normalized to the distance between the atomizer and the substrate. The inset is the normalized electric field distribution. | 109 |
| 5.4. | Droplet impact onto a heated surface, resulting in the spreading of a thin film in a disc-like shape. | 111 |
| 5.5. | Two-dimensional image of the hole which needs to be etched through layers of Si and SiO ₂ in order to generate a BiCS structure. | 112 |
| 5.6. | Images showing the etched SiO ₂ topography when using a fluorocarbon gas as the etchant, implemented using the described model. | 115 |
| 5.7. | Images showing the etched SiO ₂ topography when using fluorocarbon gas as the etchant for various polymer sticking coefficients s_p | 116 |
| 5.8. | The effects of SiO ₂ tapered angles during silicon etching using a HBr/O ₂ plasma. | 117 |
| 6.1. | Results of the oxidation of (100) oriented silicon in a dry ambient at 1atm pressure and 1000°C temperature for 100 minutes. The top surface (red) depicts the SiO ₂ -ambient interface, while the lower surface (blue) depicts the location of the Si-SiO ₂ interface. The volume shown is the original location of the silicon substrate. | 119 |
| 6.2. | Results of the oxidation of (100) oriented silicon in a dry ambient at 1atm pressure and 1000°C temperature for 100 minutes with 10nm of native oxide present. The top surface (red) depicts the SiO ₂ -ambient interface, while the lower surface (blue) depicts the location of the Si-SiO ₂ interface. The volumes shown are the original location of the silicon substrate and the native oxide. | 120 |
| 6.3. | Results of the oxidation of a trench etched into (100) oriented silicon with (110) oriented sidewalls. in a dry ambient at 1atm pressure and 1000°C temperature for 100 minutes. The top surface (red) depicts the SiO ₂ -ambient interface, while the lower surface (blue) depicts the location of the Si-SiO ₂ interface. The volumes shown is the original location of the silicon trench. | 122 |
| 6.4. | Geometry of the bird's beak occurrence during LOCOS processing. H_{bb} and L_{bb} describe the maximum height and length of the nitride after oxidation, respectively. | 123 |
| 6.5. | Bird's beak length and height dependences on nitride and pad oxide thicknesses from [190]. The field oxide is simulated to grow at 1000°C for a thickness of approximately 600nm. | 123 |

| | |
|-------------------------------------------------------------------------------------------------------------------------------------------------------------------------------------------------------------------------------------------------------------------------------------------------------------------------------------------------------------------------------------------|-----|
| 6.6. Thermal oxidation with the bird's beak effect. The field oxide is simulated to grow on (100) silicon at 1000°C in a wet environment for 2 hours, resulting in a field oxide thickness of approximately 600nm. The oxide thickness is 15nm and the nitride thickness is (a)-(b) 200nm and (c)-(d) 100nm. | 124 |
| 6.7. Results of the oxidation of (100) oriented silicon during immersion in a 61wt% HNO ₃ concentration at a temperature of 60°C. The top surface (red) depicts the SiO ₂ -ambient interface, while the lower surface (blue) depicts the location of the Si-SiO ₂ interface. The volume shown is the original location of the silicon substrate. | 125 |
| 6.8. Effects of pulse time on the AFM nanodot height and width. The vertical axis is scaled by 20 for better visualization. | 126 |
| 6.9. Effects of ambient humidity on the AFM nanodot height and width. The vertical axis is scaled by 20 for better visualization. | 126 |
| 6.10. Effects of bias voltage on the AFM nanodot height and width. The vertical axis is scaled by 20 for better visualization. | 127 |
| 6.11. Nanowire topography simulated using a sequence of AFM nanodots (top) and the nanowire's cross-section (bottom). | 128 |
| 6.12. Simulations of AFM-generated nanowires. | 129 |
| 6.13. Simulations of AFM-generated nanodots for ROM applications. (a) Image of π in binary code, written with oxide nanodots on a silicon surface from [59]. (b) Simulated image of π in binary code, repeating the experiment from [59], with inset of a proportional Figure 6.13c. (c) Simulated image of π in binary code. with improved aerial density. . . | 130 |
| 6.14. SiNWT generated using AFM nanolithography and wet etching [85]. . | 132 |
| 6.15. (a)-(b) Topography simulation steps for the fabrication process for a silicon nanowire transistor. (a) Initial lithography to place oxide as a mask for source, drain, and gate contacts. (b) Nanowire generated using AFM to connect the source and drain contacts. | 133 |
| 6.15. (c)-(d) Topography simulation steps for the fabrication process for a silicon nanowire transistor. (c) TMAH etching of silicon, with SiO ₂ serving as a mask. (d) HF etching of SiO ₂ , leaving the desired pattern on the silicon surface. | 134 |
| 6.16. Macroscopic spray pyrolysis simulation on a 50mm by 50mm geometry. Each spray cycle contains 100,000 droplets. | 137 |
| 6.17. Microscopic spray pyrolysis simulation on a 250 μ m by 250 μ m geometry. | 138 |
| 6.18. Schematic for the PSD spray pyrolysis process used at AIT, serving as a basis for the presented topography simulations. | 139 |
| 6.19. Images showing the deposited SnO ₂ film as a results of a PSD deposition step. The good step coverage confirms a chemical and not physical reaction takes place during deposition. | 140 |
| 6.20. The initial and final topographies after applying Si and SiO ₂ etching models for the fabrication of BiCS memory holes. | 142 |

List of Tables

| | |
|---------------------------------------------------------------------------------------------------------------------------------------------------------------------------------------------------------------------------------------------------------------------------------|-----|
| 2.1. Important properties of silicon dioxide (SiO_2). | 19 |
| 2.2. Rate constants describing (111) oriented silicon oxidation kinetics at 1atm pressure. For the corresponding values for (100) oriented silicon, C_2 values should be divided by 1.68. | 35 |
| 2.3. Rate constants describing oxidation kinetics at 1atm pressure using the Massoud model for various silicon orientations and temperatures from [143]. | 38 |
| 2.4. Arrhenius expressions for pre-exponential constants K_1^0 and K_2^0 , time constants τ_1^0 and τ_2^0 , and activation energies E_{K_1} , E_{K_2} , E_{τ_1} , and E_{τ_2} from the Massoud model presented in [143] and given in (2.40)-(2.44). | 39 |
| 3.1. Effects of wire orientation on the nanowire height and width, with $t=0.1\text{ms}$, $V_b=7\text{V}$, and $h=55\%$. | 75 |
| 4.1. Characteristics of atomizers commonly used for spray pyrolysis. | 89 |
| 6.1. Characteristics of the precursor solutions used for the simulations. | 136 |

List of Abbreviations

| | |
|--------------|--------------------------------------------------|
| AFM | atomic force microscope |
| ALE | atomic layer epitaxy |
| BiCS | bit cost scalable |
| CM | contact mode |
| CMOS | complementary metal oxide semiconductor |
| CMP | chemical mechanical planarization |
| CPD | cumulative probability distribution |
| CVD | chemical vapor deposition |
| DC-SF | dual control-gate with surrounding floating-gate |
| DFT | density functional theory |
| DTG | dynamic tubular grid |
| ESD | electrostatic spray deposition |
| EUV | extreme ultraviolet |
| FDM | finite difference method |
| FEM | finite element method |
| FN | Fowler-Nordheim |
| FWHM | full width at half maximum |
| H-RLE | hierarchical run length encoding |
| HPCVD | high pressure chemical vapor deposition |
| HTO | high temperature oxide |
| IC | integrated circuit |
| ICM | intermittent contact mode |
| LAO | local anodic oxidation |
| LCD | liquid crystal display |
| LOCOS | local oxidation of silicon |
| LON | local oxidation nanolithography |
| LS | Level Set |
| MC | Monte Carlo |
| MOS | metal oxide semiconductor |
| MPI | message passing interface |
| NAOS | nitric acid oxidation of silicon |
| NCM | non-contact mode |
| PDF | probability density function |
| PECVD | plasma enhanced chemical vapor deposition |
| PSD | pressurized spray deposition |
| PVD | physical vapor deposition |

| | |
|--------------|-----------------------------------|
| RAH | relative air humidity |
| RF | radio frequency |
| RLE | run length encoding |
| ROM | read only memory |
| RTA | rapid thermal annealing |
| SCD | surface charge density |
| SiNWT | silicon nanowire transistor |
| SOI | silicon on insulator |
| SPM | scanning probe microscopy |
| STI | shallow trench isolation |
| STM | scanning tunneling microscope |
| TCAD | technology computer aided design |
| TCAT | terabit cell array transistor |
| TEOS | tetraethyl orthosilicate |
| TFT | thin film transistor |
| TM | tapping mode |
| TMAH | tetramethylammonium hydroxide |
| TVD | total variation diminishing |
| UHV | ultra high vacuum |
| USB | universal serial bus |
| UV | ultraviolet |
| VSAT | vertical stacked array transistor |
| YSZ | yttria-stabilized zirconia |

List of Symbols

Level Set Framework

| | |
|-------------------------|--------------------------------------------------------------------|
| F | Flux on surface \mathcal{S} |
| F^{src} | Flux on source plane \mathcal{P} |
| F^{tot} | Total flux through plane \mathcal{P} |
| G | Re-emission probability function |
| H | Hamiltonian |
| \mathcal{L} | Layer of grid points, $\mathcal{L} \subseteq \mathcal{G}$ |
| M | Number of different material regions |
| \mathcal{M} | Material region number |
| \hat{n} | Normal unit vector on \mathcal{S} |
| $\vec{n}_{\mathcal{P}}$ | Normal unit vector on \mathcal{P} pointing towards \mathcal{S} |
| p | Pressure |
| \vec{p} | Grid point index |
| \mathcal{P} | Source plane |
| q | Particle species |
| \hat{r} | Unit vector in the direction of vector motion |
| R | Surface rate |
| \mathcal{S} | Description of the LS surface |
| t | Process time |
| $V(\vec{x})$ | Surface velocity |
| \vec{x} | Point in space, $\vec{x} = (x_1, \dots, x_D) \in \mathbb{R}$ |
| Y^{tot} | Total sputter rate |
| Γ | Flux distribution on \mathcal{S} |
| η | Surface reaction order |
| κ | Mean curvature |
| ν | Exponent in power cosine distribution |
| ρ | Bulk density |
| Θ | Surface coverage |

Oxidation of Silicon

| | |
|-------------|---------------------------------------------------------------|
| B | Parabolic rate constant |
| B/A | Linear rate constant |
| C^* | Equilibrium concentration of oxidants in the ambient |
| C_O | Concentration of oxidants at the oxide surface |
| C_S | Concentration of oxidant at the Si-SiO ₂ interface |
| D | Diffusivity |
| h | Gas-phase transport coefficient |
| H | Inverse Henry's law constant |
| H_{bb} | Maximum height of the nitride after oxidation |
| F_1 | Oxidant flux entering the gas ambient from the bulk |
| F_2 | Oxidant flux diffusing through the oxide |
| F_3 | Oxidant flux reacting on the silicon surface |
| k_B | Boltsmann constant |
| k_s | Reaction rate at the Si-SiO ₂ interface |
| L_{bb} | Maximum length of the nitride after oxidation |
| N | Number of oxidant molecules per unit volume of oxide grown |
| N_{Si} | Molecular density of silicon |
| N_{SiO_2} | Molecular density of silicon dioxide |
| p | Partial pressure |
| t | Time |
| T | Temperature |
| x_i | Initial oxide growth |
| x_o | Oxide thickness |
| τ | Time parameter accounting for x_i |

AFM Nanolithography

| | |
|--------------------|---------------------------------------------------------|
| $2a'$ | Barrier width between two interstitial sites |
| C | Normalization constant |
| D | Distance of point charge from the silicon surface |
| E_0 | Fitting parameter $E_0 = 45\text{V/nm}$ |
| $\vec{E}(\vec{p})$ | Electric field strength at \vec{p} |
| h | Humidity |
| $h(t, V_b)$ | Nanodot height |
| M | Lorentz distribution r_{max} dependent constant |
| N | Total number of charged dots for a rough needle tip |
| q | Electronic charge of an electron |
| Q | Effective point charge |
| Q_{tot} | Total effective charge after adding all point charges |
| r | Desired distribution along the radius |
| R | Fitting parameter ($1.5 \times 10^3 \text{nm/s}$) |
| t | Pulse time |
| $V(\vec{p})$ | Applied potential at point \vec{p} |
| V_b | Bias voltage |
| $w(t, V_b)$ | Nanodot width, full width at half maximum |
| x_r | Value distributed according to the desired distribution |
| $\Phi(r)$ | CPD function |
| $\sigma(x, y, z)$ | Surface charge density on the wafer surface |
| σ_{max} | maximum surface charge density |
| θ | Wire orientation with respect to the (010) direction |
| ξ | Evenly distributed value |

Spray Pyrolysis

| | |
|--------------|--------------------------------------------------------------|
| $a_r(t)$ | Radial droplet acceleration |
| $a_v(t)$ | Vertical droplet acceleration |
| c_{ev} | Vertical linearization constant for the electric field |
| $d_r(t)$ | Radial droplet displacement |
| $d_v(t)$ | Vertical droplet displacement |
| $D_{v,f}$ | Average diffusion coefficient |
| E | Generated electric field strength |
| F_e | Force due to the applied electric field |
| F_g | Force due to gravity |
| F_S | Stokes force |
| F_t | Thermophoretic force |
| q_d | Droplet charge |
| q_{max} | Maximum droplet charge |
| H | Distance between wafer and atomizing nozzle |
| K | Surface evaporation rate |
| l | Effect of the thermophoretic force on droplet's acceleration |
| K_V | H/R ratio dependent value |
| M_W | Molecular weight of evaporating liquid |
| N_A | Avogadro's number |
| r_d | Droplet radius |
| r_n | Nozzle outlet radius |
| R | Outer nozzle radius |
| Re | Reynolds number |
| Sc | Schmidt's number |
| t_{life} | Lifetime of a droplet traveling through a heated ambient |
| t_{th} | Thickness of the thermal zone |
| T_a | Air temperature |
| T_d | Droplet temperature |
| ∇T_a | Air temperature gradient |
| v_a | Air velocity |
| $v_r(t)$ | Radial droplet velocity |
| $v_v(t)$ | Vertical droplet velocity |
| W_{crit} | Critical Weber number |
| γ | Liquid-gas surface tension |
| η_a | Viscosity of air |
| κ_a | Conductivity of air |
| κ_d | Conductivity of droplet |
| ρ_a | Density of air |
| ρ_d | Droplet density |
| ρ_e | Fluid charge density |
| Φ_0 | Applied electrical potential |
| Φ^* | Normalized potential (Φ/Φ_0) |

BiCS Memory Hole Etching

| | |
|------------------------|---------------------------------------------------|
| $DR_p(\vec{x})$ | Deposition rate during SiO ₂ etching |
| $ER_p(\vec{x})$ | Polymer etch rate during SiO ₂ etching |
| $F_{Br}(\vec{x})$ | Bromine flux |
| $F_O(\vec{x})$ | Oxygen flux |
| $F_e(\vec{x})$ | Total etchant flux |
| $F_i(\vec{x})$ | Total ion flux |
| $F_p(\vec{x})$ | Total polymer flux |
| k | Bromine chemical etch rate constant |
| $V_{SiO_2}(\vec{x})$ | SiO ₂ etch rate |
| β | Oxygen chemical etch rate constant |
| $\Theta_{Br}(\vec{x})$ | Bromine coverage during silicon etching |
| $\Theta_O(\vec{x})$ | Oxygen coverage during silicon etching |
| $\Theta(\vec{x})_e$ | Etchant surface coverage |
| $\Theta(\vec{x})_e/p$ | Surface coverage of active sites on polymer |
| $\Theta(\vec{x})_p$ | Polymer surface coverage |

1. Introduction

1.1. Traditional Semiconductor Process Technologies

The fabrication of silicon-based integrated circuits (ICs) begins with a uniformly doped silicon wafer. A set of sequential processing steps generates the required geometries in order to obtain a desired device. The most commonly used processing steps for IC fabrication are lithography, etching, deposition, chemical mechanical planarization (CMP) oxidation, ion implantation, and diffusion. Those processes are briefly discussed in this section.

1.1.1. Lithography

Lithography is a general name given to a series of processing steps which transfer the information from a mask to a desired surface. Essentially, these steps are used to selectively remove material from the wafer surface. Initially, a photoresist is deposited on the wafer surface and desired areas of the photoresist are exposed to ultraviolet (UV) or other radiation using a photomask to allow the rays access to desired photoresist areas. The wafer is then placed in a developer, where the portions of the photoresist exposed to (for positive resists) or protected from (for negative resists) the UV rays are removed. The surface below the photoresist can now be etched with the photoresist serving as an etching mask for further processing steps.

1.1.2. Etching

Etching is a commonly used process in microelectronics. It is used to partly or fully remove materials in order to generate desired patterns on a wafer surface during device manufacturing. The two main properties of the etching process are its selectivity and isotropy. Selectivity refers to the etchant's ability to remove a certain material while leaving another material in tact to serve as an etchant mask. Isotropy refers to the etchant's ability to remove materials in multiple directions. When a mask is used, isotropy determines how much underetch occurs below the mask.

The common etching processes are wet, which use liquids which chemically react with the materials in question and dry, which use a plasma process where ions and neutral radicals are accelerated toward the surface required to be etched and the physical

interaction between the accelerated ions and neutral radicals cause the removal of a material. Wet chemical processes are frequently isotropic, etching in all directions with the same rate. However, they can also be anisotropic by causing an etch rate which varies with different material crystalline orientation. Underetch frequently occurs during chemical etching processes. A plasma process is more anisotropic, where the etch rate is mainly in the direction of the accelerating ions. However the neutral radicals which are natively isotropic also play a role in the etching process causing some isotropy in plasma etching as well.

1.1.3. Deposition

The ability to deposit films on a semiconductor wafers is an essential building block of IC fabrication. A variety of processing methods are in use today and the most important among them can be divided between physical vapor deposition (PVD) and chemical vapor deposition (CVD). PVD refers to a variety of deposition processes which are performed in a vacuum environment. No chemical reaction occurs at the deposition site, but rather a material is released from a source and transferred to the substrate. The most commonly used PVD processes are evaporation and sputtering. CVD, on the other hand, relies on a chemical reaction at the deposition site in order for a new material to be generated. A high deposition temperature is usually required in order to drive the reaction and the resulting thin film has a very good step coverage and better uniformity when compared to PVD.

1.1.4. Chemical Mechanical Planarization

CMP is a process which combines chemical and physical mechanisms in order to smooth desired surfaces and flatten an irregular wafer surface. Imperfections in wafer topology can lead to adverse affects in the lithographic process used to etch a desired pattern on the wafer. Many modern devices contain multiple layers, which makes it difficult for the photolithographic optical tools to maintain their focus. Applying a CMP step after each material deposition improves material planarity and a high manufacturing yield can still be maintained with coarse photolithographic steps.

1.1.5. Oxidation

A highly relevant reason why silicon has become such an important material in the microelectronics industry and IC fabrication is the relative ease with which it can be oxidized to form silicon dioxide (SiO_2) with good material properties. This process relies on providing an oxidant species (O_2 or H_2O), which reacts with the silicon atoms to grow silicon dioxide at high temperatures. The thermal oxidation process can be divided into two main mechanisms: dry oxidation, where the silicon wafer is placed in an oxygen gas ambient and wet oxidation, where the silicon wafer is placed in a water

ambient. However, silicon dioxide can also be deposited, which is the case, when it must be grown on non-silicon surfaces. This type of deposition is usually performed using tetraethyl orthosilicate (TEOS) or silane pyrolysis. The oxidation process is discussed in more detail in Chapter 2.

1.1.6. Ion Implantation

The ion implantation process is a technique by which dopants are introduced into the semiconductor. Ions of a desired material are accelerated via an electric field to impact a solid surface, in our context the silicon wafer. Dopant ions such as boron, phosphorus, or arsenic are generally created from a gas source, for purity reasons, prior to their acceleration towards the silicon interface, where they penetrate into the silicon crystalline lattice. After the penetration into the top layers of the lattice, an annealing step is performed, resulting in the generation of a charge carrier in the semiconductor for each dopant atom in the lattice. The generated charge carrier can be a hole or an electron depending on whether the dopant used is of p-type or n-type, respectively. An alternative doping method for semiconductors is the diffusion of dopants into the material. Some advantages of ion implantation over diffusion, as described next, are the short process times, good homogeneity and reproducibility, relatively low temperatures required during processing, a range of materials being available as masks (oxide, nitride, metals, resist, etc.), and the ability to implant thin layers, resulting in surfaces with high dopant concentration gradients.

1.1.7. Diffusion

The diffusion of dopants from the wafer surface into the semiconductor is an alternative to ion implantation for the introduction of charge carriers. The dopants can be introduced as a gas, a liquid, or from a previously deposited layer, which provides a constant concentration at the semiconductor interface. The depth of diffusion within the semiconductor is a function of temperature, so it must be carefully executed in order for further processing steps which require high temperatures, such as oxidation, do not damage the desired dopant concentration profile. The main advantages of diffusion over ion implantation is that diffusion does not cause damage to the semiconductor surface, since there is no ion bombardment of the surface, and it is able to create very shallow and predictable charge concentration profiles.

1.2. Approaches to Semiconductor Modeling

There are two major approaches when considering semiconductor process simulations: the atomistic approach, which deals with molecular-level problems, and the contin-

uum approach which treats each material as one single entity with a single set of properties.

1.2.1. Atomistic Approach

Since all materials are made up of atoms, a material's atomic structure plays an essential role in determining material properties and deformations under various ambient conditions. Atomistic methods are used to describe fundamental properties of materials, material deformation during various processes, and material interfaces. Atomistic (or molecular) modeling attempts to model or mimic the behavior of molecules by implementing all available theoretical methods and computational techniques.

The goal of atomistic simulations is to understand and model the motion of each atom in the material, resulting in an analysis of the collective behavior of atoms. The collective behavior provides an understanding of material deformations, phase changes, stress and other phenomena, linking atomic scale events to material meso-scale phenomena. The information which is required on the molecular level in order for a simulation to proceed is the position of atoms, atom vibrations, atom velocities, forces acting on each atom, and the force exerted from an atom onto surrounding atoms.

One simulation method relies on placing atoms in an unstable environment, such as an oxide layer sharing a sharp interface with a crystalline silicon surface. The forces acting on the individual atoms will result in the interface rearranging into an environment where the interface is stable, meaning that the force exerted by each atom is equal to the force acted upon the atom.

Another method refers to introducing new atoms, such as oxygen, into a crystalline silicon environment. The forces exerted by the atom on the silicon structure can generate a simulation showing how the oxygen atom bonds with the surface silicon atoms.

The density functional theory (DFT) is a method in which atomic modeling is implemented in order to investigate the electronic structure of a many-body system. The properties of the system containing multiple electrons are determined with the use of functionals (functions of the spatially dependent electron density).

Ab-initio quantum chemistry methods are another form of molecular simulations which deal with quantum-level chemistry to calculate the ground state of individual atoms and molecules, as well as their excited and transition states which occur during chemical reactions. Calculations of quantum chemistry use semi-empirical or iterative solvers in order to deal with time dependent problems.

This leads to the main limitations of such methods - the computation time and cost increases as a power of the number of atoms involved in the simulation.

The main dilemmas which arise with simulations on the molecular level are based on timescales. No matter how many processors and how powerful the computer in use, often only nanosecond-long simulations can be performed. The time domain computation cannot be parallelized. In order to simulate the timely evolution of a large number of particles, statistical mechanics and stochastic methods are implemented. Therefore, in order to convert the microscopic information gathered through atomistic modeling to macroscopic properties such as pressure, stress, strain, energy, heat capacity, etc, statistical mechanic strategies are developed. Although atomistic simulations are very powerful and complement experiment and theory, the limitations with time simulations must be understood.

In order to deal with the large-scale problems introduced with atomistic simulations, stochastic techniques utilizing Monte Carlo (MC) methods are developed. They overcome some of the limitations of atomistic calculations, whereby the integration of all energies associated with the movement of atoms and electrons is replaced by a random walk of particles in order to measure desired properties. The geometry of the molecular system is probed with a random distribution, which enables the diffusion and other slower processes to be modeled. MC methods are very useful when systems with multiple degrees of freedom must be simulated. Such systems usually involve fluids, disordered materials, strongly coupled solids, and cell structures or extremely scaled down systems where atomistic and quantum properties cannot be neglected.

1.2.2. Continuum Approach

A material, whether it be solid, liquid, or gas, is composed of molecules separated by empty space. On a macroscopic scale, these materials have cracks, deformation and discontinuities, while some properties can be viewed as uniformly affecting the entire material as a continuum. Therein lies the basic concept of continuum mechanics. These properties are modeled with the assumption that the matter which composes the material fills the entire region of space which it occupies, with no cracks, deformation, different molecular structures, atoms, electrons, or distributed densities, but rather one single entity with a single set of parameters.

In semiconductor processing, various methods are implemented in order to modify wafer surfaces. There is value in analyzing the different materials and their changing interfaces on a molecular level using atomistic simulations. These simulations use cellular automata or MC techniques to describe interface changes. However, atomistic analysis are very computationally intensive and are limited to structures on the level of several molecules and simulations of several nanoseconds. In order to generate a simulation for a complete semiconductor process, a continuum model is the only viable method with current computer capabilities. Continuum modeling methods for physical phenomena are traditionally formed in terms of differential equations. These can describe an array of physical properties such as density, conductivity, diffusivity, etc. in addition to inter-material properties such as stress, strain, and cracking caused by

material deposition, growth, or interaction of highly charged ions with a material. The finite difference method (FDM) and finite element method (FEM) are numerical techniques which are widely used to study models based on partial differential equations for continuum mechanical modeling.

If the typical structure size is much larger than the typical lattice constant, the solid body under simulation should be represented as a continuum. When a simulation is only performed in order to predict the final shape of a given structure after one or several processing steps, then a continuum model involving a topography simulation is the sole requirement. These types of simulations do not offer physical material properties, but can be performed very quickly for large structures and for long simulation times. The Level Set (LS) method is one way in which topography simulations can be performed with high efficiency and speed [50]. A particular downside of topography processing is the assumption that material interfaces are abrupt and can be defined by a single surface evolution, which is known not to be the case for some complex processes such as oxidation. Another downside is that material properties relevant to the simulated processing steps are homogeneous within the material region. Although these downsides of topography processing exist, their efficiency and speed in the determination of material interfaces after one or several processing steps make them a valuable modeling tool. The scope of this work deals with modeling several processing techniques using continuum topography models within the LS environment.

1.3. Motivation for Novel Processing Techniques

In any research and technology field, there is a constant drive for innovation. Microelectronics, and more precisely, processing tools for microelectronics, are no exception. Since the initial introduction of the basic processing steps to generate transistors, there has been a constant innovation for new materials, structures, devices, and even processing steps. The first transistor has very few similarities to the common transistor in use today. Figure 1.1 depicts how the semiconductor technology has scaled since the early 1970's and some projections into the near future. It can be observed that Moore's law is still expected to endure for the next several years [154].

The reduction in size, which for the most part follows Moore's law, became only possible because of innovations in processing and material technologies. In order to continue this miniaturization trend, novel processing techniques have been introduced. Some of those processes and their modeling techniques are discussed in this work.

The constant reduction in device sizes demands a reduction in thermal oxidation times, since high temperature processes influence the distribution of impurities in the silicon bulk at the Si-SiO₂ interface. Therefore, a novel process is required which can grow high quality oxide at low temperatures. Although oxide deposition processes exist, which can deposit SiO₂ at low-enough temperatures, the grown oxide is of low quality. Recently, nitric acid oxidation of silicon (NAOS) has been suggested in order to solve

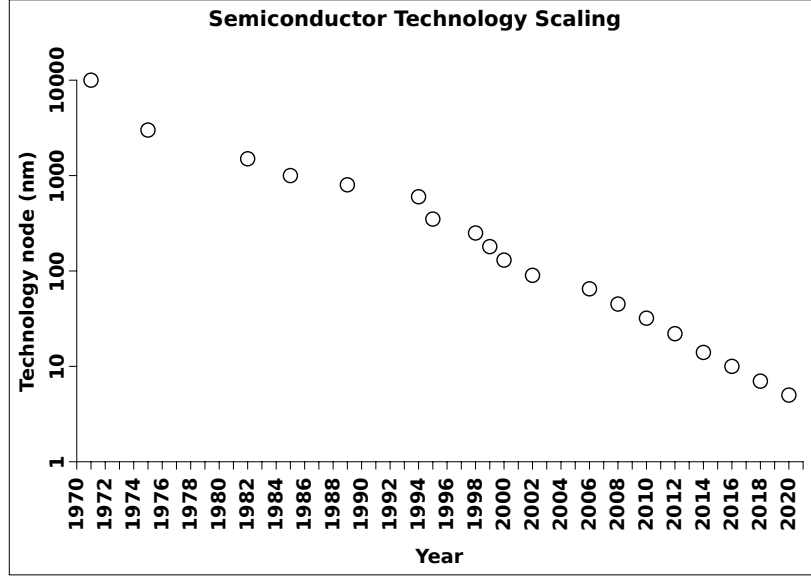


Figure 1.1.: Comparison of sizes of semiconductor manufacturing process nodes since the early 1970s.

this issue as it can grow high quality oxides at much lower temperatures than thermal oxidation. NAOS is discussed in some detail in Section 3.3.

In addition to a reduction in the technology node, there is a constant drive in the semiconductor industry to fit as much memory capacity as possible within the area of the chip. There is a desire to provide memory capacities which have the capability to store the complete amount of human activities. The drive to achieve this lofty goal has lead researchers onto a path where memory was no longer laid out in two-dimensional patterns along the area of the chip, but rather three-dimensional structures were introduced. One such emerging technology is the three-dimensional bit cost scalable (BiCS) memory recently introduced by Toshiba Corporation, but not yet in full production. It is suggested that the BiCS flash memory has the potential of up to 10Tbit/chip. This novel memory technology will be discussed in further detail in Section 4.2.

The atomic force microscope (AFM) is a tool which has been used for many decades in order to read bumps and protuberances on a nanosized section of a desired surface. However, it has been found that it can also be used to generate patterns on a silicon surface using oxide growth. This processing technique is now capable of generating patterns with sizes much smaller than those covered by traditional lithography techniques. As scaling continues, as is suggested in Figure 1.1, such processes garner more interest. As the capability and knowledge regarding the utilization of the AFM for surface patterning grew, new devices were introduced and the full potential for this processing technique were investigated. A method to use an AFM to generate nanodots for high density storage was introduced, as well as a suggestion that an AFM can be used to generate nanowires, essential to the fabrication of the silicon nanowire

transistor (SiNWT). Technologies using an AFM and local oxidation nanolithography (LON) are covered in Section 2.4.

So far, it appears that the miniaturization of the technology node is the major cause for the introduction of novel processing techniques. However, the true driving force behind most innovations in the semiconductor industry has to do with economic potential of a technology versus its financial burden. Some process technologies do not necessarily introduce any technical solutions to existing problems, but are much more cost-effective and easy to use when compared to their alternatives. Spray pyrolysis deposition is an example of such a technology. Spray pyrolysis is used to deposit material on the surface of a semiconductor wafer. The simplicity of the process means that a laboratory or a start-up need not invest much in order to have its own deposition tool. In addition it has been shown that materials deposited using spray pyrolysis can be further annealed to grow, e.g., vertical nanowires with excellent gas-sensing properties. More information regarding the spray pyrolysis deposition process can be found in Section 4.1.

1.4. Simulator Implementation

In order to simulate topography modifications a method which is able to describe geometric deformations over time is required. The initial topography surface $\mathcal{S}(t=0)$ is extracted from the desired geometry and is known to the simulator. After a specific time for processing $t_{process}$, the surface is modified under surface velocities $V(\vec{x})$ acting in the surface normal direction for all points $\vec{x} \in \mathcal{S}(t)$. With the initial surface, surface velocities, and processing time known, the final surface $\mathcal{S}(t=t_{process})$ can be found. It was shown by Sethian [165], [185] that this type of topography problem for microelectronics simulations can be solved using the LS method. A LS simulator for traditional semiconductor processes was subsequently created at the Institute for Microelectronics, TU Wien, by Ertl [50]. This simulator serves as the basis for the simulations and models presented in this document. All models are incorporated within the original simulator, allowing for these techniques to be used together with traditional processing techniques in subsequent steps in order to generate a desired device structure.

In this section, a summary of the topography simulator which is based on the LS framework from [50] will be described. For a more detailed description of the LS functions, refer to [50]. This section serves to summarize the implemented simulator by first introducing the LS framework, including the sparse field method for the surface description and the hierarchical run length encoding (H-RLE) data structure. Subsequently, the calculations of the surface rate and velocity field required for topography movement are explained.

1.4.1. Fast Level Set Framework

The presented simulations and models function fully within the process simulator presented in [50]. The LS method is utilized in order to describe the top surface of a semiconductor wafer as well as the interfaces between different materials. The LS method describes a movable surface $\mathcal{S}(t)$ as the zero LS of a continuous function $\Phi(\vec{x}, t)$ defined on the entire simulation domain,

$$\mathcal{S}(t) = \{\vec{x} : \Phi(\vec{x}, t) = 0\}. \quad (1.1)$$

The continuous function $\Phi(\vec{x}, t)$ is obtained using a signed distance transform

$$\Phi(\vec{x}, t=0) := \begin{cases} -\min_{\vec{x}' \in \mathcal{S}(t=0)} \|\vec{x} - \vec{x}'\| & \text{if } \vec{x} \in \mathcal{M}(t=0) \\ +\min_{\vec{x}' \in \mathcal{S}(t=0)} \|\vec{x} - \vec{x}'\| & \text{else} \end{cases} \quad (1.2)$$

where \mathcal{M} is the material described by the LS surface $\Phi(\vec{x}, t=0)$. The implicitly defined surface $\mathcal{S}(t)$ describes a surface evolution, driven by a scalar velocity $V(\vec{x})$, using the LS equation

$$\frac{\partial \Phi}{\partial t} + V(\vec{x}) \|\nabla \Phi\| = 0. \quad (1.3)$$

In order to find the location of the evolved surface, the velocity field $V(\vec{x})$ must be found. When simulating various processes, both traditional [50] and those covered in this work, the velocities can be a scalar value or a value calculated using the technique described in Section 1.4.2.

The LS equation can be solved using numerical schemes developed for the solution of Hamilton-Jacobi equations, since the LS equation belongs to the class of Hamilton-Jacobi equations, given by

$$\frac{\partial \Phi}{\partial t} + H(\vec{x}, \nabla \Phi, t) = 0 \text{ for } H(\vec{x}, \nabla \Phi, t) = V(\vec{x}) \|\nabla \Phi\|, \quad (1.4)$$

where H denotes the Hamiltonian. The LS equation can then be solved using finite difference schemes such as the Euler method [176], the Upwind scheme, based on the Engquist-Osher scheme [49], or the Lax-Friedrichs Scheme for non-convex Hamiltonians [185]. Another advantage of using the LS method is that calculations of geometric variables such as the surface normal or the curvature are available directly from the implicit surface representation. The normal at a point \vec{x} on the surface is given by

$$\vec{n}(\vec{x}) = \frac{\nabla \Phi}{\|\nabla \Phi\|} \quad (1.5)$$

and the curvature is

$$\kappa(\vec{x}) = \nabla \cdot \vec{n}(\vec{x}) = \nabla \cdot \frac{\nabla \Phi}{\|\nabla \Phi\|}. \quad (1.6)$$

Sparse Field Method

The initially proposed LS method uses a LS function which is defined on the entire simulation domain. However, memory requirements for the discretization of the LS function scale with domain size. Therefore, alternatives were proposed in the form of the narrow band method, where only a few layers around the LS surface are active grid points, and sparse field method [226], where a single layer of active grid points are considered for time integration. The steps required to implement the utilized process simulator are described by [50]

1. Update the LS values of all active grid points $\vec{p} \in \mathcal{L}_0^{(t)}$ in time using a finite difference scheme. \mathcal{L}_0^t represents the most inner layer of grid points nearest to the LS surface.
2. If there are two neighboring points $\vec{p}_-, \vec{p}_+ \in \mathcal{L}_0^{(t)}$ for which $\Phi(\vec{p}_-) < -\frac{1}{2}$ and $\Phi(\vec{p}_+) > \frac{1}{2}$ the absolute LS value for both points are reduced to $-\frac{1}{2}$ and $\frac{1}{2}$ respectively.
3. The LS values of all grid points $\vec{p} \in \mathcal{L}_i^{(t)}$ belonging to outside layers i , where $i = \pm 1, \pm 2, \dots$ are updated

$$\Phi^{(t+\Delta t)}(\vec{p}) = \begin{cases} \min_{\vec{p}' \in \eta(\vec{p}) \cap \mathcal{L}_{i-1}^{\{(t)\}}} \Phi^{(t+\Delta t)}(\vec{p}') + 1 & \text{if } i > 0, \\ \min_{\vec{p}' \in \eta(\vec{p}) \cap \mathcal{L}_{i+1}^{\{(t)\}}} \Phi^{(t+\Delta t)}(\vec{p}') - 1 & \text{if } i < 0 \end{cases} \quad (1.7)$$

4. Finally, the layers $\mathcal{L}_i^{\{(t+\Delta t)\}}$ which contain active grid points in the next time step are determined.

H-RLE Data Structure

For the calculation of finite difference schemes, the LS framework needs only to store the LS values of defined grid points, which is the union of all active grid points and their neighbors. The H-RLE data structure [83] is used in order to store the discretized LS function. This structure is a hybrid between the dynamic tubular grid (DTG) and the run length encoding (RLE) data structures. It combines the linear scaling memory requirements of the DTG with adaptation to all grid directions. The H-RLE data structure is organized hierarchically, similar to the DTG, where in place of storing a sequence of defined grid points, RLE is applied. Therefore, the structure is capable of storing the sign of the LS function for undefined grid points, while having the memory consumption of a DTG structure. The details of the implementation and examples showing the differences between the different data structures are described in [50]

Multiple Material Regions

Another important aspect of the LS framework is the ability to describe multiple LS surfaces for different material regions. The definition of different material regions in the LS framework was designed with etching processes in mind. When simulating traditional semiconductor processes, deposition is usually performed on the top layer, making masking not necessary. However, etching is almost always a masked process. Therefore the mask must be identifiable within the multi-LS framework. Figure 1.2 shows how material regions are labeled, resulting in an etch-friendly environment. When material \mathcal{M}_2 needs to be etched, with \mathcal{M}_1 serving as a mask, the LS defined by Φ_2 needs to be moved in the negative direction, but only at the locations where it is not touching the Φ_1 surface. If material \mathcal{M}_2 is deposited or grown with \mathcal{M}_1 serving as

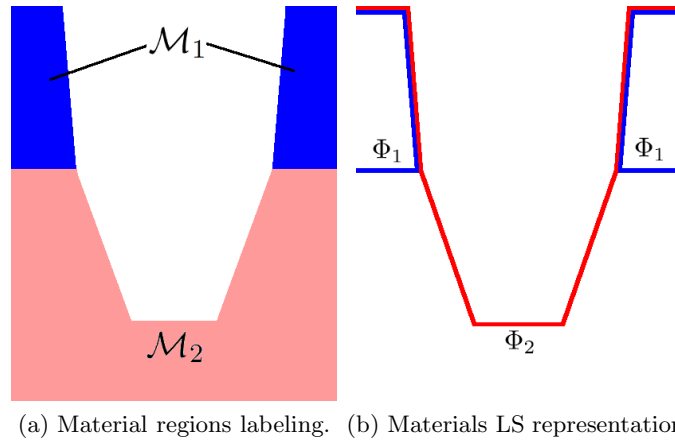


Figure 1.2.: Numbering of material regions in (a) leads to the Level Set description in (b).

a mask, it is evident that the LS definitions from Figure 1.2b will result in the material deposition on top of \mathcal{M}_1 , which is undesired. Therefore, when Φ_2 needs to be grown with Φ_1 serving as a mask, as is the case with the oxidation process, the LS definition and numbering must be changed.

1.4.2. Surface Rate Calculation

When modeling topography evolution caused by traditional semiconductor processes with particle transport, the velocity field for the LS equation must be found. This section discusses the particle transport to the surface and the surface reactions, which are treated using a combination of fluxes and MC distributions.

Transport Kinetics

The simulation domain is divided into the reactor-scale, feature-scale, and bulk regions, as depicted in Figure 1.3. Particle transport must be treated differently when within the reactor-scale or the feature-scale regions. The bulk region represents the silicon wafer.

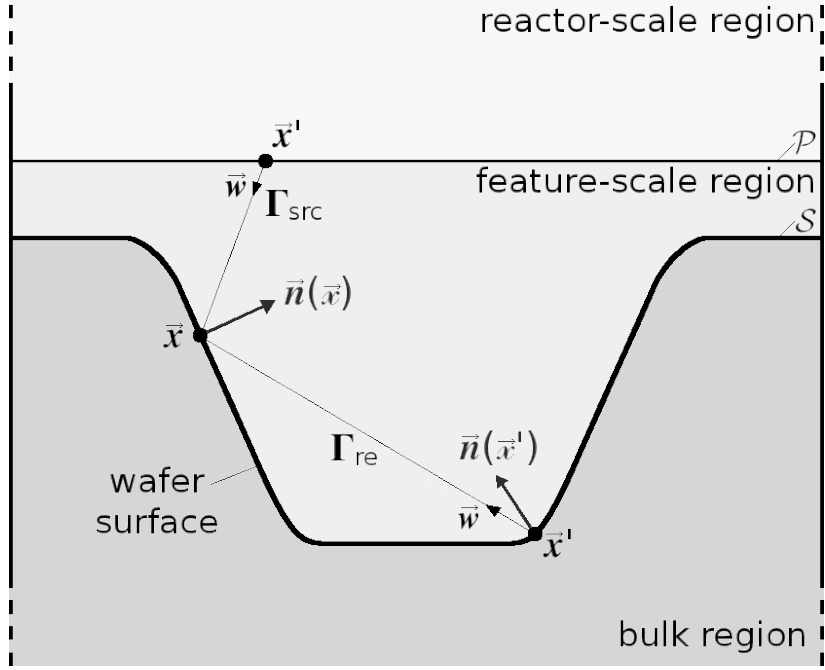


Figure 1.3.: The simulation of particle transport, which is divided into the reactor-scale and feature-scale regions.

The feature-scale region is separated from the reactor scale region by a flat plane \mathcal{P} depicted in Figure 1.3. The particle transport is generally characterized by the mean free path $\bar{\lambda}$, which for an ideal gas is given by

$$\bar{\lambda} = \frac{k_B T}{\sqrt{2} \pi d^2 p}, \quad (1.8)$$

where k_B is the Boltzmann constant, T is the gas temperature, p is the ambient pressure, and d is the collision diameter of a gas molecule. In the reactor-scale region, the mean free path is much smaller than the physical scale, so the velocities of a neutral species can be assumed to follow the Maxwell-Boltzmann distribution, leading to a cosine dependence of the flux distribution at \mathcal{P} , Γ_{src}

$$\Gamma_{src,neu} = F_{src,neu} \frac{1}{\pi} \cos \theta, \quad (1.9)$$

where θ is the angle between the incident direction and the surface normal at the impact location. $F_{src,neu}$ is the flux of neutral particles on \mathcal{P} .

When ions are also used in transport, and not only neutral particles, their transport towards the wafer surface is modeled by a plasma sheath potential. A narrower angle distribution is noted when compared to neutral particle transport, leading to a power cosine distribution for charged particles

$$\Gamma_{src,ion} \sim (\cos \theta)^v. \quad (1.10)$$

For large exponents v , this amounts to a normal distribution

$$(\cos \theta)^v \approx e^{-\beta \theta^2} \quad \text{with } v = 2\beta \gg 1. \quad (1.11)$$

The arrival flux of ions can then be expressed as

$$\Gamma_{src,ion} = F_{src,ion} \frac{1+v}{2\pi} (\cos \theta)^v \epsilon_{ion}(E), \quad (1.12)$$

where $\epsilon_{ion}(E)$ is the normalized energy distribution. Plasmas which are based on radio frequency (RF) result in a more complex energy distribution which is solved using MC techniques. Most processes generate a relatively even flux distribution Γ_{src} along \mathcal{P} , excluding processes which include local particle bombardments.

The feature scale is encompassed by the plane \mathcal{P} , the surface \mathcal{S} , and simulation domain boundaries shown in Figure 1.3. The arriving flux Γ_{src} is known at \mathcal{P} , while the re-emitted flux distribution is given by Γ_{re} for all points along the surface \mathcal{S} . The summation of these two fluxes determines the surface rates. The frequency of particle-particle interaction at the feature scale is neglected for most processes [27].

The average particle velocity for an ideal gas particle is given by

$$\bar{v} = \sqrt{\frac{8 k_B T}{\pi m}}, \quad (1.13)$$

where m is the gas molecular weight. The typical particle velocities are much higher than the surface rates, therefore the surface rate can be seen as a constant and the time required for particles to reach the surface can be regarded as relatively infinite with constant arrival at the substrate surface. The re-emitted arrival flux distribution must be known in order to calculate the total flux at the surface \mathcal{S} . The re-emitted flux distribution requires that the reflected particle direction distribution also be known. This distribution can be generated by different cosine distributions dependent on the particle type (ion, diffusive, or high-energy ion), while neutral particles are neglected. High energy ions can sputter away pieces of the impacted surface, which deposit elsewhere. This is incorporated using a yield function, which depends on the particle's incident energy E , the threshold energy E_{th} , and the incident angle

$$Y(\theta, E) = (\cos \theta)^{-C_1} \cdot e^{(C_2(1-1/\cos \theta))} \cdot \max\left(0, \sqrt{E} - \sqrt{E_{th}}\right), \quad (1.14)$$

where C_1 and C_2 are fitting parameters. Therefore, the particle transport at the feature scale is described by

$$\Gamma d\Omega = \begin{cases} \frac{-\vec{w} \cdot \vec{n}(\vec{x})}{\|\vec{x} - \vec{x}'\|^2} \Gamma_{src} dA' & \text{if } \vec{x}' \in \mathcal{P}, \\ \frac{-\vec{w} \cdot \vec{n}(\vec{x})}{\|\vec{x} - \vec{x}'\|^2} \Gamma_{re} dA' & \text{if } \vec{x}' \in \mathcal{S} \end{cases}, \quad (1.15)$$

where dA' is an infinitesimal surface element of \mathcal{S} or \mathcal{P} around \vec{x}' .

Surface Kinetics

This section summarizes the implementation of surface velocity calculations performed in the LS framework used for topography modeling from [50]. Once the particles have been transported to the surface, the deposition or etch rates can be found. These rates are needed in order to find the velocity field $V(\vec{x})$ which can be applied to the LS equation (1.3). The surface velocity can be written as a function of all local arriving fluxes $\Gamma(\vec{x})$

$$V(\vec{x}) = V(\Gamma(\vec{x})). \quad (1.16)$$

In order to numerically represent the flux Γ , a discretization is performed. Introducing a series of functions $r_l(\vec{x})$ with $1 \leq l \leq N_R$, $\Gamma(\vec{x})$ can be mapped to a finite number of scalar values

$$R_l(\vec{x}) := \sum_{q=1}^Q \int_0^\infty \int_{\vec{w} \cdot \vec{n}(\vec{x}) < 0} r_l(\vec{x}) \Gamma(\vec{x}) d\Omega dE, \quad (1.17)$$

where Q is the number of process-relevant particle species, q refers to a single particle species, N_R is the number of surface rates, and Ω represents the solid angle between the particle direction and the surface normal at the point of impact. The surface velocity is then found as a combination of the scalar values from (1.17)

$$V(\vec{x}) = V(R_1(\vec{x}), R_2(\vec{x}), \dots, R_{N_R-1}(\vec{x}), R_{N_R}(\vec{x})). \quad (1.18)$$

When a particle of species q' is accelerated to the surface its flux is determined by $F_{q'}(\vec{x})$, where

$$R_l(\vec{x}) = F_{q'}(\vec{x}). \quad (1.19)$$

This simplifies (1.17), since the information needed from the flux distribution for a certain particle type is mapped to a single value.

For high energy particles, the incident angle θ and energy E are the values which are used to calculate the yield and the surface rate caused by the particles. For an individual high energy particle of species q' , the total sputter rate determines its flux

$$R_l(\vec{x}) = Y_{q'}^{tot}(\vec{x}). \quad (1.20)$$

The values of R_l represent the rates on the surface, whether they are referenced to a particle flux or a total sputter rate. Therefore, they are interpreted as the surface rates, because $V(\vec{x})$ is a function of these rates $R_l(\vec{x})$.

For systems with a linear surface reaction, the surface velocity is represented by the rates directly $V(\vec{x}) = R(\vec{x})$. The surface velocity caused by a single species is modeled by

$$V(\vec{x}) = \frac{1}{\rho} \Delta m s F(\vec{x}), \quad (1.21)$$

where F is the total incident flux, s is the sticking probability of the reacting particles, Δm is the mass deposited or removed from the surface per particle, and ρ is the bulk density ($\rho_{Si} \approx 5 \times 10^{28} m^{-3}$).

For non-linear surface reactions, where the sticking probability depends on the particle flux, the surface velocity is described using the Langmuir adsorption model. The presence of multiple etchants, such as is the case for ion-enhanced etching, results in an etch rate which is higher than that obtained by summing the individual contributions of the physical and chemical components. The etch rate is composed of three contributions

$$V(\vec{x}) = \underbrace{-\alpha_{ch} \cdot \Theta(\vec{x})}_{\text{chemical etching}} \underbrace{-\alpha_{ph} \cdot Y_{ph}^{tot}(\vec{x})}_{\text{physical sputtering}} \underbrace{-\alpha_{ie} \cdot \Theta(\vec{x}) \cdot Y_{ie}^{tot}(\vec{x})}_{\text{ion-enhanced etching}}, \quad (1.22)$$

where $\Theta(\vec{x})$ represents the coverage of the surface which is exposed to the adsorbed byproducts and is expressed by

$$\Theta(\vec{x}) = \frac{\beta_{ad} F(\vec{x})}{\beta_{ad} F(\vec{x}) + \beta_{ch} + \beta_{ie} Y_{ie}^{tot}(\vec{x})}, \quad (1.23)$$

where the constants β_{ad} , β_{ch} , and β_{ie} are model-dependent parameters.

1.5. Outline of the Thesis

This document deals primarily with a method of simulating topography modifications caused by the application of novel processing techniques which are not found in commercial simulators. However, before those are introduced the thermal oxidation of silicon will be described in Chapter 2. A novel process for localized silicon oxidation, LON, which has garnered much attention as of late is also introduced in this chapter. The requirements for a topography simulation of thermal oxidation and LON will be tackled in Chapter 3, where the state-of-the-art in thermal oxidation simulations is presented. The required modifications to the LS framework in order to enable the modeling of multiple topographies in an oxidation process are also described here. This chapter also includes descriptions of MC methods and particle distributions generated in order to enable the simulation of LON.

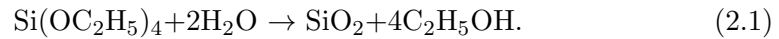
Chapter 4 introduces deposition and etching processes which have garnered attention recently and describes their functionality and the reasons for the increased interest in these technologies. The technologies introduced are spray pyrolysis deposition and BiCS memory hole etching. The models and techniques used in order to simulate these technologies are described in Chapter 5.

The applications of the mentioned technologies and their simulations are presented in Chapter 6. Here, several simulations of AFM lithography including some applications for device generation, are presented. Simulations of thermal oxidation are also presented, which use linear-parabolic equations to describe the oxide growth, while also incorporating some two-dimensional effects and silicon crystal orientation in the material growth. The topography modification due to spray pyrolysis deposition is also shown, along with an etched BiCS memory hole. Finally, Chapter 7 concludes with a brief summary and gives suggestions for future work.

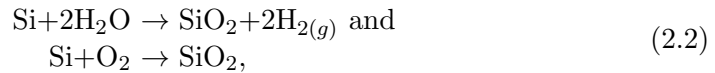
2. Silicon Oxidation Techniques

Oxidation is a process by which a metal or semiconductor is converted to an oxide. Although oxidation of many materials plays a role in technology, the main oxidation reaction which will be addressed is the conversion of parts of a silicon semiconductor wafer into silicon dioxide (SiO_2). The chemical reaction between oxygen and silicon to generate SiO_2 is usually driven by a high-heat environment; however, even at room temperature, a shallow layer of native oxide, approximately 1nm thick can form in an air environment. In order to grow thicker oxides in a controlled environment, several methods can be implemented:

Plasma Enhanced Chemical Vapor Deposition (PECVD) using TEOS as a precursor is one way by which silicon dioxide can be grown on a silicon wafer [22]. This method is mainly used to grow a pad/buffer oxide layer during local oxidation of silicon (LOCOS) [131]. The reaction which takes place during plasma enhanced chemical vapor deposition (PECVD) using TEOS is

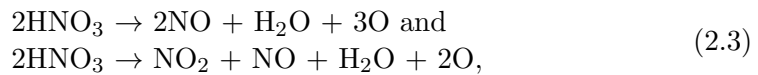


Thermal oxidation of silicon surfaces is usually performed at high temperatures ($800^\circ\text{C} - 1200^\circ\text{C}$), resulting in a High Temperature Oxide (HTO) layer. The ambient environment can either be “wet” using water vapor or steam, or “dry” using molecular oxygen as the main oxidant. The reactions which take place during wet and dry thermal oxidation are



respectively.

Nitric Acid Oxidation of Silicon (NAOS) is performed at low temperatures ($200^\circ\text{C} - 400^\circ\text{C}$) and is used in order to grow thin (1.3nm – 1.4nm) oxide structures. Similar to thermal oxidation, NAOS can be performed in liquid or vapor environments. The chemical reactions which take place during wet and vapor NAOS are



respectively.

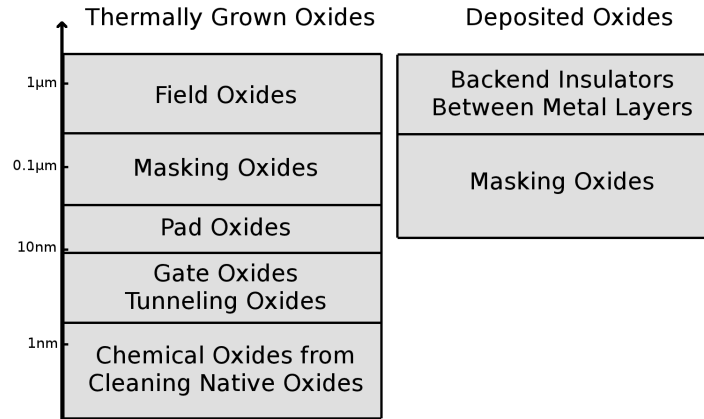


Figure 2.1.: Difference in uses of thermally grown versus deposited silicon dioxide in silicon technology.

The different uses for thermally grown versus deposited oxides are laid out in Figure 2.1 [175]. Silicon dioxide layers are mainly used as high quality insulators or masks for ion implantation and the ability to form high quality silicon dioxide is the main reason why silicon is still the dominating material for IC fabrication [175].

This chapter also introduces a novel technique for localized silicon oxidation, which allows nanosized oxide patterns to be grown on a silicon surface far smaller than those available through traditional photolithography and electron beam lithography techniques. The technique Local Oxidation Nanolithography (LON), also known as AFM-induced oxidation or Local Anodic Oxidation (LAO), uses the charged needle tip of an AFM in order to generate the desired patterns.

2.1. Silicon Dioxide Properties

The growth of silicon dioxide is one of the most important processes in the fabrication of metal oxide semiconductor (MOS) transistors [175]. The attributes of SiO_2 which make it appealing for the semiconductor industry are [80, 175]:

- It is easily deposited on various materials and grown thermally on silicon wafers.
- It is resistant to many chemicals used during the etching of other materials, while allowing itself to be selectively etched with certain chemicals or dry-etched with plasmas.
- It can be used as a blocking material for ion implantation or diffusion of many unwanted impurities.

- The interface between silicon and silicon dioxide has relatively few mechanical and electrical defects, although with newer technology nodes and reduced geometries, even slight defects must be addressed.
- It has a high dielectric strength and a relatively wide band gap, making it an excellent insulator.
- It has high a temperature stability of up to 1600°C, making it a useful material for process and device integration.

Table 2.1 shows some important properties of silicon dioxide [47]. It can be noted that oxides grown in a dry atmosphere have a higher density, which implies less impurities and a better quality oxide than when grown in a wet atmosphere. Thermal expansion refers to the oxide's volume expansion or shrinkage, when exposed to a range of temperatures. For oxides, the thermal expansion coefficient is very low, meaning it does not exert much stress and strain on other materials which are in contact with it. Young's modulus and Poisson's ratio measure the oxide's stiffness and its negative ratio of transverse to axial strain, respectively, which are important measures of a material's mechanical stability. The thermal conductivity, which varies for thin sputtered (1.1W/m-K), thin thermally grown (1.3W/m-K), and bulk (1.4W/m-K) oxides is an important parameter which affects power during operation [25]. It is also found that the thermal conductivity of oxides changes depending on the oxide thickness [25]. The high dielectric strength shows the stability of SiO₂ under high electric fields, suggesting that the oxide film is very suitable for dielectric isolation.

| | |
|-------------------------------|---------------------------------------|
| Crystal structure | Amorphous |
| Atomic weight | 60.08g/mole |
| Density (thermal, dry/wet) | 2.27/2.18g/cm ³ |
| Molecules | 2.3·10 ²² /cm ³ |
| Specific heat | 1.0J/g-K |
| Melting point | 1700°C |
| Thermal expansion coefficient | 5.6·10 ⁻⁷ /K |
| Young's modulus | 6.6·10 ¹⁰ N/m ² |
| Poisson's ratio | 0.17 |
| Thermal conductivity | 1.1W/m-K – 1.4W/m-K |
| Relative dielectric constant | 3.7 - 3.9 |
| Dielectric strength | 10 ⁷ V/cm |
| Energy bandgap | 8.9eV |
| DC resistivity | ≈10 ¹⁷ Ωcm |

Table 2.1.: Important properties of silicon dioxide (SiO₂).

The silicon dioxide molecule can be described as a three-dimensional network of tetrahedra cells, with four oxygen atoms surrounding each silicon ion, shown in Figure 2.2a. The length of a Si-O bond is 0.162nm, while the normal distance between two oxide bonds is 0.262nm. The Si-Si bond distance depends on the SiO₂ arrangement, but is

approximately 0.31nm and the bond angle O-Si-O is approximately 109° . The bond angle Si-O-Si is ideally approximately 145° , but it can vary between 100° and 170° with minimal change in bond energy. The tetrahedral form is the basic unit from which a SiO_2 structure is formed, even though SiO_2 can exist in a crystalline structure. The reason for the amorphous oxide structure is the absence of any crystalline form of SiO_2 whose lattice size closely matches the silicon lattice [175]. The tetrahedra bond together by sharing oxygen atoms as illustrated in Figure 2.2b in a sample six-membered ring.

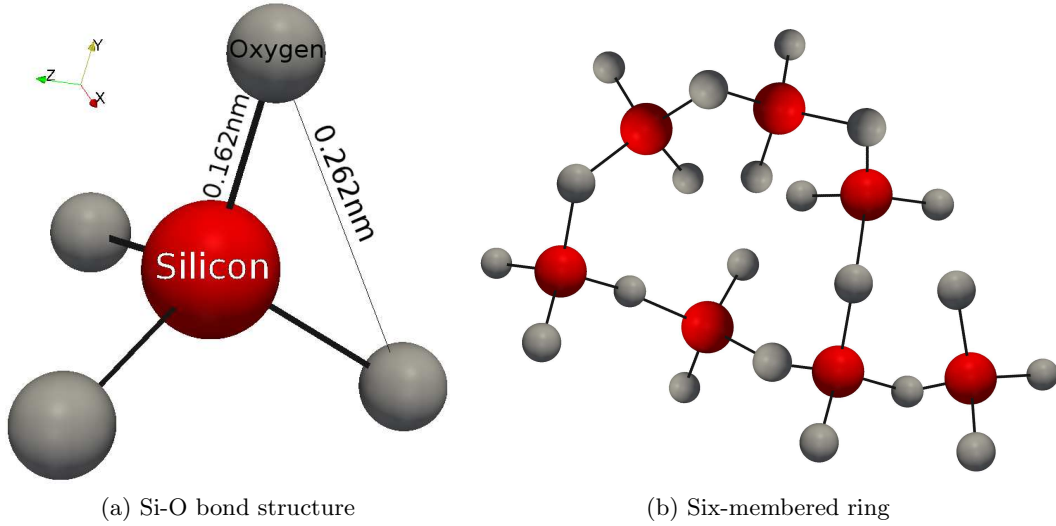


Figure 2.2.: (a) Structure of fused silica glass along with (b) a six-membered ring structure of SiO_2 .

From the above analysis, it can be concluded that, as the oxide grows, it consumes the silicon atoms at the surface of the wafer. This causes the silicon-silicon dioxide interface to move into the wafer while the oxide grows. The equation which governs the amount of consumed silicon is

$$X_{Si} = X_{SiO_2} \cdot \frac{N_{SiO_2}}{N_{Si}}, \quad (2.4)$$

where N_{SiO_2} is the molecular density of the oxide, N_{Si} is the atomic density of the silicon wafer, and X_{SiO_2} and X_{Si} are represented in Figure 2.3. These values are known, resulting in the amount of silicon consumed with respect to the oxide thickness

$$X_{Si} = X_{SiO_2} \cdot \frac{2.3 \times 10^{22} \text{ molecules/cm}^3}{5 \times 10^{22} \text{ atoms/cm}^3} = 0.46 X_{SiO_2}, \quad (2.5)$$

Therefore approximately 46% of the silicon dioxide which is grown on a silicon wafer is found within the bounds of the original silicon, while approximately 54% is new

volume, which grows into the ambient. Figure 2.3 shows the location of the original silicon surface followed by the oxide-silicon and oxide-ambient interfaces after an oxidation step.

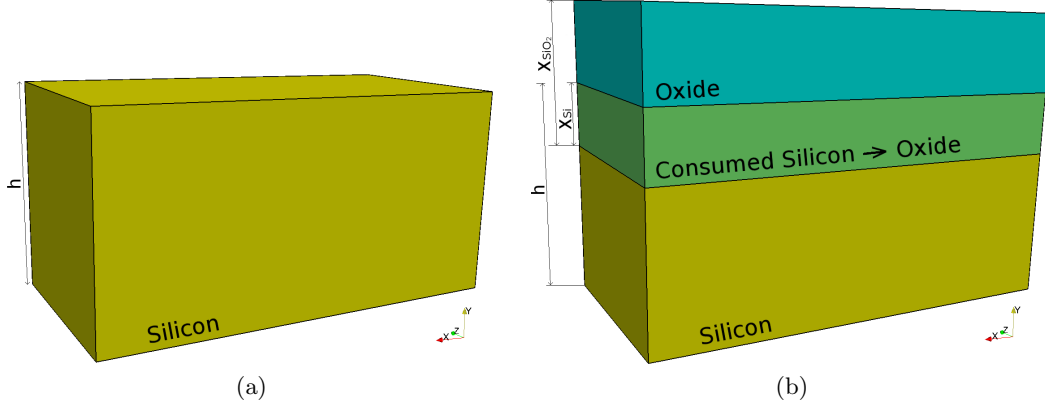


Figure 2.3.: Moving interfaces and volume expansion after silicon oxidation.

2.1.1. Molecular Structure of the Silicon-Silicon Dioxide Interface

An in-depth analysis of the interface between silicon and silicon dioxide and how the molecular structure changes during the oxidation process is outside the scope here as this work mainly concerns itself with changing topographies and interfaces rather than atomistic-level simulations. However, it is worth mentioning that the interface between silicon and the grown oxide is not a perfect transition between a crystalline silicon and an amorphous SiO_2 . There are many suggestions regarding the molecular make-up of the interface and how the interface is built during the initial stages of oxidation [47], [87], [160], [186], [199], [208].

The initial proposed model for the atomic configuration of the $\text{Si}(100)\text{-SiO}_2$ interface is shown in Figure 2.4a [47]. However, as noted a small amount of surface silicon atoms remain unbonded, resulting in unpaired electrons to localize on the defect silicon atom, forming a “dangling bond” [47]. Figure 2.4b and Figure 2.4c illustrate the modified interface, when a “dangling bond” is introduced to a (100) and a (111) oriented silicon, respectively. More recently, it has been proposed, and widely accepted, that the oxide layer, although amorphous, contains a crystalline structure close to the Si interface [186]. It has also been suggested that the bulk oxide itself is not a simple amorphous structure, but rather that, throughout the bulk of the oxide, an ordered bond structure exists, having an epitaxial relation with the silicon substrate [208].

Much effort has also been spent in order to investigate the initial steps of silicon oxidation at the molecular level [20], [37], [75], [169], [214], [219]. Watanabe et al. [219] suggest a layer-by-layer oxidation, whereby nucleation of nanometer-scale two-dimensional

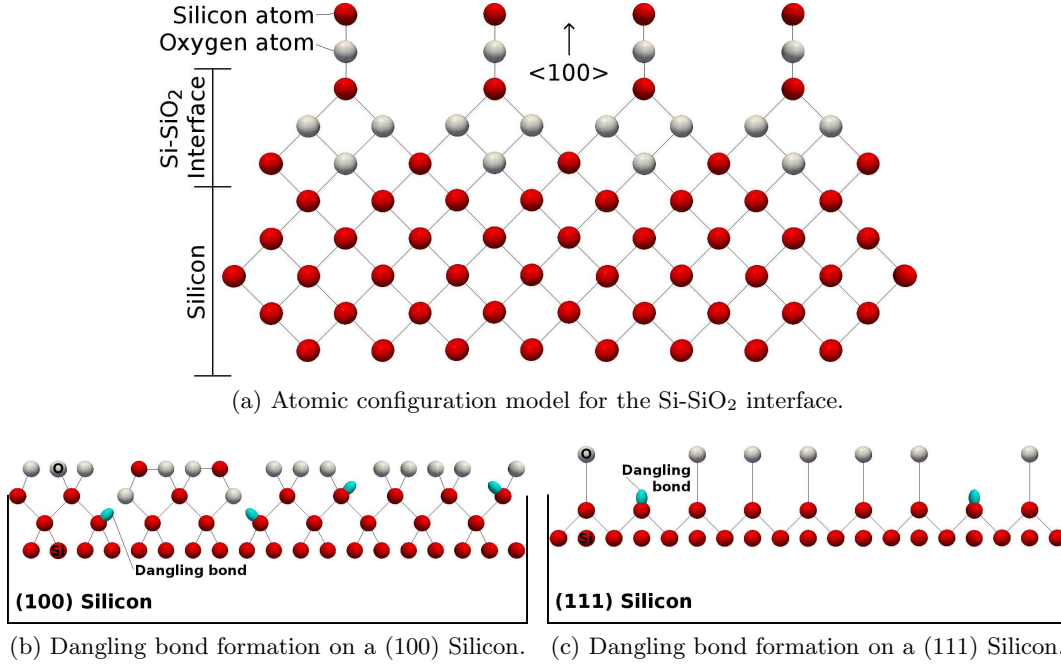


Figure 2.4.: Atomistic configurations of the Si-SiO₂ interface.

oxide islands at the interface explains the initial stages of oxidation. It is suggested that atomically flat terraces, separated by single atomic steps, approximately 0.13nm in height, are formed as oxidation is initiated. Pasquarello et al. [169] suggest that the interface between Si and SiO₂ can only be explained with the introduction of transition regions, which do not follow the properties of SiO₂ or bulk Si, at the interface. Their suggested model gives a disordered Si layer (0.5nm – 1nm) containing a dense Si arrangement, which links the bulk silicon to the oxide layer. However, the oxide layer is also represented using an interface region (~ 1 nm) which acts as a sub-oxide transition region and contains silicon atoms in intermediate stages of oxidation. More recently, Hemeryck et al.[75] indicated that the penetration of oxygen atoms into the top layers of crystalline silicon depends on the starting and final surrounding environment, with activation energies ranging from 0.11eV to 2.59eV, and is not a simple case of the atom hopping from one Si-Si bond to another. The exact mechanism by which the oxidation process progresses is not yet fully understood at the atomistic level.

2.2. Thermal Oxidation of Silicon

Thick thermally grown oxide is mainly used for isolation in semiconductor devices. The two types of processes which are used in order to isolate neighboring MOS transistors are LOCOS and shallow trench isolation (STI). The general steps required for LOCOS and STI are shown in Figure 2.5 and Figure 2.6, respectively. One aspect of LOCOS

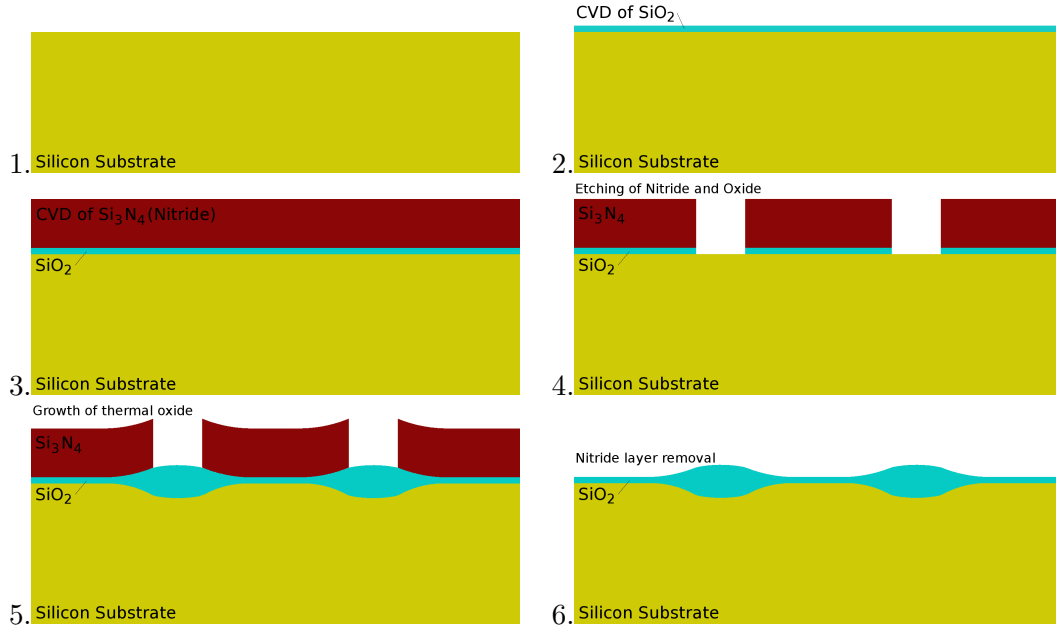


Figure 2.5.: LOCOS processing steps

which can be noted from Figure 2.5 is that, as the oxide grows, the nitride mask bends to generate a “bird’s beak” effect as the oxide is pinched under the nitride mask at the edges. For a deeper understanding of these methods, refer to [177]. It is important to note that, although CVD of oxide is possible, as explained above, the quality of deposited oxide is below that of thermally grown oxides. Quality, in this case, refers to the electrical properties of the silicon-oxide interface and the oxide density. Thermal oxidation is also a highly refined process which can be finely controlled for oxides below 10nm, unlike deposited oxides [34].

Thermal oxidation of silicon is a chemical process, whereby oxygen from the ambient interacts with a silicon surface at high temperatures in order to grow silicon dioxide (SiO_2). Some oxidation also takes place at room temperature, resulting in a thin oxide growth of approximately 1nm in height. The oxidation cannot proceed further at room temperature, because the oxygen molecules (O_2), which are the main contributors of oxygen in the oxidation process, do not have enough energy to diffuse through the $\sim 1\text{nm}$ thick oxide.

When attempting to understand thermal oxidation of silicon, it is important to note that it is a complex process, which includes the diffusion of oxidants through existing oxide, a chemical reaction at the silicon-oxide interface, and a volume expansion simultaneously. These three events must be viewed as one system where:

1. Oxidants from the ambient reach the oxide-ambient interface. When they gather enough energy, they penetrate the surface and begin to diffuse through the existing oxide until reaching the oxide-silicon interface.

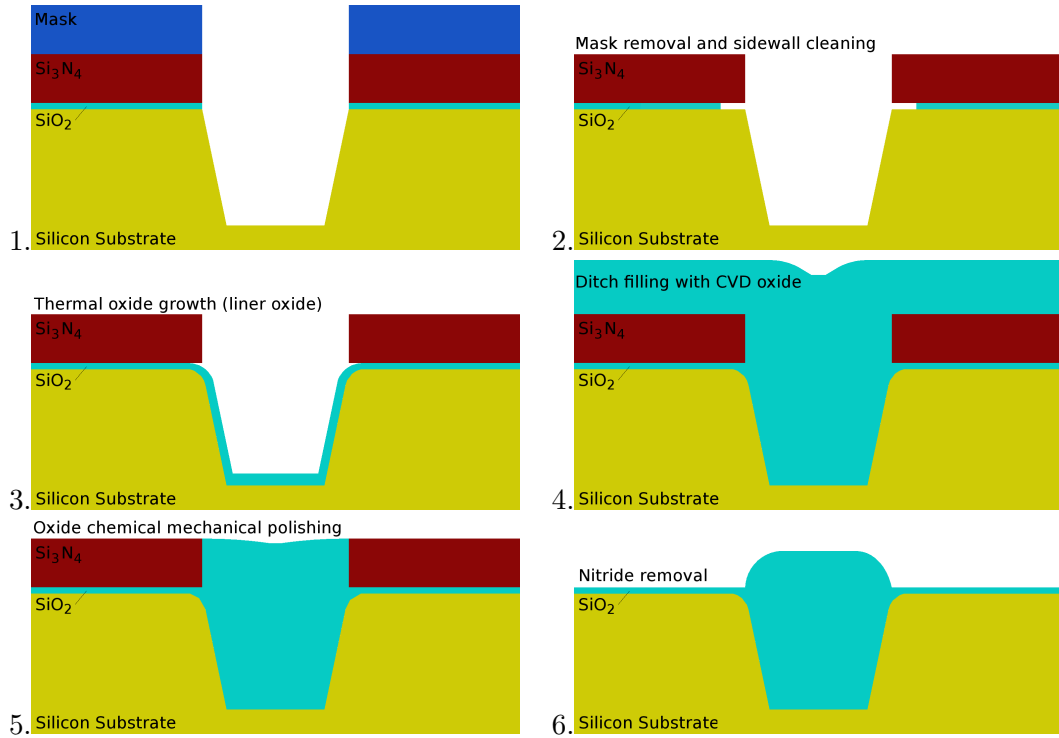


Figure 2.6.: STI processing steps

2. The oxidant species which reach the oxide-silicon interface can now interact with the surface silicon atoms in order to form more SiO_2 using chemical reaction (2.2).
3. Since the oxidant, together with a silicon atom, forms a molecule which has a larger volume than the oxidant plus the silicon atom in a crystalline arrangement, a volume expansion occurs. This volume expansion causes the entire oxide to expand, leading to the increased height of the oxide at the ambient-oxide interface.

2.2.1. Kinetics and Growth of Silicon Dioxide

The main ambient parameter used to control oxide growth during silicon oxidation is temperature. However, it is also possible to vary the hydrostatic pressure in the reaction chamber. Whether the oxidation environment is wet (H_2O) or dry (O_2) also plays a role in determining the growth rate, in addition to the role played by the crystal orientation of the silicon wafer.

Dry Oxidation

During dry oxidation, the wafer is placed in a pure oxygen gas (O_2) environment and the chemical reaction which ensues is between the solid silicon atoms (Si) on the surface of the wafer and the approaching oxide gas



Figure 2.7 shows the oxide thickness as a function of oxidation time for dry oxidation.

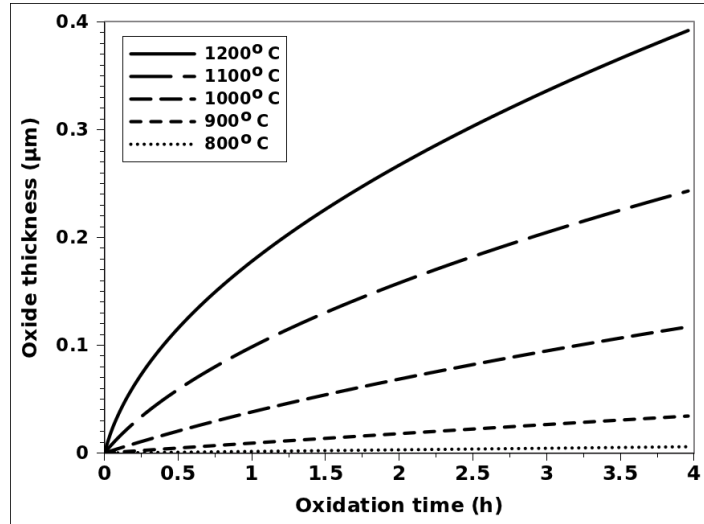


Figure 2.7.: Oxide thickness versus oxidation time for dry (O_2) oxidation of a (100) oriented silicon wafer under various temperatures.

It can be noted that the oxidation rate does not exceed $\sim 150\text{nm/h}$, making it a relatively slow process which can be accurately controlled in order to achieve a desired thickness. The oxide films resulting from a dry oxidation process have a better quality than those grown in a wet environment, which makes them more desirable when high quality oxides are needed. Dry oxidation is generally used to grow films not thicker than 100nm or as a second step in the growth of thicker films, after wet oxidation has already been used to obtain a desired thickness. The application of a second step is only meant to improve the quality of the thick oxide.

Wet Oxidation

During wet oxidation, the silicon wafer is placed into an atmosphere of water vapor (H_2O) and the ensuing chemical reaction is between the water vapor molecules and the solid silicon atoms (Si) on the surface of the wafer, with hydrogen gas (H_2) released as a byproduct

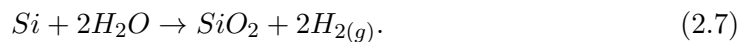


Figure 2.8 shows the oxide thickness as a function of oxidation time for wet oxidation processing. It is evident that wet oxidation operates with much higher oxidation

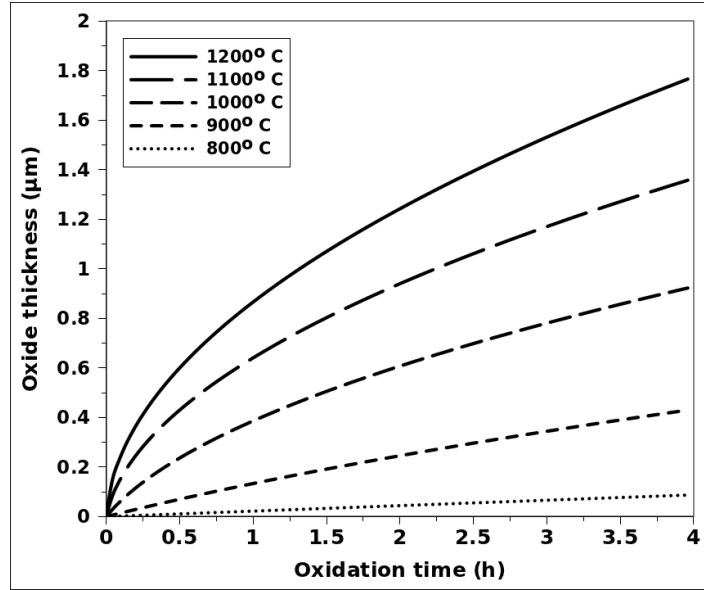


Figure 2.8.: Oxide thickness versus oxidation time for wet (H_2O) oxidation of a (100) oriented silicon wafer under various temperatures.

rates than dry oxidation, up to approximately 600nm/h. The reason is the ability of hydroxide (OH^-) to diffuse through the already-grown oxide much quicker than O_2 , effectively widening the oxidation rate bottleneck when growing thick oxides, which is the diffusion of species. Due to the fast growth rate, wet oxidation is generally used where thick oxides are required, such as insulation and passivation layers, masking layers, and for blanket field oxides.

Temperature Effects

As the temperature in the oxidation environment is increased, the oxidation rate can increase significantly, both in wet and dry processes. The temperature dependence on the oxidation rate can be observed in Figure 2.7 and Figure 2.8 for dry and wet oxidation, respectively. In Figure 2.9, the ratio between oxide thickness and temperature is visualized, suggesting the existence of an exponential relationship between the thickness (x_o) and inverse negative temperature

$$x_o \propto e^{-1/T}. \quad (2.8)$$

The dramatic increase in oxide thickness with increasing temperature is not surprising, since the diffusivity (D) of oxygen and water through the oxide depends greatly on temperature,

$$D \propto e^{-c/T}, \quad (2.9)$$

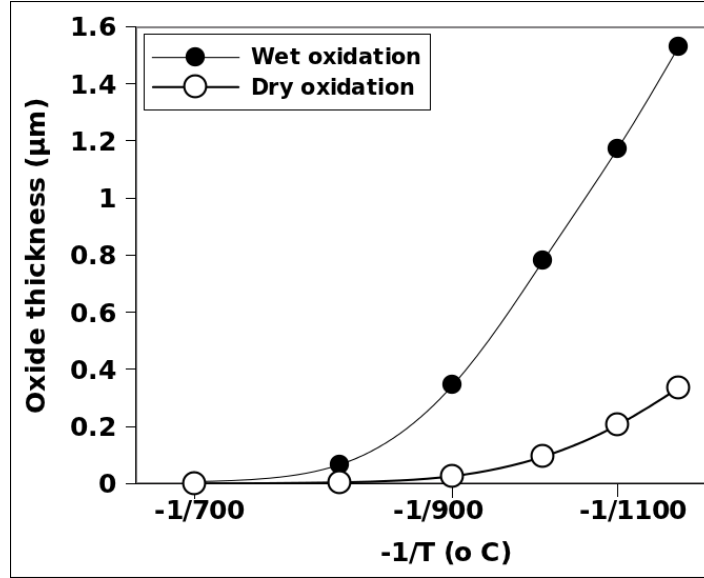


Figure 2.9.: Oxide thickness versus process temperature for wet (H_2O) and dry (O_2) oxidation of a (100) oriented silicon wafer at 1000°C.

where c is a parameter independent of temperature T . Since the oxidant diffusivity increases exponentially with increasing temperature, so should the oxidation rates, because the diffusivity of oxidants is the rate-limiting step when thicker oxides ($\sim 30\text{nm}$) are grown. A higher diffusivity rate means that more oxidants will be allowed to penetrate through the already grown oxide to reach the silicon surface.

Pressure Effects

The effect of hydrostatic pressure on thermally grown oxides in dry and wet environments is shown in Figure 2.10a and Figure 2.10b, respectively, while Figure 2.10c shows the direct relationship between the oxide thickness and the applied pressure. It is evident that increasing the pressure results in thicker oxides and a faster oxidation rate. A logarithmic relationship appears to exist between the thickness of oxide grown and the applied pressure. The main advantage of increasing the pressure during oxidation is to achieve relatively fast oxidation rates at reduced temperatures [124], [179]. Reducing the processing temperature results in less impurities and minimal movement of the junction during multiple subsequent oxidation steps required for complex IC device manufacturing [125]. Oxides grown in a high pressure ambient have also been found to have significantly reduced stacking faults, leading to an improved device performance [98].

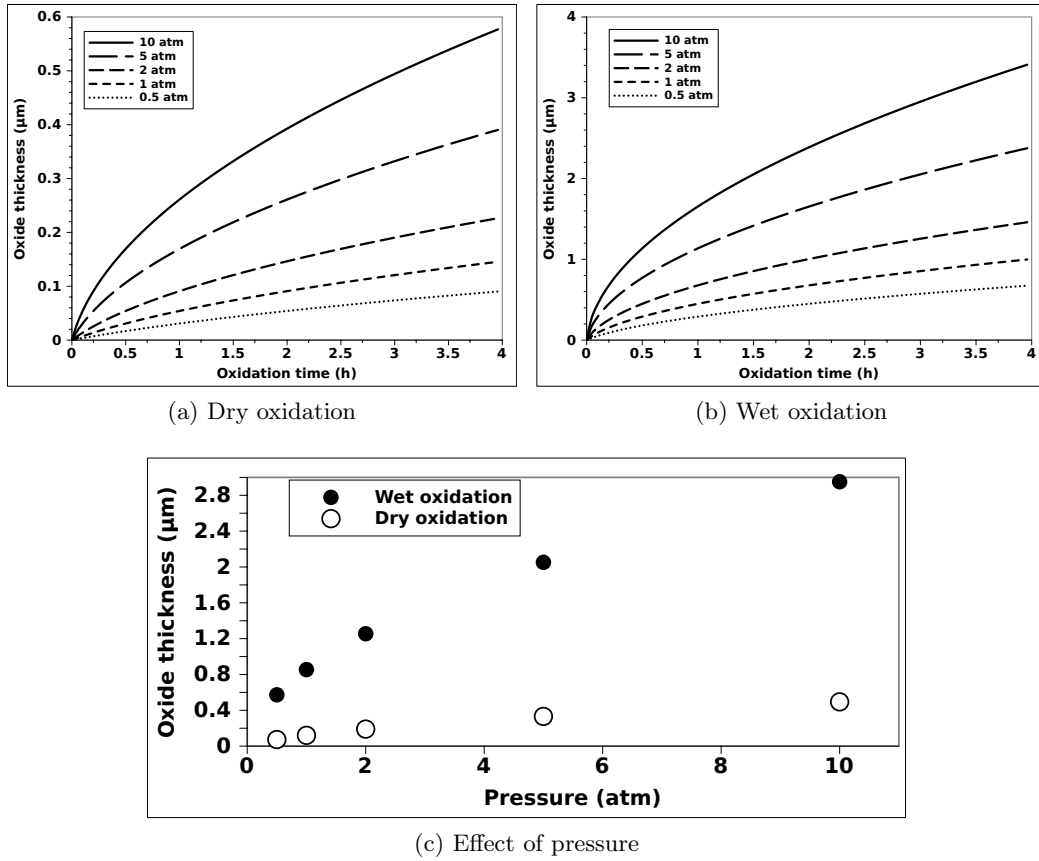


Figure 2.10.: Effects of hydrostatic pressure on thermally grown oxide thickness for a (100) oriented silicon wafer in a) dry (O_2) and b) wet (H_2O) ambients.

Crystal Orientation Effects

Multiple studies have shown that silicon is not oxidized at the same rate in each crystalline direction [122]. Therefore, the crystal orientation of the wafer plays a role in determining the oxide thickness, as can be seen in Figure 2.11. Oxide growth appears to be faster on (111) oriented silicon when compared to (100) oriented silicon. In fact, in [122] it is shown that the (111) and (100) orientations represent the upper and lower bound for oxidation rates, respectively. All other silicon orientations lie between these extrema. Ligenza [126] argued that the crystal orientation effect on the oxidation rate is due to the differences in the densities of silicon atoms on the various crystal faces. Since silicon atoms are required in order to generate the oxide, having a larger number of bondable Si atoms available on the (111) face meant that the oxide would grow faster in the (111) direction, as is observed experimentally.

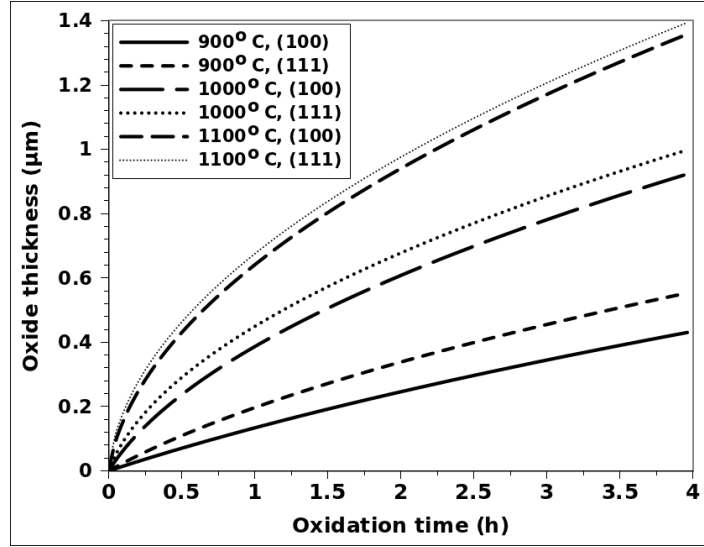


Figure 2.11.: Oxide thickness versus oxidation time for (100) and (111) oriented silicon by wet oxidation at various temperatures.

2.3. Linear Parabolic Description of Thermal Oxidation Growth

Even though experimental results have been able to show, with reproducibility, the ability to control oxide thickness and quality using various parameters such as temperature, pressure, crystal orientation, and oxidation environment, a complete understanding for how the oxide grows is not yet given. The initial first-order model for oxide growth kinetics was suggested by Bruce Deal and Andrew Grove at Fairchild Semiconductor in 1965 [42]. This linear parabolic model, more commonly referred to as the Deal-Grove model, is used as a starting point for many more recent works attempting to model oxidation kinetics [175]. Although the Deal-Grove model can, within an acceptable accuracy, predict oxide growth beyond 30nm, its main drawbacks are the inability to explain oxide features, when two- and three-dimensional geometries are required and its inability to accurately describe the initial oxidation for very thin layers ($< 30\text{nm}$). This led to the introduction of a model by Massoud et al. [143], [144], which is meant to deal with thinner oxides. Many other models have been proposed after Massoud in order to deal with the thin oxide regime, which is suggested to have a growth rate limited by the chemical reaction and not by the diffusion of oxidants, as Deal-Grove and Massoud suggest.

2.3.1. Deal-Grove Model

The main idea behind the Deal-Grove model is illustrated in Figure 2.12 [42]. The figure represents the materials and interfaces involved during oxidation in a one-dimensional form. The transport and interaction of oxidants is viewed as going through the following stages:

1. Oxidant is transported from the bulk, gas ambient to the outer surface of the oxide, where it is adsorbed with a flux F_1 .
2. Oxidant diffuses through the oxide film with a flux F_2 .
3. Oxidant reaches the surface with a flux F_3 and reacts with silicon atoms to form new SiO_2 .

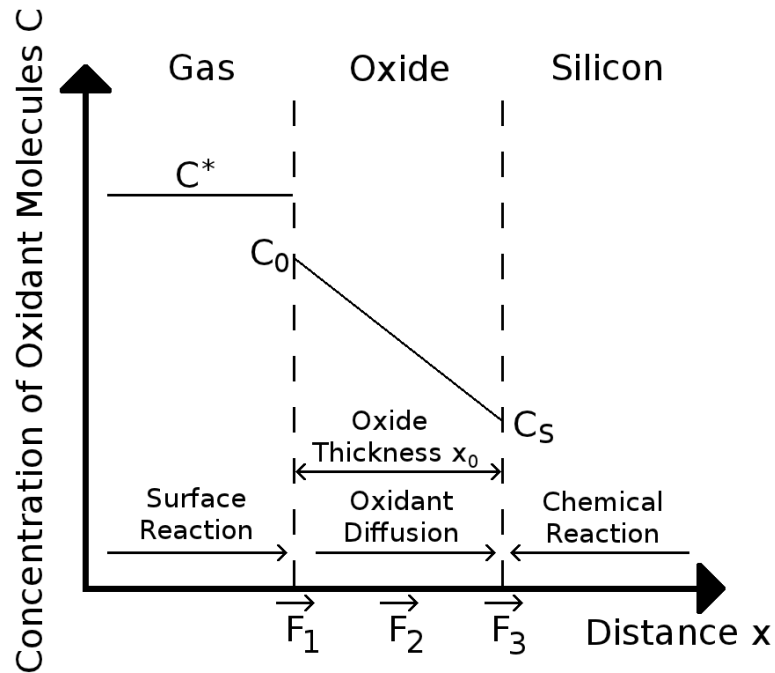


Figure 2.12.: One-dimensional Deal-Grove model for the oxidation of silicon.

The first step in the model is characterized by the surface reaction of free oxidants in the gas phase interacting with the oxide surface. The adsorption of oxidants through the top surface of the oxides is written as

$$F_1 = h(C^* - C_0), \quad (2.10)$$

where h is the gas-phase transport coefficient, C^* is the equilibrium concentration of the oxidants in the gas ambient, and C_0 is the concentration of oxidants at the oxide surface at any time during oxidation. Experiments have shown that variations in gas flow rates in the furnace, changes in spacing between wafers, and changes in wafer

orientation (vertical or horizontal) have very little influence on the oxidation rate. This suggests that a large value for h or that a small $(C^* - C_0)$ is required to provide the necessary F_1 .

Assuming an over-saturation of oxidant in the gas, C^* is effectively the solubility limit in the oxide. This value is related to the partial pressure in the atmosphere using Henry's law

$$C^* = H \cdot p, \quad (2.11)$$

where p is the partial pressure and H is the inverse Henry's law constant, which depends on the solute, solvent, and temperature. At an atmospheric pressure of 1atm and a temperature of 1000°C, the solubility limits C^* for dry and wet oxidation are $5.2 \times 10^{16} \text{cm}^{-3}$ and $3.0 \times 10^{19} \text{cm}^{-3}$, respectively. During the oxidation process, the diffusivity of oxidants from the ambient to the SiO_2 surface is much faster than the other two processes (diffusion through the oxide and chemical reaction at the Si surface). Therefore, F_1 is largely unimportant in determining the overall growth kinetics.

The second flux F_2 from Figure 2.12 represents the diffusion of the oxidant from the oxide surface to the oxide-silicon interface. Using Fick's law, the diffusion can be expressed as

$$F_2 = D \frac{\partial C}{\partial x} = D \frac{C_0 - C_S}{x_o}, \quad (2.12)$$

where D is the oxidant diffusivity in the oxide, C_S is the concentration of oxidant at the Si- SiO_2 interface, and x_o is the thickness of the oxide film. Since Fick's law assumes steady state conditions, the environment must not change significantly with time in order for this relationship to be valid. This means that there must be no loss of oxidants as they diffuse through the oxide, but rather it is direct movement from regions of high oxidant concentration to regions of low oxidant concentration. The diffusion of oxygen (O_2) is quite straightforward, as it maintains its molecular form throughout the process; however, a water molecule diffuses in a more complex manner, interacting with the SiO_2 matrix.

The final flux F_3 presented in Figure 2.12 is the flux of oxidants consumed during the chemical reaction with silicon atoms at the substrate surface, given by

$$F_3 = k_s \cdot C_S, \quad (2.13)$$

where k_s is the surface rate constant. The parameter k_s is a simplified value which represents many ongoing reactions at the interface, such as Si-Si bond breaking, Si-O bond formation, and possibly O_2 and H_2O bond dissociation into 2O and H/OH, respectively.

Since steady-state conditions are assumed, the three fluxes representing the different stages of the oxidation process must be equal. The processes occur in series with each

other and the rate of the overall process will be determined by the rate of the slowest process. Equating all fluxes results in

$$F_1 = F_s = F_3 = F = \frac{C^*}{\frac{1}{k_s} + \frac{1}{h} + \frac{x_o}{D}}. \quad (2.14)$$

Physically, the system can be viewed as one involving two interfaces (k_s and h), with a diffusion process. Since h is very large, it can be neglected and the physical idea of oxidation reduces itself to a diffusion of oxidant followed by a chemical reaction. For thin oxides ($k_s \cdot x_o/D \ll 1$), the chemical rate of reaction occurs much slower than it takes the oxidant to fall through the oxide, making it the limiting step. For thick oxides ($k_s \cdot x_o/D \gg 1$), it is the diffusion which is much slower than the chemical reaction rate, making it the limiting step for the overall oxidation process.

The overall oxidation rate is proportional to the flux of oxidant molecules,

$$\frac{dx}{dt} = \frac{F}{N} = \frac{\frac{C^*}{N}}{\frac{1}{k_s} + \frac{1}{h} + \frac{x_o}{D}}, \quad (2.15)$$

where N is the number of oxidant molecules per unit volume of oxide grown. $N = 2.2 \times 10^{22} \text{cm}^{-3}$ for dry oxidation and is approximately double that value for wet oxidation.

The differential equation (2.15) can be simplified to

$$\frac{dx}{dt} = \frac{B}{A + 2x_o}, \quad (2.16)$$

where A and B are the physically based parameters

$$A = 2D \left(\frac{1}{k_s} + \frac{1}{h} \right), \quad (2.17)$$

$$B = 2D \frac{C^*}{N}. \quad (2.18)$$

By integrating (2.15), from an initial oxide thickness x_i to a final oxide thickness x_o , a final result regarding oxide kinetics can be written as

$$N \int_{x_i}^{x_o} \left[1 + \frac{k_s}{h} + \frac{k_s x}{D} \right] dx = k_s C^* \int_0^t dt. \quad (2.19)$$

Introducing the simplified form from (2.16), (2.19) can be re-written to

$$\int_{x_i}^{x_o} (A + 2x) dx = B \int_0^t dt, \quad (2.20)$$

yielding the quadratic equation

$$x_o^2 + Ax_o = B(t + \tau), \quad (2.21)$$

where the parameter τ is introduced in order to account for the initial oxide x_i , given by

$$\tau = \frac{x_i^2 + Ax_i}{B}. \quad (2.22)$$

Although the parameters τ and x_i are meant to account for any oxide present at the start of oxidation, they can also be useful fitting parameters when a better fit to data in the thin oxide regime is required.

Sometimes, it is useful to view (2.21) in the following form

$$t + \tau = \frac{x_o^2 + x_i^2}{B} + \frac{x_o + x_i}{B/A}, \quad (2.23)$$

enabling a direct calculation for the time required to grow a desired thickness of oxide. However, solving (2.21) in order to directly enable the calculation of the oxide thickness after a specific oxidation time t results in

$$x_o = \frac{A}{2} \left(\sqrt{1 + \frac{4B}{A^2}(t + \tau)} - 1 \right). \quad (2.24)$$

Observing (2.23) and (2.24), it is clear why the Deal-Grove model survives after so many decades. Being able to directly calculate the oxide thickness, when the oxidation time is known and vice-versa, is the main strength of this model.

A closer look at (2.23) suggests that there are two limiting forms of the linear parabolic growth law. The parabolic or linear limiting form occur when $\frac{x_o^2}{B}$ or $\frac{x_o}{B/A}$ are the dominant terms in (2.23), respectively. From (2.24), a limiting case can be identified when the oxidation time is given by $t \gg \tau$ and $t \gg A^2/4B$

$$x_o \cong \sqrt{B \cdot t}, \quad (2.25)$$

where B is known as the parabolic rate constant given by (2.18). The second limiting case can be identified when the oxidation time is given by $t \ll A^2/4B$

$$x_o \cong \frac{B}{A}(t + \tau), \quad (2.26)$$

where B/A is defined as the linear rate constant:

$$\frac{B}{A} = \frac{C^*}{N \left(\frac{1}{k_s} + \frac{1}{h} \right)} \cong \frac{C^* \cdot k_s}{N}, \quad (2.27)$$

The parabolic term (2.25) dominates for large x values, while the linear term (2.26) dominates for small x values.

The rate constants B and B/A which are the main idea behind the linear-parabolic oxide growth model are sometimes referred to as the Deal-Grove parameters. These parameters have been extracted from experimental data and evaluated under a wide range of experimental conditions [175].

Temperature

The effects of temperature on the overall oxidation process have been examined in Section 2.2.1 where it was shown that increasing the processing temperature resulted in an increased oxide thickness and a faster oxidation rate. Therefore, in order to model oxidation using the linear-parabolic approach, both the linear (B/A) and parabolic (B) parameters must be adjustable for temperature effects. From experimental data, it was found that Arrhenius expressions well describe the temperature effects on B and B/A

$$B = C_1 e^{\left(-\frac{E_1}{k_B T}\right)}, \quad (2.28)$$

$$\frac{B}{A} = C_2 e^{\left(-\frac{E_2}{k_B T}\right)}, \quad (2.29)$$

where E_1 and E_2 are the activation energies associated with the physical processes that B and B/A represent, respectively and C_1 and C_2 are pre-exponential constants. Table 2.2 lists the experimentally determined parameters required to solve (2.28) and (2.29) for a (111) oriented silicon surface. For a (100) oriented silicon surface, only the parameter C_2 must be modified by dividing the (111) value by a factor of 1.68 [175]. The remaining parameters remain the same for both crystal orientations.

An analysis of the parabolic rate constant B from Table 2.2 shows that the activation energy E_1 for O_2 and H_2O ambients are quite different. This suggests that the physical mechanism characterized by E_1 might be the oxidant diffusion through SiO_2 , since the diffusivity of O_2 and H_2O in oxide are different, N is a constant value, and C^* is not expected to exponentially increase with temperature. This suggests that the parameter B from the linear parabolic model represents the oxidant diffusion process.

The activation energy E_2 for B/A in the table seems to be close to $2eV$ for a O_2 system as well as a H_2O system. This suggests that the physical origin of E_2 might

| Ambient: | B | B/A |
|----------------|--------------------------------------------------------|--------------------------------------------------------|
| Dry (O_2) | $C_1 = 7.72 \times 10^2 \mu m^2/hr$ $E_1 = 1.23 eV$ | $C_2 = 6.23 \times 10^6 \mu m^2/hr$ $E_1 = 2.00 eV$ |
| Wet (H_2O) | $C_1 = 3.86 \times 10^2 \mu m^2/hr$ $E_1 = 0.78 eV$ | $C_2 = 1.63 \times 10^8 \mu m^2/hr$ $E_1 = 2.05 eV$ |

Table 2.2.: Rate constants describing (111) oriented silicon oxidation kinetics at 1atm pressure. For the corresponding values for (100) oriented silicon, C_2 values should be divided by 1.68.

be the chemical reaction at the silicon-silicon dioxide interface k_s . The $2eV$ activation energy has been associated with the Si-Si bond breaking process as confirmed by measurements performed by Pauling, which suggested the correlation between the B/A values and the activation energies of Si-Si bond breaking [170].

Hydrostatic Pressure

The effects of pressure on the oxide growth kinetics have been examined in Section 2.2.1, where it was shown that increasing pressure causes an increased oxide film thickness when temperature is kept constant. Henry's law, relating to oxide growth shown in (2.11) suggests a linear relationship between pressure and the oxidation rate. Since C^* is proportional to p , from (2.11) and both B and B/A are proportional to C^* from (2.18) and (2.27), respectively, then the growth rate should be proportional to p . Experimental measurements of H_2O oxidation have shown this prediction to be correct for pressures ranging from below to well above atmospheric [175]:

$$B_{wet}(p) = B_{wet}(1atm) \cdot p, \quad (2.30)$$

$$\frac{B}{A}_{wet}(p) = \frac{B}{A}_{wet}(1atm) \cdot p, \quad (2.31)$$

where p is the hydrostatic pressure in atm.

However, in the case of dry oxidation with O_2 , the situation is somewhat unclear. Experimental results have consistently shown that a linear relationship does not exist between the linear and parabolic rate constants and the applied pressure. In fact, the linear rate constant is proportional to the pressure $B \propto p$, but the parabolic rate constant varies with $B/A \propto p^n$, where $0.5 < n < 1$. Since the linear rate constant is proportional to pressure, it can be concluded that (2.11) is correct and $C^* \propto p$, but that the rate of reaction at the silicon surface k_s depends on p in a nonlinear fashion. In order to adjust the Deal-Grove model to satisfy the pressure effects in dry oxidation, the values of B and B/A should be modified by:

$$B_{dry}(p) = B_{dry}(1atm) \cdot p, \quad (2.32)$$

$$\frac{B}{A}_{dry}(p) = \frac{B}{A}_{dry}(1atm) \cdot p^{0.7-0.8}, \quad (2.33)$$

where p is the hydrostatic pressure in atm and the value of $\sim 0.7 - 0.8$ is an experimentally observed parameter.

Crystal Orientation

The crystal orientation of the oxidized silicon surface affects the oxide growth kinetics, as examined in Section 2.2.1. This effect has been observed even before the Deal-Grove model was suggested [126]. In order to associate the differences in oxidation kinetics with varying silicon crystal orientation, an analysis regarding the linear and parabolic rate constants is needed.

When observing the linear rate constant, except at the initial stage of oxidation, the oxide grows on silicon in an amorphous way. Therefore, no information regarding the crystal structure of the underlying silicon is known as the oxide volume increases. The linear rate constant B should not change with a changing crystal orientation of the underlying silicon. This is also observed in experiments by extracting growth data for various crystal orientations [122].

$$B_{\langle 111 \rangle} = B_{\langle 100 \rangle} \quad (2.34)$$

However, the parabolic rate constant B/A should depend on the silicon crystal orientation. The reason is that it involves the chemical reaction which occurs directly on the Si/SiO₂ interface. The speed of this reaction should depend on the amount of silicon atoms available for the reaction. It was found experimentally that surfaces which provide more available reaction sites to silicon have a higher oxidation rate [122]. The ratio for the parabolic rate constant in silicon crystal orientations (111):(100) was found to be 1.68:1. This can be adjusted in the Deal-Grove model by

$$\frac{B}{A}_{\langle 111 \rangle} = 1.68 \cdot \frac{B}{A}_{\langle 100 \rangle}. \quad (2.35)$$

Similarly, it has been suggested that the ratio for the parabolic rate constant in crystal orientations (110):(100) is approximately 1.45:1, noticeable on thicker oxide along sidewall surfaces. However, this value is not readily accepted as there is not a sufficient amount of data to be certain of this value [175]

$$\frac{B}{A}_{\langle 110 \rangle} = 1.45 \frac{B}{A}_{\langle 100 \rangle}. \quad (2.36)$$

2.3.2. Limitations of the Deal-Grove Model

It should be noted that the Deal-Grove model, although good in many aspects when attempting to model the thermal oxidation of silicon, has several limitations. Mainly, the model does not describe several observed phenomena:

- The surface reaction, which converts Si and O₂ or H₂O into SiO₂, is influenced by pressure and the silicon surface doping concentration. This is dealt with in ways which go beyond the Deal-Grove model, such as introducing an additional expression for the effects of the atmospheric pressure on the linear and parabolic rate constants. This is implementable as an additional feature to the Deal-Grove model.
- The Deal-Grove model does not include the influence of treatment prior to oxidation, which is standard for any silicon processing, such as wafer cleaning or UV treatment, which was found to cause an oxide growth of up to 1.5 nm, reduce the carbon content in the subsequent thermal oxide growth, and improve the dielectric strength in gate oxides [181].
- In a dry ambient, ultra-thin oxides (10 - 30nm) experience accelerated growth. The Deal-Grove model does not deal with this phenomenon, but it will be addressed within Section 2.3.3.
- Two-dimensional effects are also not a part of the Deal-Grove model. These effects cause oxide thinning at trench corners and steps. Although not covered by Deal-Grove, some effects can be added to a Deal-Grove model.
- The growth of a thin layer (~1nm) of native oxide even at room temperature is not described or explained by the model.

2.3.3. Massoud Model

As previously described in Section 2.3.1, the Deal-Grove model can only describe oxidation growth for oxides with thicknesses above 30nm. At the time when the Deal-Grove model was introduced (1965), the semiconductor industry did not require such thin films. However, as the device sizes and geometries began to shrink, the limitations of the Deal-Grove model became evident. It has been observed experimentally that the oxidation rate is much faster than predicted by the Deal-Grove model at the initial stages of oxidation and for thin oxide growths [34]. Several researchers have suggested that the cause of the increased oxidation rate are electrochemical effects such as field-enhanced oxidation, structural effects such as microchannels, stress effects modifying oxidant diffusivity, and changes in oxygen solubility in the oxide with little success. Those that had more success suggested the increased rate is due to parallel oxidation mechanisms such as silicon interstitials injected into the oxide, oxygen

vacancies, diffusion of atomic oxygen, surface oxygen exchange, and the effects of a finite non-stoichiometric transition region between amorphous SiO_2 and Si [34].

Massoud et al., in 1985 [143], [144] suggested an update to the Deal-Grove model for dry oxidation, which was to address the thin oxide growth regime. They provided an analytical model based on parallel oxidation mechanisms to fit experimental data with good success. The price for the improved model for thin oxides is an increased complexity of the model.

Massoud introduced additional terms to the oxidation rate equation (2.16) and changed the values of the linear and parabolic constants. The oxidation rate is given by

$$\frac{dx_o}{dt} = \frac{B}{A + 2x_o} + C_1 e^{\left(-\frac{x_o}{L_1}\right)} + C_2 e^{\left(-\frac{x_o}{L_2}\right)}, \quad (2.37)$$

where the first term on the right hand side is identical to the Deal-Grove model, but the values for the Massoud model are different, as shown in Table 2.3. The Arrhenius expressions for B and B/A can be written as

$$B = C_B e^{\left(-\frac{E_B}{k_b T}\right)}, \quad (2.38)$$

$$\frac{B}{A} = C_{B/A} e^{\left(-\frac{E_{B/A}}{k_b T}\right)}. \quad (2.39)$$

The values for the pre-exponential constants C_B , $C_{B/A}$ and the activation energies E_B , $E_{B/A}$ for different crystal orientations and temperatures are listed in Table 2.3. It should also be noted that the values for C_B , $C_{B/A}$, E_B , and $E_{B/A}$ change with temperature, which was not the case with the original Deal-Grove model.

| Temperature: | $T < 1000^\circ\text{C}$ | | | $T > 1000^\circ\text{C}$ | |
|---------------------------------|--------------------------|-----------------------|-----------------------|--------------------------|-----------------------|
| Orientation: | (100) | (111) | (110) | (100) | (111) |
| $C_B \text{ (nm}^2/\text{min)}$ | 1.70×10^{11} | 1.34×10^9 | 3.73×10^8 | 1.31×10^5 | 2.56×10^5 |
| $E_B \text{ (eV)}$ | 2.22 | 1.71 | 1.63 | 0.68 | 0.76 |
| $C_{B/A} \text{ (nm/min)}$ | 7.35×10^6 | 1.32×10^{71} | 4.73×10^{81} | 3.53×10^{12} | 6.50×10^{11} |
| $E_{B/A} \text{ (eV)}$ | 1.76 | 1.74 | 2.10 | 3.20 | 2.95 |

Table 2.3.: Rate constants describing oxidation kinetics at 1atm pressure using the Massoud model for various silicon orientations and temperatures from [143].

In (2.37), the second and third term on the right hand side are additional terms which represent the rate enhancement in the thin regime. They are defined by pre-exponential constants C_1 and C_2 and characteristic lengths L_1 and L_2 . The first characteristic length L_1 is in the order of 1nm and is meant to deal with the rate increase in the first 5nm of oxide growth, after which it vanishes. The second characteristic length L_2 , with a value in the order of 7nm, is meant to decay until approximately

25nm, after which it no longer influences the oxidation rate and the rate becomes linear-parabolic once again.

Another way to express (2.37) in terms which are easier to manipulate and mathematically solve is presented in [142]

$$\frac{dx_o}{dt} = \frac{B + K_1 e\left(-\frac{t}{\tau_1}\right) + K_2 e\left(-\frac{t}{\tau_2}\right)}{2x_o + A}, \quad (2.40)$$

where all additional parameters, other than A and B are fitted to an Arrhenius expression

$$K_1 = K_1^0 e\left(-\frac{E_{K_1}}{k_b T}\right), \quad (2.41)$$

$$K_2 = K_2^0 e\left(-\frac{E_{K_2}}{k_b T}\right), \quad (2.42)$$

$$\tau_1 = \tau_1^0 e\left(-\frac{E_{\tau_1}}{k_b T}\right), \quad (2.43)$$

$$\tau_2 = \tau_2^0 e\left(-\frac{E_{\tau_2}}{k_b T}\right). \quad (2.44)$$

The pre-exponential constants and activation energies of the above expressions (2.41)-(2.44) are given in Table 2.4 for dry oxidation in a temperature range from 800–1000°C.

| Crystal orientation: | (100) | (111) | (110) |
|----------------------|-----------------------|-----------------------|-----------------------|
| $K_1^0 (nm^2/min)$ | 2.49×10^{11} | 2.70×10^9 | 4.07×10^8 |
| E_{K_1} | 2.18 | 1.74 | 1.53 |
| $K_2^0 (nm^2/min)$ | 3.72×10^{11} | 1.33×10^9 | 1.20×10^8 |
| E_{K_2} | 2.28 | 1.76 | 1.56 |
| $\tau_1^0 (min)$ | 4.14×10^{-6} | 1.72×10^{-6} | 5.38×10^{-9} |
| E_{τ_1} | 1.38 | 1.45 | 2.02 |
| $\tau_1^0 (min)$ | 2.71×10^{-7} | 1.56×10^{-7} | 1.63×10^{-8} |
| E_{τ_2} | 1.88 | 1.90 | 2.12 |

Table 2.4.: Arrhenius expressions for pre-exponential constants K_1^0 and K_2^0 , time constants τ_1^0 and τ_2^0 , and activation energies E_{K_1} , E_{K_2} , E_{τ_1} , and E_{τ_2} from the Massoud model presented in [143] and given in (2.40)-(2.44).

As already performed for the Deal-Grove expression in Section 2.3.1, inverting (2.40) gives a convenient expression for the oxide thickness as a function of oxidation time and vice-versa. Therefore, (2.40) is re-written as

$$(2x_o + A) dx_o = \left[B + K_1 e\left(-\frac{t}{\tau_1}\right) + K_2 e\left(-\frac{t}{\tau_2}\right) \right] dt \quad (2.45)$$

and integrated with time varying from 0 to t and oxide thickness from x_i to x_o

$$x_o^2 + Ax_o = B \cdot t + M_1 \left[1 - e^{\left(-\frac{t}{\tau_1}\right)} \right] + M_2 \left[1 - e^{\left(-\frac{t}{\tau_2}\right)} \right] + M_0, \quad (2.46)$$

where M_0 , M_1 , and M_2 are given by

$$M_0 = (x_i^2 + Ax_i), \quad M_1 = K_1 \cdot \tau_1, \quad M_2 = K_2 \cdot \tau_2. \quad (2.47)$$

Equation (2.46) can be solved in order to obtain an analytic expression for the oxide thickness as a function of oxidation time

$$x_o = \sqrt{\left(\frac{A}{2}\right)^2 + B \cdot t + M_1 \left[1 - e^{\left(-\frac{t}{\tau_1}\right)} \right] + M_2 \left[1 - e^{\left(-\frac{t}{\tau_2}\right)} \right] + M_0} - \frac{A}{2}. \quad (2.48)$$

The relationship (2.48) is meant to give a valid expression for the oxide thickness after an oxidation time t in a dry ambient from the native oxide thickness conditions. Figure 2.13 shows the difference between the Deal-Grove model and the Massoud model for the initial stages of oxidation. It is evident that the Massoud model depicts a faster initial oxidation rate.

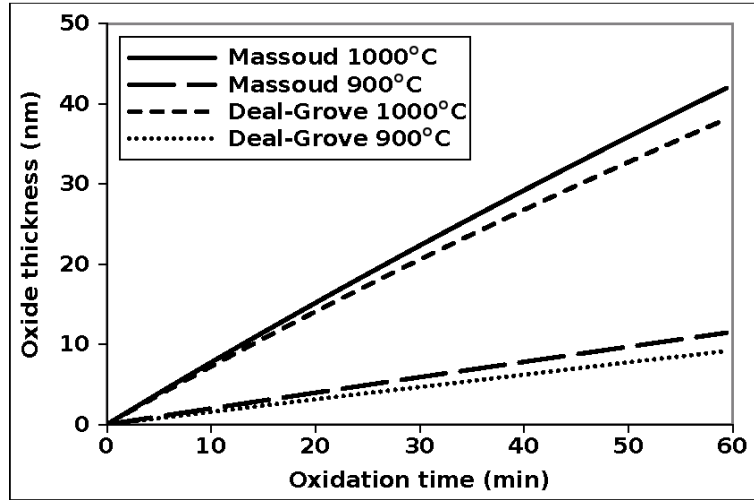


Figure 2.13.: Comparison between the Deal Grove and Massoud models for the oxide thickness during the first hour of oxidation in a dry ambient on (100) oriented silicon.

2.3.4. Other One-Dimensional Oxide Growth Models

Massoud's model attempted to correct what was lacking from the Deal-Grove model, mainly the inability of the model to accurately represent thin oxide growth. Since

Massoud, many other attempts to model the thin oxide have been suggested in literature. Some have a very similar approach to that presented by Massoud, where additional terms are added to the linear parabolic model in order to introduce additional fitting parameters [37], [218], [220], [221]. However, in most of the presented models, extracting an explicit expression for the oxide thickness as a function of oxidation time is not possible. The model described in [218] suggests the addition of a term with a logarithmic dependence on the oxide thickness, while the model from [220], [221] inserts an error function in the parabolic rate constant B/A .

Another direction in which researchers have attempted to improve on the initial idea is by neglecting the effect of diffusion altogether and only concentrating on modeling the extra thin film oxide growth [132]. This led to the idea that there might be silicon atoms penetrating into the oxide and even being pushed to the oxide surface, where they can react to grow more oxide.

More recently researchers have looked at a reaction rate approach to oxide growth, which is gaining some traction [41], [110]. The idea behind this model is that the main assumption made by the Deal-Grove model of a steady state regime is incorrect. It is also suggested that it is wrong to assume a sharp Si-SiO₂ interface where all reactions take place. It is quite well known today that the interface between silicon and silicon dioxide is not a smooth one and many researchers are studying the interface at a molecular level, which is the most promising way to understand ultra-thin oxides needed for modern IC devices. Section 2.1.1 gives a further discussion regarding the atomistic view of the Si-SiO₂ interface.

It should also be noted that, even with the introduction of the Massoud model, and other linear-parabolic models some limitations discussed regarding the Deal-Grove model are still present. Mainly, two- and three-dimensional effects are not described by these models, nor is the growth of a thin native oxide even at room temperature.

2.4. Local Oxidation Nanolithography

In Section 1.1, an overview of Complementary Metal Oxide Semiconductor CMOS processing technologies is given. However, the semiconductor industry is continuing to attempt to follow Moore's law [154] using the recently coined "More Moore" and "More-than-Moore" [2] approaches. "More Moore" is the scientific community's attempt to continue doubling the number of transistors every \sim two years, while "More-than-Moore" relates to solving challenges for application driven components. It is essential that these approaches work together in order to continue current scaling trends into the near and distant future [2].

In order to continue with "More Moore", it is evident that standard lithographic techniques are not sufficient in providing the necessary steps for the generation of modern nanosized devices. The drive to generate smaller and smaller devices leads to various

attempts to replace conventional optical and electron beam lithographies with other lithographic technologies [61], [198]. The 248nm and 193nm ultraviolet lithography is approaching the limit of its potential and in order to continue with “More Moore” various alternatives have been examined [69]. Although 157nm lithography has been introduced in order to enable the production of sub-50nm features, the scientific community opted to mainly employ high-index immersion lithography [182] to the 193nm technology instead of dealing with numerous technical and economic issues which arise with the introduction of a new 157nm technology [24]. With high-index immersion lithography, the 193nm node was used to generate sub-40nm features [182]. Beyond this node, the global semiconductor manufacturer consortium International Sematech, suggested that extreme ultraviolet (EUV), or X-ray lithography [18], is likely to become the community standard [198]. More recently, EUV has been studied in order to generate sub-10nm patterns [166]. However, many issues still remain unsolved and the lithographic performance for patterns generated by IBM and AMD showed much to be desired with regard to uniformity, overlay, and defect generation [70]. AMD suggested that it is attempting to include EUV in its high-volume processing chain for the 16nm node by 2014 [70]. Although a promising technology Extreme Ultra Violet (EUV) is a very expensive and complex technique which must be performed in a vacuum. Additional sources of contention with EUV is equivalent to issues which arise with electron beam lithography; the mirror responsible for collecting the light is directly exposed to the plasma, making it vulnerable to damage from the high-energy ions [194]. Due to these combined issues for optical, electrical, and X-ray lithographies, a possible low cost route for lithography was sought out, which uses a direct localized printing technique [30].

Some nanoprining techniques that were experimented with through the 1990’s in order to advance lithography techniques for nanosized devices are magnetolithography [48], soft lithography [230], and Scanning Probe Microscopy (SPM), which include nanoimprint lithography [31], dip-pen nanolithography [174], and Local Oxidation Nanolithography (LON) [38].

Magnetolithography is based on applying a magnetic field on the substrate using magnetic masks in order to define a spatial distribution of magnetic nanoparticles. The nanoparticles react chemically with the substrate, acting as a mask for desired substrate regions. Magnetolithography is a bottom-up technique, which has the drawback of a relatively low throughput, which can be overcome with expensive and defect-prone parallelism [1], [8], [129], [212].

In soft lithography, an elastometric stamp with patterned relief structures on its surface is applied to generate structures with feature sizes ranging from 30nm to 100 μ m. This lithographic method results in stamp deformations, with the stamp shrinking or swelling during the curing process, as well as substrate contamination, resulting in a reduced quality printed image [230].

Nanoimprint lithography deals with printing a template pattern on a mask using a UV photoresist or a spin coated polymer on the substrate. The simplicity of the method

makes it attractive for manufacturing; however problems persist with overlay, defects, and template wear [79].

Dip-pen nanolithography is used to directly imprint chemical patterns on surfaces with nanoscale precision using an AFM [23].

Similarly, LON uses an AFM in order to deposit a new layer on a wafer surface, such as the deposition of silicon dioxide on a silicon wafer [38]. The main advantage which LON has over other attempts to generate nanosized patterns on a wafer surface is its ability to be performed at room temperature in an air ambient and across a large range of materials [198]. This section deals with the development of the LON technique and how the interactions between a scanning tunneling microscope (STM) or AFM with the silicon surface results in oxide growth.

2.4.1. Technology Background

In the early 1980's the STM was developed at IBM Zürich as an instrument to image surfaces at the atomic level [13]. A schematic of the basic operations of a STM is shown in Figure 2.14. After the initial patent, the scientists involved won a Nobel Prize in Physics for their design in 1986 [15]. Countless publications followed, as the STM was perfected as a tool to utilize tunneling current between a conductive metal tip and a sample surface in order to detect depressions and protuberances on a nanometer sized section of the test surface. The test surfaces initially considered include $\text{CaIrSn}_4(110)$ [16], $\text{Au}(110)$ [16], $\text{Si}(111)$ [17], and $\text{GaAs}(111)$ [14]. The STM allows for a 0.1nm lateral resolution and a 0.01nm depth resolution [7]. Shortly after, the discoverer of the STM, Binnig was involved in the discovery of the AFM [12], which has a much higher resolution and is today one of the foremost tools for imaging surfaces at the atomistic level [74], [114], [116], [184], some even suggesting that different bond orders of individual carbon-carbon bonds can be visualized using an AFM [67], [173], [223]. The AFM monitors the surface by sensing the van der Waals force between the tip and the surface, in order to achieve a much finer resolution than the STM. A basic schematic of AFM operation is shown in Figure 2.15, where a cantilever is brought close to a test surface, while the movements of the cantilever needle are recorded by the photodiode. The AFM has been used extensively, not only in the semiconductor industry, but also in physics, chemistry, biology, biochemistry, and other disciplines where the chemical or physical properties of a surface are required [136], [207]. An additional advantage of AFM over STM is that AFM offers the advantage of realizing local oxidation and reading the topography of the generated pattern [197].

LON of semiconductor surfaces was first suggested by Dagata et al. at the National Institute of Standards and Technology, where a STM was used in order to chemically modify a hydrogen-passivated $\text{Si}(111)$ surface in an air ambient with 100nm precision [38]. By 1993, Day and Alle used an AFM in order to generate sub-100nm SiO_2 lines on a silicon wafer, thereby introducing the AFM as a lithographic tool and solving

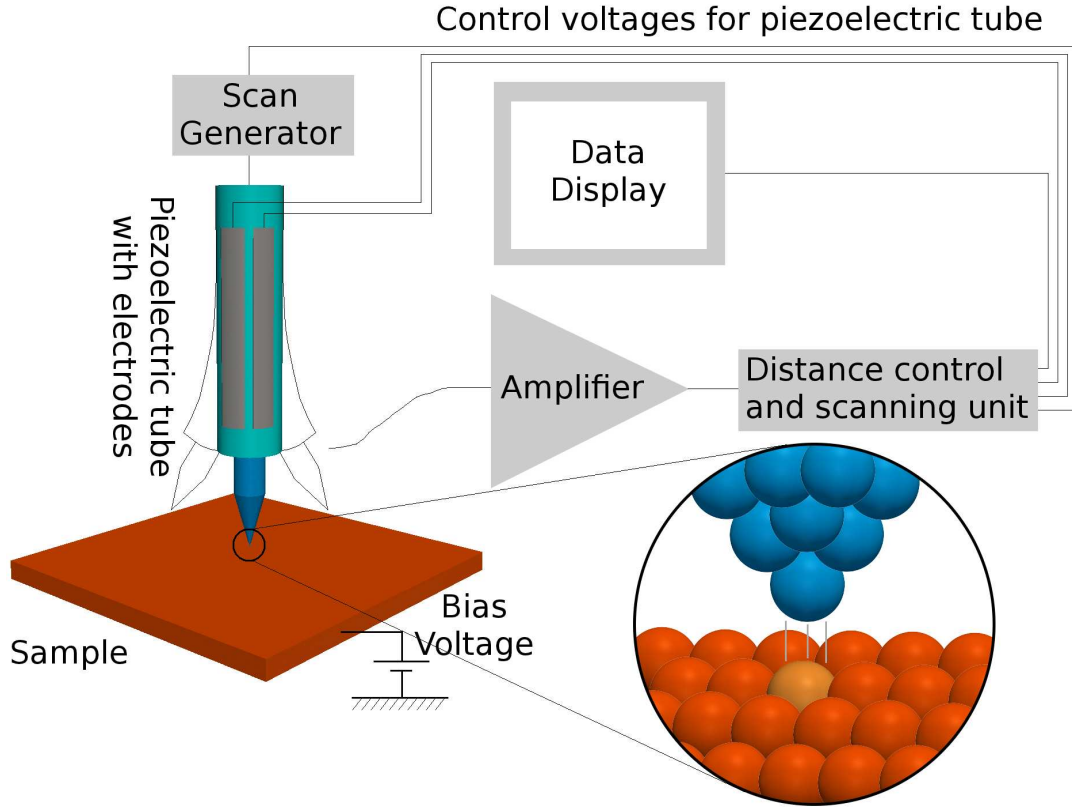


Figure 2.14.: Typical STM schematic for surface imaging.

the issues that were persistent with STM lithography [40]. The main disadvantage of STM is that the tip sample spacing cannot be chosen independently from the tunneling current and tip voltage. Therefore, the tip can often crash into the insulating structure, because it is frequently not possible to keep the tip above the highest insulating feature while simultaneously having the optimum bias voltage and tunneling current for ultrathin resolution [40]. Both methods worked in such a way that a potential difference was applied between the tip (STM or AFM) and the sample substrate. A positive bias voltage is applied to the STM tip, while a negative was applied to the AFM tip, with respect to the silicon substrate. The negative voltage results in the ability to produce thicker insulating oxides [4], [40], [73], [191], [231].

2.4.2. Scanning Tunneling Microscope Lithography

The initial LON was performed on a hydrogen-passivated silicon surface using a STM in an air ambient with a positive tip bias voltage [38]. However, due to the poor reliability of the STM tip during the nano-oxidation process, very few LON studies have been performed with this technique in the mid 1990s [54], [55], [108], [134], [201],

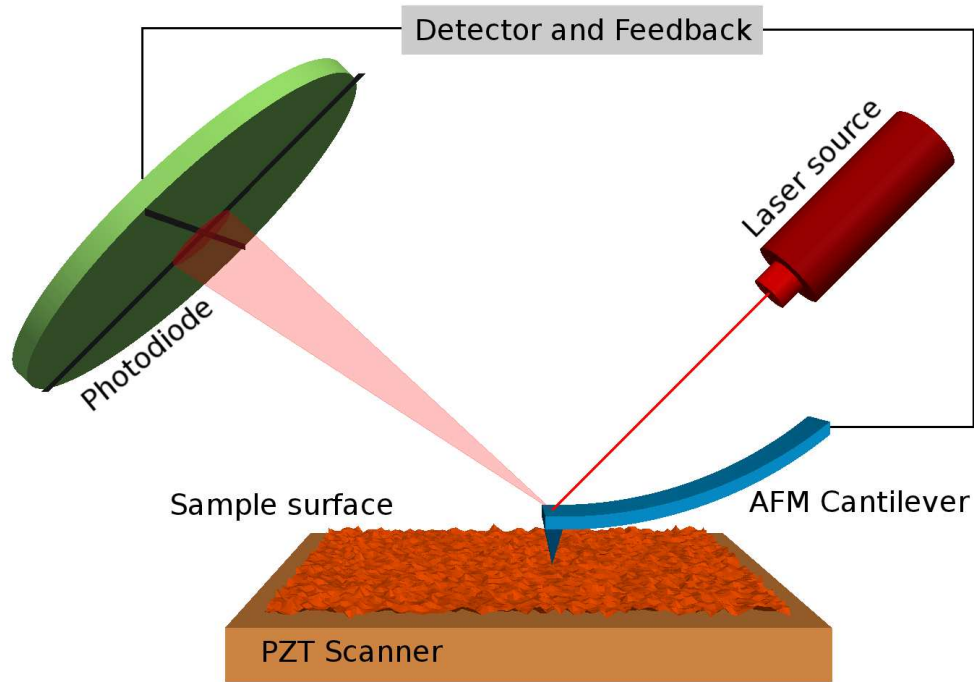


Figure 2.15.: Typical AFM schematic for surface imaging.

[227]. Since the STM tip cannot identify the grown oxide from the air ambient, it views a generated nanopattern as a depression on the surface. Therefore, in order for the STM to maintain its current constant, the feedback loop pushes the tip towards the surface, risking contact with the oxide [198], [200]. Many systems which use a STM in order to generate oxide nanopatterns use a subsequent AFM imaging step in order to be able to visualize the pattern which has been generated [55]. With pure STM systems, the apparent depth is considered as a measure of oxide height. It has been shown that increasing the tunneling current results in an increase in apparent depth [68]. In order for the STM to function at heights required not to contact the oxide surface, it must have an apparent depth of several nanometers [198], meaning that a nanometer-sized water meniscus forms in the area between the tip and the surface. The presence of water suggests that an electrochemistry process is responsible for the nanooxidation process and not current tunneling [52]. As the tunneling current increases, the distance between the tip and the surface decreases causing an increased electric field in the area, thus causing the oxide depth to increase. A logarithmic decay of the oxide depth is also noted when the tip speed is increased [198]. Due to the close interactions between the STM tip and the surface, tip damaging is often observed, leading to poor reliability for nanooxidation. AFM has much finer control of the tip-surface distance and is therefore seen as an improved tool for nanooxidation; AFM is explored further in the section to follow.

2.4.3. Atomic Force Microscope Lithography

Applying a negative potential to the AFM needle tip, while the silicon substrate is held grounded causes a negative electric field to be generated in the region. When the ambient is highly humid, a water meniscus forms between the AFM needle tip and the silicon substrate, shown in Figure 2.16. The water meniscus, together with the

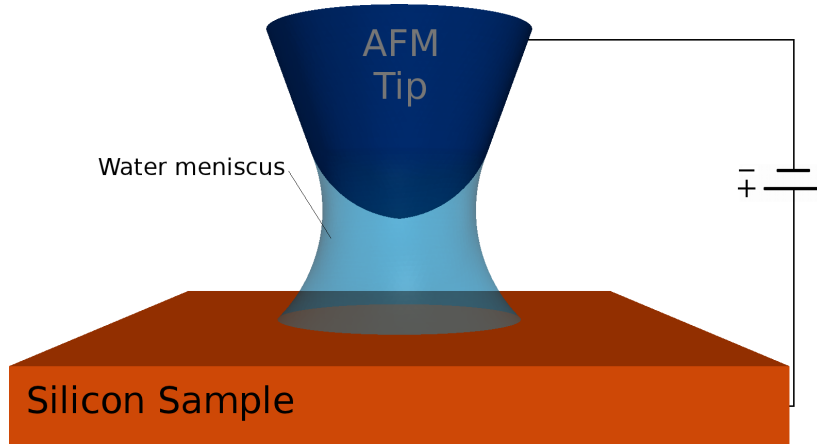


Figure 2.16.: Generation of a water meniscus between the AFM tip and silicon substrate after a negative voltage is applied.

high electric field, causes the water molecules to break up into oxyanions (H^+ , OH^- , O^-) [198], [212]. The negatively charged oxyanions (mainly OH^-) are accelerated along the electric field lines towards the substrate, where they interact with the silicon to form silicon dioxide and byproducts. Since the introduction of the AFM as a lithographic tool by Day [40], countless other researchers have helped grow the technology into one of the most promising methods for localized oxidation of silicon [4], [57], [60], [63], [202]. The generated oxide can act as a mask for subsequent etching steps or as an insulating barrier for thin semiconductor film on insulator processes [55]. LON of graphene using AFM has also shown promise in growing oxide layers [224]. Graphene has recently been demonstrated to provide remarkable electronic properties and large effort is placed towards implementing graphene based fast electronic and optoelectronic devices [5]. A distinct advantage of AFM over STM is its ability to read back the actual topography of the generated pattern, while STM is unable to give the real height [198]. Over the years, empirical and analytical models have been suggested in order to predict how the semiconductor topography changes, when different voltages, pulse times, and tip velocities are applied to the AFM system [4], [6], [28], [38], [39], [84], [95], [192], [198]. LON with an AFM can be used in several operation modes: contact mode (CM), non-contact mode (NCM), and intermittent contact mode (ICM), also known as tapping mode (TM).

Contact Mode Lithography

When LON is performed using AFM in contact mode, a small tip load is required, with a bias voltage variation of approximately 5 to 20V, and a typical tip speed from 0.1 to 10 μ m/s [212]. The applied force is an additional variable required for CM operation, and it ranges from 10 to 100mN [198]. The tip separation is zero, since the AFM needle is brought in contact with the sample surface. The electric field, generated due to the tip/sample interaction is in the order of 10⁷V/cm.

The dependence of the applied force on the oxide height is independent of the applied voltage and is of the order of 0.01nm/nN [198]. The height is shown to vary linearly with voltage [73], with a limit of 0.4nm/V for low speeds, while having a logarithmic variation with respect to the probe speed [55]. The width of the generated oxide has a similar dependence on the experimental factors as those stated for the oxide height. The widths are relatively large due to the large size of the AFM needle tip used in CM [198].

In CM, the surface experiences both compressive forces due to the contact between the tip and sample, as well as shear forces, due to the lateral scanning motion of the needle tip across the sample surface [234]. Due to this direct interaction of the needle with the silicon surface, the needle tip tends to degrade and lose its hemispherical shape relatively quickly [197].

Intermittent Contact Mode Lithography

ICM lithography using an AFM, which is also known as TM and AC mode, is a dynamical mode, where the AFM needle tip is driven to oscillate at a frequency close to the resonant frequency of the cantilever (approximately 300kHz) [198]. The amplitude of this oscillation typically varies between 20 and 100nm [234] and the surface is struck by the needle tip at each oscillation. The main motivation behind ICM oxidation is to minimize the contact and lateral forces between the needle tip and the silicon surface, thereby increasing the process' reliability and needle lifetime [234].

The influence of bias voltage and tip speed on the heights of ICM-generated oxides is identical to the previously mentioned CM-generated oxides. Mainly, bias voltage has a linear influence, while pulse time has a logarithmic influence on the oxide height. However, using ICM over CM, the resolution is improved and the growth limit at low speeds is also improved to 0.25nm/V [55]. The oxide width is mainly governed by the shape of the needle tip, and for a hemispherical shape, the width-to-height ratio is approximately half of the needle tip diameter [198]. This can be understood by noting that the water meniscus which forms during the intermittent contact of the needle tip with the silicon surface limits the spread of the electric field. The water bridge provides the oxidizing ions and the spacial confinement required to pattern the silicon surface [198]. Since the meniscus shape is driven by the shape of the needle tip, it can

be concluded that the tip shape is the main factor which determines the oxide width dimensions [55]. Several ICM versus CM comparative studies have observed that ICM lithography enjoys a higher aspect ratio, allowing for the generation of smaller oxide widths, and produces higher oxidation rates [53], [55], [209].

It was reported in [192] that, for oxides with heights of a few nm and pulse times below 10ms, the main driving agent for the growth rate is the generation of OH^- ions. Only when the oxide is thick and the pulse time is in the 100ms range does ion diffusion and stress begin to play a role in the oxide growth rate [192], [198]. Thick oxides generated using an AFM, whose growth is driven by ion diffusion and stress, are beyond the scope of this work and will not be addressed in the LON modeling Section 3.4.

Non-Contact Mode Lithography

In 1998, Garcia et al. demonstrated that a process similar to ICM lithography can be used to generate oxide dots on a silicon surface [60]. The use of milliseconds pulsed voltages generates a water meniscus bridge even if the AFM needle tip does not directly strike the surface [133]. This is possible, when the bias voltage, applied between the AFM needle tip and the silicon surface is sufficiently large. The presence of the water meniscus and the high electric field is enough to cause localized oxidation to occur, therefore no direct contact between the needle tip and surface is required [133], [140]. Since no contact occurs, surface nanooxidation is easily reproducible and no degradation of the needle tip occurs, allowing for enhanced tip lifetimes and significantly reducing surface defects.

For NCM lithography, the needle tip is brought close to the silicon surface. An external voltage pulse is applied between the needle tip and the silicon substrate such that the needle tip is negatively charged with respect to the silicon substrate. The cantilever is then excited at its resonance frequency ($\sim 300\text{kHz}$), similar to ICM operation. However, the cantilever is controlled to oscillate with an amplitude of only a few nm and not 20 to 100nm, which is the case for ICM lithography. This allows for the cantilever to oscillate, but always remain above the silicon surface, thereby never striking it [28]. When the ambient humidity and bias voltage are sufficiently large, a water meniscus, such as the one described in the ICM section above and shown in Figure 2.16, is generated. The liquid bridge provides oxyanions (OH^- , O^-) needed to interact with the silicon in order to form SiO_2 . In addition, it confines the lateral expansion of the patterned oxide, allowing for widths below those associated with CM- and ICM minima [28].

The procedure required in order to generate a single oxide nanodot using an AFM in NCM is laid out in [141]:

- 1- The AFM needle tip is oscillated above the sample surface, followed by the application of the bias voltage pulse.

- 2- The oscillator amplitude is reduced by the electrostatic interaction, which deflects the AFM needle tip position and modifies the AFM cantilever's resonant frequency.
- 3- The bias voltage is turned off; however, the AFM cantilever oscillation remain reduced due to the capillary force of the water meniscus.
- 4- Finally, the tip is lifted away from the water meniscus, allowing for its oscillations to return to their initial amplitude.

A well known drawback of NCM lithography is that the applied voltage in the feedback loop is off during silicon oxidation, resulting in the inability for the AFM needle to move during oxidation. Therefore, nanowires and continuous patterns cannot be generated with a single needle motion [198]. However, when pulses of the order of a few microseconds are introduced [120] and the lateral distance between pulses is smaller than the size of the individual nanodots [141], a SiO₂ nanowire can be generated.

3. Simulating Silicon Oxidation

3.1. Thermal Oxidation Simulators

Current numerical models for oxidation cover a wide variety of techniques. Each technique is not without its limitations which vary depending on the numerical analysis used or the underlying theory. Some approaches to oxidation modeling are described in this section, but some of them go beyond the scope of this work and of the presented LS simulator.

3.1.1. History of Oxidation Simulators

Several numerical techniques for the visualization and modeling of silicon oxidation have been published and implemented in commercial and educational simulation tools. The Institute of Microelectronics at TU Wien is no exception, with several works on silicon oxidation being published [80], [178]. Both works implement simulations using the FEM and follow the Deal-Grove concept, with [80] using the FEDOS simulation tool, developed at the Institute of Microelectronics. The advantage of using the Deal-Grove concept, with two rate constants and two moving boundaries is the existence of the calibrated rate constant for a variety of oxidation conditions.

A tool developed at Stanford University's Department of Electrical Engineering for process simulations is SUPREM-IV [195]. This tool is a pioneer in technology computer aided design (TCAD) simulations, with its roots as a one-dimensional processing tool. SUPREM-IV now has a compress and a viscous mechanical model for the oxidation of silicon and gallium arsenide (GaAs) [196]. The compress model treats the oxide as a compressible liquid, while the viscous model treats it as an incompressible viscous liquid. Its predecessor SUPREM-III is the basis for two commercial tools, TSUPREM-IV and ATHENA.

TSUPREM-IV is an enhanced version of SUPREM-IV, which was commercialized by Technology Modeling Associates Inc. (TMA), a company which was founded at Stanford University and introduced the commercial TCAD business. TMA was acquired by Avant! Corp. in 1998 and by 2002, TSUPREM-IV grew to offer oxidation simulations for compress, viscous, and visco-elastic modeling. In 2002, Avant! was purchased by Synopsys and is still offering TSUPREM-IV.

The Integrated Systems Laboratories at ETH Zurich developed a two-dimensional process simulator DIOS and a one-dimensional simulator TESIM in 1992. Later, the company Integrated Systems Engineering AG (ISE) was formed, distributing DIOS as a commercial simulation tool. By 2004, DIOS had viscous, elastic, or visco-elastic models for the mechanical oxidation problem, at which time it was purchased by Synopsys.

At approximately the same time, TMA developed a three-dimensional process and device simulator Taurus, which was only released after acquisition by Avant!. The mechanics of oxidation were described with a visco-elastic model, but many problems with the moving boundary in three dimensions existed and Taurus was not able to become a complete process simulator until Avant!'s acquisition by Synopsys. Currently, Synopsys has combined the TSUPREM-IV tool with the Taurus tool and it is being offered commercially as Taurus TSUPREM-IV [205].

Around 1994, the first version of the Florida Object Oriented Process Simulator (FLOOPS) was released. Already in 1996, the FLOOPS interface was extended to include three-dimensional models. FLOOPS was commercialized by ISE in 2002 and with additional development from ISE, a new tool FLOOPS-ISE became a stable three-dimensional oxidation simulator. FLOOPS-ISE contained the same mechanical models as ISE's other software, DIOS, but extended to three-dimensional structures. As mentioned previously, ISE along with its software package was sold to Synopsys in 2004. The combination of DIOS and Taurus TSUPREM-IV, released in the FLOOPS-ISE platform was released as a three-dimensional tool, Sentaurus Process [204] by Synopsys.

The company Synopsys, Inc was founded in 1986. After it acquired Avant! and ISE, it became the largest company in the TCAD industry. It now has nearly an 80% share in the TCAD market with Silvaco its sole competitor.

ATHENA is the commercial version of SUPREM-IV from Silvaco Inc., which still distributes ATHENA [188]. While ATHENA has not modified much and is still a two-dimensional simulation tool, Silvaco offers VICTORY Process [189], a three-dimensional process simulator which has empirical models based on the Deal-Grove and Massoud models in addition to physical models which include the reaction at the Si-SiO₂ interface, viscous flow, material deformation, and stress formation. A more detailed look into the oxidation tool offered by Silvaco, which uses a LS environment is described in Section 3.1.3.

Other non-commercialized tools still exist. One process simulator PROPHET was created around 1994 at Bell labs which later became Agere and then, after merging with LSI Logic Corporation, LSI Corporation. Besides these simulators, there are numerous other university and commercial simulators such as PROMIS [91], a two-dimensional process simulator developed at the Institute for Microelectronics, TU Wien.

3.1.2. Visco-Elastic model using FEM

A visco-elastic oxide growth model has been developed at our institute using FEM as the simulation environment [80]. The model is three-dimensional and does not rely on a simple expression for the interface motion, but rather relies on calculations of oxidant diffusion and oxide volume expansion in three dimensions to move the FEM mesh appropriately. A major limitation of FEM analysis is related to the mesh used for simulations. As either the time or space increments are decreased, or the mesh is made finer, the number of calculations necessary to simulate oxide growth can increase by a factor dependent on the model itself [34], [159]. Some models also do not account for orientation dependence adequately or the error can be a non-linear function which can amplify significantly with further iterations [229].

The model presented in [80] is based on a few main equations. The first equation is meant to describe oxidant diffusion

$$D(T) \Delta C(\vec{x}, t) = k(\eta) C(\vec{x}, t), \quad (3.1)$$

where $\Delta = \frac{\partial^2}{\partial x^2} + \frac{\partial^2}{\partial y^2} + \frac{\partial^2}{\partial z^2}$ is the Laplace operator, $C(\vec{x}, t)$ is the oxidant concentration in the material, and $D(T)$ is the temperature dependent low stress diffusion coefficient. $k(\eta)$ is the strength of a spatial sink and not a simple reaction coefficient at a sharp interface

$$k(\eta) = \eta(\vec{x}, t) \cdot k_{max}, \quad (3.2)$$

where k_{max} is the maximal possible strength of the sink.

The next equation is meant to deal with the dynamics of η

$$\frac{\partial \eta(\vec{x}, t)}{\partial t} = -\frac{1}{\lambda} \cdot \frac{k(\eta) C(\vec{x}, t)}{N}, \quad (3.3)$$

where λ is the volume expansion factor ($=2.25$) for the reaction from Si to SiO_2 , and N is the number of oxidant molecules incorporated into a unit of SiO_2 volume.

The volume increase of the generating oxide occurs successively and not abruptly because of the diffuse interface concept. A volume increase of the oxidized material is calculated using the η and C values. After a given time Δt , the normalized additional volume is given by

$$V_{rel}^{add} = \frac{\lambda - 1}{\lambda} \cdot \frac{\Delta t k(\eta) C(\vec{x}, t)}{N}. \quad (3.4)$$

An important aspect of (3.4) is that the sum of V_{rel}^{add} over all time steps must not exceed 125%, which is the maximum volume expansion of the material during oxidation.

Since the principal axis components of the residual strain tensor $\tilde{\epsilon}_0$ are linearly proportional to V_{rel}^{add} in the form

$$\epsilon_{0,xx} = \epsilon_{0,yy} = \epsilon_{0,zz} = \frac{1}{3} V_{rel}^{add}, \quad (3.5)$$

the normalized additional volume directly loads the mechanical problem. Using Hook's law, the stress tensor $\tilde{\sigma}$ is given by

$$\tilde{\sigma} = \mathbf{D} (\tilde{\epsilon} - \tilde{\epsilon}_0) + \tilde{\sigma}_0, \quad (3.6)$$

where \mathbf{D} is the so-called material matrix, constructed in Lamé's form [80], $\tilde{\epsilon}$ is the strain tensor, $\tilde{\epsilon}_0$ is the residual strain tensor, and $\tilde{\sigma}_0$ is the residual stress tensor. The material matrix is rebuilt and (3.6) becomes

$$\begin{pmatrix} \sigma_{xx} \\ \sigma_{yy} \\ \sigma_{zz} \\ \sigma_{xy} \\ \sigma_{yz} \\ \sigma_{zx} \end{pmatrix} = \frac{E(1-\nu)}{(1+\nu)(1-2\nu)} \begin{pmatrix} 1 & \frac{\nu}{1-\nu} & \frac{\nu}{1-\nu} & 0 & 0 & 0 \\ \frac{\nu}{1-\nu} & 1 & \frac{\nu}{1-\nu} & 0 & 0 & 0 \\ \frac{\nu}{1-\nu} & \frac{\nu}{1-\nu} & 1 & 0 & 0 & 0 \\ 0 & 0 & 0 & \frac{1-2\nu}{2(1-\nu)} & 0 & 0 \\ 0 & 0 & 0 & 0 & \frac{1-2\nu}{2(1-\nu)} & 0 \\ 0 & 0 & 0 & 0 & 0 & \frac{1-2\nu}{2(1-\nu)} \end{pmatrix} \begin{pmatrix} \epsilon_{xx} - \epsilon_{0,xx} \\ \epsilon_{yy} - \epsilon_{0,yy} \\ \epsilon_{zz} - \epsilon_{0,zz} \\ \gamma_{xy} - \gamma_{0,xy} \\ \gamma_{yz} - \gamma_{0,yz} \\ \gamma_{zx} - \gamma_{0,zx} \end{pmatrix}, \quad (3.7)$$

where E is the Young's modulus, ν is the Poisson ratio, and γ are the shear strain components.

The effective shear modulus G_{eff} can be added to \mathbf{D} to handle elastic and visco-elastic materials. For elastic materials

$$G_{eff} = G = \frac{E}{2(1+\nu)}, \quad (3.8)$$

while for visco-elastic materials

$$G_{eff} = G \frac{\tau}{\Delta T} \left(1 - e^{(-\Delta T/\tau)} \right), \quad (3.9)$$

where τ is the Maxwellian relaxation time constant and G is the effective shear modulus.

3.1.3. Simulating Oxide Growth using Volume Expansion

Silvaco, Inc., as mentioned in Section 3.1.1, offers a three-dimensional process simulation tool which includes empirical and mechanical oxidation simulations. Their approach to simulating the mechanics of silicon oxidation includes the use of the LS method [203]. Instead of using unstructured meshes, their approach makes use of a fixed Cartesian mesh in a LS environment, solving the problem of moving boundaries which arise when unstructured meshes are used.

The model includes four major steps which work together to generate a moving oxide interface:

1. Oxidant diffusion through the oxide is modeled using the well-known diffusion equation

$$\frac{\partial}{\partial x_i} \left(D \frac{\partial C}{\partial x_i} \right) = 0, \quad (3.10)$$

$$-D \frac{\partial C}{\partial \vec{n}}|_{Si/SiO_2} = k_s C, \quad -D \frac{\partial C}{\partial \vec{n}}|_{SiO_2/O_2} = h(C^* - C), \quad (3.11)$$

where D is the diffusion coefficient, k_s is the reaction rate, h is the gas-phase mass-transfer coefficient, C^* is the equilibrium bulk concentration in the oxide, and \vec{n} is the normal to the corresponding interface. The diffusion equation is obviously identical to the one presented in Section 2.3.1.

2. Propagation of the oxide-silicon interface is solved after the diffusion equation for a time step δt . To find the new position of the SiO_2 -Si interface, the LS is solved for the distance function

$$\frac{\partial \Phi}{\partial t} + V_{react} \cdot \left| \vec{\nabla} \phi \right| = 0, \quad V_{react} = \frac{kC}{N\gamma}|_{Si/SiO_2}, \quad (3.12)$$

where N is the number of oxidant molecules incorporated into a unit of oxide and γ is the $Si \rightarrow SiO_2$ expansion coefficient. An up to third order Total Variation Diminishing (TVD) Runge-Katta scheme is used for discretization [66].

3. The volume expansion resulting from the chemical reaction is calculated using the creep equation

$$\frac{\partial S_{ij}}{\partial s_i} = 0, \quad (3.13)$$

where S_{ij} is a Cauchy stress tensor. Assuming a Maxwell visco-elastic fluid, the Cauchy stress tensor becomes

$$S_{ij} = -p \cdot \delta_{ij} + \sigma_{ij}, \quad \sigma_{ij} + \frac{\mu}{G} \frac{\partial \sigma_{ij}}{\partial t} = u \left(\frac{\partial u_i}{\partial x_j} + \frac{\partial u_j}{\partial x_i} \right), \quad (3.14)$$

where u_i is a velocity component.

The system of equations (3.13) and (3.14) make up the Stoke's equations with the boundary conditions

$$\vec{u}|_{Si/SiO_2} = \frac{\gamma - 1}{\gamma} \cdot \frac{kC}{N} \cdot \vec{n}, \quad [p] - [\mu \cdot n_i \sigma_{ij} n_j] = \beta \cdot \kappa, \quad (3.15)$$

where $[\cdot]$ denotes the jump across a liquid-liquid interface, β is the surface tension coefficient, and κ is the surface curvature.

4. Propagation of the interfaces in the deformation velocity field is the step during which all interfaces above the Si-SiO₂ interface are updated. This includes the SiO₂-Nitride interface, SiO₂-ambient interface, and Nitride-ambient interface. The interfaces are updated using the LS representation

$$\frac{\partial \Phi}{\partial t} + \vec{u} \cdot \vec{\nabla} \phi. \quad (3.16)$$

The main advantage of the LS method when compared to the FEM for solving visco-elastic problems is that all potential errors which arise due to unstructured mesh irregularities are removed. The LS also makes it very easy to follow shape topologies which change with time. The LS method natively handles complex surfaces, which can split or recombine during a simulation process.

3.2. Oxidation Modeling using Linear Parabolic Equations

When modeling the topography motion during oxidation within a LS environment, there are a few aspects to be considered, which are not covered in the LS interface presented in Section 1.4.1. The first consideration which must be taken into account is that oxidation requires the movement of two different interfaces in opposite directions. LS from Section 1.4.1 allows for multiple LS interfaces being etched at different rates, but when the interfaces move in different directions, an extra consideration must be made. In addition, material interfaces must be labeled differently. In order to correctly identify the movement of LS interfaces during oxidation, material and LS labeling shown in Figure 1.2 was implemented. However, for processes such as oxidation, this is insufficient. In some instances, when a mask is used for deposition, material interfaces must be identified as being separate from each other in order for the deposition, or material growth, to be appropriately modeled.

3.2.1. Multiple moving interfaces

In order to model multiple moving interfaces in the LS method from Section 1.4.1, two separate LS systems are analyzed. One system is used for the Si-SiO₂ interface, which is an etch-like process, proceeding with a relative negative velocity, while a separate system is used for the SiO₂-ambient interface, which is a deposition-like process, proceeding with a relative positive velocity. Three different scenarios can lead to different methods by which the LS system should be described: An initial LS description of one interface, which will grow to two interfaces at the onset of oxidation, pre-grown material such as a native oxide layer which will grow further during the oxidation process, and the existence of a mask layer, which should affect the movement of both interfaces.

One initial LS description

When the initial geometry is described by a single material interface, which must split and simultaneously move in opposite directions, the LS systems are straightforwardly implemented. If we label the initial interface Φ , then the split is performed by simply introducing a new LS interface $\Phi_{up} = \Phi$. We now have a system with LS Φ_{up} which should move in the positive deposition-like direction and Φ which should move in the negative etching-like direction. Figure 3.1 depicts such a scenario for a 500×500 geometry where the top surface moves at a rate of 0.25grid/time and the bottom surface moves at a rate of -0.75grid/time for 10 time units. Therefore, $V_{up} = 0.25$ and $V_{down} = -0.75$ is set and the LS equations

$$\begin{aligned} \frac{\partial \Phi}{\partial t} + V_{down} \cdot |\vec{\nabla} \phi| &= 0, \\ \frac{\partial \Phi_{up}}{\partial t} + V_{up} \cdot |\vec{\nabla} \phi_{up}| &= 0 \end{aligned} \quad (3.17)$$

are solved. When processing is complete, Φ_{up} is added to the top of the stack in the Φ LS system.

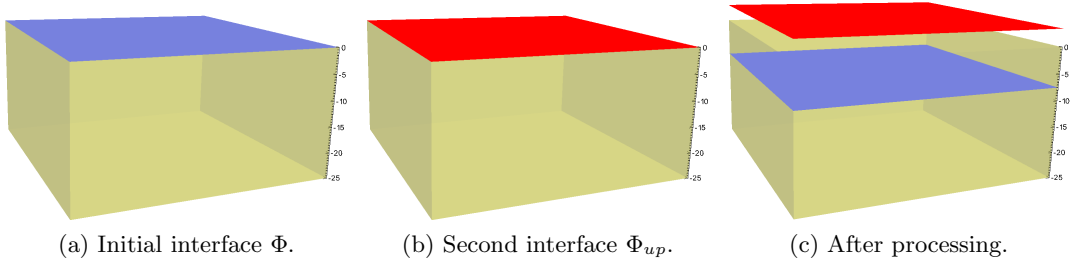


Figure 3.1.: Modeling approach when a single LS interface is split into two interfaces, which move in opposite directions for a 500×500 geometry moving at velocities 0.25 and -0.75 for the top and bottom surfaces, respectively.

LS describes pre-existing native material

When the initial geometry involves two level set interface systems Φ_{down} and Φ_{up} and the goal of the simulation is to move them downward and upward, respectively, no interface splitting is required. Only the separation of the two interfaces into two different LS systems is required. Therefore, assuming the initial interface system Φ , then we introduce a second LS system $\Phi_{up} = \Phi$. The top LS interface from Φ is removed, while the bottom interface from Φ_{up} is also removed. The two systems are now separated as shown in Figure 3.2a and Figure 3.2b, respectively. Figure 3.2c depicts the scenario after the following LS equations were processed for the individual

surfaces on a 500×500 geometry:

$$\begin{aligned} \frac{\partial \Phi}{\partial t} + V_{down} \cdot |\vec{\nabla} \phi| &= 0, \\ \frac{\partial \Phi_{up}}{\partial t} + V_{up} \cdot |\vec{\nabla} \phi_{up}| &= 0, \end{aligned} \quad (3.18)$$

where the top surface moves at a rate of 0.25grid/time and the bottom surface moves at a rate of -0.75grid/time for 10 time units: $V_{up} = 0.25$ and $V_{down} = -0.75$. When processing is complete, Φ_{up} is added to the top of the stack in the Φ LS system resulting once again in the LS system Φ which contains two LS interfaces.

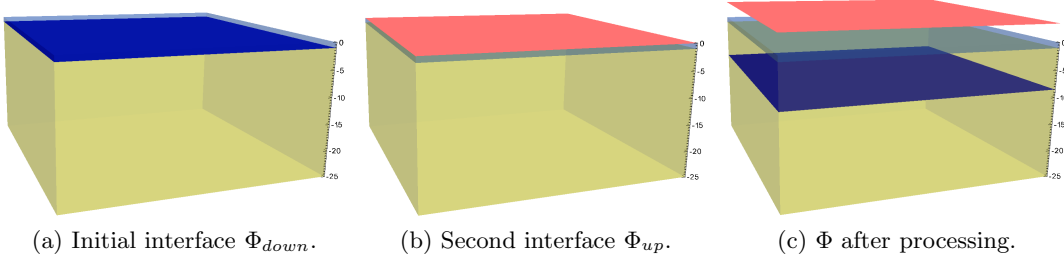


Figure 3.2.: Modeling approach when the initial LS geometry contains two interfaces which need to be moved in opposite directions, for a 500×500 geometry at velocities 0.25 and -0.75 for the top and bottom surfaces, respectively.

LS describes existence of a mask layer

When a mask layer is introduced into a system where a material is grown in such a way that two LS interfaces need to be simultaneously moved in opposite directions, the mask layer influences the movement of both level sets. Therefore, when the LS system is split, such as those from Figure 3.1 and Figure 3.2, the mask layer must remain in both LS systems. Another aspect which must be considered is the manner in which the different LS interfaces are labeled. This will be addressed in Section 3.2.2, while here only the initial separation of materials to form the two LS systems will be described. Assuming we start with a LS description LS_{down} which includes two surfaces. One describes the location of the mask and the second the location of the material which will be grown and is located below the mask. A second LS description can now be initiated LS_{up} , which only holds the mask LS from LS_{down} . LS_{down} contains Φ_{mask} and Φ_{down} and it is a simple matter of moving the desired interface by

$$\frac{\partial \Phi_{down}}{\partial t} + V_{down} \cdot |\vec{\nabla} \phi| = 0, \quad (3.19)$$

which is analogous to an etching process with a mask, described in [50]. An additional LS interface, Φ_{up} is added to the LS_{up} stack at the interface between the mask and the

bottom-most material. Therefore, when a positive velocity is applied to Φ_{up} according to

$$\frac{\partial \Phi_{up}}{\partial t} + V_{up} \cdot \left| \vec{\nabla} \phi_{up} \right| = 0, \quad (3.20)$$

the mask will act as a block, similar to the way it blocks an etching process. Figure 3.3 shows this event for a geometry $15 \times 15 \times 5$ where the lower surface is prepared to be “etched” while the top surface is prepared to undergo mask-blocking “deposition”.

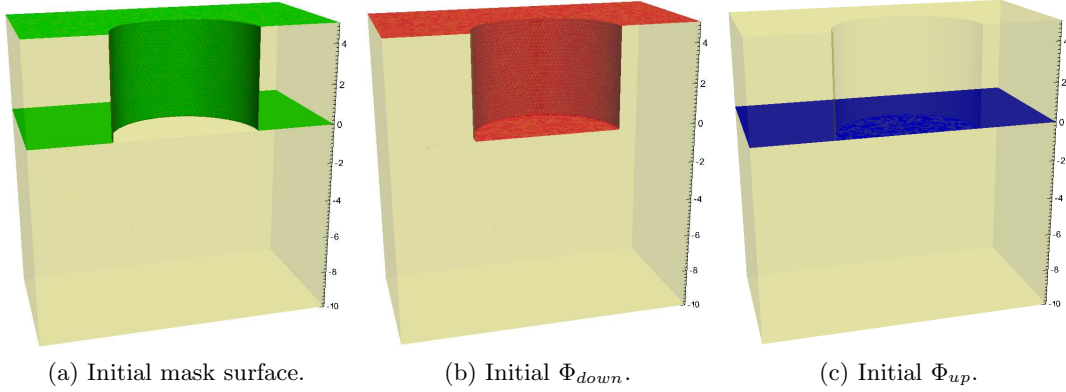


Figure 3.3.: Modeling approach when the initial LS geometry contains two interfaces, one a mask and one a surface to be grown. A $15 \times 15 \times 5$ geometry is used.

3.2.2. Separating Material Interfaces

Some interactions between different materials during the oxidation process may not be described using the suggested LS labeling from Figure 1.2. An example is the movement of the Φ_{up} surface with a mask present. Instead, materials must be labeled separately and fully enclosed within their own volume, as shown in Figure 3.4.

This allows for interactions between different surfaces which do not necessarily result in those surfaces joining, but rather being completely separate entities. Such an event is shown in Figure 3.5, where the system from Figure 3.3 undergoes simultaneous growth at a velocity of 0.75 at the top surface and -0.25 at the bottom surface.

3.2.3. LS Surface Vector Motion

The level set is used to describe the motion of a surface when its rate of growth is given in the surface normal direction. However, when a LS surface fully encompasses a material in all directions, a rate of growth in the normal direction would result in a volume expansion of the material. When the entire material must be moved in a single direction, independent of the surface normals, while preserving the material’s surface

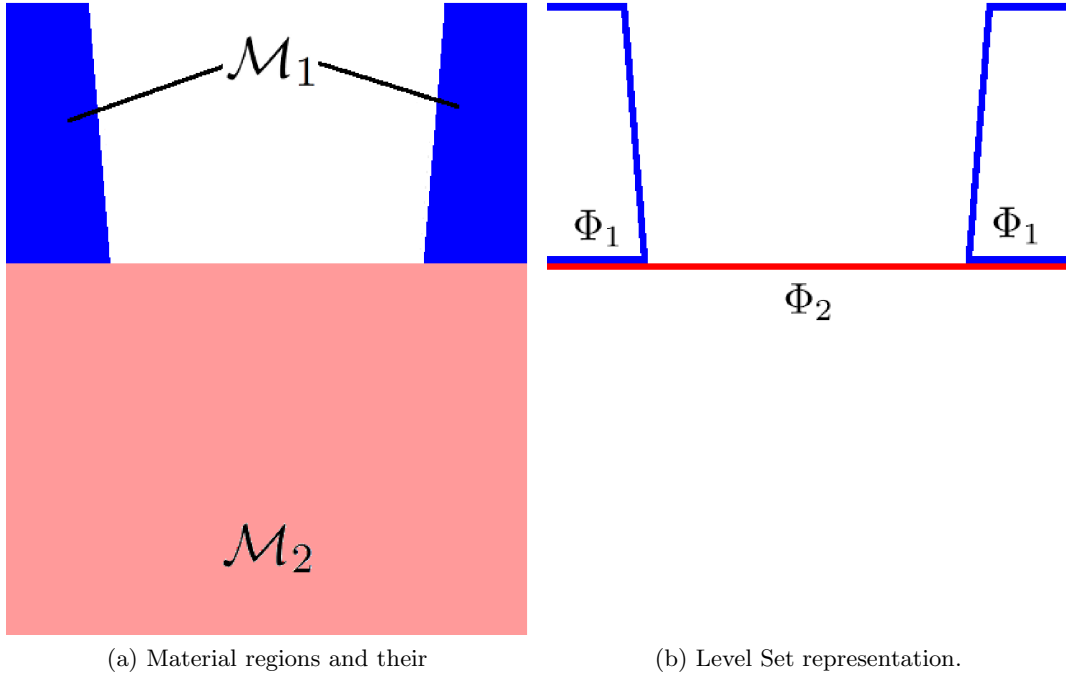


Figure 3.4.: Geometry of a mask and its LS labeling when the mask is used for a material growth or deposition process.

normals, curvature, and volume, the LS surface must be advanced using the velocity equation

$$V(\vec{x}) = S \times (\hat{r} \cdot \hat{n}), \quad (3.21)$$

where S is the speed of the surface motion, $\hat{r}(x, y, z)$ is the unit vector in the direction of the desired motion, and $\hat{n}(x, y, z)$ is the unit normal vector to the surface. Equation (3.21) is applied to a sphere moving towards a flat disk in Figure 3.6. The simulation depicts a sphere with a diameter of 100 grid units moving downward at a speed of 1 grid unit per second, towards a stationary surface used as a reference point. The total translation is 200 grid units (50 grid units per image) prior to contact with the bottom surface. The sphere does not appear to experience any deformation.

The type of simulation depicted in Figure 3.6 is quite sensitive to errors because any error in the surface definition after a single time step will multiply with subsequent steps. The grid also plays a role in the accuracy of the generated result. A finer grid will result in a more accurate representation of the initial surface after it has transposed. Therefore, depending on the accuracy required, the simulation can require extensive amounts of memory, processing power, and time.

The grid density will determine how well the surface curvature will be transferred as it moves through the grid. It is not recommended to perform simulations where the surface will transpose a significant distance away from its original location as it is

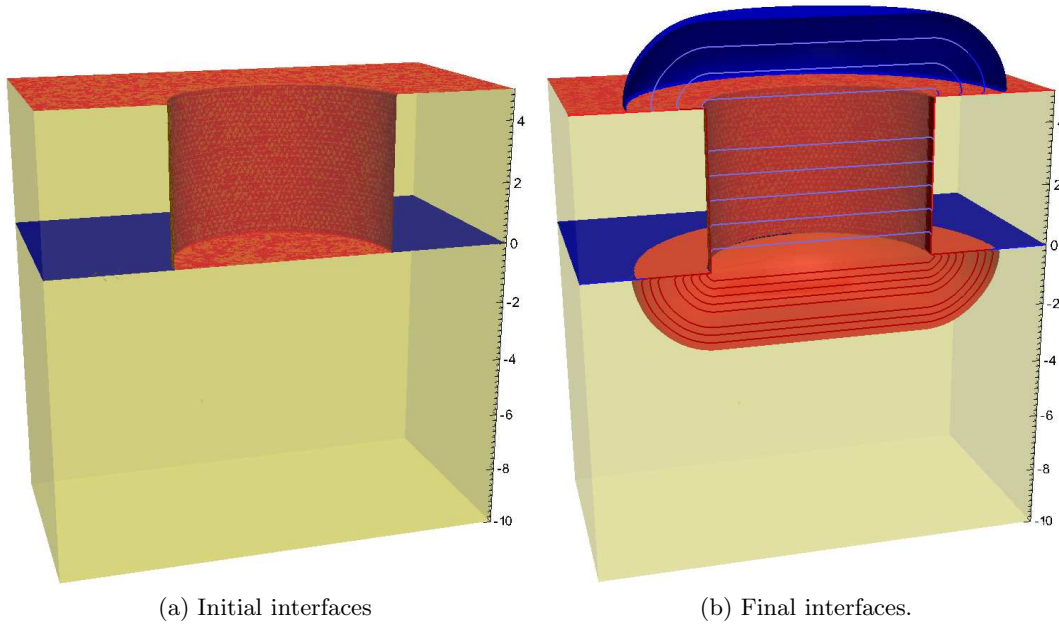


Figure 3.5.: The initial and final geometry after surface evolution of Φ_{down} downward and Φ_{up} upward at rates of -0.25 and 0.75, respectively.

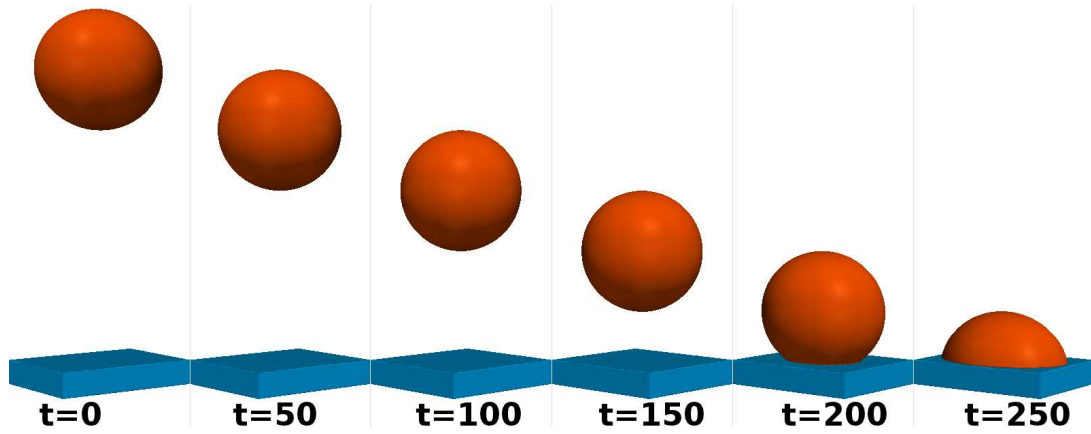


Figure 3.6.: Simulation of the translation of a sphere under vector motion. The sphere has a radius of 50 grid points and is moving downward at a rate of 1 grid point per time unit for 250 time units.

inevitable that many surface edges will be lost. However, for slight movements of a surface, such as the bending that a nitride mask experiences during oxidation, this type of LS motion can be implemented.

3.3. Nitric Acid Oxidation

The continuous decrease in semiconductor device sizes demands a reduction in oxidation times for high-temperature oxidation because high temperatures influence the distribution of impurities in the silicon bulk and at the Si-SiO₂ interface. The movement of impurities affects device size and its electrical properties. Therefore, alternatives to high temperature oxidation have been sought out to grow thin oxides which have good electrical properties found in thermally grown oxides [78]. Similarly, the fabrication of Thin Film Transistors (TFTs) for flat-panel displays requires low temperatures because of the presence of glass substrates [78]. The use of Rapid Thermal Annealing (RTA) and high pressure thermal oxidation can reduce the amount of time during which a high temperature is applied. However, processes which perform oxidation at low temperature (< 600°C) are preferred. Plasma oxidation of silicon [155] started to gain at traction, because it can be performed at low temperatures. In plasma oxidation, oxygen ions O⁻ are the responsible species and the reaction which takes place is



where e^- represents a single electron [21].

Plasma-assisted oxidation of silicon has been performed in microwave, RF, and DC plasmas. It has been shown that, compared to thermal oxidation, film growth rates are accelerated by plasma-enhanced generation of the reactive species (O⁻). The primary limitation in the use of plasma-grown oxides in ultra large scale integration is the inability to control oxide properties such as the oxide charge density [21]. Although some researchers achieved good dielectric properties for plasma-grown oxides, this was only possible with post-oxidation high-temperature treatment. Even after such treatments, low field leakage currents were found, thought to be due to oxide damage caused by the plasma radiation [78]. A proposed alternative involves the growth of a thin oxide using low-power discharge followed by a CVD deposition of additional oxide, which adds complexity to the growth process and an additional interface in the oxide [78]. Metal-enhanced oxidation and UV ozone oxidation have also been used to generate thin oxide layers, but uniformity, controllability, and good electrical characteristics of SiO₂ layers have not been achieved with these methods [103].

More recently, Nitric Acid Oxidation (NAOS) was suggested by Asuha et al. [88], [3], [89], [103], [104]. NAOS is developed as a process to grow gate oxide layers for TFTs, which require good chemical properties on very thin films. These films require the electrical properties of thermally grown films, but because they are grown on a glass substrate cannot be exposed to a high temperature environment. However, when the films are deposited using CVD or high pressure chemical vapor deposition (HPCVD), the electrical properties of the film are not sufficient for thin film transistor (TFT) applications. Several experimental results regarding the growth of oxide on silicon using NAOS in azeotropic [3] and vapor [90] environments have been published [103], [105]. In addition, a two-step process [152] involving a combination of NAOS processes

is suggested to enable the growth of SiO_2 layers with thicknesses larger than 10nm with good electrical properties.

3.3.1. NAOS Modeling

In order to model NAOS, experimental results from several publications from the group of Asuha et al. at the Institute of Scientific and Industrial Research at Osaka University and from Imai et al. at the Display Technology Development Group at Sharp Corporation are analyzed [88], [89], [103]. The phase diagram of the $\text{HNO}_3/\text{H}_2\text{O}$

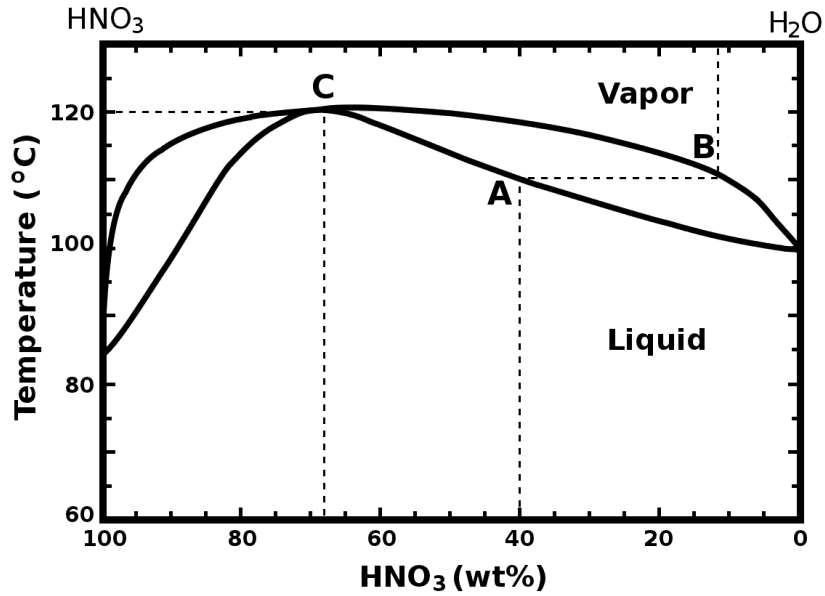
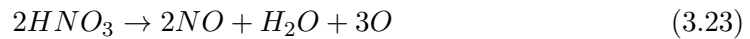


Figure 3.7.: Phase diagram of the Nitric acid ($\text{HNO}_3/\text{H}_2\text{O}$) system.

system is shown in Figure 3.7.

Azeotropic NAOS Method

For the azeotropic NAOS method the silicon substrate is submerged in a nitric acid (HNO_3) liquid at its boiling temperature. The method is usually performed with a 61wt% concentration of HNO_3 at the boiling temperature of 112°C. An alternative is a 68wt% concentration (location C in Figure Figure 3.7), at the boiling temperature of 120.7°C. The chemical reaction which takes place in order to generate the oxygen required for the oxidation process is



The maximum thicknesses of SiO_2 reached are 1.2nm and 1.4nm by oxidation with 61wt% and 68wt% HNO_3 , respectively within 10 minutes, while prolonged oxidation does not increase the SiO_2 thickness. However, until the final thickness is reached, there is still a time dependence on the immersed oxide thickness. This is shown in Figure 3.8a where the thickness of the NAOS oxide is plotted with respect to the immersion time at an ambient temperature of 25°C immersed in a 61wt% HNO_3 solution. Similarly, the temperature dependence on oxide thickness is shown in Figure 3.8b. The thicknesses obtained are after immersion for 10 minutes in a 61wt% HNO_3 solution. At the final experimental dot, at a temperature of 112°C , the oxide reaches its maximum thickness of 1.3nm within the 10 minutes provided.

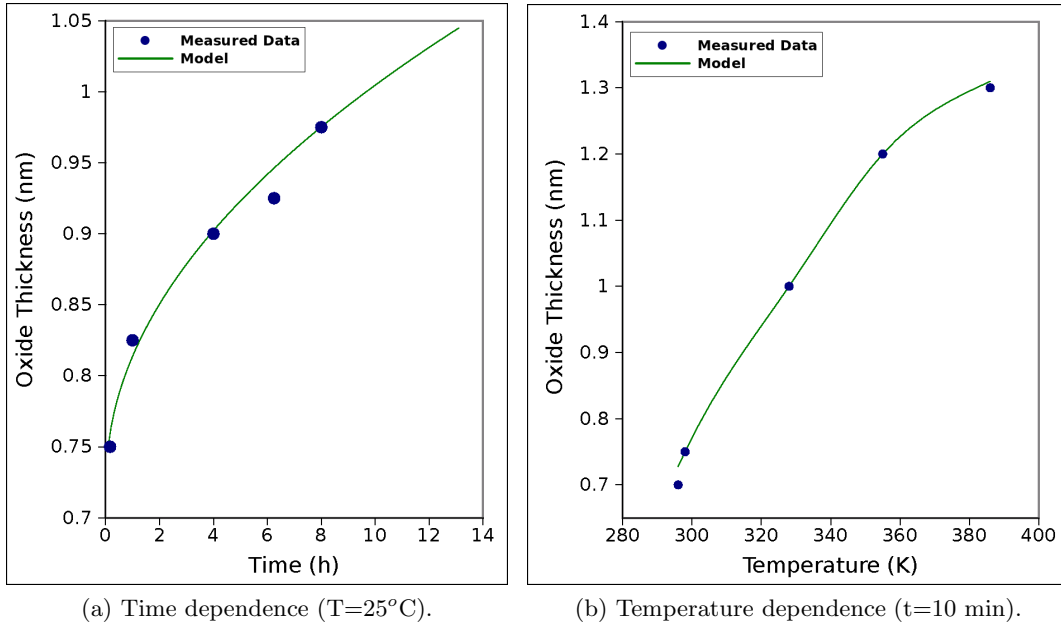


Figure 3.8.: The dependence of immersion time and temperature on the growth of NAOS oxide submersed in a 61wt% HNO_3 solution.

The model must take into account both the influence of immersion time and temperature. From observing Figure 3.8, a linear-parabolic type of relationship seems to dominate the NAOS type of oxidation. The presented model proceeds to fit the experimental data into the linear-parabolic model for the oxide rate

$$\frac{dx_o}{dt} = \frac{B}{A + 2x_o} \mu m, \quad (3.24)$$

where x_o is the oxide thickness in m, B and A are rate constants analogous to those suggested for the Deal-Grove model with different values. As with the Deal-Grove model, the rate constants have an Arrhenius-type relationship with regard to temperature

$$A = -19 e^{\frac{-0.66\text{eV}}{k_B T}} \mu m, \quad (3.25)$$

$$B = 1.32 e^{\frac{-0.132\text{eV}}{k_B T}} \mu\text{m}^2/\text{hr}, \quad (3.26)$$

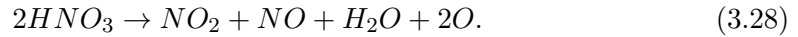
where k_B is the Boltzmann constant in eV/K and T is the temperature in Kelvin. Integrating (3.24), an explicit expression for the oxide thickness x_o can be found

$$x_o = \frac{A}{2} \left(-\sqrt{1 + \frac{4B}{A^2}(t - \tau)} - 1 \right), \quad (3.27)$$

where τ is an adjustment coefficient which accounts for the initial oxide observed in Figure 3.8a. In Figure 3.8, the model is shown to have a good fit to the measured results from [103].

Vapor NAOS Method

The vapor NAOS oxidation method should be performed at temperatures above 200°C when the Nitric acid HNO_3 is in a vapor phase. The chemical reaction which takes place in order to generate the oxygen required for the oxidation reaction is



In Figure 3.9 the thickness of the SiO_2 layer is plotted as a function of oxidation time for various temperatures (300°C, 400°C, 450°C, and 500°C). At these temperatures, thermal oxidation would not be able to grow layers larger than the native oxide due to the oxidants not having enough energy to diffuse through the oxide network. The oxide thickness appears to increase with increased time; however the oxidation rate tends to decrease. This parabolic relationship suggests that the diffusion of oxygen atoms through the growing oxide is the rate-determining step.

An empirical model which is to follow the oxide growth due to vapor NAOS oxidation must take into account the temperature and time dependence on the oxide thickness. At first the relationship between the oxide thickness and oxidation time is shown to be logarithmic

$$x_o = A \ln(t) + B, \quad (3.29)$$

where t is the oxidation time and A and B are temperature dependent parameters

$$A = 8.2 \times 10^4 e^{\frac{-0.672\text{eV}}{k_B T}} \mu\text{m}, \quad (3.30)$$

$$B = \frac{1060 \mu\text{m} K}{T} - 2.95 \times 10^5 e^{\frac{-0.673\text{eV}}{k_B T}} \mu\text{m}^2/\text{hr}, \quad (3.31)$$

where k_B is the Boltzmann constant in eV/K and T is the temperature in Kelvin. The fit of the empirical model to the measured data from [103] is shown in Figure 3.9.

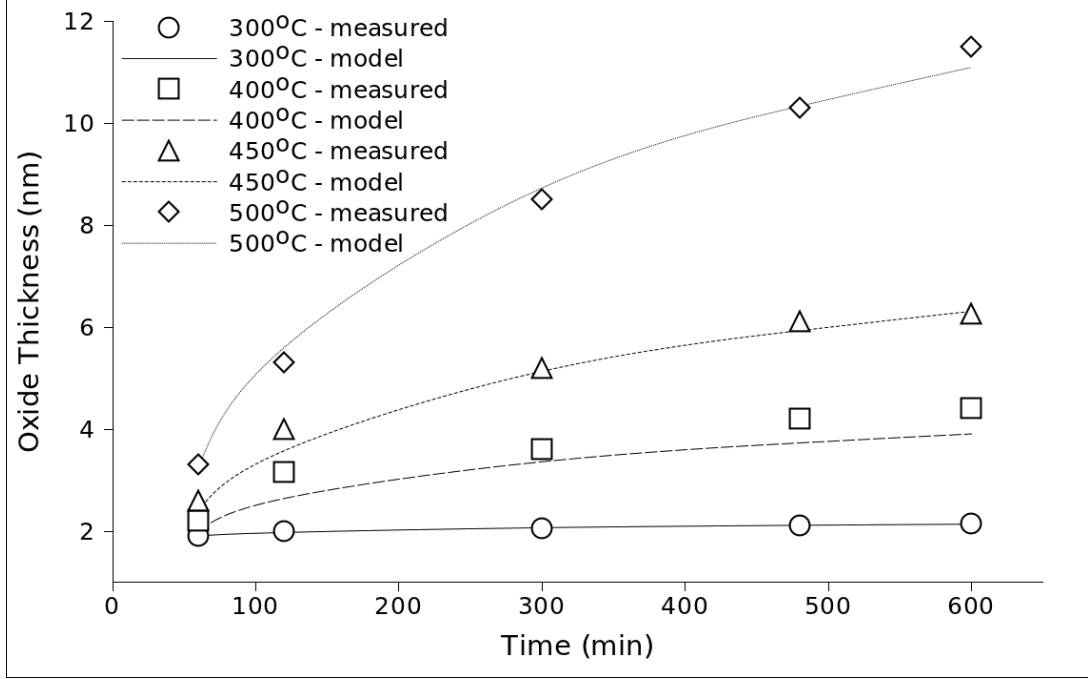


Figure 3.9.: Plots of the SiO_2 thickness with respect to the oxidation time at different temperatures when the vapor NAOS method is used. Dots are experimental results from [103] and lines are the results of the presented empirical model.

3.4. Local Oxidation Nanolithography

Section 2.4 describes the evolution of the LON technology from the discovery of the scanning probe microscope to the development of AFM lithography for local anodic oxidation of silicon surfaces. Due to the significant advantages which ICM and NCM lithography possess over STM and CM lithographies, the modeling of those two methods for nano-oxidation of silicon surfaces have been implemented in the simulator. However, models for all scanning probe microscopy (SPM) methods will be analyzed in this section. The mechanism and kinetics of AFM oxidation will be described in order to determine the best modeling technique for AFM LON. Empirical models for nanodot and nanowire sizes will be presented, along with the MC approach, implemented in order to generate the required nanodot and nanowire shapes within the LS simulator.

3.4.1. AFM Oxidation Mechanism and Kinetics

In order to be able to predict and control the fabrication of nanostructures with LON, the mechanisms and kinetics behind the oxidation process must be understood. The first attempt to understand the mechanisms behind AFM oxidation was proposed

by Gordon et al. [65] in 1995. There, it is suggested that the rate is limited by the initial density of surface OH^- ions and that the oxide growth follows the Mott-Cabrera model [26], where the growth is consistent with electric field limited diffusion. Gordon et al. were also the first to identify that oxyion species (OH^- or O^-) recombine with holes (h^+) present on the surface of the silicon sample. It is now understood that

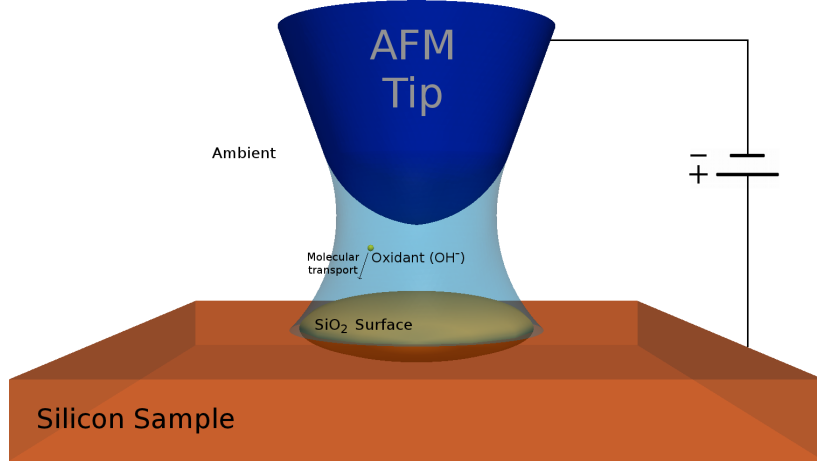
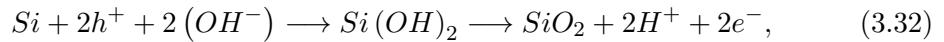


Figure 3.10.: Oxidation driven by oxyions, which are generated due to the presence of the strong electric field, interacting with the silicon surface.

when a negatively charged AFM tip is brought near a grounded silicon surface, as is shown in Figure 3.10, an electric field is generated in the formed water meniscus. The presence of the strong field breaks up the water into ions (O^- , OH^- , and H^+) and causes the downward acceleration of the negatively charged ions towards the surface. The combination of these ions with holes (h^+) present at the surface results in the localized growth of SiO_2 , which grows into the silicon wafer as well as into the water meniscus. In the case of a silicon surface, the oxidation at the anode end (Si) follows the chemical reaction



where h^+ is a free hole in the Si sample and e^- is a free electron [62], [213]. Similarly, the chemical reaction taking place at the AFM needle tip (cathode) follows



where e^- is a free electron.

The goal of LON models is to give a predictable shape for a nanodot or nanowire under various ambient conditions, while it is within the scope of this work to incorporate these models into the LS simulator described in Section 1.4.1.

3.4.2. Empirical Models for LON

Empirical Models for LON started with the initial attempt to understand the physical mechanisms by Gordon et al. [65]. Teuschler et al. [123], [210] in the same year suggested that the height of the generated nanodot is proportional to the 4th root of the pulse time, ($h \propto t^{1/4}$). Although this empirical power law was a good fit to the experimental data, there was no relation to the traditional idea of oxide growth models, such as those mentioned in Chapter 2. The first model based on the physical interactions during LON was introduced in 1997 by Stievenard et al. [197]. After analyses were done with thick oxides [4], it was found that a logarithmic time dependence of h versus t is a good fit to the available experimental data with t ranging from 0.01 to 1000s and h up to 50nm. More refined models for ICM-AFM and NCM-AFM lithographies were later suggested by Snow et al. [192] and Calleja et al. [28], respectively. The models are for relatively thin oxides and pulse voltages below 30V, while for oxides grown under very high voltage (30 to 50V), the Faradic current, which is present in the water meniscus, turns to ohmic current, and an additional ring of oxide is grown along the outside of the nanodot [135]. These structures, grown under very high voltage, are beyond the scope of the models presented in this work, but similar methods may be used in the future in order to include such features in LON simulations.

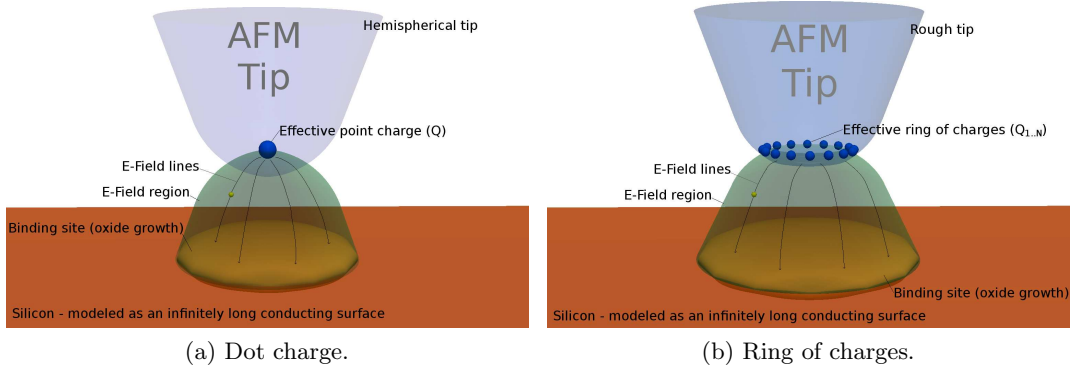


Figure 3.11.: Modeling approach for a hemispherical AFM needle tip versus a rough AFM needle tip. (a) Dot charge used to model AFM with a hemispherical needle tip and (b) Ring of charges used to model AFM with a rough needle tip.

Three types of AFM tip shapes have been analyzed in the literature [45]. The different shapes are for a rough, hemispherical, and blunt tip configuration, which can be modeled using a ring charge, point charge, and ring charge, respectively. We present two models: one for a hemispherical tip shape, which involves only one charged dot and one for all other tip shapes, where multiple charged dots are required in order to model the needle tip. The schematics of this approach are shown in Figure 3.11a and Figure 3.11b, valid for a hemispherical and blunt needle tip, respectively. For the implemented model, it is assumed that all oxyanions are generated at the effective

point source of the AFM needle tip. This simplifies the model, while not having a significant consequence on the model's accuracy [164]. The oxyanions traverse through the water meniscus along electric field lines, finally colliding with the sample surface, whose evolution is visualized using the LS method [50], [51].

Using the method of image charges, the voltage and electric field strength in the water meniscus region has been calculated [149], [164]. The effects of surrounding ions on the electric field strength and recombination reactions between ions to form water were neglected [45]. Mesa et al. [149] suggest that each AFM needle can be represented as a series of charged particles distributed along the structure of the needle. The presented model implements this idea with the use of point charges, which is valid for all types of AFM needles.

Surface Charge Density Distribution for a Hemispherical Needle Tip

As discussed in the previous section, the model representing the shape of a hemispherical AFM generated nanodot follows the Surface Charge Density (SCD) distribution, which is derived by replacing the AFM needle tip with an effective point source Q and the silicon substrate surface by an infinitely long conducting plane. The image charge method is then applied to find the voltage at every location in the water meniscus region $\vec{p}(x, y, z)$:

$$V(\vec{p}) = kQ \left[\frac{1}{\left(x^2 + y^2 + (z - D)^2\right)^{1/2}} - \frac{1}{\left(x^2 + y^2 + (z + D)^2\right)^{1/2}} \right], \quad (3.34)$$

where $k = \frac{1}{4\pi\epsilon_r\epsilon_0}$, Q is the effective point charge at a distance D from the surface, and ϵ_r is the relative permittivity of water. Given $\vec{E} = -\vec{\nabla}V$, the electric field in each direction can be found:

$$\begin{aligned} E_x &= kQ \left[\frac{x}{\left(x^2 + y^2 + (z - D)^2\right)^{3/2}} - \frac{x}{\left(x^2 + y^2 + (z + D)^2\right)^{3/2}} \right] \\ E_y &= kQ \left[\frac{y}{\left(x^2 + y^2 + (z - D)^2\right)^{3/2}} - \frac{y}{\left(x^2 + y^2 + (z + D)^2\right)^{3/2}} \right] \\ E_z &= kQ \left[\frac{z - D}{\left(x^2 + y^2 + (z - D)^2\right)^{3/2}} - \frac{z + D}{\left(x^2 + y^2 + (z + D)^2\right)^{3/2}} \right] \end{aligned} \quad (3.35)$$

The induced surface charge density (SCD) on the surface is represented as

$$\sigma(x, y, 0) = \epsilon_r \epsilon_0 E_z(x, y, 0), \quad (3.36)$$

leading to the expression

$$\sigma(x, y, 0) = \frac{-DQ}{2\pi(x^2 + y^2 + D^2)^{3/2}}. \quad (3.37)$$

A model has been developed which utilizes (3.37) in order to generate a topographical representation of an AFM generated nanodot. This model implements a MC rejection technique, or accept-reject algorithm, to build the nanodot, which is very time and memory expensive, when large aspect ratio problems are required. Having an explicit particle distribution is preferred.

Surface Charge Density Distribution for a Rough Needle Tip

As mentioned in Section 3.4, in order to simulate the nanodot growth, initiated using a rough AFM tip, the needle may be modeled as a ring of charges at a given height above the silicon surface. The ring of charges is modeled by a desired number of dot charges surrounding the AFM tip circumference. When multiple dot charges are used to represent the AFM needle, the equation for the surface charge density becomes

$$\sigma(x, y, 0) = -\frac{D}{2\pi} \sum_{i=1}^N \frac{Q_i}{\left[(x - x_i)^2 + (y - y_i)^2 + D^2\right]^{3/2}}, \quad (3.38)$$

where N is the total number of charged dots, Q_i and (x_i, y_i, D) are the effective charge and the location of the i^{th} dot, respectively. The maximum possible SCD distribution occurs, when all the charges are concentrated at a single point, making the charged circle's radius zero:

$$|\sigma_{max}| = N \frac{Q_{tot}}{2\pi D^2}. \quad (3.39)$$

With (3.38), simulations of AFM needle tips are not limited to those represented with a ring of charges. Rather, they can include charges which are located at any position, allowing it to properly mimic the behavior of the applied needle. The equation may also be used to study the effects of placing a second needle nearby. Performing multiple AFM oxidations in parallel with an array of needles is a popular way by which LON can have higher throughput and faster processing times.

Model for scanning tunneling microscope lithography

There are not many models for LON with a scanning tunneling microscope. The reason for this is that, quickly after the discovery of STM nano-oxidation, the AFM

was introduced and shown to be a better tool for LON. The limitations of STM lithography when compared to AFM lithography are higher tip degradation due to reduced conductivity, difficulty in evaluating the exact lithography after printing due to the STM's inability to distinguish SiO_2 from the ambient, slow dip velocity required for stable operation, and the requirement for STM to be operated in ultra high vacuum (UHV) [46]. An analysis of STM-induced oxidation was performed by Kramer et al. [108], [109], which indicated that oxidation is induced by the electrical field between the tip and silicon sample and not by the energetic electrons from the tip directly. With decreasing Relative Air Humidity (RAH), the generated oxide also decreases in size, down to a threshold humidity of 10%, beyond which, no oxidation takes place [109]. Increasing the applied reverse bias voltage also increases the oxide size, in both height and width. However, it is shown that the inverse oxide line width has a logarithmic influence from the applied bias, as seen in Figure 3.12, which is a reproduction of Figure 3 from [109].

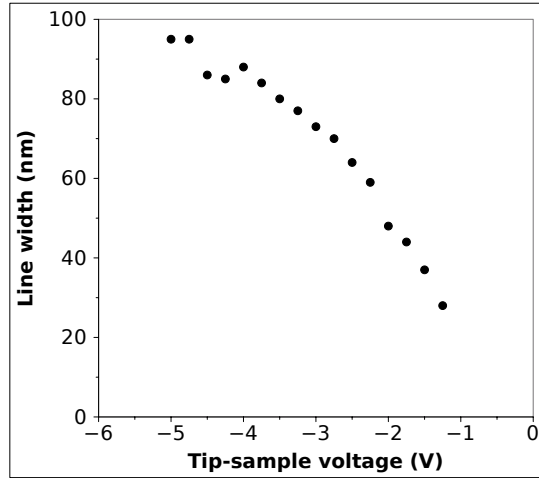


Figure 3.12.: The width of the oxide lines on a silicon substrate as a function of the applied bias, from [109].

Model for contact mode lithography

The first physical-based model for CM nano-oxidation with an AFM was suggested by Stievenard et al. [197]. The model is based on the Cabrera and Mott model and it suggests a linear relation between the oxide height (h) and bias voltage (V_b) and a logarithmic relationship between $1/h$ and t , [$1/h \propto \text{Log}(t)$]. Another model, which shows the same patterns as those presented in [197] is shown in [46]. Both models assumed a static RAH, with Stievenard's model setting it to 70%. This is ignored as a parameter; however, it is well known that the amount of water which is available during oxidation influences the growth rate and size of the oxide pattern [53].

From the initial assumption that the oxidation reaction is similar to the Cabrera and Mott model, but adapted for very thin oxide films, a model is developed in [197]:

If W is the energy which an ion must overcome to diffuse, the kinetics of growth can then be given by:

$$\frac{dh}{dt} = u \cdot e^{h_1/h}, \quad (3.40)$$

where

$$h_1 = \frac{q a' V}{k_B T}, \quad (3.41)$$

with $V = V_o + V_{bias}$, q is the electronic charge of an electron, k_B is the Boltzmann constant, T is the temperature, $2a'$ is the barrier width between two interstitial sites, and u is given by

$$u = u_o e^{-W/k_B T}, \quad (3.42)$$

with u_o in the order of 10^4 cm/s [197]. The kinetics of the oxide width are not included in the model, because they depend strongly on the AFM needle tip and, therefore, on the generated water meniscus.

Model for intermittent contact mode lithography

In order to simulate oxidation patterns using an AFM operating in ICM, the model presented in [192] is implemented. The equation which governs the height of the grown oxide is given by

$$h(t, V_b) = \frac{V_b}{E_0} \ln \left(\frac{R E_0 t}{V_b} + 1 \right), \quad (3.43)$$

where t is the pulse time, V_b is the bias voltage, and E_0 and R are fitting parameters, with $E_0=45$ V/nm and $R=1.5 \times 10^3$ nm/s. At high voltages and long pulse times, the height deviates significantly due to the formation of a water bridge between the tip and the wafer [192]. The simulator is adjusted to handle this behavior by increasing R to 2.3×10^7 nm/s and introducing a series voltage drop [192]. Figure 3.13 shows the measured and modeled heights for this process.

The simulator also requires a dependence relationship for the Full Width at Half Maximum (FWHM) of the grown oxide, which is required in order to be able to generate a complete oxide nanodot. The work presented in [192] provides some measured results, shown in Figure 3.14. An empirical equation for the full width at half maximum (FWHM) developed to fit the measured results is

$$w(t, V_b) = w_0(V_b) + w_1(V_b) \ln \left(\frac{C_1 t}{V_b} \right) \text{ nm}, \quad (3.44)$$

where

$$\begin{aligned} w_0(V_b) &= \frac{R}{E_0} (C_2 + C_3 V_b) \text{ nm} \\ w_1(V_b) &= C_4 V_b \text{ nm}, \end{aligned} \quad (3.45)$$

where t is given in seconds, V_b in volts, and C_1 , C_2 , C_3 , and C_4 are fitted values, $C_1 = 7 \text{ V s}^{-1}$, $C_2 = 1 \text{ s}^{-1}$, $C_3 = 0.5 \text{ V}^{-1} \text{ s}^{-1}$, and $C_4 = 2.9 \text{ nm V}^{-1}$. The developed model suggests that the width of the profile has a logarithmic dependence on the pulse time and inverse logarithmic dependence on the applied voltage, similar to the dependence observed from the oxide height model. Once again, the model had to be adjusted for the case, when high voltages and long pulse times are applied.

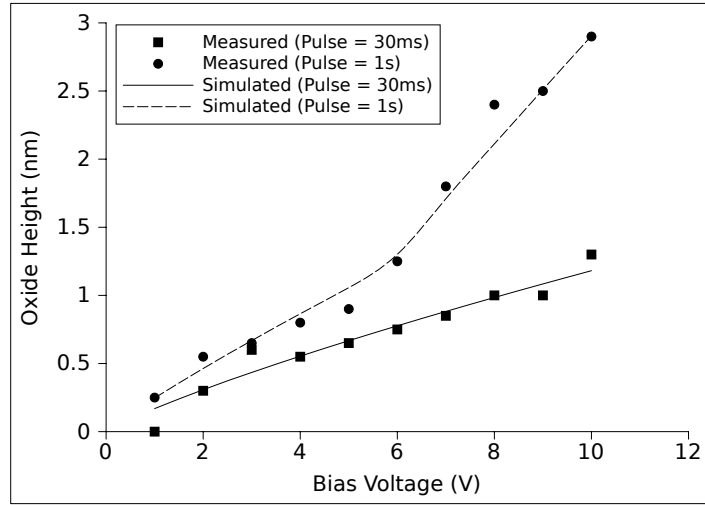


Figure 3.13.: Height of the oxide as a function of the applied voltage, as presented in [192] and implemented in the presented simulator.

Model for nanodots generated in NCM

When operating the AFM in NCM mode, the formation of a field-induced liquid bridge is required in order to provide oxyanions (OH^- , O^-), used to form the oxide. The liquid bridge also limits the lateral extensions of the region to be oxidized. The model, implemented in the process simulator, is described in [28], where it is suggested that the width and height of a produced pattern have a linear dependence on the applied bias voltage, while a logarithmic dependence exists for the pulse duration.

The empirical equation which governs the height of the oxide dot, produced using NCM, and presented in [28] is

$$h(t, V_b) = h_0(V_b) + h_1(V_b) \ln(t) \text{ nm}, \quad (3.46)$$

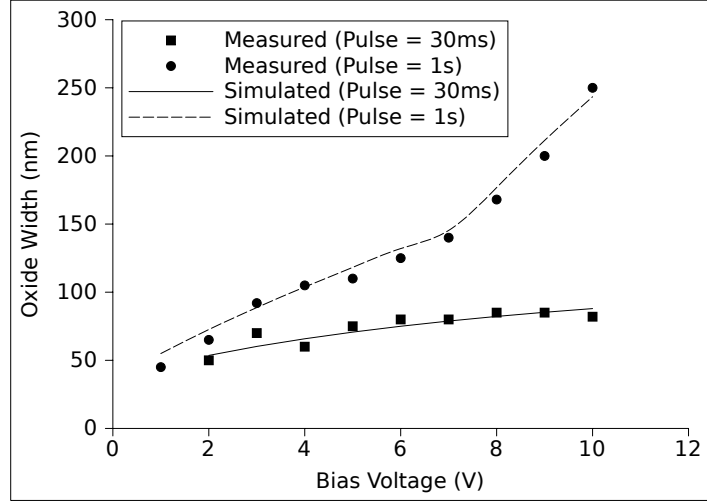


Figure 3.14.: FWHM of the oxide as a function of the applied voltage. Measurements are from [192], while the simulations are from (3.44).

where

$$\begin{aligned} h_0(V_b) &= -2.1 \text{ nm} + 0.5 \frac{\text{nm}}{\text{V}} V_b - 0.006 \frac{\text{nm}}{\text{V}^2} V_b^2 \\ h_1(V_b) &= 0.1 \text{ nm} + 0.03 \frac{\text{nm}}{\text{V}} V_b - 0.0005 \frac{\text{nm}}{\text{V}^2} V_b^2. \end{aligned} \quad (3.47)$$

Similarly, the equation which governs the width of the oxide dot, represented as the FWHM is [28]

$$w(t, V_b) = w_0(V_b) + w_1(V_b) \ln(t) \text{ nm}, \quad (3.48)$$

where

$$\begin{aligned} w_0(V_b) &= 11.6 \text{ nm} + 9 \frac{\text{nm}}{\text{V}} V_b \\ w_1(V_b) &= 2.7 \text{ nm} + 0.9 \frac{\text{nm}}{\text{V}} V_b, \end{aligned} \quad (3.49)$$

and size, voltage, and time are expressed in nanometers, volts, and seconds, respectively. The dependence behavior of the oxide height and width with respect to the bias voltage and pulse time is evident from Figure 3.15, where (3.46) and (3.48) are represented graphically. The linear relationship between voltage and nanodot size (height or width) at a single pulse time value is evident, while the logarithmic relationship between the pulse time and nanodot size (height or width) at a single voltage level is also visualized.

In [53] the effect of humidity on the nanodot size is presented and the relationship is shown in Figure 3.16. A nearly linear relationship between humidity and the nanodot height is seen, while the width increases more rapidly, when the humidity is increased to 90%. This can be explained by the increase in water meniscus size with increased humidity, which provides more oxyanions to take part in the oxidation reaction.

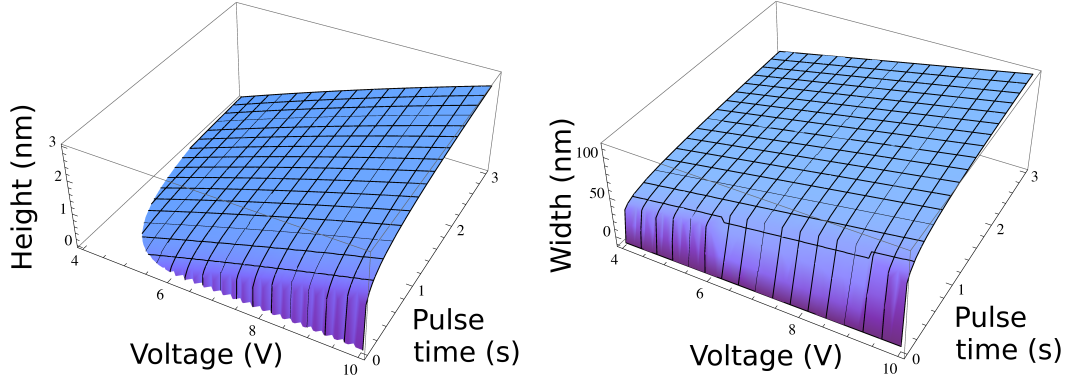


Figure 3.15.: Height and width of the oxide nanodot as a function of the applied voltage and pulse time.

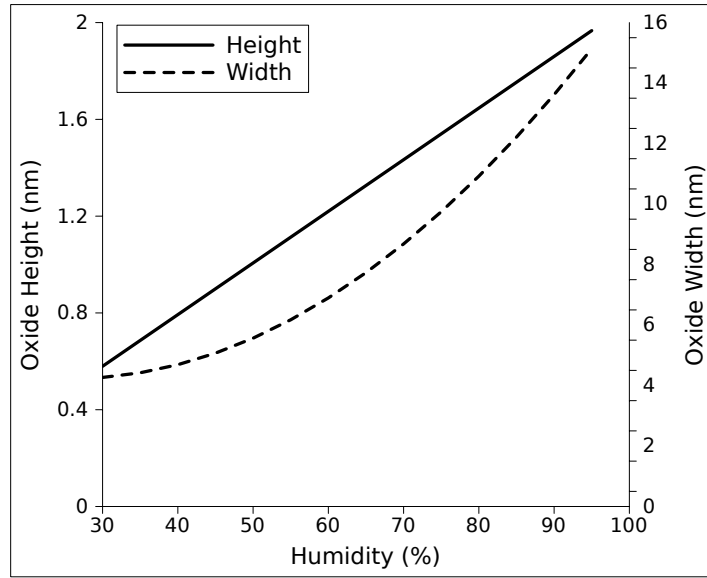


Figure 3.16.: Effects of humidity on the nanodot height and width, as presented in [53].

The derived empirical equation which describes the effect of all three parameters (time, voltage, and humidity) on the height and width of the oxide dot in nanometers, produced using the AFM in NCM is given by:

$$\begin{aligned} H(t, V_b, h) &= [h_0(V_b) + h_1(V_b) \ln(t)] \cdot [0.00037 h^2 - 0.019 h + 0.928], \\ W(t, V_b, h) &= [w_0(V_b) + w_1(V_b) \ln(t)] \cdot [0.019 h - 0.051], \end{aligned} \quad (3.50)$$

where t is the pulse time in seconds, V_b is the applied voltage in volts, and h is the RAH in percent.

Model for nanowires generated in NCM

In addition to using experimental observations in order to implement an empirical model for nanodots in the LS simulator, the simulator has also been extended to include the generation of nanowires using an AFM in NCM. Although a nanowire can be generated using a sequence of nanodots placed such that the lateral distance between each dot is smaller than a dot's width, having a separate model for nanowires can help to speed up simulation times. Simulating a nanowire as a sequence of nanodots means that each nanodot needs its own simulation step, while having a single empirical equation which governs nanowire generation requires only one simulation step. From the experimental results found in [53], relevant information is extracted in order to include the effects on the nanowire shape due to variations in applied voltage, oxidation time, relative air humidity (RAH), and wire orientation, shown in Figure 3.17. The wire orientation is represented as an angle, where the (010) direction is 0° while (100) is 90° for a Si (100) sample, shown in Figure 3.18 and Table 3.1.

| Orientation w.r.t. (010) | Height (nm) | FWHM (nm) |
|--------------------------|-------------|-----------|
| 0° | 1.07 | 38.3 |
| 30° | 1.93 | 65.1 |
| 60° | 1.30 | 83.4 |
| 90° | 1.19 | 62.8 |

Table 3.1.: Effects of wire orientation on the nanowire height and width, with $t=0.1\text{ms}$, $V_b=7\text{V}$, and $h=55\%$.

It is evident that increasing the oxidation time, the applied voltage, or the RAH results in an increased nanowire height and width. However, the effect of the wire orientation is less predictable. The smallest nanowire is noted at an orientation of 0° , while the largest nanowire height is noted at 30° and the largest FWHM is noted at 60° . The effect of the wire orientation on the height and width of the nanowire is not identical. The empirical equation, derived using the experimental results from [53] and implemented in the LS simulator is given by

$$\begin{aligned}
H(t, V_b, h, \theta) = & [-0.527 - 0.45 \ln(0.029 - t)] \cdot (0.56 V_b - 2.92) \cdot \\
& (-0.019 h - 0.051) \cdot (2.2 \theta^3 - 6.02 \theta^2 + 4.1 \theta + 1), \\
W(t, V_b, h, \theta) = & [530 + 107 \ln(t + 0.01)] \cdot (0.0157 V_b^2 - 0.156 V_b + 1.32) \cdot \\
& (0.00037 h^2 - 0.019 h + 0.928) \cdot (-0.92 \theta^3 + 1.04 \theta^2 + 1.044 \theta + 1),
\end{aligned} \tag{3.51}$$

where t is the oxidation time in seconds, V_b is the applied voltage in volts, h is the RAH in percent, and θ is the wire orientation in radians, represented as the angle between the nanowire and the (010) direction.

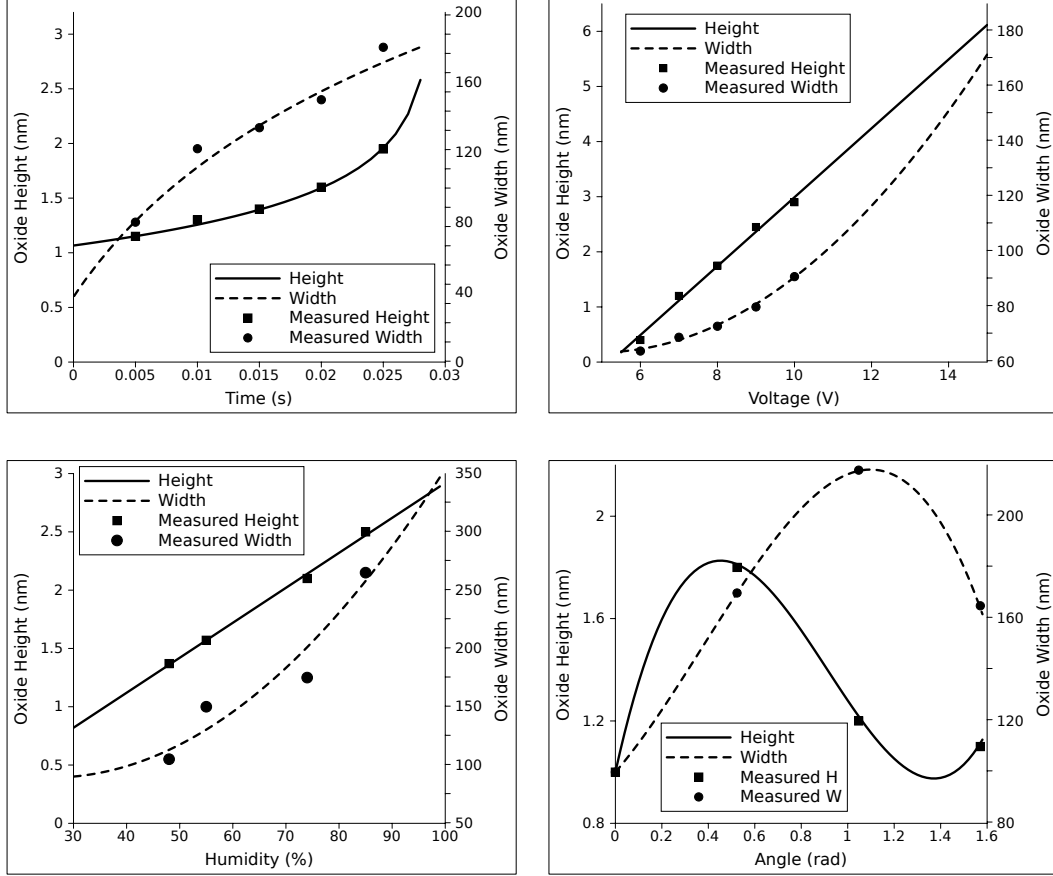


Figure 3.17.: Effects of time, voltage, humidity, and orientation on the nanowire height and width. Experimental (dots) and model (lines) values are shown.

In Figure 3.17 the results of the empirical equation (3.51) generated for this work are compared to the experimental data from [53].

3.4.3. Nanodot Modeling Using the MC Method

The simulator is implemented by first calculating the shape of the nanodot or nanowire with the previously mentioned empirical equations which depend on the oxidation time, applied voltage, ambient humidity, and nanowire orientation. Afterwards, a given number of particles is distributed above the silicon surface, their position following the pattern of the desired surface deformation. Finally, each particle is accelerated towards the surface, causing it to collide with the wafer. Upon impact, the silicon dioxide is advanced deeper into the silicon, while it simultaneously grows into the ambient. The result is an oxide nanodot or nanowire having the desired height and width, depending on the processing variables of voltage, time, humidity, and orienta-

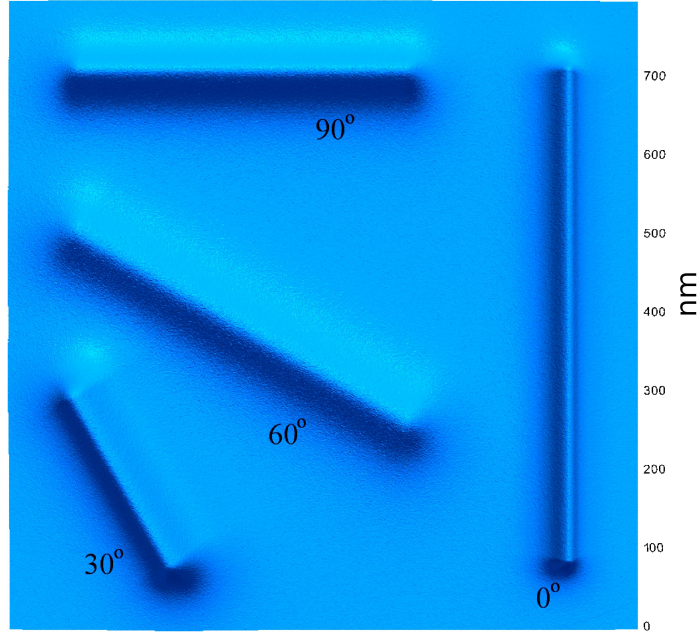


Figure 3.18.: Effects of wire orientation on the nanowire height and width, with $t=0.1\text{ms}$, $V_b=7\text{V}$, and $h=55\%$. The vertical axis is scaled by 100 for better visualization. The top surface represents the oxide-ambient interface, while the lower surface represents the oxide-silicon interface.

tion. The method of imprinting a desired particle distribution onto a wafer surface is represented graphically in Figure 3.19.

A flow chart summarizing the simulation steps is given in Figure 3.20, which describes how the desired particle distribution is effectively imprinted onto the LS surface using the MC method.

Gaussian Particle Distribution

As seen from the previous discussion regarding the MC model for AFM oxidation from Figure 3.20, a method to distribute particles according to a desired distribution is required. Some literature approximate the final oxide dot topography with a Gaussian curvature [162], while some suggest a Lorentzian profile [84]. The quantile function of the one-dimensional Gaussian distribution, required for the generation of a random particle position x_r , is

$$x_r \equiv \sqrt{2} \operatorname{erf}^{-1}(2\xi - 1), \quad \xi \in (0, 1). \quad (3.52)$$

Because of the error function, the quantile Gaussian function is not easily implementable with a random distribution in the MC environment and hence another model is desired. The model implemented in the simulator is based on the well known

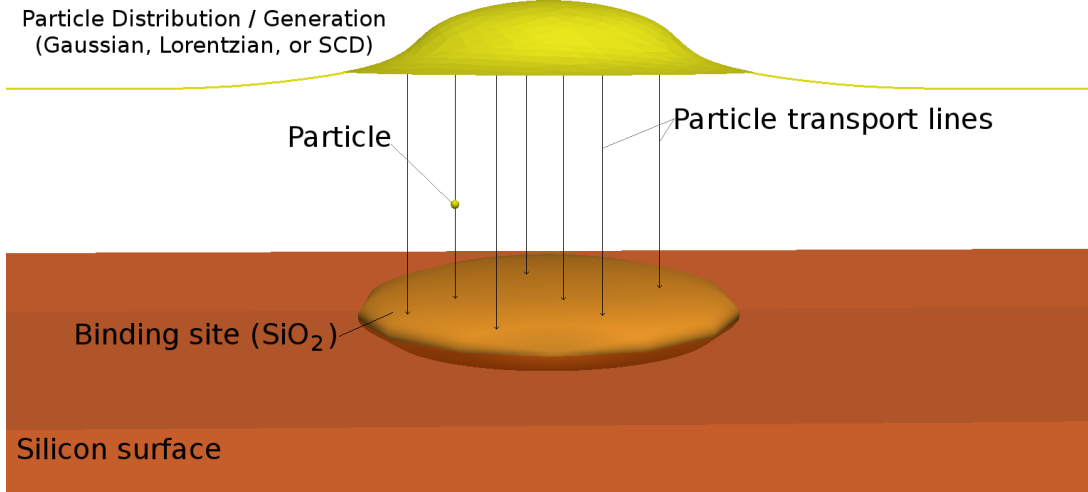


Figure 3.19.: Image representation of the MC method of “imprinting” a desired particle distribution onto the silicon surface in order to generate an oxide growth. The particles are accelerated using ray tracing techniques within the LS simulator environment.

Marsaglia polar method [139]. This method suggests a way to generate two independent standard normal random variables. The first step is the generation of an evenly distributed random location (r_x, r_y) within a circle of unity radius $s = r_x^2 + r_y^2$, where r_x and r_y are evenly distributed random numbers $\in (-1, 1)$. The Gaussian distributed coordinates (x_r, y_r) can then be calculated using the Marsaglia equations

$$x_r = r_x \sqrt{\frac{-2 \ln(s)}{s}}, \quad y_r = r_y \sqrt{\frac{-2 \ln(s)}{s}}. \quad (3.53)$$

A sample Gaussian distributed nanodot is shown in Figure 3.21.

The Gaussian distribution is well known; however from Figure 3.22, it is suggested that a Lorentzian distribution is a better fit to the final shape of the desired nanostructure [84].

The implementation of the Gaussian distribution was performed successfully, while a similar approach to the Lorentzian distribution was attempted without much success. Therefore, in order to generate particles according to a Lorentzian distribution, a novel technique for a particle distribution which follows the Lorentzian equation is developed. The technique results in equations similar to the Marsaglia-Polar equations from (3.53).

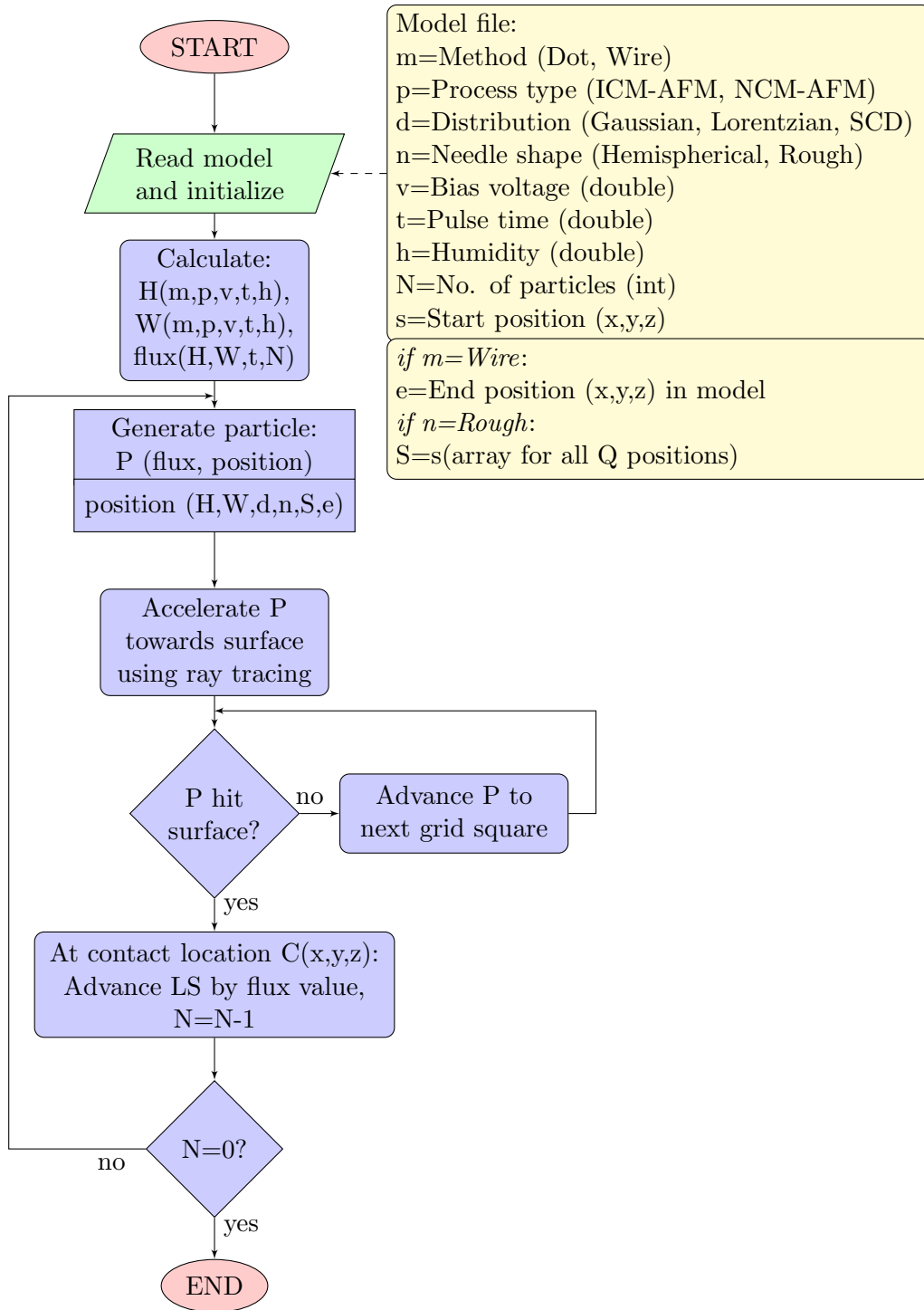


Figure 3.20.: Flow chart of the simulation process implementing the Monte Carlo method with ray tracing in a LS environment.

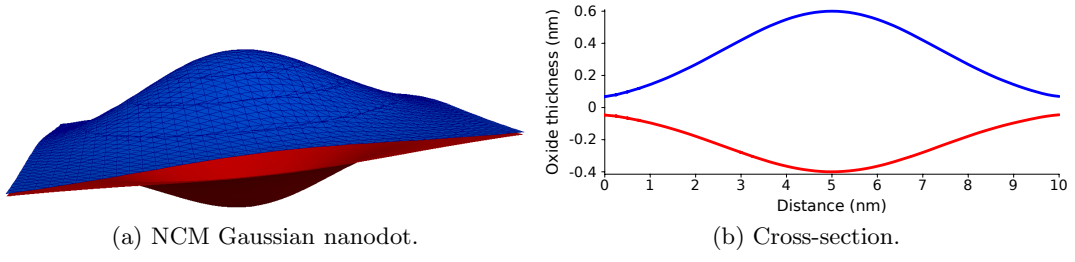


Figure 3.21.: Nanodot generated using Gaussian particle distribution. The vertical dimension has been scaled by 20 for better visualization. (a) NCM nanodot generated using a Gaussian distribution of particles and (b) Diagonal cross-section of the nanodot from Figure 6.13a

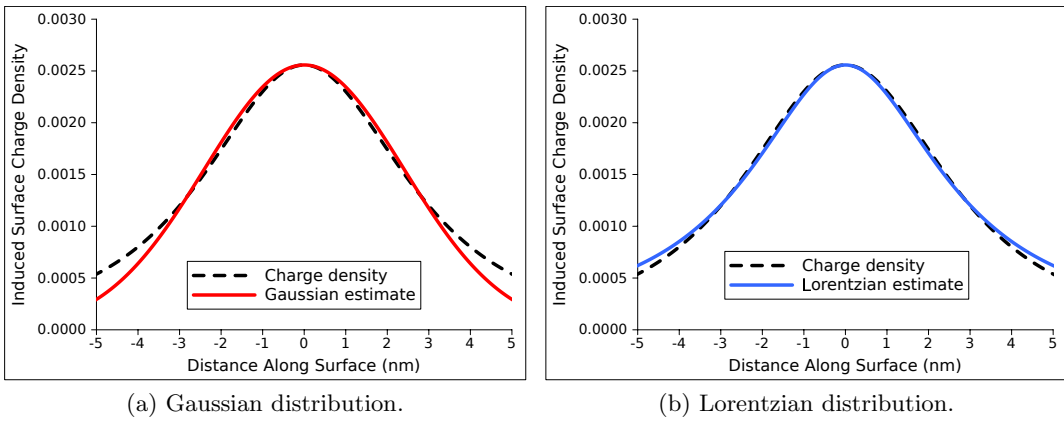


Figure 3.22.: (a) Comparison between the Gaussian distribution and the surface charge density and (b) comparison between the Lorentzian distribution and the surface charge density.

Lorentzian Particle Distribution

One-Dimensional Distribution The normalized Probability Density Function (PDF) of the Lorentzian distribution is given by:

$$f(x) = \frac{1}{\pi} \cdot \frac{1}{1 + x^2}. \quad (3.54)$$

The Cumulative Probability Density (CPD) is found by integrating the PDF to obtain $\Phi(x) = \int_{-\infty}^{x_r} f(x) dx$

$$\Phi(x_r) = \frac{1}{\pi} \arctan(x_r) + \frac{1}{2}. \quad (3.55)$$

The quantile function of the Lorentzian distribution, required for particle generation, is the inverse CPD

$$x_r = \Phi^{-1}(\xi) \equiv \tan \left[\pi \left(\xi - \frac{1}{2} \right) \right], \quad (3.56)$$

where $\xi \in (0, 1)$ is a uniformly distributed random number. Therefore, using (3.56), a random particle can be generated to follow the Lorentzian distribution by first generating an evenly distributed value for ξ .

Two-Dimensional Distribution The same analysis shown for the one-dimensional Lorentzian distribution must be performed in order to generate a two-dimensional Lorentzian quantile function. The two-dimensional Lorentzian distribution is required when a three-dimensional nanodot needs to be simulated.

The PDF of the two-dimensional Lorentzian distribution can be represented as

$$f(x_r, y_r) = \frac{C}{1 + x_r^2 + y_r^2}, \quad (3.57)$$

where C is the normalization constant. Using polar coordinates, where $x_r^2 + y_r^2 = r^2$ and $dx_r dy_r = r dr d\theta$, it can easily be shown that the PDF cannot be normalized in the entire real space \mathbb{R}^2 . We therefore must normalize the equation to a desired maximum radius r_{max} .

$$1 = 2\pi C \int_0^{r_{max}} \frac{1}{1 + r^2} r dr = C \pi \ln(1 + r_{max}^2). \quad (3.58)$$

The normalization constant follows from the CPD, normalized to r_{max}

$$C = \frac{1}{\pi \ln(1 + r_{max}^2)}. \quad (3.59)$$

The CPD for the two-dimensional distribution, normalized to r_{max} can then be written as

$$\Phi(r) = \frac{\ln(1 + r^2)}{\ln(1 + r_{max}^2)}, \quad (3.60)$$

where $\ln(1 + r_{max}^2)$ is treated as a r_{max} -dependent constant M . By inverting the CPD and solving for r the two-dimensional Lorentzian quantile function is found, which is required for particle generation

$$r = \sqrt{e^{\xi M} - 1}, \quad (3.61)$$

where $\xi \in (0, 1)$ is a uniformly distributed random number. Using (3.61), a random particle location can be generated in two-dimensional space to follow

the Lorentzian distribution. The generated location is a radial distance from the center of the distribution.

An evenly distributed angle θ between 0 and 2π is generated and the final particle position is given by $(x_r, y_r) = (r \cos \theta, r \sin \theta)$. It can be observed that the choice of r_{max} affects the height of the Lorentzian distribution, thereby affecting the height of the desired nanodot. Therefore, an additional contribution, dependent on r_{max} , is needed in the equation for the height generated by each particle. This contribution is

$$\ln(1 + r_{max}^2). \quad (3.62)$$

The resulting nanodot cross section, shown in Figure 3.23 matches the ideal one-dimensional Lorentzian distribution. This method allows the generation of nanodots, such as the one shown in Figure 3.24, which follow a Lorentzian distribution, as desired for the AFM oxidation simulator.

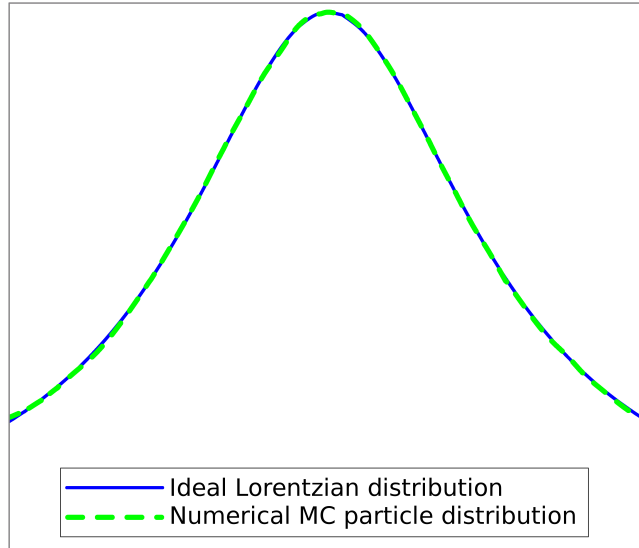


Figure 3.23.: Cross-sectional nanodot height generated using a Lorentzian distribution.

The expression for the quantile function in (3.61) suggests a potential connection to the Marsaglia polar method. A Lorentzian distribution can be generated using a similar procedure. The first step is, once again, the generation of an evenly distributed random location in two dimensions (r_x, r_y) within a circle with radius $s = \sqrt{r_x^2 + r_y^2}$. The Lorentzian distributed coordinates (x_r, y_r) can then be expressed as:

$$x_r = r_x \sqrt{\frac{e^{sM} - 1}{s}}, \quad y_r = r_y \sqrt{\frac{e^{sM} - 1}{s}}, \quad (3.63)$$

where $M = \ln(1 + r_{max}^2)$.

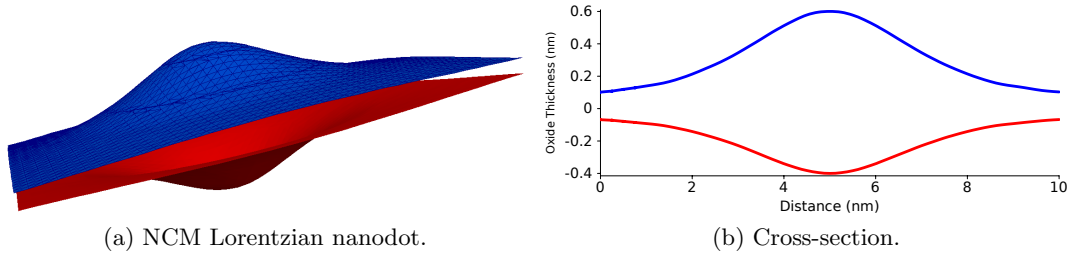


Figure 3.24.: The vertical dimension has been scaled by 20 for better visualization. (a) NCM nanodot generated using a Lorentzian distribution of particles and (b) Diagonal cross-section of the nanodot from Figure 3.24a.

One-Dimensional Surface Charge Density Particle Distribution

SCD charge density on the silicon wafer is advantageous since a nanodot can then be generated which directly follows the applied electric field, a function of the applied voltage at the AFM needle. When performing nanodot oxidation simulations using an AFM for a two-dimensional model, a one-dimensional particle distribution is required. The equation (3.37), for a SCD distribution of a hemispherical needle tip can be rewritten in a one-dimensional form:

$$\sigma(x, 0) = \frac{-DQ}{2\pi(x^2 + D^2)^{3/2}}. \quad (3.64)$$

(3.64) can then be used to generate a one-dimensional PDF

$$f(x) = -C \frac{DQ}{2\pi(x^2 + D^2)^{3/2}}, \quad (3.65)$$

where C is the normalization constant. C is found by integrating $f(x)$ over the entire simulation domain and equating it to unity:

$$\int_{-\infty}^{\infty} f(x) dx = -C \int_{-\infty}^{\infty} \frac{DQ}{2\pi(x^2 + D^2)^{3/2}} dx = 1. \quad (3.66)$$

By solving (3.66), the normalization constant C is found

$$C = -\frac{\pi D}{Q}, \quad (3.67)$$

which is then substituted into (3.65) to form the normalized PDF for a one-dimensional SCD distribution

$$f(x) = \frac{D^2}{2(x^2 + D^2)^{3/2}}. \quad (3.68)$$

The next step is finding the CPD function, derived by integrating the normalized PDF,

$$\Phi(r) = \int_{-\infty}^r f(x)dx, \quad (3.69)$$

where r is the SCD distributed radius. Because of the symmetry of the SCD distribution on either side of the charged particle Q , generating a CPD distributed radius becomes easier, when $-0.5 \leq \Phi \leq 0.5$. Therefore, we set

$$\Phi(r) = \int_0^r f(x)dx, \quad (3.70)$$

leading to

$$\Phi(r) = \xi = \left(\frac{r}{2\sqrt{r^2 + D^2}} \right). \quad (3.71)$$

Setting $\Phi(r)$ equal to an evenly distributed random number $\xi \in (-0.5, 0.5)$ and inverting (3.71) allows us to obtain the SCD quantile function required for particle generation:

$$r = 2D \frac{\xi}{\sqrt{1 - 4\xi^2}}. \quad (3.72)$$

Therefore, in order to generate particles obeying the SCD distribution along the silicon wafer surface, each particle must be generated using (3.72), where ξ is an evenly distributed random number, $\xi \in (-0.5, 0.5)$.

Two-Dimensional Surface Charge Density Particle Distribution

When working with a three-dimensional model for AFM oxidation of nanodots, a two-dimensional particle distribution is required. The analysis is similar to the one-dimensional model presented in the previous section. The derivation of the quantile function is performed using polar coordinates for simplicity and for easier generation of a final radial distribution of particles. For polar coordinates (r_n, θ) it is important to note that $x_r^2 + y_r^2 = r_n^2$, and $dx_r dy_r = r_n dr_n d\theta$. This was also discussed when deriving the Lorentzian distribution. The two-dimensional PDF, in polar coordinates, derived from (3.37) is

$$f(r_n, \theta) = -C \frac{DQ}{2\pi (r_n^2 + D^2)^{3/2}}. \quad (3.73)$$

The normalization constant C is once again found by integrating the PDF over the entire simulation range and equating it to one:

$$C = -\frac{1}{Q}, \quad (3.74)$$

then the normalized two-dimensional PDF in polar coordinates becomes

$$f(r_n, \theta) = \frac{D}{2\pi (r_n^2 + D^2)^{3/2}}. \quad (3.75)$$

The CPD is found by integrating the normalized PDF over the simulation area. The angular component results in a value of 2π , while the radial component is found by first finding the radius-dependent CPD

$$\Phi(r) = \int_0^{2\pi} \int_0^r f(r_n, \theta) r_n dr_n d\theta, \quad (3.76)$$

which equates to

$$\Phi(r) = \xi = 1 - \frac{D}{\sqrt{D^2 + r^2}}. \quad (3.77)$$

The quantile function for the two-dimensional SCD distribution is found by inverting the CPD function to obtain

$$r = D \sqrt{\frac{1}{(1 - \xi)^2} - 1}, \quad (3.78)$$

where ξ is an evenly distributed random number, $\xi \in [0, 1)$. The angular component of the distribution is obtained in the same manner as the radial component for the Lorentzian distribution. An evenly distributed angle θ_r between 0 and 2π is found and the final Cartesian location for each particle is given by $(x_r, y_r) = (r \cos \theta_r, r \sin \theta_r)$. The normalized cross-section of a nanodot generated using this distribution is compared to the normalized SCD from (3.64) in Figure 3.25.

Modeling Nanodots with Additional Point Charges

As previously mentioned, a rough needle tip must be modeled using a ring of charges at a given height above the silicon surface. The SCD distribution is found using the method of image charges and summing the effects of each individual charge which makes up the charged ring, resulting in the SCD distribution shown in (3.38).

The SCD in (3.38) does not allow for a straight-forward derivation of a random distribution, such as the one shown in (3.72) and (3.78). Therefore, the MC rejection technique, or the accept-reject algorithm must be applied, whereby a test point is generated on the entire simulation domain using an even distribution, $\xi(x_t, y_t)$. An additional evenly distributed number between zero and σ_{max} from (3.39) is generated and, if this number is below $\sigma(x_t, y_t, 0)$, a particle is generated at (x_t, y_t, D) . Otherwise, the location (x_t, y_t, D) is ignored and a new test point is generated. This procedure is repeated until a sufficient number of particles is kept in order to generate a nanodot topography.

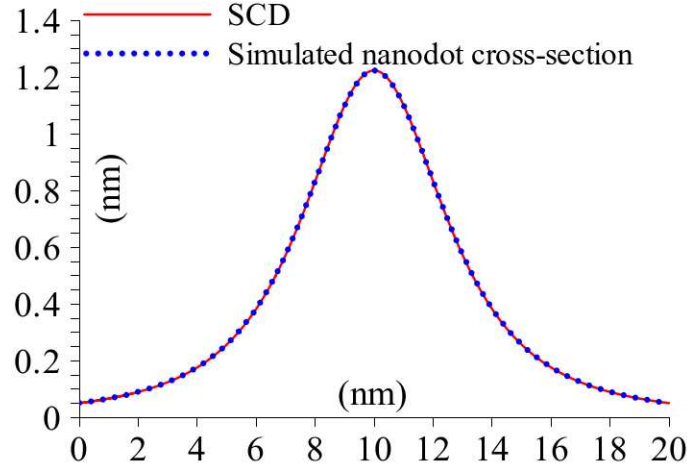


Figure 3.25.: Normalized effective nanodot cross section height and the normalized SCD function.

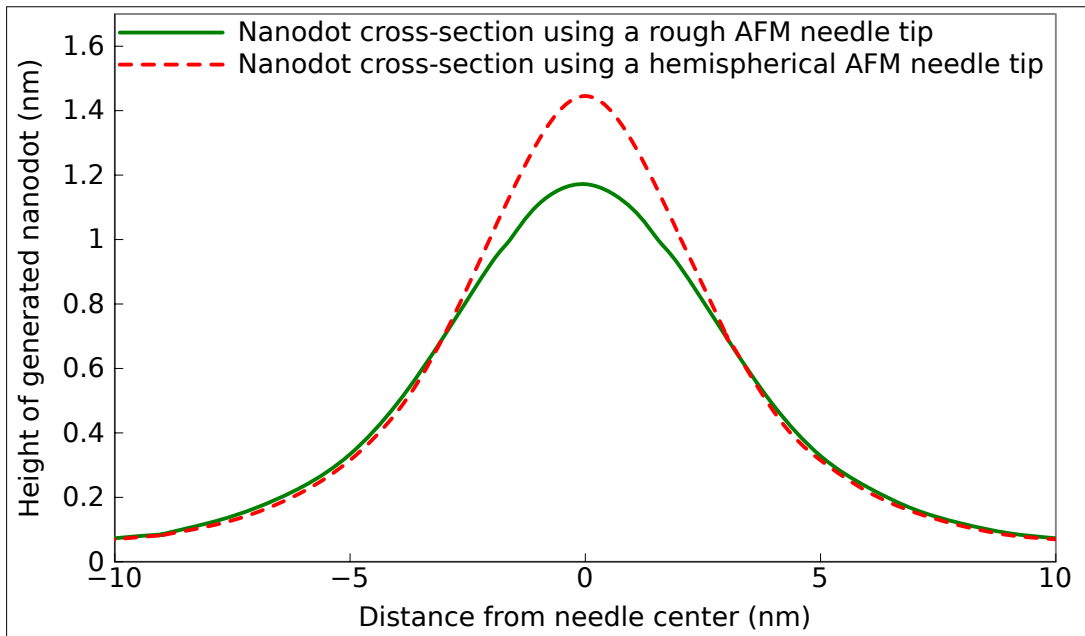


Figure 3.26.: The effective diagonal cross-section height of a nanodot when using a rough AFM needle tip versus a hemispherical AFM needle tip.

It is evident that a blunt needle tip will result in a blunt nanodot formation with a slight increase in lateral spreading. The effective height of a nanodot when using a rough AFM needle tip versus a hemispherical AFM needle tip is shown in Figure 3.26. It is visible that the height at the middle of the nanodot is lower for a rough needle tip, as the electric field is spread laterally.

4. Novel Deposition and Etch Techniques

In this section, some processing techniques which are not included in current state-of-the-art process simulators, but which are gaining more traction in the scientific community, are introduced. Spray pyrolysis deposition is an inexpensive tool for the deposition of crystalline powders [150], which can then be further annealed in order to grow nanowires for sensor and other applications. BiCS flash memory is an emerging technology, proposed by Toshiba as a low-cost memory solution, involving the etching of stacked Silicon and SiO₂ films [206].

4.1. Spray Pyrolysis Deposition

During the last several decades, coating technologies have garnered considerable attention, mainly due to their functional advantages over bulk materials, processing flexibility, and cost considerations [157]. Thin film coatings may be deposited using physical methods or chemical methods. The chemical methods can be split according to a gas phase deposition or a liquid phase deposition. These processes are summarized in Figure 4.1, where CVD and Atomic Layer Epitaxy (ALE) are the gas processes. Spray pyrolysis, as can be seen in Figure 4.1, is a technique which uses a liquid source for thin film coating.

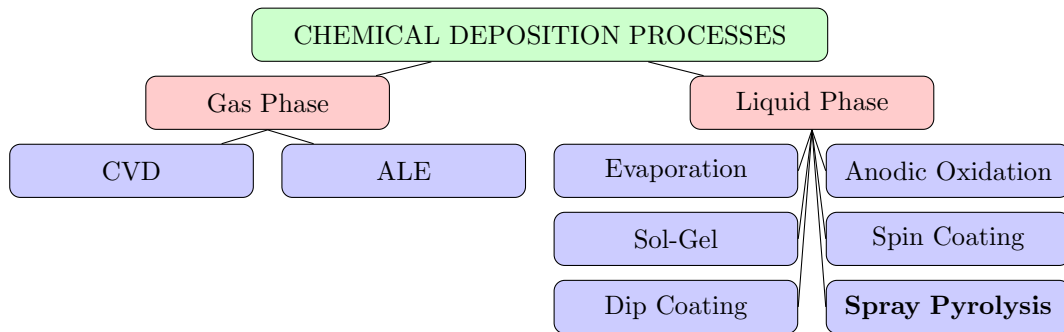


Figure 4.1.: Summary of chemical thin film deposition technologies.

4.1.1. Technology Background

The first introduction of the spray pyrolysis technique by Chamberlin and Skarman [29] in 1966 was for the growth of CdS thin films for solar cell applications. Since then, the process has been investigated with various materials, such as SnO_x [107], In_2O_3 [180], Indium Tin Oxide (ITO) [138], PbO [106], ZnO [168], ZrO_2 [150], yttria-stabilized zirconia (YSZ) [172] and others [153].

The main advantages of spray pyrolysis over other similar techniques are:

- Spray pyrolysis is cost effective and can be easily performed.
- Substrates with complex geometries can be coated.
- Spray pyrolysis deposition leads to relatively uniform and high quality coatings.
- No high temperatures are required during processing (up to $\sim 500^\circ\text{C}$).
- Films deposited by spray pyrolysis are reproducible, giving it potential for mass production.

The major interest in spray pyrolysis is due to its low cost, while it is increasingly being used for some commercial processes, such as the deposition of a transparent layer on glass [137], the deposition of a SnO_2 layer for gas sensor applications [107], the deposition of a YSZ layer for solar cell applications [172], anodes for lithium-ion batteries [161], and optoelectronic devices [19].

The general simplified scheme for spray pyrolysis deposition is shown in Figure 4.2, where three processing steps can be viewed and analyzed.

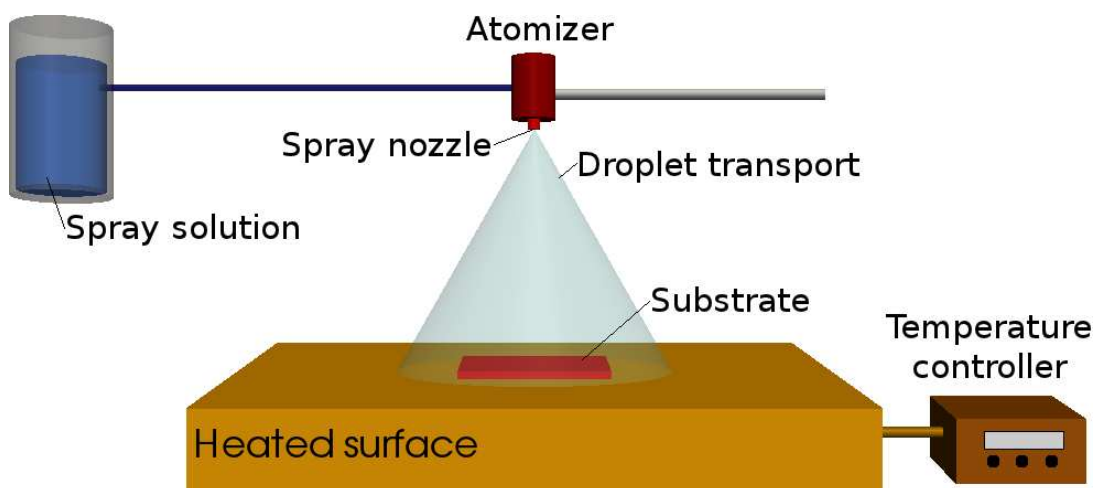


Figure 4.2.: General schematic of a spray pyrolysis deposition process.

The three processing steps for spray pyrolysis deposition are

1. Atomization of the precursor solution.
2. Aerosol transport of the droplet.
3. Droplet evaporation, spreading on the substrate, and drying and decomposition of the precursor salt to initiate film growth.

These three steps are individually addressed in the sections to follow.

4.1.2. Atomization Procedure

The atomization procedure is the first step in the spray pyrolysis deposition system. The idea is to generate droplets from a spray solution and send them, with some initial velocity, towards the substrate surface. Spray pyrolysis normally uses air blast, ultrasonic, or electrostatic techniques [171]. The atomizers differ in resulting droplet size, rate of atomization, and the initial velocity of the droplets. It has been shown that the size of the generated droplet is not related to any fluid property of the precursor solution and depends solely on the fluid charge density level ρ_e as shown in [99]

$$r^2 = \left(\frac{-\alpha'}{\beta'} \right) \frac{3\epsilon_0}{q\rho_e}, \quad (4.1)$$

where ϵ_0 is the permittivity, q is the elementary charge, and $\frac{-\alpha'}{\beta'}$ is a constant value equal to $\sim 1.0 \times 10^{-17}$ J. The mass of a droplet, assuming a spherical shape depends on its density

$$m = \frac{4\pi}{3} \rho_q r^3, \quad (4.2)$$

where r is the droplet radius and ρ_q is the droplet density. The initial leaving velocity of the droplet is an important parameter as it determines the rate at which the droplets reach the substrate surface, the heating rate of the droplet, and the amount of time the droplet remains in the spray pyrolysis environment. Table 4.1 summarizes the properties of droplets for different atomizers commonly used for spray pyrolysis deposition.

| Atomizer | Droplet diameter (μm) | Droplet velocity (m/s) |
|---------------|------------------------------|------------------------|
| Pressure | 5 - 50 | 5 - 20 |
| Ultrasonic | 1 - 100 | 0.2 - 0.4 |
| Electrostatic | 5 - 70 | 1 - 4 |

Table 4.1.: Characteristics of atomizers commonly used for spray pyrolysis.

The ultrasonic nozzles apply a relatively small amount of energy and can produce droplets with a radius down to approximately $2\mu m$, but at the cost of a low atomization rate ($< \sim 2 \text{ cm}^3/\text{min}$) [150]. Due to ease of production, many companies chose to

use pressure atomizers instead of the ultrasonic atomizers. Therefore, this section will mainly concern itself with the pressure and electrostatic atomizers, characterized in [107], [171], respectively.

An air blast atomizer uses high speed air in order to generate an aerosol from a precursor solution. Increasing the air pressure causes a direct decrease in the generated mean droplet diameter. Inversely, increasing the liquid pressure causes a direct increase in the mean droplet diameter [193]. Increasing the distance between the spray nozzle and the surface to be coated reduces the heating effect, resulting in a reduced deposition rate, but an increased coating area. Another way to achieve the same effect is to increase the spray angle of the nozzle in use. Perednis [171] showed that all droplets sprayed from an air blast atomizer are contained within a 70° spray cone angle, while half are within a narrower 12° angle. It was also determined that the flow rate has a very small influence on the spray characteristics, which can be mostly ignored for modeling.

For Electrostatic Spray Deposition (ESD), the cone-jet mode is suitable for thin film deposition. There are two types of ESD nozzles: the cone-jet mode and the multi-jet mode. Their differences are shown in Figure 4.3.

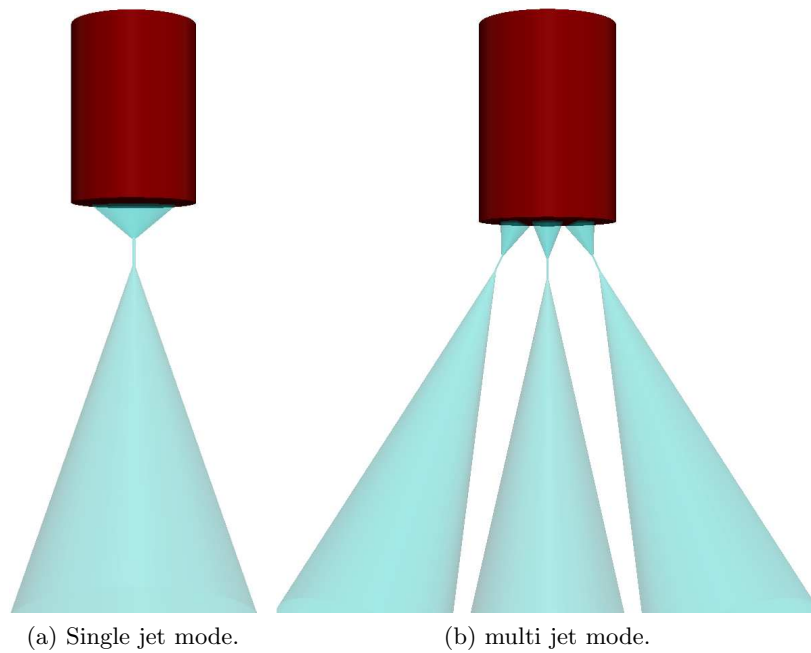


Figure 4.3.: Single jet and multi jet modes of electrostatic spray deposition.

For the cone jet mode nozzle, the convex shape of the liquid surface is distorted by an electric field to form a Taylor cone, which is extended at its apex by a permanent jet with a small diameter. In multi jet mode, the liquid is distorted at the tip of the tube nozzle into many different jets of small diameter. The flow rates which were achieved

with the two methods are 2.8ml/h and 5.7ml/h for the multi-jet and single-jet modes, respectively [171].

4.1.3. Aerosol Transport of Droplets

After the droplet leaves the atomizer, it travels through the ambient with an initial velocity determined by the atomizer. In the aerosol form, the droplets are transported with the aim of as many droplets as possible reaching the surface. As the droplets move through the ambient, they experience physical and chemical changes depicted in Figure 4.4.

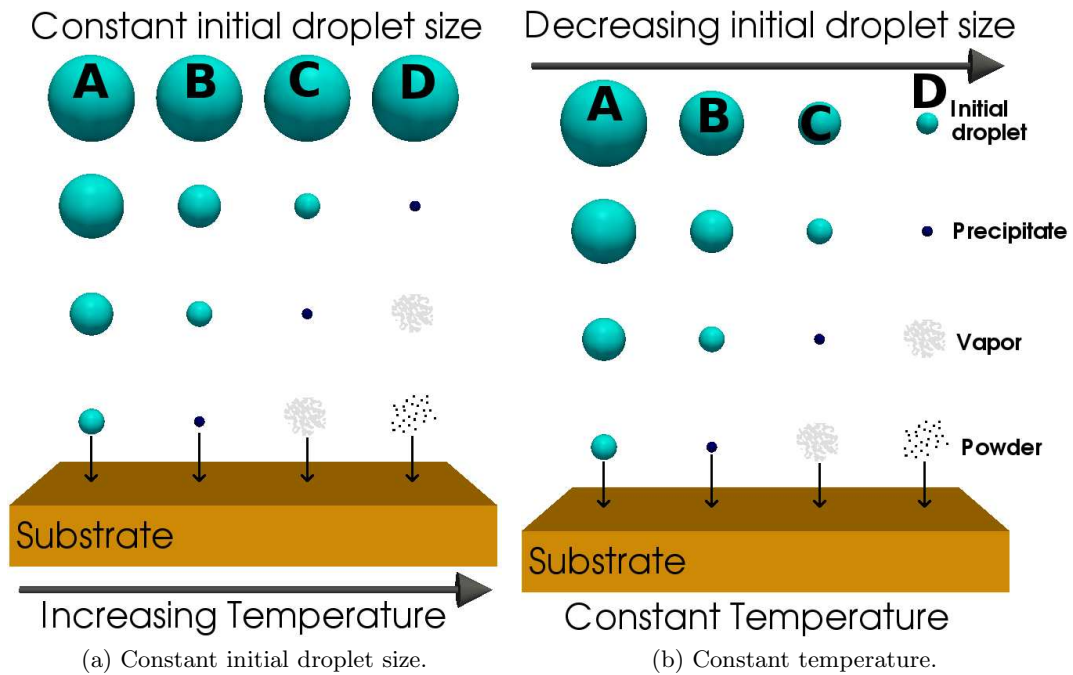


Figure 4.4.: Spray pyrolysis droplets modifying as they are transported from the atomizing nozzle to the substrate. Whether the temperature [216] or the initial droplet size [187] are varied, there are four potential paths which the droplet can take as it moves towards the substrate (A-D).

As the droplet traverses the ambient, there are four forces simultaneously acting on it, describing its path. Those forces are gravitational, electrical, thermophoretic, and the Stokes force. As shown in Figure 4.4, the droplets experience evaporation during their flight, which affects the influence of the forces on their trajectory. Some experimental results from [121] indicate that solid particles could form, when the reactor temperature is low, when the precursor solution concentration is high, and when the flow rate of the carrier gas (N_2) is low.

Gravitational force

The gravitational force is the force pulling the droplet downward. The size of the force depends on the mass of the traveling droplet, which is a function of its volume and its density. The force is given by

$$F_g = \frac{4\pi}{3} \rho_d r^3 g, \quad (4.3)$$

where ρ_d is the density of the droplet and g is the acceleration due to gravity (9.81m/s^2). For small droplets the force of gravity is too small to allow it to arrive at the surface before it is fully evaporated. For larger particles, the force of gravity is the driving force behind the droplet transport.

Electrical force

The electrical force is applicable to spray pyrolysis systems which include an additional electrical source governing the droplet's trajectory. When an air blast atomizer is used, high speed air is the cause of atomization and aerosol production. Ultrasonic atomizers are electrically driven, whereby an electric generator is vibrated at ultrasonic frequencies through a titanium nozzle. Increasing the frequency can result in smaller droplet sizes. ESD atomizers use a strong electric force at the liquid-gas interface to generate charged droplets. Therefore, air blast atomizers do not have additional contributions from an electrical force and the droplet transport is driven by the gravitational force and the initial velocity, while for spray pyrolysis deposition using ultrasonic and ESD atomizers, the electrical force is the main component which drives the droplets downwards. The electrical force acting on a droplet is usually several orders of magnitude larger than the gravitational force and is given by

$$F_e = q_d E, \quad (4.4)$$

where E is the generated electric field strength and q_d is the droplet charge. q_d depends on the temporal change of the droplet and is given by

$$q_d = q_{max} \frac{t}{t + t_0} \quad (r \gg 1\mu m), \quad (4.5)$$

with

$$q_{max} = 8\pi\sqrt{\gamma\epsilon_0}r^3 \quad \text{and} \quad t_0 = \frac{4}{b\text{div}E}, \quad (4.6)$$

where γ is the liquid-gas surface tension, ϵ_0 is the electrical permittivity, and b is the ionic mobility [187].

Stokes force

The Stokes force is the drag experienced by the droplet due to the air resistance in the ambient. Because of the spherical shape and small size of the droplet, the Stokes force is not equivalent to the force experienced by an irregularly shaped body. The force is caused by the friction between the droplet and air molecules. The Stokes force is a factor of the particle's velocity and size. Therefore, large droplets which move with a high velocity will experience the largest retarding force according to

$$F_S = 6 \pi \eta_a r (v_d - v_a) \left(1 + \frac{3}{8} \text{Re} \right), \quad (4.7)$$

where η_a is the viscosity of air, r is the droplet diameter, v_d is the droplet velocity, v_a is the air velocity, and Re is the Reynolds number. For spherical particles, the Reynolds number is given by

$$\text{Re} = \frac{2r (v_d - v_a) \rho_a}{\eta_a}, \quad (4.8)$$

where ρ_a is the density of air. Because the $\frac{3}{8}\text{Re}$ term in (4.7) is very small ($\frac{3}{8}\text{Re} \ll 1$), it is often excluded from Stokes force calculations.

Thermophoretic force

The thermophoretic force is a retarding force, causing droplets to significantly decrease their velocity as they approach the heated substrate. Figure 4.5 shows the temperature distribution near a heated substrate. The results for the 210°C, 250°C, and 310°C are taken from [171], while the results for the 400°C are from [64]. It is evident that the air temperature increases steeply due to the forced convection cooling effect of the air flow when close to the heated substrate. Because the thermophoretic force depends on the thermal gradient in the transport environment, it can be concluded that it will have no effect on the droplet movement, when it is several (~ 5 -7) mm away from the substrate. However, in this high thermal gradient region, the thermophoretic force begins to dominate. This is true for pressurized spray deposition (PSD) systems where the main driving force is gravity; however, for ESD systems, the electrical force is often stronger than the thermophoretic force. Therefore, the motion of the droplet within the "thermal zone" would not change significantly, but the increased temperature would have other effects on the droplet, such as a reduction in size due to droplet evaporation in the region.

The equation governing the strength of the thermophoretic force is given by

$$F_t = \frac{3 \pi \eta_a^2 r}{\rho_a} \cdot \frac{\nabla(T_d)}{T_a}, \quad (4.9)$$

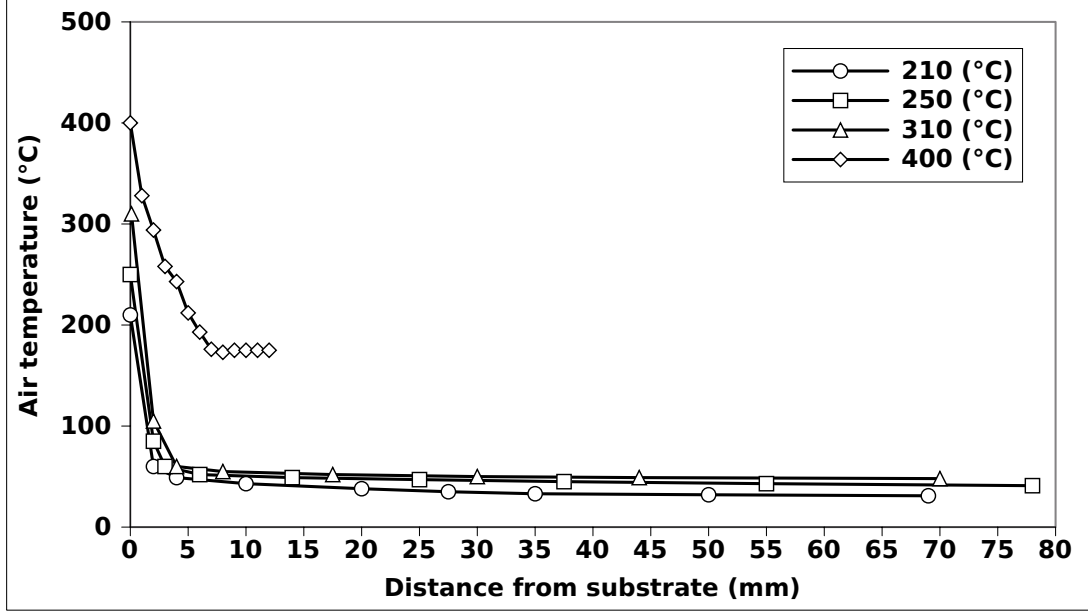


Figure 4.5.: Air temperature above a heated plate for substrate temperatures 210°C, 250°C, 310°C, and 400°C during a pressurized spray process.

where η_a is the viscosity of air, r is the droplet radius, T_d is the droplet temperature, T_a is the air temperature, ρ_a is the density of the air, and $\nabla(T_d)$ is

$$\nabla(T_d) = \frac{3\kappa_a}{2\kappa_a^2 + \kappa_d} \cdot \nabla(T_a), \quad (4.10)$$

where κ_a and κ_d are the thermal conductivities of the air and the droplet, respectively. It should be mentioned that (4.9) is only valid for droplets whose radius is much larger than the mean free path of the air molecules.

4.1.4. Precursor Decomposition

The precursor, as it moves through the heated ambient undergoes various changes, which are characterized in Figure 4.4. Evaporation, precipitate formation, and vaporization all occur depending on the droplet size and ambient temperature.

The four processes (A–D) from Figure 4.4 represent the four potential cases which the droplet can undergo during spray pyrolysis deposition as it is traveling towards the substrate. All processes occur during a spray pyrolysis process, however, it is Process C, the CVD-like deposition which is desired to yield a dense high quality film.

Process A: low temperature - large initial droplet

When the large droplets approach a heated substrate and the temperature is not sufficiently high to fully evaporate the solution, they will impact with the substrate and decompose. Upon contact, the droplet is entirely vaporized and a dry precipitate is left behind. Because droplet vaporization requires some heat, the substrate temperature is slightly decreased at the impact point, adversely affecting the reaction kinetics [187]. This process has a weak sticking probability.

Process B: lower/intermediate temperature - larger/medium droplet size

When medium-sized droplets are initially formed, some evaporation occurs. Just as the droplet reaches the surface, however, it forms a precipitate as an amorphous salt and a dry precipitate hits the surface, where decomposition occurs. Some particles evaporate and condense into gaps between particles, where surface reaction occurs. However, this process has a medium sticking probability.

Process C: intermediate/higher temperature - medium/smaller droplet size

When the processing environment causes droplets to evaporate prior to reaching the substrate vicinity, a precipitate will form early. As the precipitate reaches the immediate vicinity of the substrate, it is converted into a vapor state and it undergoes a heterogeneous reaction through the following steps [187]:

1. Reactant molecules diffuse to the surface.
2. Adsorption of some molecules at the surface.
3. Surface diffusion and a chemical reaction, incorporating the reactant into the lattice.
4. Desorption and diffusion of the product molecules from the surface.

This is a classical CVD reaction, which results in a high quality film deposition and a high sticking probability.

Process D: high temperature - small droplet size

When small initial droplets are formed, or the temperature is high enough the droplet quickly forms a precipitate. As the precipitate approaches the substrate, it is vaporized and a chemical reaction subsequently occurs in the vapor phase. This homogeneous reaction leads to the condensation of molecules into crystallites in the form of a powder precipitate. The powder falls to the substrate surface, but without a deposition reaction.

4.2. Bit Cost Scalable Memory Holes

There is a constant drive in the semiconductor industry to fit as many components as possible onto a single chip, which is consistently decreasing in size. Memory structures are also prone to such attempts at miniaturization since memory requirements and needs are constantly increasing, while chip area is decreasing. Current flash memory technologies are based on NAND or NOR gates. The NAND gate based memory cells are primarily used for memory cards, Universal Serial Bus (USB) flash drives, and solid state drives, mainly to obtain high density storage. The NOR gate based memory cells are used in mobile phones, printers, controllers and devices which require fast read access. There are signs which suggest a significant increase in the memory market in the coming years because of the extreme amounts of information which are becoming available. The amount of information produced by human activities is growing exponentially and the current storage mechanisms are unable to keep up [163]. This section will describe a novel technology for a three-dimensional stacked Bit Cost Scalable (BiCS) memory and the major concerns regarding its potential, which are due to processing complexities and limitations. A model for etching memory holes through a multi-layered silicon and silicon dioxide structure is presented.

4.2.1. Technology Background

During the previous two decades, the memory demand increased significantly. The response from the scientific community was to produce memory technology scaling by 19 generations in the last 24 years and in the process out-pacing even Moore's Law [72]. The technology node scaling over the past several years is depicted in Figure 4.6.

Masouka [145] proposed the first FLASH EEPROM, which reduced the cost of the memory array compared to that of previously-used EEPROM memories and was based on a NOR cell. A few years later, Masouka also proposed a NAND gate based FLASH EEPROM [146] which is a floating gate cell whose efficiency was far superior to that of a NOR cell. However, because of the serial architecture of the NAND cell, its read access was slow. Over the years the NAND cell has been shown as down-scalable far more than the NOR cell, down to the 15nm node. However, due to concerns regarding lithographic limitations, coupling ratio, and crosstalk interference, it is suggested that the NAND cell will not be scalable far below the 15nm node [232]. Others propose charge trapping devices which are capable of scaling the Floating Gate NAND cell beyond 15nm, but below ~ 10 nm, both charge trapping and Floating Gate devices have too few electrons for robust storage [130]. In order to find alternatives to the standard two-dimensional cell flash, research was directed towards three-dimensional structures [101], [115]. These structures do not rely on charge storage and are thereby naturally not limited by the available number of electrons.

Some three-dimensional memory structures proposed in the past 5 years include the Terabit Cell Array Transistor (TCAT) structure from Jang et al. [94], the 3D Dual

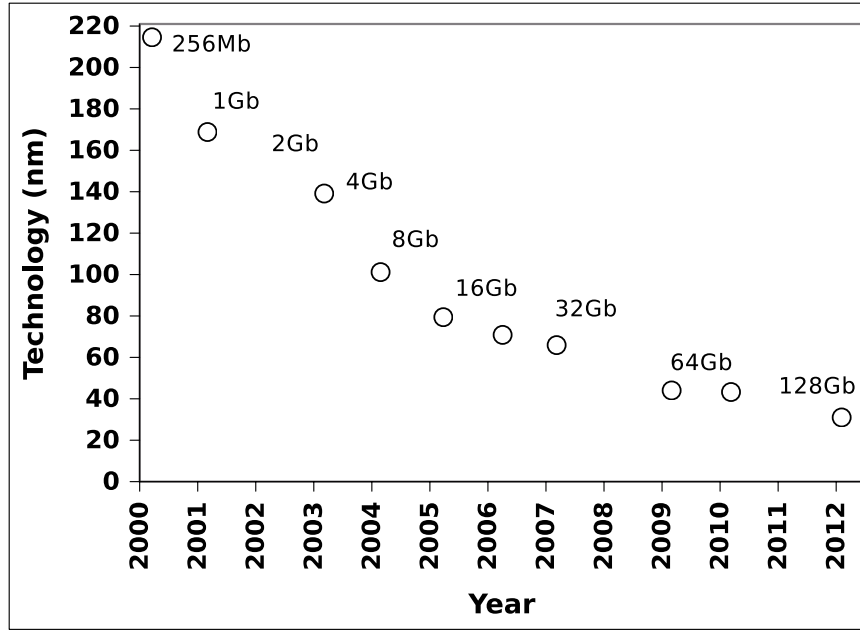


Figure 4.6.: Technology scaling for FLASH memory.

Control-gate with Surrounding Floating-gate (DC-SF) from Whang et al. [225], the Vertical Stacked Array Transistor (VSAT) [100] from Kim et al., the Vertical-gate NAND [102] from Kim et al., and the BiCS [206] structure proposed by Tanaka. One similarity between all three-dimensional structures is the use of a polysilicon active layer and deposited tunnel oxide.

The latest BiCS structure proposed by Katsumata et al. [97] is the Pipe-shaped BiCS (P-BiCS) and is meant to achieve a highly reliable memory film, whose read and write operations are governed by Fowler-Nordheim (FN) tunneling. Figure 4.7 shows a typical P-BiCS structure with only four Si-SiO₂ layers depicted. In order for the cost reduction to be significant, a 16-layer Si-SiO₂ structure is the minimum requirement [148]. The fabrication steps of such a complex structure are surprisingly simple and are described in [97]:

1. Formation of the bottom pipe connection.
2. Deposition of a sacrificial film and subsequent memory hole formation.
3. Deposition of a sacrificial film and subsequent select-gate electrode deposition.
4. Formation of the select-gate hole.
5. Removal of the sacrificial film.
6. Deposition of the memory film,
7. Deposition of the body silicon film.

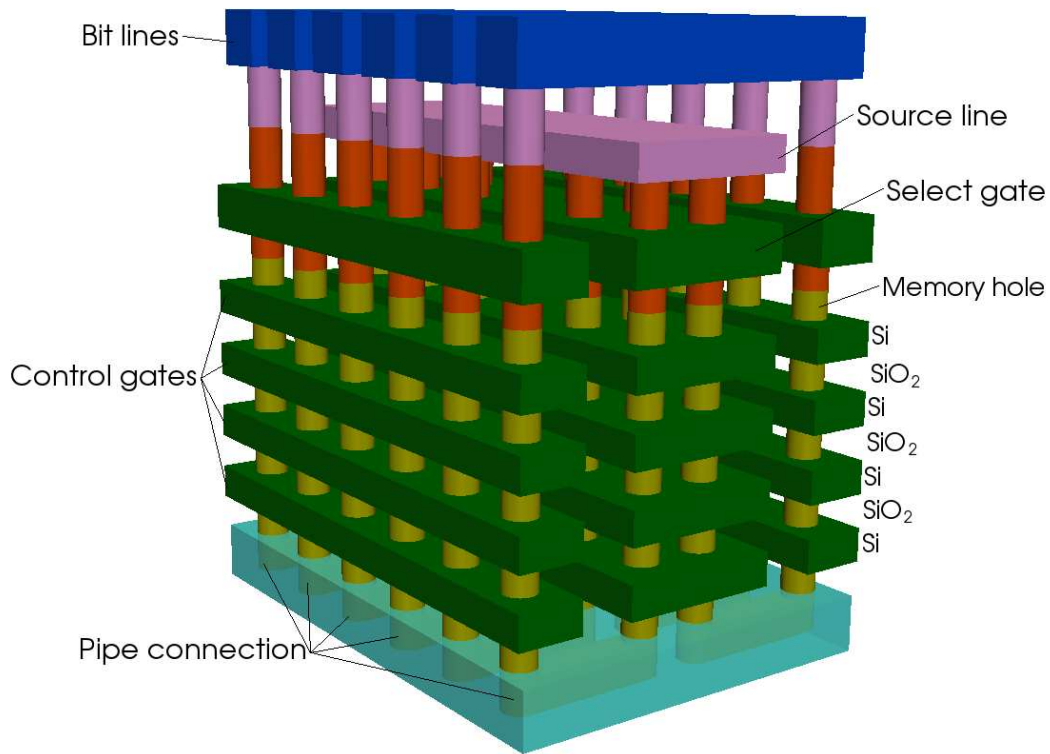


Figure 4.7.: Image of a typical BiCS structure with memory holes.

For etching of the memory hole (Step 2), the entire 16-layered structure consisting of interchanging silicon and silicon dioxide layers must be etched through for a hole approximately 50nm wide. The silicon layers must be etched using an etchant to which silicon dioxide is etch-resistant and vice versa. This way, the silicon layer serves as a mask and etch block during silicon dioxide etching and silicon dioxide serves as a mask and etch block during silicon etching. For the etching of both materials, an anisotropic etch process is preferred with flat, vertical sidewalls. Therefore, wet chemical etching is undesirable since it produces angled sidewalls which are bulk silicon orientation-dependent. Highly selective reactive ion etching could be possible, but the hole depth required and potential damage to the highly-sensitive material surfaces rules out this possibility. The best method appears to be a highly selective and anisotropic ion enhanced plasma etching process.

4.2.2. Etching of Silicon Dioxide

Similar to silicon etching, in order to etch Silicon dioxide, an etchant with high anisotropy is required. A very good wet chemical etchant for silicon dioxide with a high selectivity over silicon is HF (49% in water) [175], however, because the etching is due to a wet chemical process, the memory hole sidewalls would be lost due to the

etchant penetrating laterally into the SiO_2 layer. Some plasma etching processes for SiO_2 involve at least one of fluorine or carbon atom. SF_6 , NF_3 , CF_4/O_2 , and CF_4 are generally isotropic, but can be made more anisotropic with a higher involvement of ion species. Plasma etching of SiO_2 is most commonly performed with the injection of a fluorocarbon gas into the processing chamber, where it is ionized and accelerated to the surface for etching [77]. There are many etchants which are selective over Si and are anisotropic, such as CHF_3/O_2 , C_2F_6 , C_3F_8 , and $\text{C}_5\text{F}_8/\text{CO}/\text{O}_2/\text{Ar}$. High ratios of fluorine atoms versus carbon atoms are important in achieving a high selectivity of SiO_2 over Si. An etchant such as CF_4 gas is a viable option, but the main issue regarding SiO_2 etching with fluorocarbons is the deposition of precursors during the etching process. With CF_4 gas, the main deposition precursor is suggested in [86] to be CF_2 gas and its deposition onto the SiO_2 surface must be considered when modeling the etching process. This deposition effect affects the sidewall angles of the silicon dioxide.

4.2.3. Etching of Silicon

In order to etch the silicon layer, an etchant with high anisotropy is needed. Since the etching holes need to be vertical, the hole sidewalls should be as vertically flat as possible. The majority of silicon etching processes rely on a halogen gas such as fluorine or bromine to be involved in the reaction [77]. SF_6 and CF_4 etchant gases are isotropic or near isotropic, but can be made anisotropic with a selective combination of the amounts of gases used in the etch reaction. A gas with some selectivity over SiO_2 would be preferred, but a high selectivity is not essential, as silicon dioxide must also be etched anisotropically. Very anisotropic etchants of silicon which are non-selective over SiO_2 are CF_4/H_2 and CHF_3 . CF_4/O_2 is more selective over SiO_2 than the previous suggestions, but it is an isotropic process. A process which can be made selective with respect to SiO_2 is a combination of chemical etching with a high ion involvement, such as SF_6/O_2 or $\text{SF}_6/\text{O}_2/\text{HBr}$ plasmas. Since silicon dioxide serves as the top layer or an effective mask when silicon is etched, the tapered sidewalls created during SiO_2 etching must be incorporated into the silicon etching component of the BiCS memory hole etch process.

5. Simulating Deposition and Etch Processes

5.1. Spray Pyrolysis Deposition Modeling

Although much of the spray pyrolysis process is understood, many details regarding the deposition process are still not perfectly clear [222]. Many studies have claimed that the deposition process which occurs is much like a CVD deposition. This means that droplets released from the atomizer would vaporize in the vicinity of the substrate and the chemical would deposit on the substrate as a vapor [32], [157], [216]. Others, however, suggest a thin spreading of the liquid as it contacts the substrate as a more likely deposition method to generate the high quality dense films [172]. The spray pyrolysis mechanism analogous to CVD was suggested by Sears et al. [183]. However, the spreading of the droplets on the substrate was not considered until Perednis [171]. Beckel et al. [9] based their model on the precipitation of the precursor from the droplet before impact, followed by the impact and spreading of the droplet on the heated substrate and subsequent stacking of precipitates. They failed to mention, however, a description of the precursor solution decomposition and the subsequent film evolution. Perednis [171] and Gallage et al. [56] investigated the deposition mechanism as a combination of several processes occurring simultaneously. The full model in [56] includes the precursor atomization, droplet transport towards the heated substrate, the evaporation of the residual solvent, droplet hitting the substrate and spreading, the salt decomposition, and finally the nucleation and growth of oxide particles [222].

However, the [171] model was developed for the growth of YSZ thin films and [56] for the oxidation of Ce^{3+} and Ce^{4+} and both cannot be generalized to the formation of other oxide coatings. Recently, it has been shown that without an electrical force push, the droplets cannot reach the substrate before they vaporize. Therefore, it is suggested that for many pressure atomizers, the droplet will evaporate before reaching the substrate and a CVD-like reaction will occur. However, with an atomizer which provides an additional electrical driving force for the droplets, they are more likely to hit the substrate and deposit a thin film as the droplet spreads on the surface. The attempts to model the electrostatic spray deposition (ESD) spray pyrolysis process by Perednis [171] and the air blast atomization spray pyrolysis process from AIT [64] are described in this section.

In order to model the spray pyrolysis process in the LS environment, the MC method is employed to distribute particles which accelerate to the surface.

5.1.1. Modeling Droplet Atomization

The atomizing nozzle from a spray pyrolysis process can be simulated using random number distributions for the generated size of the droplet, the initial droplet velocity, and the droplet direction as it leaves the atomizer. The radius of a droplet, formed from a liquid which is forced through a thin circular outlet is given by [119]

$$r = \left(\frac{3 r_n \gamma}{2 \rho_d g} \right)^{1/3}, \quad (5.1)$$

where r_n is the outlet radius, ρ_d is the liquid density, and g is the gravitational constant. The variable which can be modified in order to decrease the radius of the droplet is the circular outlet radius. This radius, however, has fabrication limitations so a better method to decrease the droplet radius is to increase the force acting on the liquid as it is passing through the outlet. Equation (5.1) assumes that only gravity is acting towards this goal, but providing an additional “push” can lead to a significant reduction in the size of the droplet. The influence of an additional aerodynamic drag force is summarized with the critical Weber number:

$$W_{crit} = \frac{2 \rho_a v_{rel}^2 r}{\gamma}, \quad (5.2)$$

where ρ_a is the air gas density, v_{rel} is the relative velocity. The critical Weber number has a value of 22 for a free falling droplet and 13 for a droplet which is suddenly exposed to a high velocity. Therefore, a sudden increase in a droplet’s velocity v_{rel} is counter-acted with a decrease in the droplet radius r . The large droplets are broken up into much smaller components, useful for spray pyrolysis. This additional force is provided using air pressure in the case of a PSD system, and an electric field in the case of an ESD system. The generation of droplets can easily be modeled using the given equations; however, most atomizer manufacturers directly provide the droplet diameter distributions under various pressure conditions. If all information required for (5.1) and (5.2) is known, a model can be implemented to use this information; however, if the atomizer manufacturer’s data is available instead, then the provided information should be used in the atomization model.

The next requirement from the atomizer is the charging of the droplet. Each droplet contains charged particles from the precursor solution which will form the thin film, deposited on the wafer surface. The maximum charge for a droplet is given by the Rayleigh limit (4.6). The average charge over volume for droplets calculated by Larriba-Andaluz and Fernandez de la Mora [118] is shown to be approximately 58% of the Rayleigh limit, regardless of the liquid flow rate. This value is used in the model

to calculate the effects of the electrical force on each droplet as well as the amount of solvent available for the deposition process.

Hendricks [76] measured the droplet diameter d 's relationship with its charge and showed that a relation between $q \propto d^{1.5}$ and $q \propto d^{2.3}$ exists using an electrospray which produces a polydisperse droplet size distribution between $0.1\mu m$ and $10\mu m$. More recently, Wilhelm [228] showed that the relationship for a cone-jet ESD spray is $q \propto d^{1.5}$, while for a multi-jet electrospray system a $q \propto d^{1.82}$ is more appropriate. The presence of charges in a droplet assumes the presence of a solvent ion, which is to deposit on the wafer surface. Therefore, the amount of charge will be the deciding factor in the amount of deposited material each droplet will contribute to the film growth.

5.1.2. Modeling Droplet Transport

Forces acting on the droplet can be used in order to calculate the location where the droplet should reach the surface. This is a challenge because the simulation environment must now be divided into several segments. For an in-depth explanation of the forces involved during the droplet transport, refer to Section 4.1.3. In this section, the modeling of those forces and the droplet movements will be described. The first segment we must treat separately is the thermal zone which is within 10mm of the wafer surface. In this area, the temperature gradient shown in Figure 4.5 is high and the thermal forces play a significant role in the droplet speed as well as size, due to evaporation. In addition, when the electrical force is included, the complexity of the problem is significantly increased.

This section will first examine the droplet's motion with no influence from the electrical force outside of the thermal zone. Subsequently, the electrical force is introduced and its influence on the droplet motion is described. Finally, the thermal zone is covered by the introduction of the thermophoretic force and the idea of droplet evaporation. Figure 5.1 shows how the simulation space is divided in order to accommodate the thermal zone for droplets.

For a more detailed explanation regarding the derivation of the motion equations used in this section, refer to Appendix A.

Droplet transport using gravity and Stokes forces

In order to follow the trajectory of a droplet after leaving the atomizer and under the influence of gravity and the Stokes force, the distance required to reach the thermal zone ($H - t_{th}$), the initial velocity v_0 are the droplet radius r_d are known. The equations for the gravitational force and the Stokes force can be reformulated to equations for acceleration $a(t)$ which govern droplet movement. It is important to note that the vertical motion must be calculated first in order to know how much time t is required

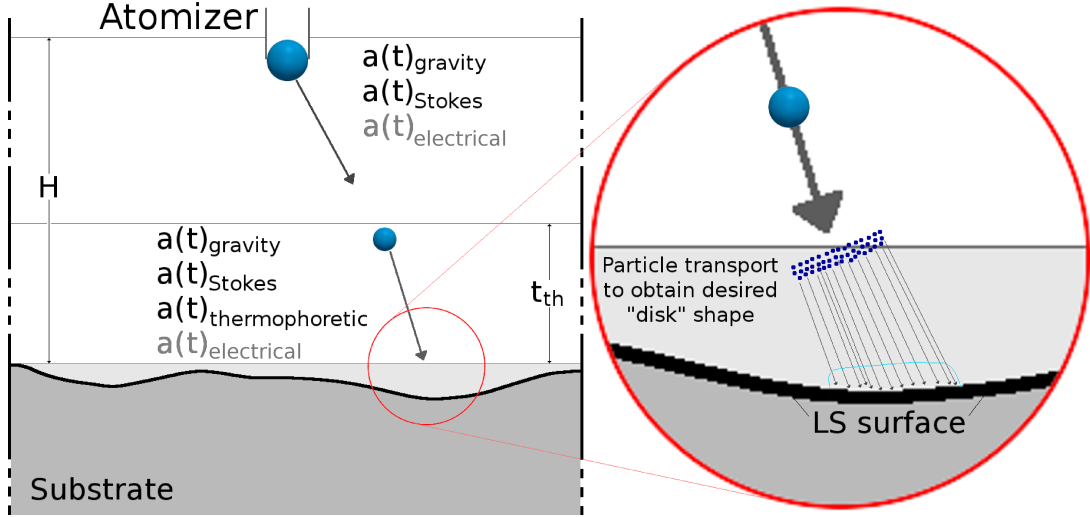


Figure 5.1.: The droplet transport in the space above the substrate surface and the accelerations which are considered in the transport model. T_{th} is the height of the thermal zone ($\sim 10\text{mm}$ for ESD, $\sim 5\text{mm}$ for PSD), and H is the distance between the substrate and atomizer.

to reach the thermal zone. The time t is then used in order to calculate how much radial distance the droplet underwent during its vertical “fall”. For the sake of simplicity, the vertical acceleration, velocity, and distance will be marked with a subscript v , while radial acceleration, velocity, and distance will be marked with a subscript r in the equations that follow.

Vertical trajectory:

Given the droplet mass (4.2), the force of gravity (4.3) and the Stokes force (4.7), the vertical acceleration experienced by the particle is given by:

$$a_v(t) = g - \frac{9\eta_a}{2\rho_d r_d^2} v_v(t), \quad (5.3)$$

where the drag component of the acceleration depends only on velocity and is direction-independent. It is defined as

$$s = \frac{9\eta_a}{2\rho_d r_d^2}. \quad (5.4)$$

(5.3) resembles a first order differential equation which can be solved for the vertical velocity $v_v(t)$ using characteristic equations

$$v_v(t) = \frac{g}{s} (1 - e^{-st}) + v_{v0} e^{-st}, \quad (5.5)$$

where v_{v0} represents the initial vertical velocity. The velocity can now be integrated in order to find an explicit equation for the distance which is the known value $(H - t_{th})$.

$$d_v(t) = \frac{1}{s} \left(\frac{g}{s} - v_{v0} \right) (1 - e^{-st}) + \frac{g}{s} t, \quad (5.6)$$

where it is assumed that $d_{v0} = 0$ and $d_v(t) = (H - t_{th})$, although it is also possible to set up the problem such that $d_{v0} = H$ and $d_v(t_{final}) = t_{th}$. In order to know how far the droplet moved in the radial direction, (5.6) must be inverted, giving the time t

$$t = \frac{gW \left[\frac{(g - s v_{v0}) \cdot e^{1 - \frac{s(v_{v0} + s(H - t_{th}))}{g}}}{g} \right] - g + s v_{v0} + s^2 (H - t_{th})}{g s}, \quad (5.7)$$

where $W[\cdot]$ is the Lambert-W function defined by

$$z = W(z) e^{W(z)}. \quad (5.8)$$

The Lambert-W function is solved iteratively, as described in [215]. Now that the time required to reach the heat zone is known, the radial trajectory can be calculated.

Radial trajectory:

In order to calculate the radial trajectory, the time t , radius r_d , and initial velocity v_{r0} must be known. Those parameters are derived using the vertical trajectory discussion. The force of gravity does not influence the radial movement of the droplet; therefore, only the Stokes force must be considered. The acceleration of the droplet is defined as

$$a_r(t) = -\frac{9\eta_a}{2\rho_d r_d^2} v_r(t) \quad \text{or} \quad a_r(t) = -s v_r(t). \quad (5.9)$$

Similar methods used for the vertical trajectory can be used to solve the radial velocity

$$v_r(t) = v_{r0} e^{-st}, \quad (5.10)$$

and the radial distance

$$d_r(t) = \frac{v_{r0} (1 - e^{-st})}{s}. \quad (5.11)$$

The vertical and radial location as well as the velocity of the droplet is now known as it contacts the thermal zone. The radius remains unchanged, as it was experimentally shown that the droplet radius is largely unaffected outside of the heat zone [171]. The droplet carries information regarding its position, velocity, and radius as it passes to the next step in the model.

Droplet transport inside the heat zone

As the droplet enters the heat zone, it experiences a large temperature gradient resulting from a rapid increase in temperature. This causes the droplet to be exposed to an additional retardant force component, which pushes it away from the hot surface (4.9). This force is assumed to have a uniform behavior throughout the heat zone, making it straightforwardly implemented in the previously-discussed trajectory calculations. The thermophoretic force is independent of the droplet velocity, therefore it causes a reduction of the gravitational force effect. This is performed by replacing g in (5.3) to (5.7) with a value $(g - l)$, where l is the addition of the negative acceleration caused by the thermal gradient

$$(g - l) = g - \frac{27 \eta_a^2 \kappa_a \nabla T}{4 \rho_a \rho_d T (2\kappa_a + \kappa_d) r_d^2}, \quad (5.12)$$

where the temperature T is defined in Kelvin and ∇T in Kelvin/m.

An additional effect which occurs in the heat zone is the significant increase in the mean droplet radius noticed in measurements [171]. The reason behind the increased mean radius is that droplets with a small radius evaporate before reaching the surface, while larger droplets, although also evaporating slightly, stay relatively complete until fully in contact with the surface [171]. Tracking of the detailed changing droplet size during its travel through the heat zone does not modify the model enough to merit the additional computational expense. Therefore, the model automatically excludes droplets which bounce away from the surface due to the thermophoretic force, while other droplets which reach the surface have their radius reduced as they enter the heat zone. The approximate relationship which governs the small droplet's lifetime is given by [81]

$$t_{life} = \frac{4 r_{init}^2}{q_0 \Delta T}, \quad (5.13)$$

where r_{init} is the initial droplet radius, q_0 is an evaporation rate constant, and ΔT is the temperature difference within the droplet. After calculating the time required for a droplet of initial radius r_{init} to traverse through the heat zone, if this time is larger than t_{life} , then the droplet is removed from the simulation, since it will not contribute to the film growth.

The exact solution for the decrease of the radius of a droplet requires the solution of a diffusion equation, since the evaporation of a droplet is given by [81]

$$\frac{dr_d}{dt} = \frac{-M_W D_{v,f}}{r_d \rho_d R T_f} \Delta p \left(1 + 0.276 Re^{1/2} Sc^{1/3} \right), \quad (5.14)$$

where M_W is the molecular weight of the evaporating liquid, $D_{v,f}$ is the average diffusion coefficient for vapor molecules in the saturated film around the droplet at the final temperature T_f , R is the gas constant, Δp is the pressure difference between

the vapor pressure near the drop and the ambient pressure, and Re and Sc are the dimensionless Reynold's and Schmidt's numbers, respectively, given by

$$Re = \frac{2\rho_a v(t) r_d}{\eta_a}, \quad \text{and} \quad Sc = \frac{\eta_a}{\rho_a D_{v,f}}. \quad (5.15)$$

The average diffusion coefficient $D_{v,f}$ is estimated using the Stokes-Einstein relationship

$$D_{v,f} = \frac{RT_f}{N_A} \frac{1}{6\pi \eta_d r_d}, \quad (5.16)$$

where N_A is Avogadro's number. The droplet radius r_d and velocity $v(t)$ are time dependent; therefore, the change in radius through the heat zone can only be solved numerically using a time discretization technique. However, large droplets do not experience significant size reduction through a zone with a non-zero temperature gradient ∇T . Also, it can be assumed that a sedimentation velocity is reached relatively quickly and does not change with time, the diffusion of the droplet can be approximated linearly by

$$K = q_0 \Delta T (1 + 2q_1 r_d), \quad (5.17)$$

where K represents the surface evaporation rate in (m^2/s) with $K = -\frac{dr_d^2}{dt}$, while q_0 and q_1 are given by

$$q_0 = \frac{2a}{\Delta T} (1 + b s_0), \quad q_1 = \frac{b r_0}{1 + b s_0}, \quad (5.18)$$

where r_0 and s_0 are constants given by $r_0 = 64.65s^{-0.5}$ and $s_0 = -1.117 \times 10^{-3}ms^{-0.5}$ and the variables a and b are given by

$$a = \frac{4\gamma M_W D_{v,f} \Delta T}{\rho_d R T_f}, \quad b = 0.276 \left(\frac{\rho_a}{\eta_a D_{v,f}^2} \right)^{1/6}, \quad (5.19)$$

where γ is a constant [81]. With the goal of a topographical simulation in mind, a full detailed analysis for the droplet size, as it changes in the heat zone is not merited. Therefore, in order for (5.13)-(5.19) to be included in the model, some assumptions are made:

1. Droplets with a radius which is too small, giving a small t_{life} will not be taken into account since those droplets will never reach the surface.
2. The droplet radius does not change during its transport through the heat zone for the calculations of the forces acting on the droplet. Rather, it is represented by a single drop in radius, which is calculated following the above discussion.
3. The velocity of the droplet through the heat zone is assumed to be constant in order for the above analysis to be valid and to calculate the size reduction due to thermal effects. The change in velocity from the time when the droplet enters the heat zone until it reaches the surface will, nevertheless, be calculated using the forces at play and the modified droplet size from (5.13)-(5.19).

Droplet transport including the electrical force

When an ESD system is used for spray pyrolysis deposition, an electric field is introduced between the atomizing needle and the metal plate on which the substrate is placed. This electric field provides additional acceleration for the droplets so that they do not need to rely only on the gravitational force, as is the case for PSD systems. The addition of the electrical force to the equations which govern droplet motion is not as straight-forward as was the case with the thermophoretic force, because the electric field which is generated in the experimental region is not uniform [228]. The external electric field is calculated by representing the atomizer as a semi-infinite line of charge and the substrate as an infinite conducting plane, separated by a distance H . The equation governing the external electric field is given by [96]

$$\vec{E}_{ext} = \frac{\Phi_0}{H} \nabla \Phi^*, \quad (5.20)$$

where Φ_0 is the applied electrical potential between the nozzle and the substrate and Φ^* is a normalized potential (Φ/Φ_0), given by

$$\Phi^*(r^*, z^*) = \frac{K_V}{\log(4H/R)} \log \left[\frac{\sqrt{r^{*2} + (1 - z^*)^2} + (1 - z^*)}{\sqrt{r^{*2} + (1 + z^*)^2} + (1 + z^*)} \right], \quad (5.21)$$

where R is the outer radius of the nozzle, K_V is a value which ranges from 0 to 1 depending on the H/R ratio [58], and r^* and z^* are normalized radial and vertical distances, respectively, given by

$$r^* = \frac{d_r(t)}{H} \quad \text{and} \quad z^* = \frac{d_v(t)}{H}. \quad (5.22)$$

For the purposes of spray deposition, it is often assumed that the value of K_V is 1, because the ratio of H/R is on the order of several hundreds, which gives a value close to 1 for K_V . This value is adjusted in the model using the relationship

$$K_V = 1 - e^{-0.021 \frac{H}{R}}. \quad (5.23)$$

In fact, assuming that $K_V = 1$ can cause erroneous results for the electric field. The negative exponential dependence on R from (5.23) is in the numerator of (5.21), which shows an additional inverse logarithmic dependence in the denominator. A plot of the fraction $K_V / [\log(4H/R)]$ for various R values is shown in Figure 5.2, when the variation in K_V is taken into account and when it is assumed that $K_V = 1$. It is clear that the effects of K_V should be included in the droplet transport model.

The individual vertical and radial components of the electric field when taking the gradient of Φ^* from (5.21) can be found

$$\frac{\delta \Phi^*}{\delta z^*} = -\frac{K_V}{\log(4H/R)} \left[\frac{1}{\sqrt{r^{*2} + (1 + z^*)^2}} + \frac{1}{\sqrt{r^{*2} + (1 - z^*)^2}} \right] \quad (5.24)$$

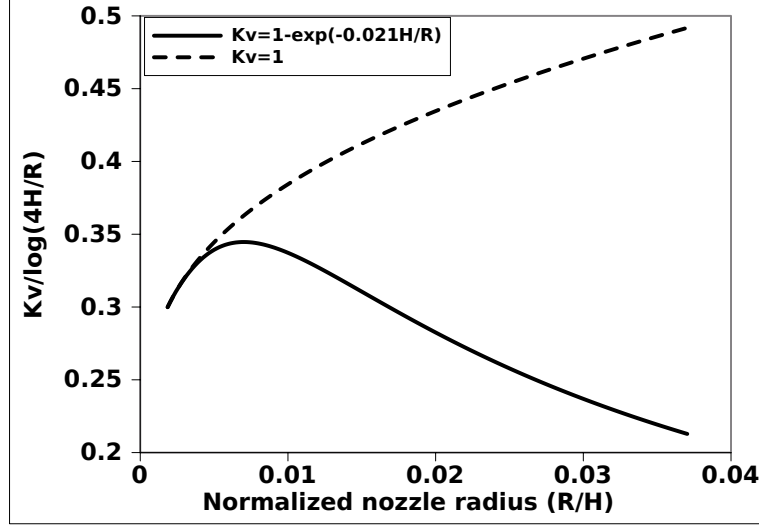


Figure 5.2.: The effects of varying the atomizing nozzle's outer radius on the strength of the electric field with and without the inclusion of the K_V effects.

and

$$\frac{\delta\Phi^*}{\delta r^*} = \frac{K_V}{r^* \log(4H/R)} \left[\frac{1+z^*}{\sqrt{r^{*2} + (1+z^*)^2}} - \frac{1-z^*}{\sqrt{r^{*2} + (1-z^*)^2}} \right]. \quad (5.25)$$

Figure 5.3 shows the value for the normalized potential $\Phi^* = \Phi/\Phi_0$ and its distribution in an ESD deposition setup. The atomizing nozzle is located at $(r^*, z^*) = (0, 1)$. The inset shows the electric field distribution in the same simulation space. It is evident that the strength of the electric field is not uniform or linear, but that the field causes charged droplets to spread radially.

Given the electric field distribution shown in Figure 5.3 (inset), which is dependent on the droplet position, the electrical force (4.4) cannot be implemented to find the vertical displacement using an explicit function in the form (5.6) from the analysis where the droplet is affected only by the gravitational and Stokes forces. The vertical acceleration, when the electric field is considered is no longer (5.3), but it changes to

$$a_v(t) = (g - l) - \frac{9\eta_a}{2\rho_d r_d^2} v_v(t) + \frac{6}{\rho_d} \sqrt{\frac{\gamma \epsilon_0}{r_d^3}} E(d_v(t)). \quad (5.26)$$

In addition, the radial acceleration changes from (5.9) to

$$a_r(t) = -\frac{9\eta_a}{2\rho_d r_d^2} v_r(t) + \frac{6}{\rho_d} \sqrt{\frac{\gamma \epsilon_0}{r_d^3}} E(d_r(t)). \quad (5.27)$$

Simplifying (5.26)-(5.27) with the assumption of a linear dependence of the electrical force on displacement $d(t)$ and dividing by the droplet mass gives the electrical

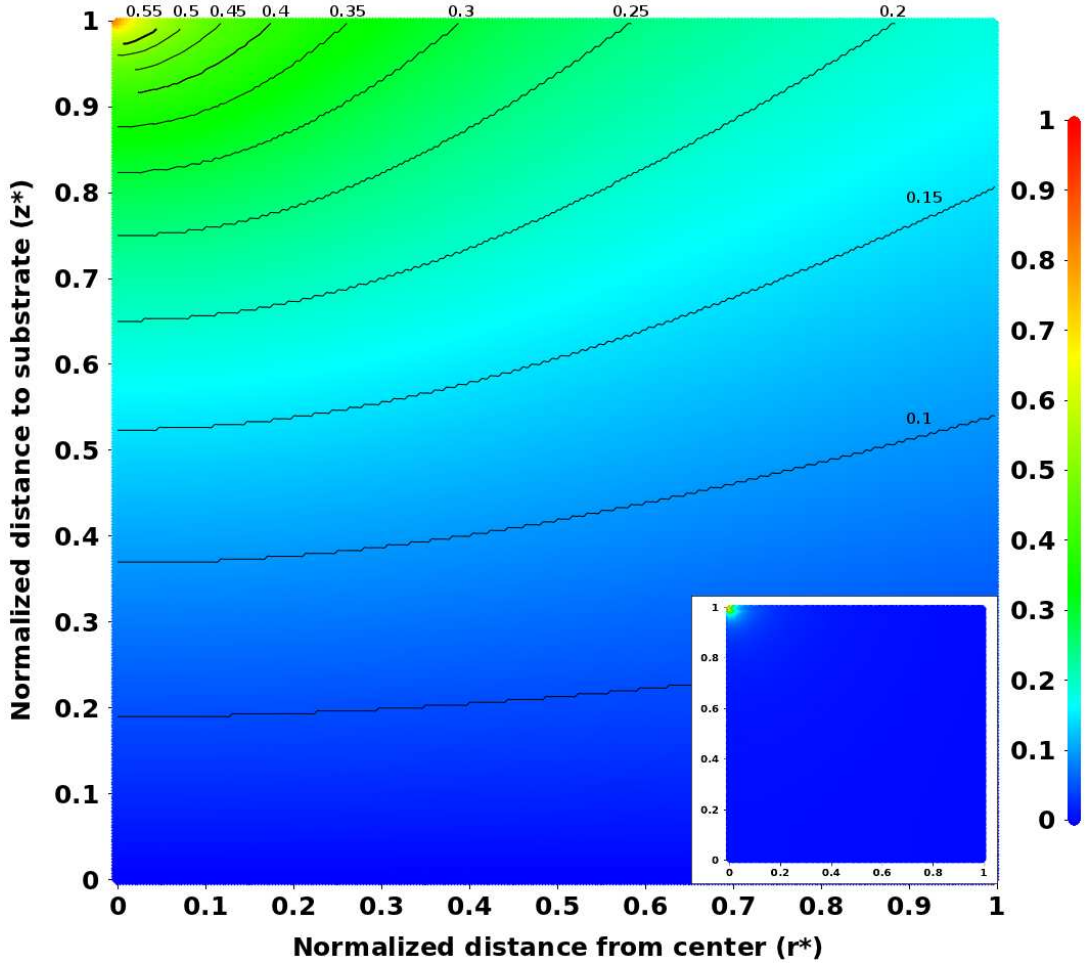


Figure 5.3.: Magnitude of the normalized electric potential Φ/Φ_0 during ESD processing. The distance between needle and deposition plate as well as the radial distance from the center are normalized to the distance between the atomizer and the substrate. The inset is the normalized electric field distribution.

component of the displacement-dependent acceleration

$$c_v = \frac{6}{\rho_d} \sqrt{\frac{\gamma \epsilon_0}{r_d^3}} \cdot \frac{\Phi_0}{H} \cdot \frac{K_V}{\log(4H/R)} c_{ev}, \quad (5.28)$$

where c_{ev} is a vertical linearization constant which is meant to estimate the $[\cdot]$ term in (5.24) with

$$c_{ev} \cdot z^* \approx \left[\frac{1}{r^{*2} + (1 + z^{*2})} + \frac{1}{r^{*2} + (1 - z^{*2})} \right]. \quad (5.29)$$

A similar estimate is made to find the radial linearization constant to estimate the electrical force effect on the droplet's acceleration for (5.25). Realizing that the location

of the droplet depends on the time it travels, the z^* from (5.29) can be viewed as the time-dependent displacement. With this linearization assumption, a system for the vertical acceleration from (5.26) can be re-stated as a combination of the displacement-dependent electrical acceleration term c_v , velocity-dependent Stokes acceleration term s , and the independent gravitational g and thermal l acceleration terms

$$a_v(t) = (g - l) - s v_v(t) + c_v d_v(t). \quad (5.30)$$

Similarly, for the radial acceleration, (5.27) is re-stated as

$$a_r(t) = -s v_r(t) + c_r d_r(t). \quad (5.31)$$

The derivation of a displacement equation, stemming from the acceleration (5.30) is discussed in Section A.2, and the resulting displacement is given by

$$d_v(t) = C_1 e^{-r_1 t} + C_2 e^{-r_2 t} + C_3, \quad (5.32)$$

where

$$r_1 = \frac{-s + \sqrt{s^2 - 4c_v}}{2}, \quad r_2 = \frac{-s - \sqrt{s^2 - 4c_v}}{2}, \quad (5.33)$$

and

$$\begin{aligned} C_1 &= r_1 v_{v0} - \frac{r_1^2 r_2}{r_1 - r_2} \left[(g - l) - v_{v0} \left(\frac{1}{r_1} + s \right) \right] \\ C_2 &= \frac{r_1 r_2^2}{r_1 - r_2} \left[(g - l) - v_{v0} \left(\frac{1}{r_1} + s \right) \right] \\ C_3 &= \frac{c_v}{1 + (g - l) + s} \end{aligned} \quad (5.34)$$

where a similar expression can be found for the radial displacement using v_{r0} and c_r as parameters in (5.33) and (5.34). The electric field is strongest at the nozzle tip, as shown in Figure 5.3. Therefore, the field will be calculated using the given equations once the droplets are generated in order to find the droplet's initial direction and to give it its vertical and radial acceleration. However, a linear approximation for the vertical and radial electrical force will be used afterwards.

An explicit equation for the time required to achieve the displacement (5.32) cannot be found. Therefore, the droplet motion must be solved by time discretization, MC methods, or iteratively in order to obtain the droplet trajectory through the electric field. For the presented topography simulator, an iterative method is used to solve for t with the initial guess t_{init} given by (5.7). Since the introduction of the electric field causes the required time for a droplet to reach the surface t to decrease, the time t with the electrical force included must be $0 < t < t_{init}$. For the purposes of a topography simulation, an assumption for a constant electric field is sufficient [171]. It is also

important to note that the full extent of the radial distance r^* need not be incorporated in the linearization process. When considering the deposition on a chip which extends 1mm radially from a spray source located at a vertical distance of 100mm, this means the radial distance $r^* \leq 0.01$ is of importance. Additional complexity may be introduced unnecessarily into the model leading to increased computational costs. The equations governing the electric field are used in the simplified model in order to determine the initial direction of the droplet. The main effect from the electrical force is seen directly as the droplet exits the nozzle. At this location, the droplet's initial speed and direction is decided.

5.1.3. Modeling Interaction between Droplet and Wafer Surface

There are two main types of depositions which have been examined in the literature and in Section 4.1. One type relies on the droplets being transported very near the surface, where they undergo evaporation and the resulting vapor causes a CVD-like deposition process on the silicon surface. The other type relies on the droplet reaching the surface before it is fully evaporated and sticking on the silicon wafer while simultaneously spreading. The former is commonly the result of a PSD deposition process, while the latter is common for ESD processes, where the droplets are accelerated at much higher speeds and therefore have enough force to overcome the retardant Stokes and thermophoretic forces to reach the substrate as a liquid.

Deposition Model

The model for the deposition of a thin film using a PSD process, which acts as a CVD process is performed by following the flux from the nozzle and its expected trajectory as it reaches the wafer area. At this moment, at the substrate surface a CVD process is modeled, where the flux direction and sticking probability are the model parameters. The thickness of the deposited film depends on the amount of droplets reaching the surface, the deposition time, and the temperature used.

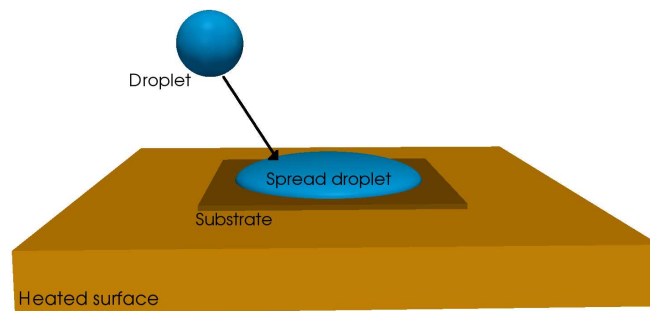


Figure 5.4.: Droplet impact onto a heated surface, resulting in the spreading of a thin film in a disc-like shape.

In order to model the deposition for a porous film, which is deposited as a result of an ESD spray pyrolysis system, each droplet's trajectory is tracked until it reaches the LS surface. At this point, at the location of the droplet's contact, a disc whose size is relative to the droplet's radius is deposited on the surface, shown in Figure 5.4 [171]. The disc is generated using evenly distributed particles which accelerate towards the LS surface and stick to generate the desired pattern.

5.2. Modeling BiCS Memory Hole Etching

In order to etch BiCS memory holes, a sequence of SiO_2 and Si etching is required, as is depicted in the two-dimensional cross section of the memory hole in Figure 5.5. It

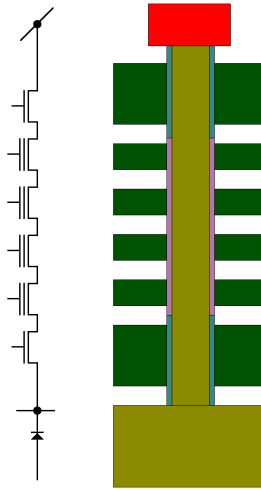


Figure 5.5.: Two-dimensional image of the hole which needs to be etched through layers of Si and SiO_2 in order to generate a BiCS structure.

is important to note that etching deformations in one layer will lead to deformation in the layer below and so on, limiting the total number of layers through which etching is possible. This limits the cost effectiveness of the BiCS memory scheme, as is explained in Section 4.2.1. This section serves to generate etch models in the LS environment for silicon and silicon dioxide, which then must be joined in order to etch the complete memory hole.

5.2.1. Carbon Fluorides for Silicon Dioxide Etching

When modeling the plasma etching of silicon dioxide, it is important to include microloading phenomena which cause tapered vertical walls on the etched SiO_2 profile [151]. The tapering is caused by a polymer depositing on the well walls during the etching process. For example, when SiO_2 is etched using CF_4 gas, the CF_4 gas

undergoes a gas phase reaction, where it breaks into CF_2 gas and F atoms. The CF_2 gas then undergoes a surface deposition reaction with the SiO_2 . In order to simulate this phenomenon in the presented LS framework, a model from [113] is implemented. It deals with an etching process with a simple chemistry such as a pure CF_2 etch of SiO_2 under Ar^+ bombardment and polymer inhibition. The model parameters and constants which are implemented here can be found in [113].

The model suggests three surface coverages, one for the etchant $\Theta_e(\vec{x})$, one for the polymer $\Theta_p(\vec{x})$, and one for the active sites on the polymer coverage $\Theta_{e/p}(\vec{x})$. The coverages are found using

$$\begin{aligned}\frac{d\Theta_e(\vec{x})}{dt} &= s_e F_e(\vec{x}) [1 - \Theta_e(\vec{x}) - \Theta_p(\vec{x})] - k_{ei}^e F_i(\vec{x}) Y_{ei}^e(\vec{x}) \Theta_e - k_{ev} F_{ev}(\vec{x}) \Theta_e(\vec{x}), \\ \frac{d\Theta_p(\vec{x})}{dt} &= s_p F_p(\vec{x}) - F_i(\vec{x}) Y_{ei}^p(\vec{x}) \Theta_p(\vec{x}) \Theta_{e/p}(\vec{x}) = 0, \\ \frac{d\Theta_{e/p}(\vec{x})}{dt} &= s_{e/p} F_e(\vec{x}) (1 - \Theta_{e/p}(\vec{x})) - F_i(\vec{x}) Y_{ei}^p(\vec{x}) \Theta_{e/p}(\vec{x}),\end{aligned}\tag{5.35}$$

where $F_i(\vec{x})$, $F_e(\vec{x})$, and $F_p(\vec{x})$ are the total fluxes of the ion, etchant, and polymer, respectively and $F_{ev}(\vec{x})$ is an evaporation flux which is proportional to $F_e(\vec{x})$ and temperature dependent. The constants s_e , s_p , and $s_{e/p}$ are the sticking coefficients of the etchant on SiO_2 , polymer on SiO_2 , and etchant on the deposited polymer, respectively. $Y_{ei}^e(\vec{x})$ and $Y_{ei}^p(\vec{x})$ are etching yield functions.

Assuming steady state conditions, (5.35) can be used to find the surface coverages for each particle species

$$\begin{aligned}\Theta_{e/p}(\vec{x}) &= \frac{s_{e/p} F_e(\vec{x})}{s_{e/p} F_e(\vec{x}) + F_i(\vec{x}) Y_{ei}^p(\vec{x})}, \\ \Theta_p(\vec{x}) &= \frac{s_p F_p(\vec{x})}{F_i(\vec{x}) Y_{ei}^p(\vec{x}) \Theta_{e/p}}, \\ \Theta_e(\vec{x}) &= \frac{s_e F_e(\vec{x}) (1 - \Theta_p(\vec{x}))}{s_e F_e + k_{ei} F_i(\vec{x}) Y_{ei}^e(\vec{x}) + k_{ev} F_{ev}}.\end{aligned}\tag{5.36}$$

The deposition rate of the polymer gas onto the wafer surface is given by the polymer flux and the sticking coefficient

$$DR_p(\vec{x}) = \frac{1}{\rho_p} s_p F_p(\vec{x}),\tag{5.37}$$

where ρ_p is the polymer bulk density. The polymer can also be etched and this rate is given by the chemical sputtering rate

$$ER_p(\vec{x}) = \frac{1}{\rho_p} F_i(\vec{x}) Y_{ei}^p(\vec{x}) \Theta_{e/p}(\vec{x}). \quad (5.38)$$

If the polymer deposition rate is higher than its etch rate, then no etching on the surface occurs, but rather a deposition whose rate is given by

$$V_{SiO_2}(\vec{x}) = DR_p(\vec{x}) - ER_p(\vec{x}). \quad (5.39)$$

However, if the polymer deposition rate is lower than its etch rate, the film etching rate is given by

$$V_{SiO_2}(\vec{x}) = -\frac{1}{\rho_{SiO_2}} [F_i(\vec{x}) Y_{ie}^e(\vec{x}) \Theta_e(\vec{x}) + F_i(\vec{x}) Y_s(\vec{x}) (1 - \Theta_e(\vec{x})) + F_{ev} \Theta_e(\vec{x})], \quad (5.40)$$

where ρ_{SiO_2} is the SiO_2 bulk density and $Y_s(\vec{x})$ accounts for the sputter yield of the silicon dioxide which is not covered by the etchant.

The threshold yield functions depend on the ion energies and the impact direction of the ions onto the surface. In the case of physical sputtering, the yield is given by

$$Y_s(\vec{x}) = A_{sp}^e \left(\sqrt{E} - \sqrt{E_{th,sp}} \right) (1 + B_{sp} \sin^2(\theta)) \cos(\theta), \quad (5.41)$$

where θ is the impact angle, $E_{th,sp}$ is the sputtering threshold energy, E is the ion impact energy, and A_{sp} is a sputtering yield factor. For ion enhanced chemical etching, the yield function is given by

$$Y_i(\vec{x}) = A_{ei}^{e/p} \left(\sqrt{E} - \sqrt{E_{th}^{e/p}} \right) \cos(\theta), \quad (5.42)$$

where $E_{th}^{e/p}$ is the threshold energy and $A_{ei}^{e/p}$ the etchant yield factor for ion enhanced chemical etching.

Figure 5.6 shows a simulation of the silicon dioxide etching process when various ion, etchant, and polymer fluxes are used. It is clear that the ratio of etchant to polymer flux will decide how much polymer will be present on the sidewalls. Therefore, as the amount of polymer is decreased with respect to the amount of etchant, shown from Figure 5.6a to 5.6c, the sidewalls show an increasing vertical profile and higher etch rates. The simulation is performed through a 300nm diameter hole with an ideal mask for 80s. The profile is shown at 2s intervals. This means that when etching the silicon dioxide layers for BiCS memory holes, an etchant should be used which produces less deposition-inducing byproducts. When using C_4F_8 , which was the etching process described in [113], the ratio of etchant to polymer inhibitor flux is shown to be 2.5:1.

$$\begin{array}{c|c|c}
 F_i = 5.6 \times 10^{16} s^{-1} cm^{-1} & F_i = 5.6 \times 10^{16} s^{-1} cm^{-1} & F_i = 5.6 \times 10^{16} s^{-1} cm^{-1} \\
 F_e = 1.0 \times 10^{17} s^{-1} cm^{-1} & F_e = 3.0 \times 10^{17} s^{-1} cm^{-1} & F_e = 3.0 \times 10^{17} s^{-1} cm^{-1} \\
 F_p = 1.0 \times 10^{17} s^{-1} cm^{-1} & F_p = 1.0 \times 10^{17} s^{-1} cm^{-1} & F_p = 3.0 \times 10^{16} s^{-1} cm^{-1}
 \end{array}$$

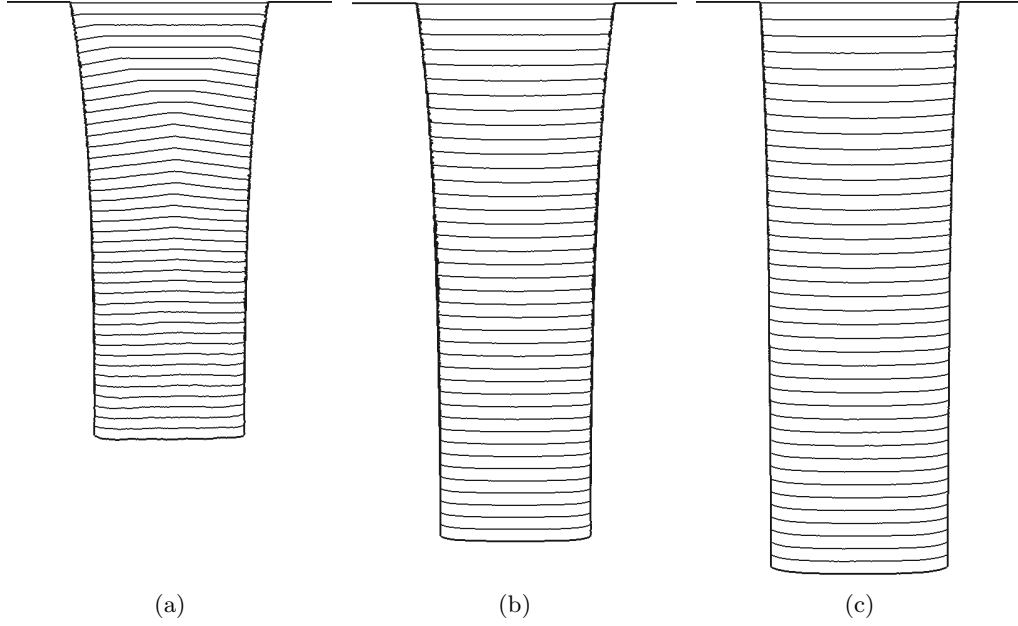


Figure 5.6.: Images showing the etched SiO₂ topography when using a fluorocarbon gas as the etchant, implemented using the described model.

The ratio of etchant to polymer flux is not the only process parameter governing the final etched profile. Another important factor is the sticking coefficient of the inhibitor species. The process described by the model in [113] suggests a sticking probability of 0.26. However, it would be beneficial for a process with a lower sticking probability to be used when sharp vertical etch profiles are required. In [86] a process using CF₄ is suggested for SiO₂ etching for BiCS memory holes, which has the deposition precursor CF₂ with a 0.0292 sticking probability. Figure 5.7 shows how varying the sticking probability influences the etched profile when the flux of ion, etchant, and polymer species are $F_i = 5.6 \times 10^{16} s^{-1} cm^{-1}$, $F_e = 2.5 \times 10^{17} s^{-1} cm^{-1}$, and $F_p = 1.0 \times 10^{17} s^{-1} cm^{-1}$, respectively. The simulations were performed through a 50nm opening, which is the approximate width required for etching BiCS memory holes, for 5s which should be sufficient for the required depth (~ 33 nm).

5.2.2. Halogen Gas for Silicon Etching

When etching silicon, HBr plasma is chosen due to its high selectability against SiO₂, when compared to fluorocarbon based plasmas. When analyzing silicon etching under HBr plasma, the etch rate is assumed to only have the ion enhanced component,

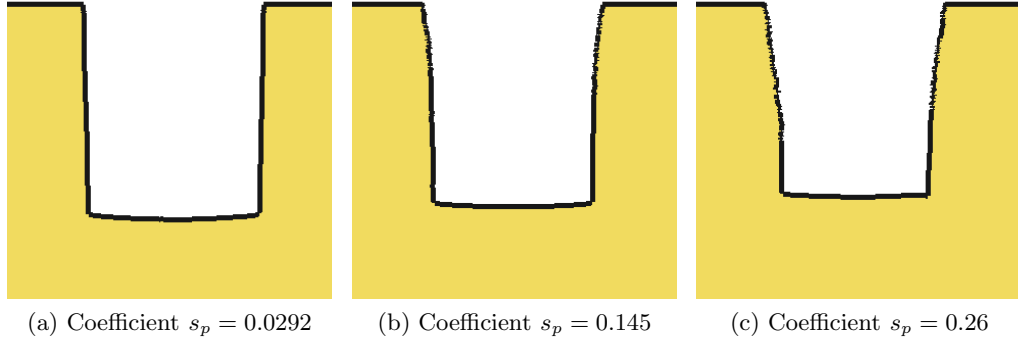


Figure 5.7.: Images showing the etched SiO₂ topography when using fluorocarbon gas as the etchant for various polymer sticking coefficients s_p .

because the neutral component is negligible. Several experiments noted that under neutral-flux-only conditions no etching of silicon is observed with an HBr plasma [11], [33], [217]. However, the LS framework can handle a model similar to the SF₆ silicon etching model suggested in [10] and implemented in the LS in [50] to be created for HBr/O₂ silicon etching. The corresponding balance equations can be written as

$$\begin{aligned} \sigma_{Si} \frac{d\Theta_{Br}}{dt}(\vec{x}) &= s_{Br} F_{Br}(\vec{x}) [1 - \Theta_{Br}(\vec{x}) - \Theta_O(\vec{x})] - k_{Br} \sigma_{Si} \Theta_{Br}(\vec{x}) - 2\Theta_{Br}(\vec{x}) Y_{ie}^{tot}(\vec{x}) \\ \sigma_{Si} \frac{d\Theta_O}{dt}(\vec{x}) &= s_O F_O(\vec{x}) [1 - \Theta_{Br}(\vec{x}) - \Theta_O(\vec{x})] - \beta \sigma_{Si} \Theta_O(\vec{x}) - 2\Theta_O(\vec{x}) Y_O^{tot}(\vec{x}), \end{aligned} \quad (5.43)$$

where σ_{Si} is the surface density of silicon, $s_{Br/O}$ is the sticking probability of bromine or oxygen on silicon, $(1 - \Theta_{Br}(\vec{x}) - \Theta_O(\vec{x}))$ is the fraction of free surface sites, $F_{Br/O}(\vec{x})$ are the total bromine or oxygen fluxes, k is the bromine chemical etch rate constant, β is the oxygen chemical etch rate constant, $Y_{ie}^{tot}(\vec{x})$ is the total ion-enhanced etch rate, $Y_O^{tot}(\vec{x})$ is the total oxygen sputter rate, and Θ_{Br} and Θ_O refer to the total surface kinetic coverage of bromine and oxygen, respectively. The surface velocity is given by the total etch rate, as

$$V(\vec{x}) = -\frac{1}{\rho_{Si}} \left(\frac{k_{Br} \Theta_{Br}(\vec{x})}{3} + Y_{ph}^{tot}(\vec{x}) + \Theta_{Br}(\vec{x}) Y_{ie}^{tot}(\vec{x}) \right), \quad (5.44)$$

where ρ_{Si} is the silicon bulk density.

This model uses bromine properties from [11] in order to generate the topography of the etched silicon profile shown in Figure 5.8. The simulations use the following fluxes during the etching process: $F_{Br}=1 \times 10^{18} \text{s}^{-1} \text{cm}^{-1}$, $F_O=3 \times 10^{17} \text{s}^{-1} \text{cm}^{-1}$, and $F_{ion}=1 \times 10^{16} \text{s}^{-1} \text{cm}^{-1}$.

The SiO₂ mask opening is set to 70nm while etching continued for 410s, as was performed in [86]. The simulation was performed in order to analyze the effects on the

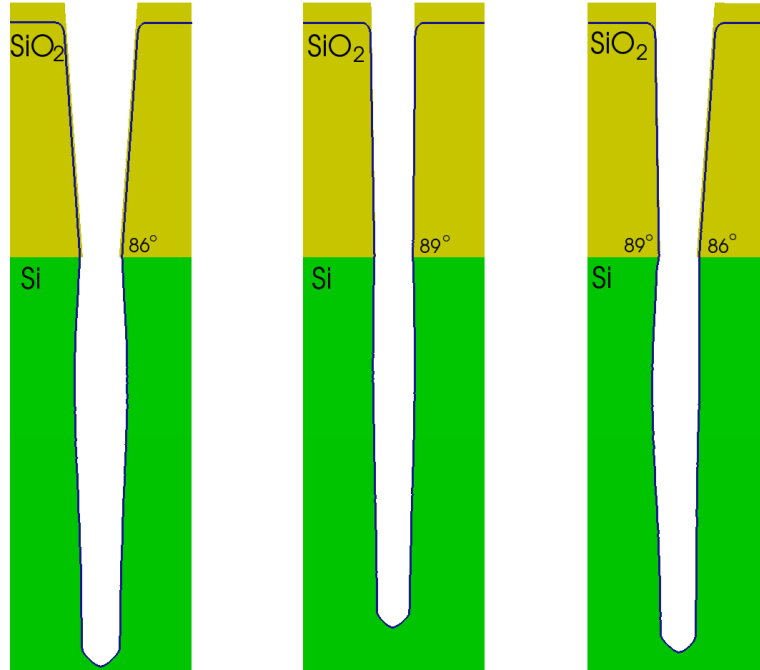


Figure 5.8.: The effects of SiO₂ tapered angles during silicon etching using a HBr/O₂ plasma.

etching process, when the silicon dioxide layer has tapered walls. As can be seen, when the SiO₂ is angled at 89°, a relatively flat vertical sidewall is seen in the silicon. However, even a slight tapering, shown at 86°, results in a silicon etched sidewall topography with an additional erosion width. These simulations confirm the experimental and simulated results from [86].

6. Applications

In this chapter the previously described processing techniques are simulated in the LS environment. The models implemented are described in Chapter 5. This chapter also addresses how the various processing techniques can be utilized in order to fabricate modern devices. The main technologies which will be considered are silicon oxidation, AFM nanolithography, spray pyrolysis deposition, and the etching of BiCS memory holes.

6.1. Silicon Oxidation

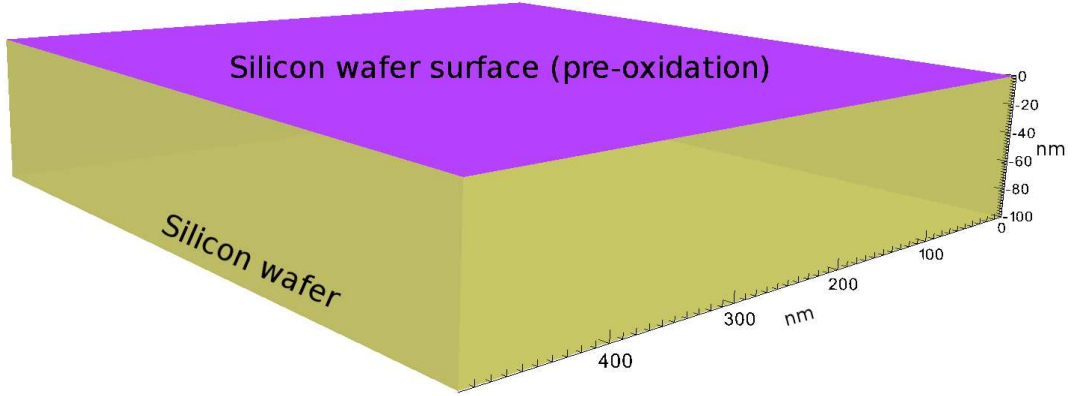
The oxidation of silicon has been described in detail in Chapter 2. Some interesting examples for the oxidation of silicon using Deal-Grove and Massoud models based on linear parabolic equations are shown here.

6.1.1. Oxide Growth without Native Oxide

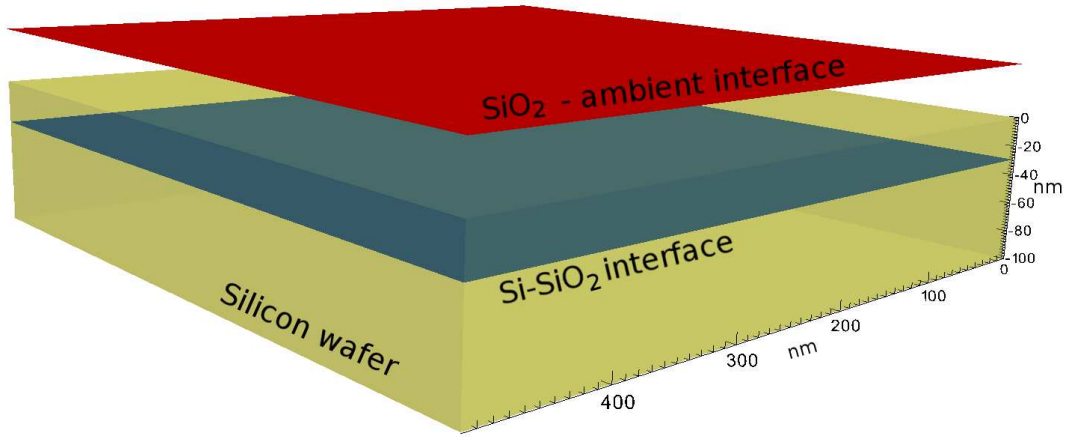
When no native oxide is present, a flat interface representing a Si-ambient interface is grown into SiO_2 with a thickness dependent on the oxidation time, temperature, ambient (wet- H_2O or dry- O_2), pressure, and the crystal orientation of the underlying silicon. The modifications and requirements of the LS method to include oxidation are presented in Section 3.2.1.

When no native oxide is present, the oxidation process begins with $x_o = 0$, as shown in Figure 6.1a, where the surfaces representing the Si- SiO_2 interface and SiO_2 -ambient interface are overlapping. As the oxidation process begins, the Si- SiO_2 interface goes deeper into the initial Si wafer, while the SiO_2 -ambient interface moves towards the ambient.

Using the Massoud model, after 100 minutes of oxidation of a (100) oriented silicon wafer in a dry ambient at 1atm pressure and 1000°C temperature, an oxide with a thickness of 66.5nm is grown, depicted in Figure 6.1.



(a) Initial state of the processing environment before oxidation.



(b) State of the processing environment after oxidation.

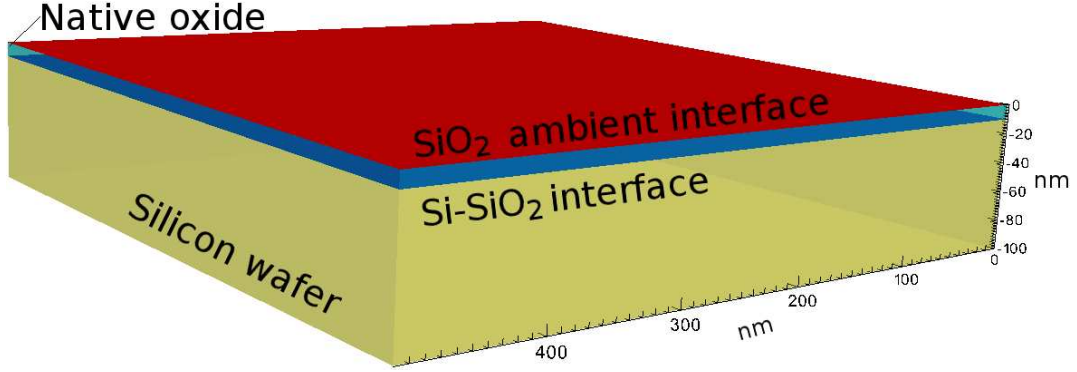
Figure 6.1.: Results of the oxidation of (100) oriented silicon in a dry ambient at 1atm pressure and 1000°C temperature for 100 minutes. The top surface (red) depicts the SiO_2 -ambient interface, while the lower surface (blue) depicts the location of the Si-SiO₂ interface. The volume shown is the original location of the silicon substrate.

6.1.2. Oxide Growth with Native Oxide Present

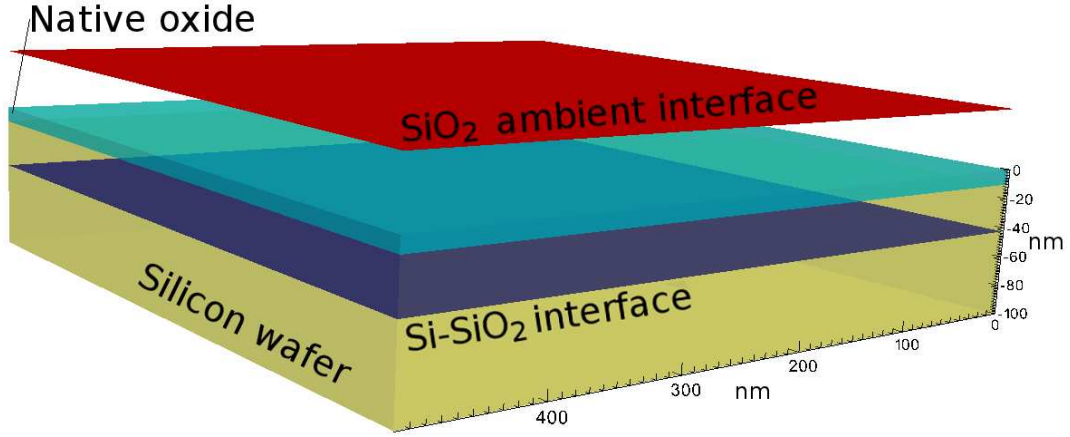
When some native oxide is present, both interfaces, Si-SiO₂ and SiO₂-ambient already exist and the oxide does not need to grow from scratch. How much additional oxide will grow depends on the oxidation time, temperature, ambient, pressure, crystal orientation of the silicon, as well as the thickness of native oxide already present on the surface. The implementation of such velocity fields within the LS is described in Section 3.2.1, while the Massoud model is used to determine the oxidation rate.

When 10nm of native oxide is present, the oxidation process begins with $x_o = 10\text{nm}$, as shown in Figure 6.2a, where the surface representing the Si-SiO₂ is the bottom

(blue) surface, the SiO_2 -ambient interface is the top (red) surface and the volumes depicted are of the silicon substrate (yellow-bottom) and the native oxide (blue-top). As the process begins, the Si- SiO_2 interface moves deeper into the Si wafer, while the SiO_2 -ambient interface grows towards the ambient.



(a) Initial state of the processing environment before oxidation.



(b) State of the processing environment after oxidation.

Figure 6.2.: Results of the oxidation of (100) oriented silicon in a dry ambient at 1atm pressure and 1000°C temperature for 100 minutes with 10nm of native oxide present. The top surface (red) depicts the SiO_2 -ambient interface, while the lower surface (blue) depicts the location of the Si- SiO_2 interface. The volumes shown are the original location of the silicon substrate and the native oxide.

Using the Massoud model, after 100 minutes of oxidation of a (100) oriented silicon wafer in a dry ambient at 1atm pressure and 1000°C temperature, a total oxide thickness of 73.8nm is found, meaning that 63.8nm of new oxide has been grown, depicted in Figure 6.2b. Even though the oxidation conditions were identical to the process shown in Figure 6.1, less oxide is grown, when there is already some initial oxide present. This is expected since oxidation is fastest during the initial stages of oxidation.

6.1.3. Oxidation with Orientation effects

The rate of silicon oxidation depends in part to the orientation of the silicon crystals, as previously discussed in Section 2.2.1 and Section 2.3. Orientation effects can be observed, when oxidizing a trench in a (100) silicon surface. A thicker oxide is expected on the sidewalls since their orientation is (110). This effect is implemented in the presented LS model framework.

The effects of silicon orientation are visible in Figure 6.3 where the (110) sidewalls are seen as having a thickness greater than that of the (100) surfaces. The corners also experience pinching due to the amorphous nature of the oxidant diffusion through the oxide.

6.1.4. Oxidation with LOCOS

When performing LOCOS steps for thermal oxidation growth, a bird's beak effect is commonplace. As the oxide grows, the nitride mask, which is meant to block the oxide from growing everywhere, is slightly bent due to stress caused by the oxide pushing the nitride as it grows.

The geometry of the bird's beak, depicted in Figure 6.4 depends on several physical factors [190]:

The thickness of the nitride mask plays an important role in determining the size of the LOCOS bird's beak. From a simple physical point of view, the force required to lift up a beam by a certain distance is proportional to the third power of the beam thickness. Even though the oxidation mechanism is more complex, the basic concept can still be applied. It is evident that thicker nitride layers are less prone to bending due to their increased stiffness, which leads to a shorter bird's beak.

The thickness of the pad oxide also has an influence on the length of the bird's beak, but does not seem to affect the height in a meaningful way. The effects of the nitride and pad oxide thicknesses on the bird's beak geometry, when 600nm of oxide is grown thermally at 1000°C in a vapor environment, is shown in Figure 6.5. Based on this data, a topographical simulation can be performed, as shown in Figure 6.6.

The length of the birds beak depends on the silicon crystal orientation, mainly due to the difference in the amount of silicon available for bonding at the (111) surface compared to the (100) surface. The ratio of L_{bb} to the oxide thickness decreases as the field oxide thickness increases until L_{bb} reaches a saturation length.

When thermal oxidation is performed at high temperatures, less nitride lifting, and therefore a shorter and lower bird's beak is seen. This is due to the increased oxidation rate compared to the diffusion rate. Since the diffusion of oxidant

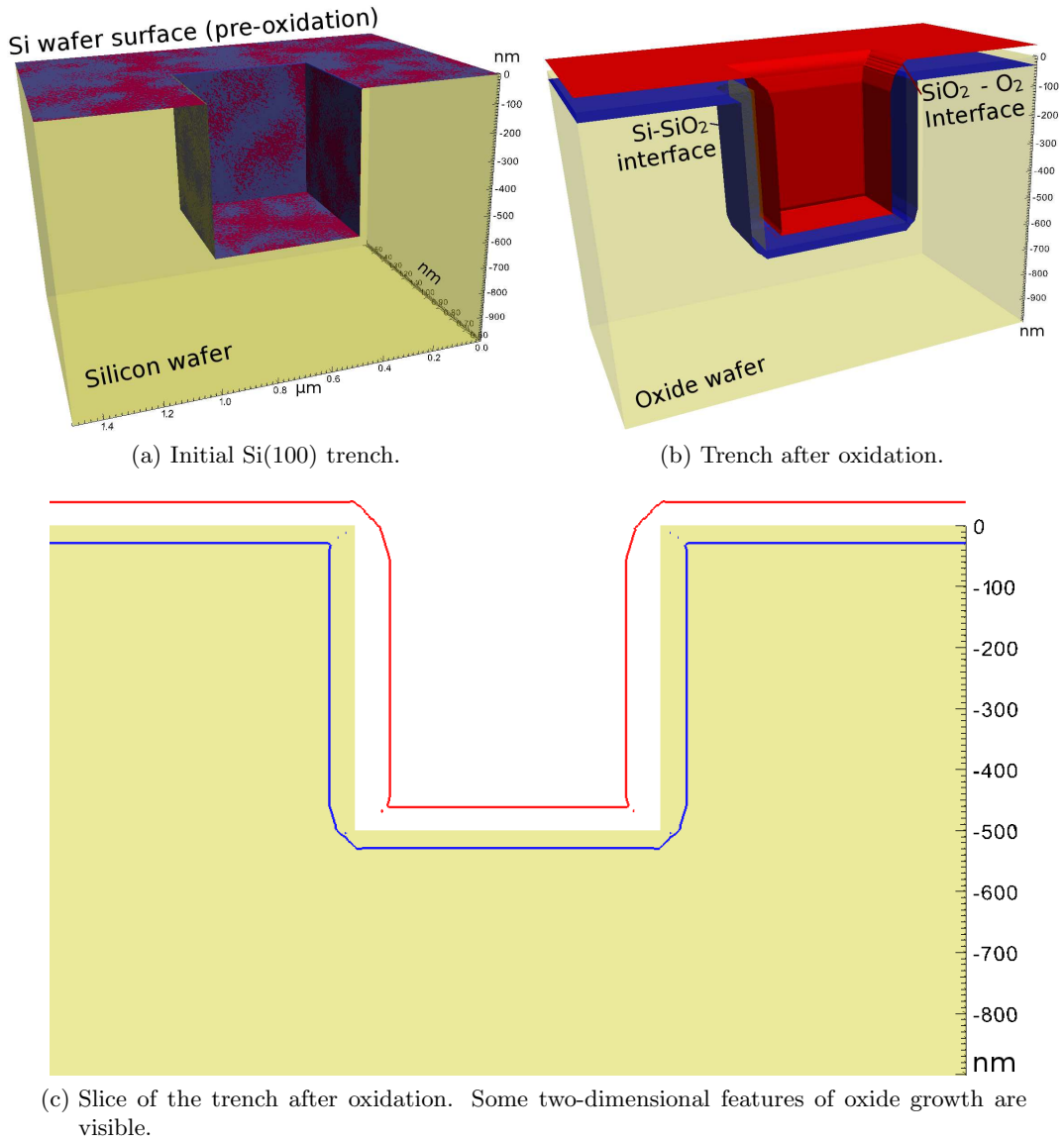


Figure 6.3.: Results of the oxidation of a trench etched into (100) oriented silicon with (110) oriented sidewalls. in a dry ambient at 1atm pressure and 1000°C temperature for 100 minutes. The top surface (red) depicts the SiO_2 -ambient interface, while the lower surface (blue) depicts the location of the Si-SiO₂ interface. The volumes shown is the original location of the silicon trench.

under the nitride layer is the main reason for the bird's beak phenomenon, less diffusion exposure results in decreased bird's beak effects.

Figure 6.6 depicts a topographical simulation of a nitride mask lifting as thermal oxidation progresses. The geometry of the lifting nitride is taken from the results in

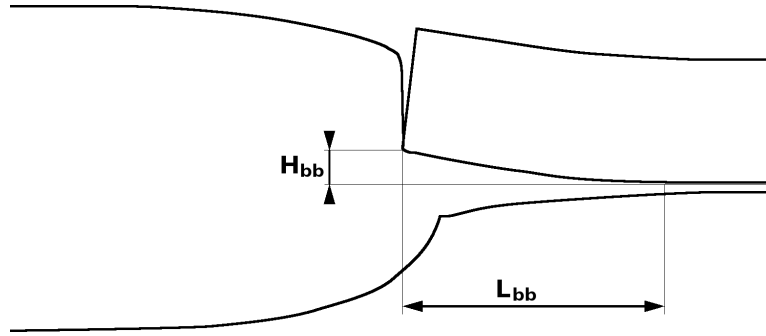


Figure 6.4.: Geometry of the bird's beak occurrence during LOCOS processing. H_{bb} and L_{bb} describe the maximum height and length of the nitride after oxidation, respectively.

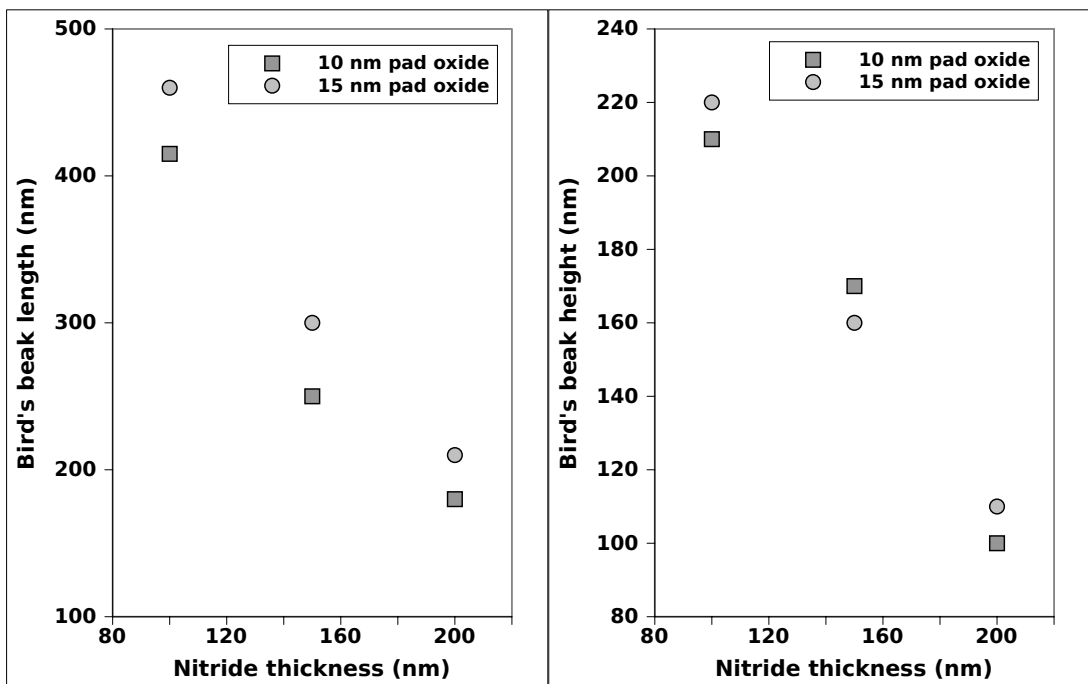


Figure 6.5.: Bird's beak length and height dependences on nitride and pad oxide thicknesses from [190]. The field oxide is simulated to grow at 1000°C for a thickness of approximately 600nm.

Figure 6.5 for a 200nm nitride mask layer and a 15nm of pad oxide. The topography moves as a results of silicon oxidation at 1000°C for 2 hours, resulting in an expected oxide thickness of approximately 600nm.

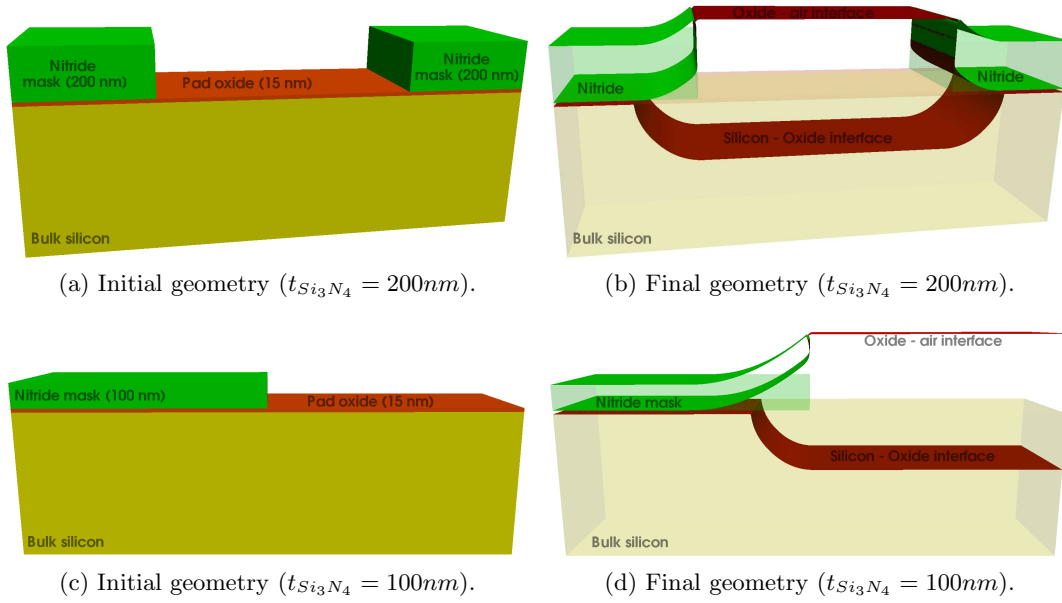


Figure 6.6.: Thermal oxidation with the bird's beak effect. The field oxide is simulated to grow on (100) silicon at 1000°C in a wet environment for 2 hours, resulting in a field oxide thickness of approximately 600nm. The oxide thickness is 15nm and the nitride thickness is (a)-(b) 200nm and (c)-(d) 100nm.

6.2. Nitric Acid Oxidation

Section 3.3.1 explains the NAOS model and suggests that the main use for this processing technology is for the manufacture of TFTs for liquid crystal displays (LCDs). For this technology, the oxide must grow evenly across polycrystalline or doped silicon, which is possible with NAOS and is the main reason for the continuing interest in this technology [111], [112], [147]. Using the azeotropic NAOS model, after four hours of immersion in a 61wt% HNO_3 concentration of a (100) oriented silicon wafer at 60°C temperature, an oxide with a thickness of 1.18nm is grown, depicted in Figure 6.7.

6.3. Atomic Force Microscope Lithography

AFM nanolithography is an emerging processing technique which can be utilized for many different applications. As mentioned in Chapter 5, a MC technique is combined with the LS method in order to simulate nanodots and nanowires with a topography which follows nanodots and nanowires generated with an AFM on a silicon surface. In this section, the AFM lithography technique will be utilized to generate nanodots and nanowires under various ambient conditions. The application of nanodots to generate

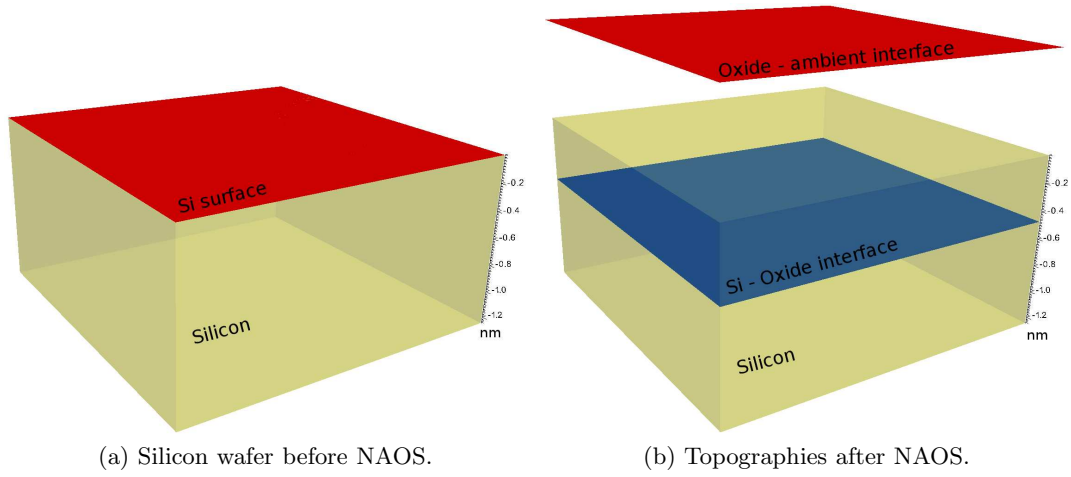


Figure 6.7.: Results of the oxidation of (100) oriented silicon during immersion in a 61wt% HNO_3 concentration at a temperature of 60°C . The top surface (red) depicts the SiO_2 -ambient interface, while the lower surface (blue) depicts the location of the Si- SiO_2 interface. The volume shown is the original location of the silicon substrate.

read only memory (ROM) dots will also be shown, in addition to the generation of nanowires in order to design a junctionless transistor.

6.3.1. AFM Nanodot Generation

As described in Chapter 4, LON with an AFM is becoming an increasingly applicable tool for manufacturing nanosized devices. At the core of the nanolithographic potential of AFM is the generation of a SiO_2 nanodot on a silicon surface. AFM allows for a nanodot to be applied on a silicon surface with nanosized precision of the location and size. As discussed in Chapter 5, the ambient factors which influence the nanodot size are the pulse time, ambient humidity, and the potential difference between the AFM needle tip and the silicon substrate. The AFM nanodots shown in Figure 6.8, Figure 6.9, and Figure 6.10 are generated using the described model from [28] with added humidity effects and the two-dimensional SCD distribution described in Chapter 5. In the figures, the top topography represents the surface between the silicon dioxide and the air/water ambient, while the bottom topography represents the interface between silicon dioxide and silicon. The heights of all nanodots have been scaled by 20 with respect to the widths for improved visualization. The results confirm the experimental results gathered from [28] and [53], on which the models are based.

Figure 6.8 shows the distribution of nanodot sizes caused by a variation of pulse times. The voltage and humidity were kept constant at 20V and 55%, respectively, while the time was set to 0.2ms, 0.3ms, 0.5ms, and 1ms. With increasing pulse times, the

nanodot height and width also increase, as expected. The height varied from 1.24nm to 2.05nm, while the FWHM varied from 15nm to approximately 50nm with pulse times set to 0.2ms and 1ms, respectively.

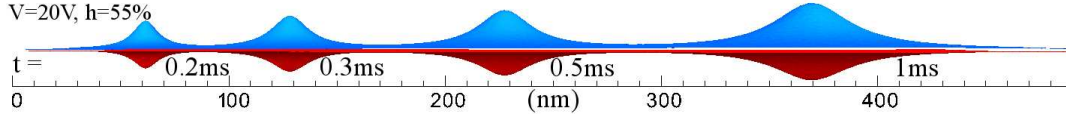


Figure 6.8.: Effects of pulse time on the AFM nanodot height and width. The vertical axis is scaled by 20 for better visualization.

Figure 6.9 shows the distribution of nanodot sizes caused by a variation of the ambient humidity. The pulse time and applied voltage were kept constant at 0.2ms and 20V respectively, while the humidity was set to 30%, 50%, 70%, and 90%. With an increasing ambient humidity, the nanodot height and width also increase, as expected. The height varied from 0.65nm to 2.07nm, while FWHM varied from 10.6nm to approximately 34nm with the ambient humidity set to 30% and 90%, respectively. In addition, a cross-section of the nanodots is shown, where the nanodot heights are more evident.

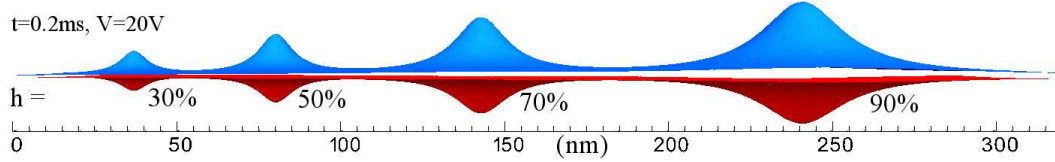


Figure 6.9.: Effects of ambient humidity on the AFM nanodot height and width. The vertical axis is scaled by 20 for better visualization.

Figure 6.10 shows the distribution of nanodot sizes caused by a variation of the applied voltage. The pulse time and humidity were kept constant at 0.2ms and 55%, respectively, while the voltage was varied at 16V, 18V, 20V, and 22V. With an increasing applied voltage, the nanodot height and width also increase, as expected. The height varied from 0.51nm to 1.58nm, while FWHM varied from 10nm to approximately 18nm with the applied voltage set to 16V and 22V, respectively.

6.3.2. AFM Nanowire Generation

In [28] it is suggested that a nanowire, which is patterned using a combination of AFM nanodots, separated at 0.5nm intervals will have an increased half-width due to the increased time for the lateral diffusion of anions. This phenomenon was added to the simulator and a nanodot was generated in the LS simulator to mimic the one presented in [28], as is shown in Figure 6.11. As in [28], generating nanodots with 20V pulses for 1ms, while displacing the tip laterally by 0.5nm resulted in a nanowire with a height of approximately 1nm and a half-width of 13nm.

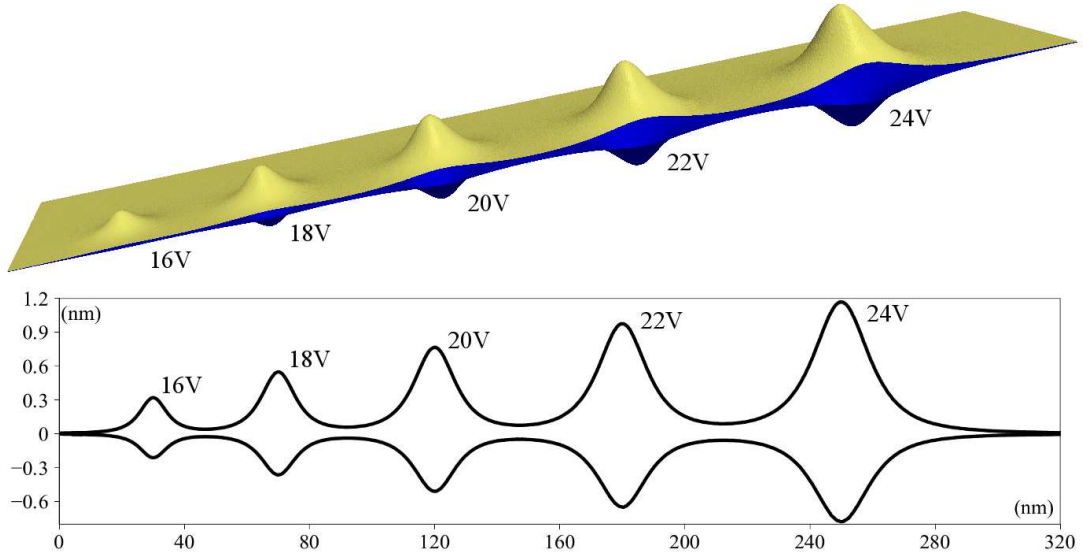


Figure 6.10.: Effects of bias voltage on the AFM nanodot height and width. The vertical axis is scaled by 20 for better visualization.

Instead of generating nanowires as a series of nanodots, an approach using empirical equations which govern nanodot height and half-width under various conditions, from [53] was implemented in the simulator, as described in Chapter 5. This type of simulation is much quicker as it allows for a nanowire to be treated in a single simulation step as opposed to thousands of single nanodot generation steps. The nanowires also exhibit a shape based on the SCD distribution. Figure 6.12b shows simulated nanowires alongside the experimental sample from [53] in Figure 6.12a, at bias voltages ranging from 6V to 10V, with a 5ms pulse time and 72% humidity.

6.3.3. High Density Data Storage using AFM

Already in 1999, Cooper et al. [36] showed that by anodically oxidizing titanium with the AFM, an aerial density of 1.6Tbits/in² can be reached. In the same year, Namin et al. [158] used the atomic force microscope in order to manufacture high density data storage. The main idea behind the technique is generating nanodots in a pattern such that the presence of a nanostructure (nanodot) is read as a bitwise 1 while the lack of a nanostructure is read as a bitwise 0. The increase in the sharpness of the AFM needle tip down to approximately 10nm allowed for very high densities to be imprinted on silicon surfaces. Namin [158] achieved an areal density of 65Gbit/in² with readback rates larger than 10Mbit/s. More recently, storage densities of up to 3.3Tbits/in² have been reported [71]. For several years, the efficiency of this method was questioned due to the speed with which nanodots can be written with a single cantilever. However, many research groups are working on AFM nanopatterning using arrays of AFM nee-

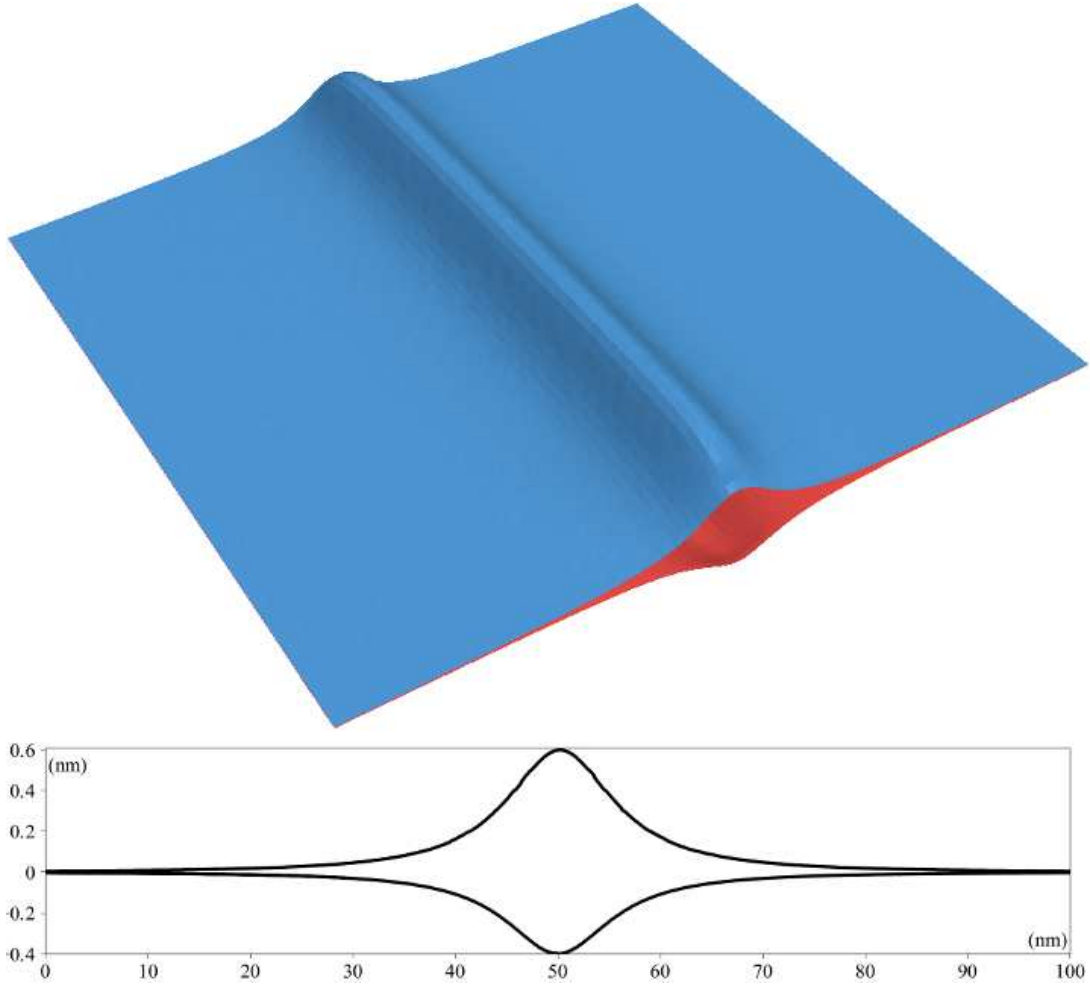
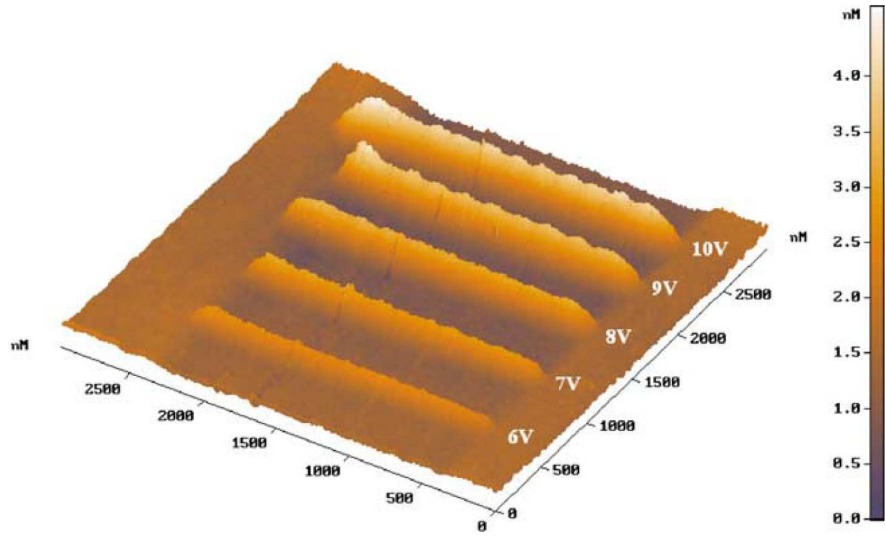


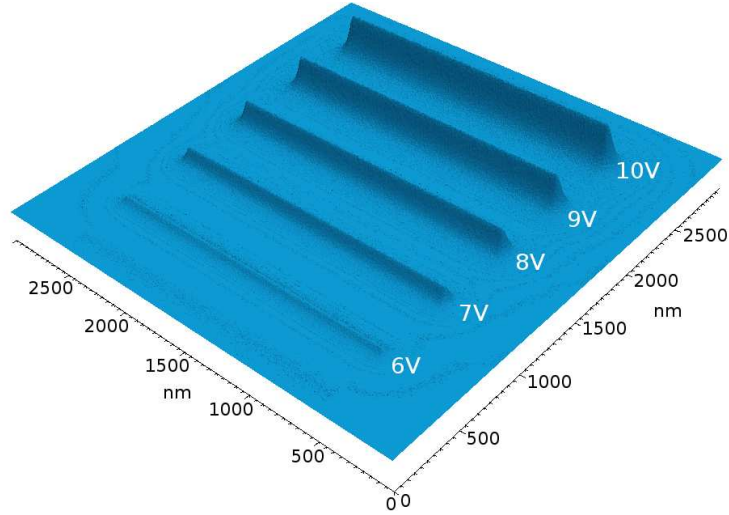
Figure 6.11.: Nanowire topography simulated using a sequence of AFM nanodots (top) and the nanowire's cross-section (bottom).

dles, which could simultaneously generate multiple nanodots for a desired memory dot pattern [82], [207], [233], [235]. IBM has also developed a nanopatterning array, which spans 32×32 AFM cantilevers per pattern application [44], [167]. In 2004, Garcia [59] presented an imprinted image of π , with 20-decimal place precision, written in binary code with oxide (SiO_x) nanodots on a silicon surface, as shown in Figure 6.13a. Using the models presented in Chapter 5, the pattern depicted is reproduced using a non-contact AFM needle with a bias voltage of 24V, ambient humidity of 80%, and a pulse time of 0.16ms. Each oxide dot has a width and a height of approximately 25nm and 2.5nm, respectively, as in the original experiment from Garcia, depicted in Figure 6.13b.

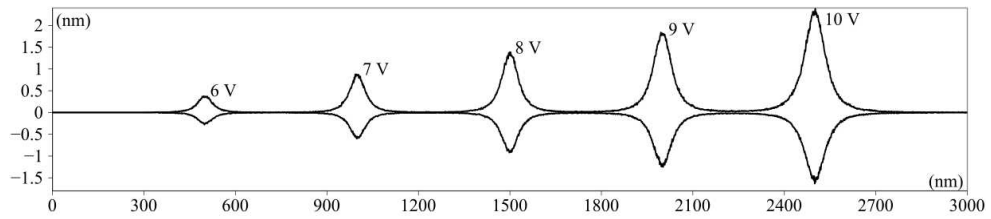
Using the models from Chapter 5 and assuming that the minimum readable height for the nanodots is 1nm, a higher aerial resolution can be achieved, when a pulse time of



(a) Effects on nanowire topography with varying bias voltages, ranging from 6V to 10, with a 5ms pulse time and 72% humidity: Experimental results from [53].



(b) Effects on nanowire topography with varying bias voltages, ranging from 6V to 10, with a 5ms pulse time and 72% humidity: Simulated results.



(c) Cross-section of the nanowires from Figure 6.12b.

Figure 6.12.: Simulations of AFM-generated nanowires.

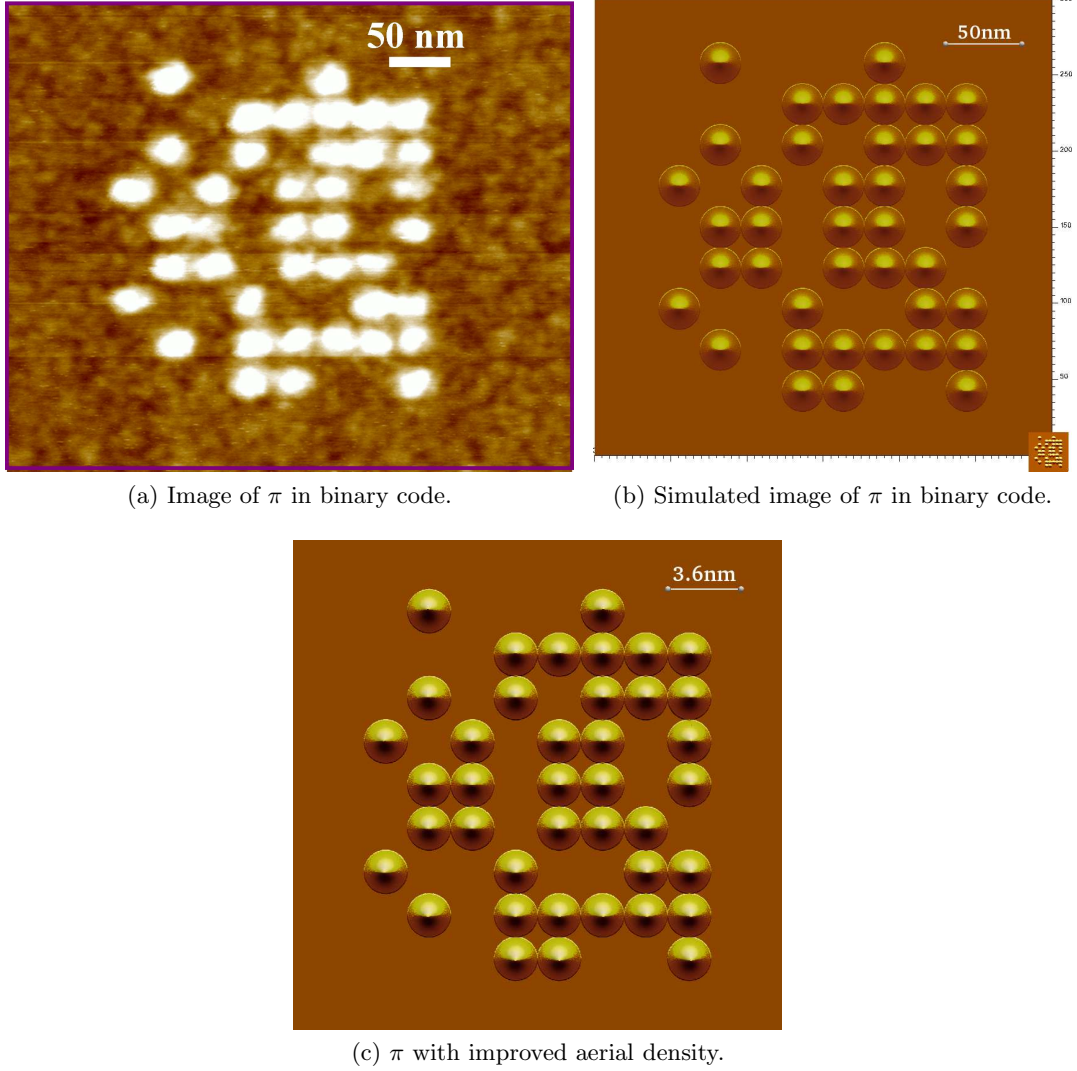


Figure 6.13.: Simulations of AFM-generated nanodots for ROM applications. (a) Image of π in binary code, written with oxide nanodots on a silicon surface from [59]. (b) Simulated image of π in binary code, repeating the experiment from [59], with inset of a proportional Figure 6.13c. (c) Simulated image of π in binary code, with improved aerial density.

0.1ms is used with an ambient humidity of 50% and an AFM needle bias voltage of 22V. This simulation results in nanodots which have an approximate height and width of 1nm and 2.1nm, respectively. The simulation results are shown in Figure 6.13c, where the improved nanodot density is evident.

6.3.4. Silicon Nanowire Transistor

All modern transistors have a gate electrode, which controls the flow of holes and electrons between the source and drain contacts. In CMOS transistors, this modulation relies on the presence of a junction between the channel and the source and drain contacts. With the decreasing dimensions of modern transistors, generating these junctions is becoming increasingly difficult [92]. The first patented field effect transistor, suggested by Julius Edgar Lilienfeld [127], [128] in the 1920's was a junction-free device. The device was designed such that charge carriers could be depleted by the actions of the gate. However, in order to be able to fully turn off the device, a very thin nanoscale channel (nanowire) is required. The technology for generating such thin structures did not exist until recently [92]. In fact, the first junctionless transistor was manufactured in 2010 by Colinge et al. [35]. Using standard Silicon on Insulator (SOI) technology and electron-beam lithography, they were able to produce the first junctionless transistor. Since then, it has been shown that AFM nanolithography processes could also be used in order to generate the nanowire required to connect the source and drain sides of the transistor [43], [117]. This process can be performed at room temperature and with minimal damage to the crystalline structure of silicon, which is commonly introduced due to the highly energetic electrons which are an integral part of electron beam lithography [93], [117]. A type of junctionless transistor, the Silicon Nanowire Transistor (SiNWT), fabricated by Hutagalung using non-contact AFM nanolithography is described in [85]. The generated SiNWT, after AFM nanolithography and selective wet etching, is shown in Figure 6.14.

The simulation process, which follows the fabrication process from [85] is shown in Figure 6.15. The yellow (top) surface represents the silicon dioxide (SiO_2) mask layer, the red (second) surface represents the top of the silicon surface, while the green (third) and dark blue (fourth) surfaces represent the top and bottom of the buried oxide (SiO_2) within the silicon on insulator (SOI) wafer. The light blue (bottom) surface depicts the bottom of the wafer, such that the volume between the two blue surfaces is the silicon wafer. The first step is the generation of the oxide mask layer, shown in Figure 6.15a, followed by the application of the silicon nanowire using an AFM in NCM in Figure 6.15b. Subsequently, TetraMethylAmmonium Hydroxide (TMAH) is used in order to selectively and anisotropically etch away the silicon, shown in Figure 6.15c. TMAH is a wet etching process which has an approximate 1:1000 etch ratio for SiO_2 with respect to silicon. The final step is the removal of the silicon dioxide, which is done once again using wet etching, but with hydrofluoric acid (HF). This acid selectively etches silicon dioxide, leaving behind the desired nanowire pattern on the SOI wafer

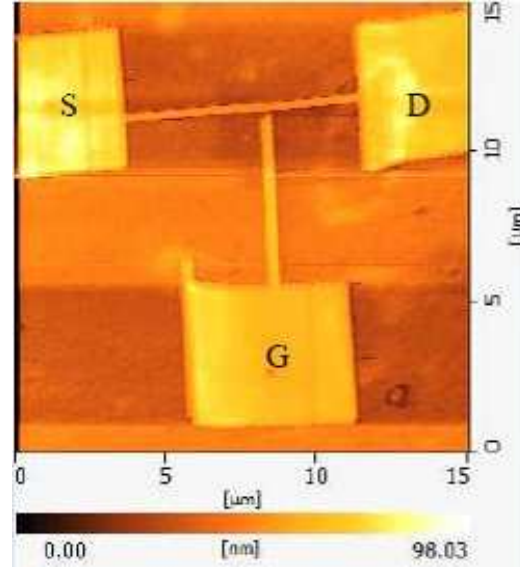


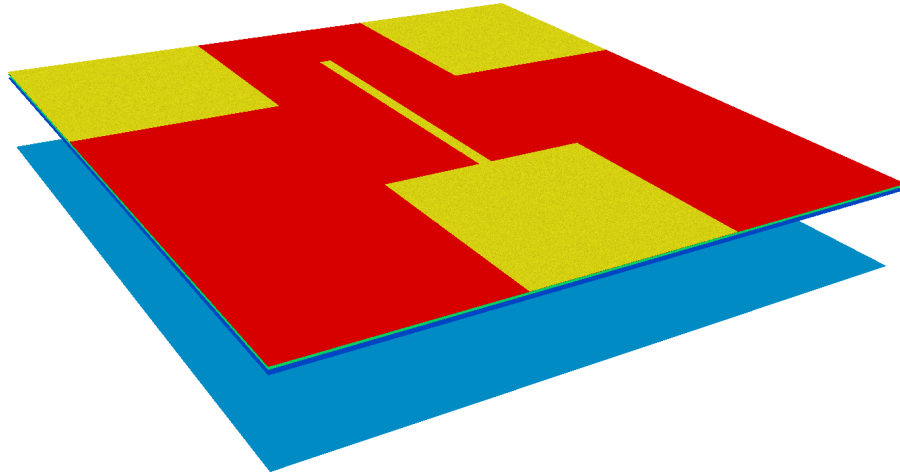
Figure 6.14.: SiNWT generated using AFM nanolithography and wet etching [85].

as shown in Figure 6.15d. The AFM lithography simulation for the nanowire assumed a pulse time of 0.25ms and a bias voltage of 16V in a 55% humidity ambient. The final nanowire has an approximate width of 100nm, such as suggested in [85].

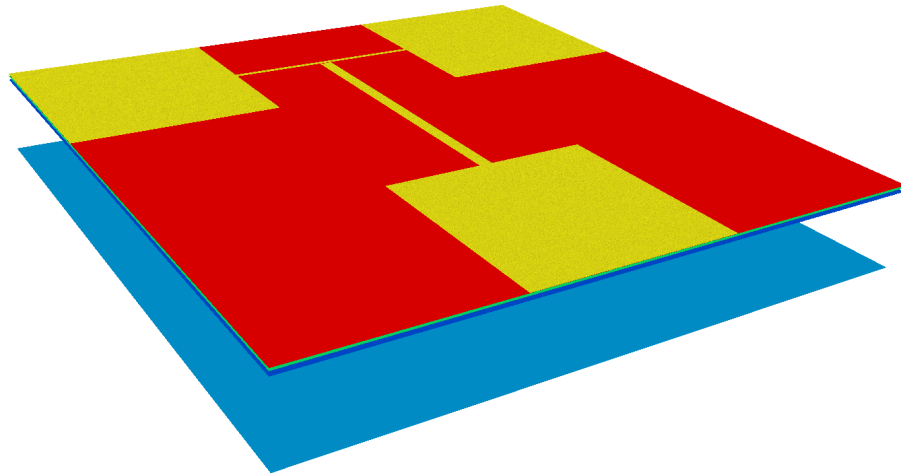
6.4. Spray Pyrolysis Deposition

The exact deposition process for spray pyrolysis is not yet known. As explained in Chapter 5, there are suggestions that the process follows a CVD-like deposition as liquid droplets approach the surface and fully convert to their vapor form due to heating. However, others suggest that the process is more a liquid layer-by-layer thin film deposition. Two different topography simulations are performed. The first simulation uses ethanol-based droplets with a YSZ precursor which is atomized using an ESD system and appears to deposit on the silicon substrate as a liquid film. The second simulation uses a water solution with a SnO_2 precursor, atomized with an air blast atomizer which appears to deposit on the silicon substrate in the form of a CVD process.

It is likely that the deposition of the liquid film using an ESD system [171] is due to relatively large particles being atomized and transported with two push forces, gravity and the electric force, towards the silicon surface. Many droplets still have most of their volume in tact as they reach the thermal zone, allowing them to come in contact with the heated silicon in order to deposit a thin disk-shaped film. The velocity of particles which reach the thermal zone in an ESD system is also shown to be higher than those using a PSD system, due to the additional electric force. Therefore, the

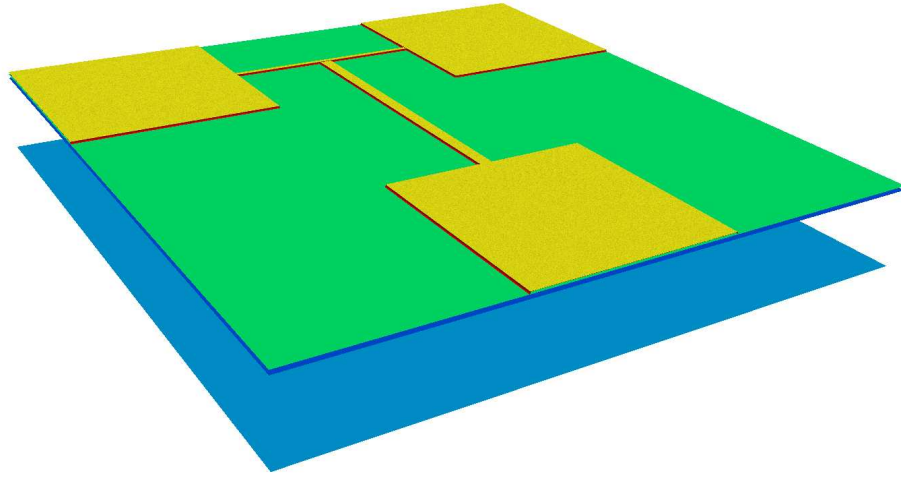


(a) Initial lithography.

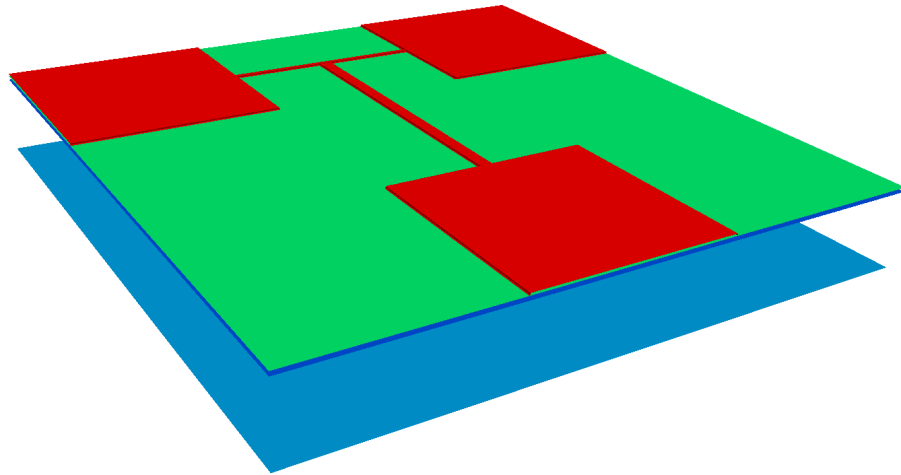


(b) Nanowire generated using AFM.

Figure 6.15.: (a)-(b) Topography simulation steps for the fabrication process for a silicon nanowire transistor. (a) Initial lithography to place oxide as a mask for source, drain, and gate contacts. (b) Nanowire generated using AFM to connect the source and drain contacts.



(c) TMAH etching of silicon.



(d) HF etching of SiO₂.

Figure 6.15.: (c)-(d) Topography simulation steps for the fabrication process for a silicon nanowire transistor. (c) TMAH etching of silicon, with SiO₂ serving as a mask. (d) HF etching of SiO₂, leaving the desired pattern on the silicon surface.

introduction of the retardant thermophoretic force is not enough to significantly slow down and evaporate the large particles present.

However, the PSD process appears to deposit in the form of a CVD-like system [64]. There are two explanations why this setup does not appear to generate a liquid thin film deposition. The first is the lack of additional pushing force to deliver unevaporated droplets to the silicon surface, meaning they rely solely on the force of gravity and the initial velocity to bring them to the surface. As will be shown, the retardant Stokes force is much stronger than the force of gravity, making the droplet quickly reach a relatively slow terminal velocity. As the droplet reaches the thermal zone, an additional retardant force causes it to slow down even further, making it spend a long time in a hot environment and subsequently evaporate. An additional explanation for the CVD-like deposition is the atomizer setup used. The atomized droplets have a relatively low size, a mean radius of $2.5\mu m$, which is much smaller than the ESD system from [171]. Table 6.1 shows the relative parameters for the solutions and droplet used in the simulations for both the ESD system (ethanol and YSZ) and the PSD system (water and SnO_2).

6.4.1. YSZ Deposition using ESD Pyrolysis

The YSZ deposition using an ESD process from [171] is simulated using the model discussed in Section 5.1. The parameters of the solution used and therefore, the properties of the droplets which are simulated are listed in Table 6.1. The first step is finding the droplet size as they exit the atomizer. The distribution of droplet sizes does not follow any standard distribution, but it is suggested that the volume fraction varies relatively evenly near the approximate value 0.05 for droplets between with a radius between $2.5\mu m$ and $55\mu m$ [171], [228]. Therefore, the distribution for the droplet radii is simulated by generating an even distribution for the volume fraction ξ_{vol} followed by finding the radius distribution for the droplet r_d . Droplets with a radius below $2.5\mu m$ are ignored, because they do not take part in the deposition reaction [171]. The distribution of the droplet's radius is derived in Appendix B and given by

$$r_d = \left\{ \xi \cdot \left[(r_{max})^{-1/3} - (r_{min})^{-1/3} \right] + (r_{min})^{-1/3} \right\}^{-3}, \quad (6.1)$$

where $r_{min} = 2.5\mu m$ and $r_{max} = 55\mu m$ are the minimum and maximum radii for the generated droplets and $\xi \in [0, 1]$ is an evenly distributed random value.

As soon as a droplet is generated and exits the atomizer, it experiences a strong electric force, much stronger than the gravitational force. This initial push from the atomizer determines the droplet's speed and direction as it enters the electric field. Because there is a very quick drop in the electric field magnitude E_{ext} from (5.20), the initial calculation is done within a very small radius of the atomizing nozzle ($0.005H$). The distribution of the initial starting position of particles will take into account the

| Droplet properties | | |
|---------------------------------------------|--------------------------------------|--------------------------------------|
| | Ethanol | Water |
| Droplet conductivity(κ_d) | 0.19 $W/m \cdot K$ | 0.609 $W/m \cdot K$ |
| Droplet density (ρ_d) | 789 kg/m^3 | 998 kg/m^3 |
| Absolute viscosity (η_d) | 0.00116 $N \cdot s/m^2$ | 0.01 $N \cdot s/m^2$ |
| Surface tension (γ) | 0.022 N/m | 0.072 N/m |
| Permittivity (ϵ) | 25 ϵ_0 | 80.1 ϵ_0 |
| Molar weight (M_W) | 46.1 $g/mole$ | 18.0 $g/mole$ |
| Average diffusion coefficient ($D_{v,f}$) | $6.314 \times 10^{-22} \times T/r$ | $7.325 \times 10^{-23} \times T/r$ |
| Saturation vapor pressure (SVP) | 5380 Pa | 2340 Pa |
| Boiling point (1atm) | 351.5 K | 373 K |
| Maximum droplet charge (q_{max}) | $1.11 \times 10^{-5} \times r^{3/2}$ | $2.01 \times 10^{-5} \times r^{3/2}$ |
| Air/ambient properties | | |
| Air viscosity (η_a) | $2.2 \times 10^{-5} N \cdot s/m^2$ | |
| Air density (ρ_a) | 1.29 kg/m^3 | |
| Air thermal conductivity (κ_a) | 0.025 $W/m \cdot K$ | |
| Gas constant (R) | 8.3144621 $m \cdot N/K \cdot mol$ | |
| Simulation properties | | |
| | ESD | PSD |
| Minimum droplet radius (r_{min}) | 2.5 μm | 1.5 μm |
| Maximum droplet radius (r_{max}) | 55 μm | 5 μm |
| Atomizer height (H) | 270mm | H_x =200mm, H_y =100mm |
| Droplet distribution angle (θ_d) | 45° | 12° |
| Flow rate | 2.8 ml/h | < 3.1 ml/h |
| Electric potential (Φ_0) | 10 kV | - |
| K_V | ~ 1 | - |
| Evaporation parameter (q_0) | ~373 $\mu m^2/s \cdot K$ | ~88 $\mu m^2/s \cdot K$ |
| Evaporation parameter (q_1) | ~8.91 $\times 10^{-5}/\mu m$ | ~4.3 $\times 10^{-3}/\mu m$ |
| Temperature (T) | 523 K | 673 K |
| Temperature gradient (∇T) | 100,000 K/m | 30,000 K/m |

Table 6.1.: Characteristics of the precursor solutions used for the simulations.

droplet distribution angle of the nozzle θ_d and will be found using spherical coordinates (r, θ, φ) .

The given equation for the electric field provides the magnitude at each location; however, in order to follow the droplet trajectory, the individual components of the electric field in each direction are required such that $\vec{E}_{ext} = (E_x, E_y, E_z)$. The individual components of the electric field in each Cartesian direction can be found by equating a unit vector in the form similar to (3.35). However, since the effects of the forces in the horizontal directions x and y are equal, calculations are easier using cylindrical coordinates, where $\vec{E}_{ext} = (E_\rho, \varphi, E_z)$. The droplet angle φ is unaffected by the applied forces since they act only in the radial ρ and vertical z directions. Therefore, the initial starting position's spherical coordinates will be converted to cylindrical coordinates, which will remain until the trajectory is complete.

Figure 6.16 shows a silicon surface geometry which extends 50mm by 50mm after 1, 10, 20, 50, and 100 spray cycles with 100,000 droplets per cycle and the spray nozzle located 270mm above the surface.

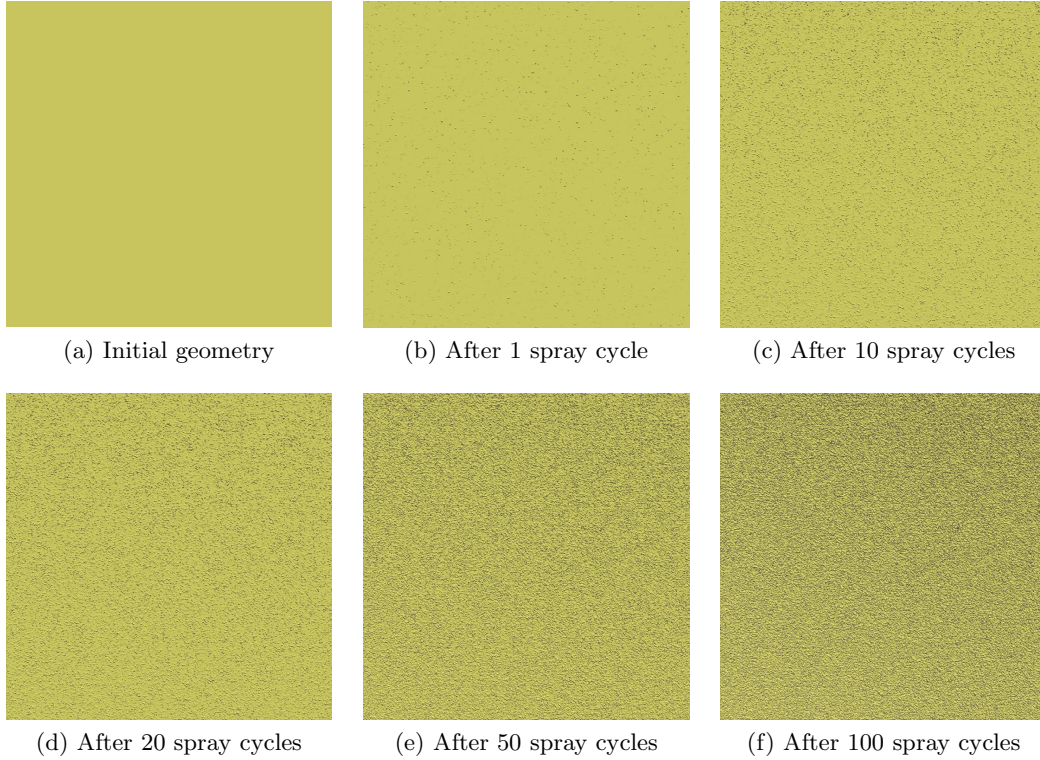


Figure 6.16.: Macroscopic spray pyrolysis simulation on a 50mm by 50mm geometry. Each spray cycle contains 100,000 droplets.

The images in Figure 6.16 show little in the way the thin film is deposited when the

deposition process is modeled as a sequence of droplets landing onto the surface and depositing a disk shaped film. Figure 6.17 shows an area which expands $250\mu\text{m}$ by $250\mu\text{m}$. Several droplets are shown including overlapping of the disk shapes on the surface as they are being deposited. The yellow surface is silicon while the orange disks are the deposited YSZ films. Each depositing droplet is modeled using 10^9 particles which accelerate to the surface and add a slight component of the overall deposited film thickness.

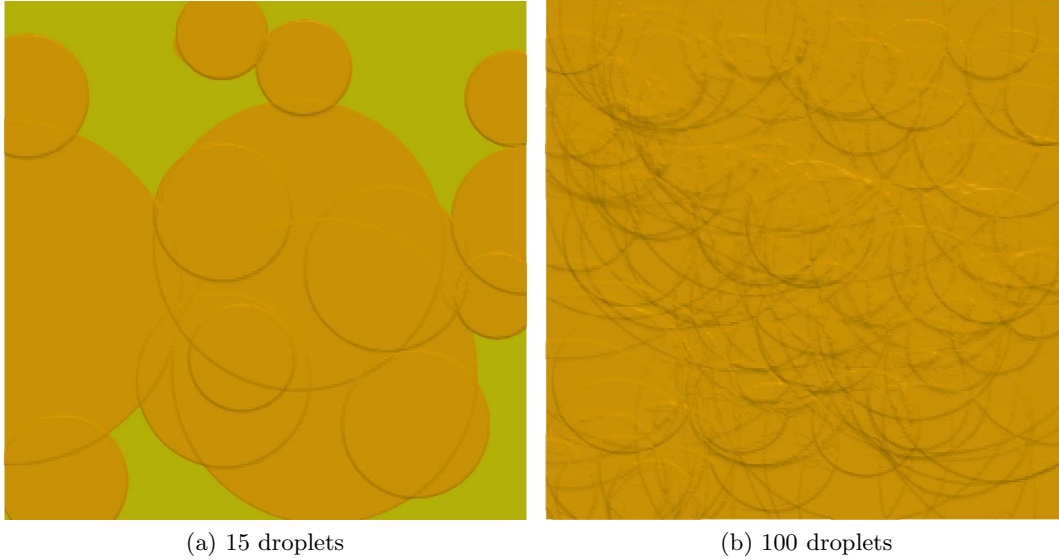


Figure 6.17.: Microscopic spray pyrolysis simulation on a $250\mu\text{m}$ by $250\mu\text{m}$ geometry.

6.4.2. Tin Oxide Deposition using PSD Pyrolysis

The deposition of tin oxide (SnO_2) on silicon dioxide using the spray pyrolysis deposition process was performed by one of our industrial partners using an air atomizer which is not located directly above the wafer, but rather on the side, as depicted in Figure 6.18. The nitrogen pressure of the atomizer was set to 2bar in air and 0.7bar in the liquid. These values are outside of the data sheet for the nozzle used [193], which is done in order to obtain smaller droplet sizes and slower deposition rates [211]. However, the data sheet information was extracted and the provided graph extended in order to find an approximate radial distribution of particles. The simulated radius of particles is set between $1.5\mu\text{m}$ and $5.5\mu\text{m}$. The spray direction is also mentioned in the data sheet; however, once again, the implemented pressure combination is not found in the available documentation and an extrapolated estimate must be used. The spray nozzle in use is one which produces a flat spray pattern with droplet dispersal proceeding mainly in the lateral axial direction. The vertical direction experiences much less particle dispersal; however, some dispersal does occur and the ratio between

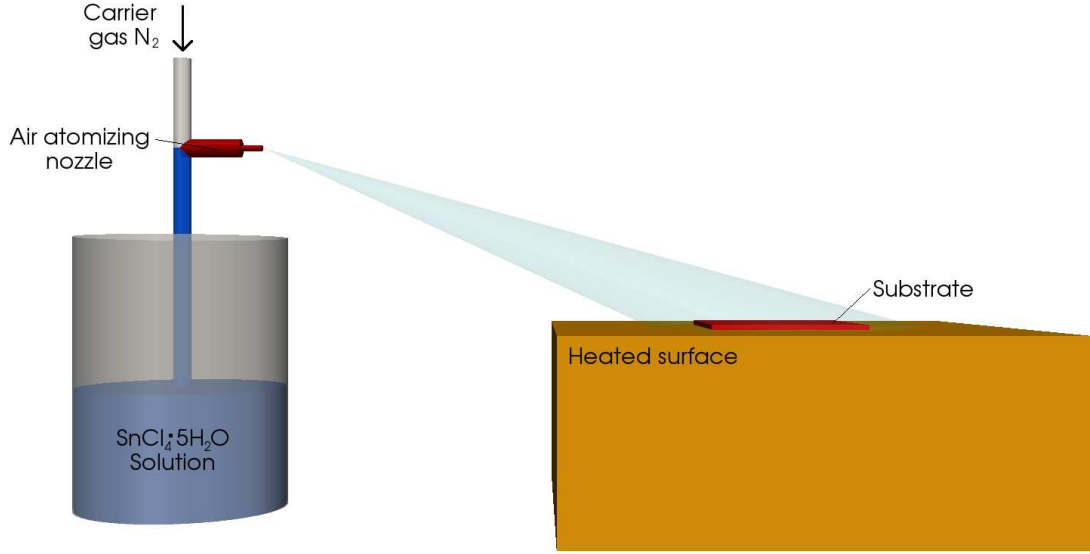


Figure 6.18.: Schematic for the PSD spray pyrolysis process used at AIT, serving as a basis for the presented topography simulations.

the lateral and vertical dispersal is approximated to 10:1. The nozzle is approximately 20cm laterally and 10cm vertically distanced from the substrate and the spray is directed such that much of it is found above the heated surface, where it can deposit onto the wafer. The parameters related to water droplets and the PSD simulation environment can be found in Table 6.1. The initial velocity of the droplets, as they are pushed out of the atomizer is not provided by the manufacturer [193]. Therefore, an approximation is made based on values found in literature which, as previously shown in Section 4.1 suggest an initial particle velocity between 5m/s and 20m/s.

As an example, a particle with a $5\mu\text{m}$ radius is analyzed. Its initial velocity is assumed to be 20m/s, fully in the horizontal direction. Therefore, the only forces which the particle experiences are the gravitational force and the Stokes force during its vertical flight and the Stokes force during its lateral flight towards the wafer sample. The droplet's vertical downward acceleration due to gravity is given by 9.81m/s^2 . The Stokes force is given by (4.7) and for the sample droplet is valued at $2.07 \times 10^{-9} \cdot v(t)\text{N}$. The mass of the droplet is given by (4.2) and is calculated to $523 \times 10^{-15}\text{kg}$. Therefore, the negative acceleration due to the stokes force is approximately $3960 \cdot v(t)\text{m/s}^2$, which is a very large negative force. When a particle is accelerated with an initial velocity of 20m/s, it will instantaneously experience a negative acceleration of $79.2 \times 10^3\text{m/s}^2$. This means that it is not possible for the droplet to travel the required distance when starting with the stated initial velocity. In fact, the initial velocity must follow

$$0 \leq \frac{d_x \cdot a_s}{v_0} < 1, \quad (6.2)$$

where d_x is the required distance, a_s is the velocity-dependent factor of the Stokes

negative acceleration, and v_0 is the initial velocity. Therefore

$$v_0 > d_x \cdot a_s. \quad (6.3)$$

In order for the sample droplet to reach the required distance to the wafer, a minimal initial velocity of $1.11 \times 10^3 \text{ m/s}$ is required. An alternative is the introduction of an additional force, such as is the case, when ESD deposition is performed as described in the previous section. It is evident that the initial velocity suggested in the literature is one which assumes no introduction of an additional air pressure. The additional pressure serves to break up the droplets due to an instantaneous increase in velocity and to introduce an additional “push” which gives the droplets the appropriate initial velocity in order for them to reach a range beyond several millimeters.

It may be noted that after leaving the atomizer, the droplets do not travel in the same manner together as they would individually. The interaction between droplets for the ESD system was ignored since, in literature [171], [228], it was suggested that they do not affect the droplet motion significantly. In the ESD system, the electric field is the main factor to the droplet’s movement. However, for the pressure system described here, it appears that interaction between droplets plays a larger role. Droplets move through air as a flux and calculating individual droplet’s movements in order to find their final location on the wafer surface does not produce a match to the experimental results, shown in Figure 6.19a from [156].

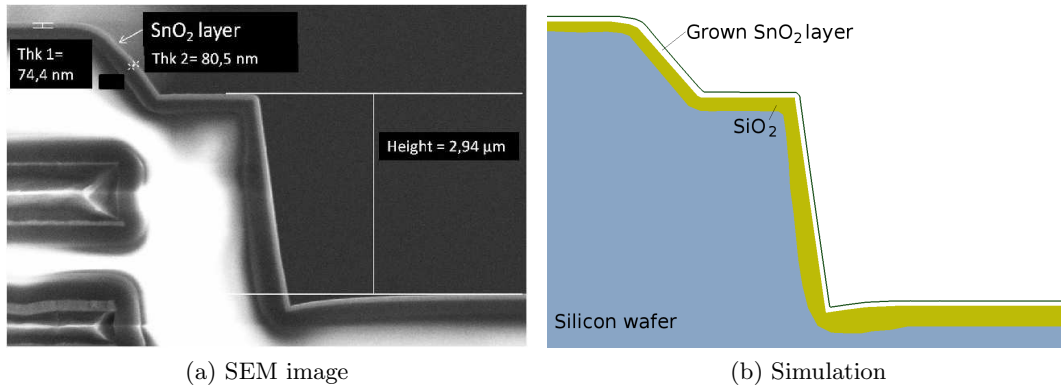


Figure 6.19.: Images showing the deposited SnO₂ film as a results of a PSD deposition step. The good step coverage confirms a chemical and not physical reaction takes place during deposition.

There are also several factors which influence the final thickness of the deposited film. Those include the spraying time, volume of the sprayed solution, air pressure, distance of the atomizer from the substrate, temperature of the pyrolysis reaction, and time of the solution (SnCl₄) aging. It was found in [107] that thicknesses of the deposited SnO₂ film decrease, when the time interval between its preparation and its use in the pyrolysis reaction increases. A suggestion is made to use either a freshly made

solution or a completely aged solution during spray pyrolysis. During the presented topography simulations, it is assumed that the nozzle distance to the substrate, air pressure, and solution aging remains constant, while the spray is constantly applied. The nozzle's distance to the substrate is set to 20cm laterally and 10cm vertically, the air pressure to 1atm, and the solution is freshly prepared. In correspondence, the time and temperature dependences are investigated in the model.

Experimental data [156], [211] suggest a linear dependence on spray time and a logarithmic dependence on wafer temperature for the growth rate of the deposited SnO_2 layer. A good agreement is given by the Arrhenius expression

$$d_{\text{SnO}_2}(t, T) = C_1 t e^{(-E/k_B T)}, \quad (6.4)$$

where $C_1 = 3.1 \mu\text{ms}^{-1}$, the thickness is given in μm , t is the time in seconds, and E is 0.427eV . Figure 6.19 depicts the (a) experimental and (b) simulated topography of a deposited SnO_2 film on a step structure after applying a PSD process for 45 seconds at 400°C . The incoming flux is set to flow in the $(1, -3) = (\text{lateral}, \text{vertical})$ direction and a CVD-like process is simulated with a reaction order of 1 and a sticking probability of 0.2, as these values produced the best fit to the experimental data. The average direction of the initial flow is $(1, 0)$, but due to the effects of gravity in the vertical direction, the droplet flux experiences a downward acceleration. However, in the lateral motion, it only experiences the retardant Stokes force. Therefore, it is obvious that the direction of the flux will change from mainly horizontal to mainly vertical as it reaches the wafer.

6.5. BiCS Memory Hole Etching

The etching of the BiCS memory hole is a combination of the SiO_2 and Si etching processes presented in Section 5.2. The initial structure which is to be etched is shown in Figure 6.20a. The width of the mask opening is 58nm, while the heights of the interchanging silicon and silicon dioxide layers are 50nm and 33nm, respectively. The silicon dioxide layer is etched using the model described in Section 5.2.1 and the silicon layer is etched with the model from Section 5.2.2 with the parameters listed in [113] and [11], respectively. Figure 6.20b shows the final topography after the sequence of processing steps are applied. The fluxes used for silicon etching are $F_{Br} = 2.5 \times 10^{18} \text{s}^{-1} \text{cm}^{-1}$, $F_O = 1.0 \times 10^{17} \text{s}^{-1} \text{cm}^{-1}$, and $F_{ion} = 1.0 \times 10^{16} \text{s}^{-1} \text{cm}^{-1}$. The fluxes used in the simulation of silicon dioxide etching are $F_e = 2.5 \times 10^{17} \text{s}^{-1} \text{cm}^{-1}$, $F_p = 1.0 \times 10^{17} \text{s}^{-1} \text{cm}^{-1}$, and $F_i = 5.6 \times 10^{16} \text{s}^{-1} \text{cm}^{-1}$. The silicon and silicon dioxide were etched for 60s and 6s, respectively.

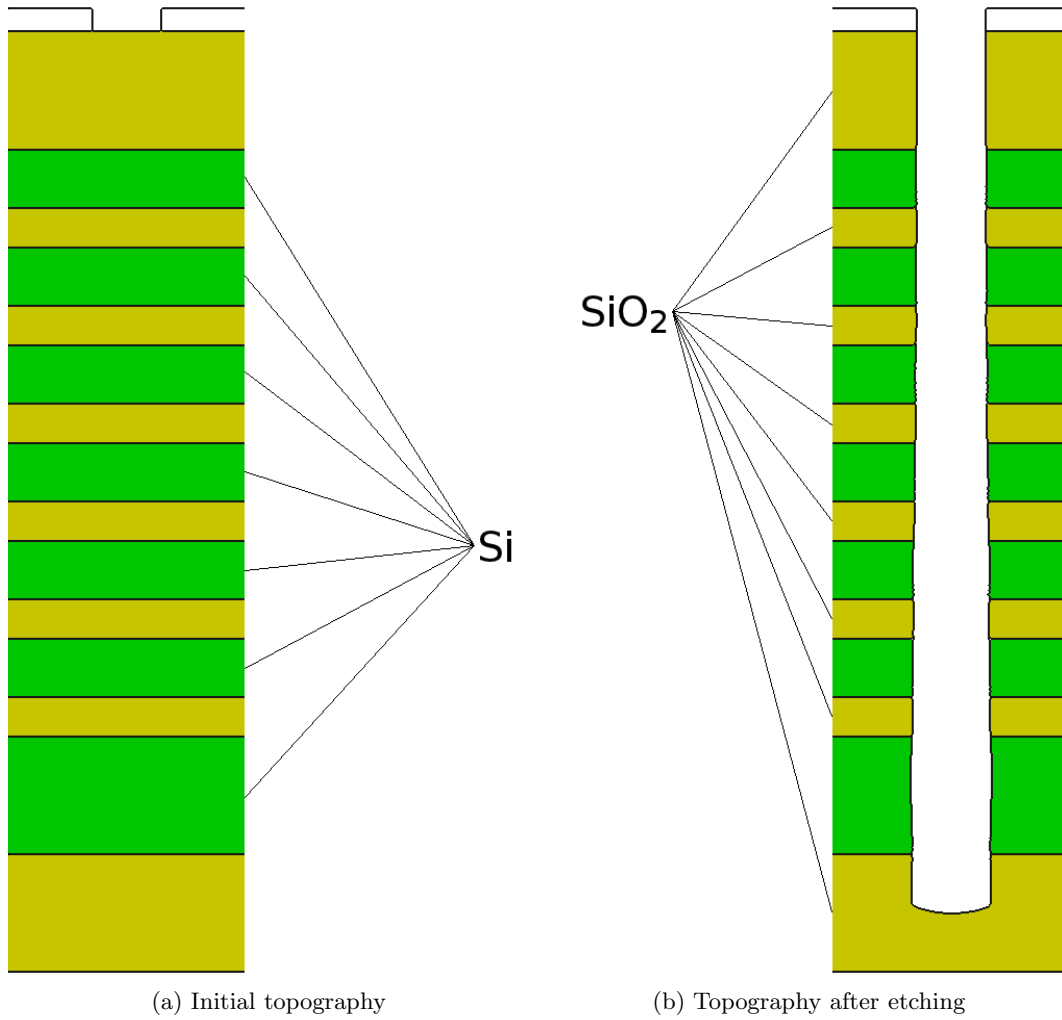


Figure 6.20.: The initial and final topographies after applying Si and SiO₂ etching models for the fabrication of BiCS memory holes.

7. Summary and Outlook

This work aims to utilize a LS framework in order to broaden the spectrum of available process topography simulations to include processes which have recently garnered attention due to numerous advantages they possess over traditional processing techniques. The framework has previously been implemented in order to simulate a topography changing due to the application of CVD, plasma etching, anisotropic wet etching, CMP, and focused ion beam processes. In this work, the framework is expanded to accommodate models for silicon oxidation, NAOS, AFM lithography, spray deposition, and BiCS memory hole etching.

Thermal oxidation of silicon is a process by which a silicon bulk is converted into silicon dioxide in an oxygen-rich environment under a high temperature. The models used in order to enable these simulations rely on a parabolic linear description of oxide growth along with some additional two-dimensional effects. The “bird’s beak” effect during LOCOS oxidation can be reproduced, when the geometrical movements of the nitride mask are known with respect to the oxide thickness. The simultaneous movement of multiple surfaces is performed, because oxide growth experiences motion on both interfaces (Si-SiO_2 and $\text{SiO}_2\text{-ambient}$). The implemented oxidation growth models are based on one-dimensional descriptions of the oxidant diffusion. However, expanding the LS framework to include the diffusion of species through a volume results in a much more accurate post-oxidation surface description. This process is quite complex; when the sparse field LS is implemented, since the explicit location of the surface or distribution of oxidant concentrations is not available. Others have solved this problem by simultaneously simulating diffusion in a separate FEM-based simulation space and feeding this information into the LS framework. This is an interesting approach but a future implementation of diffusion within the LS environment would be a valuable expansion to the present model. Through thermal oxidation, a high quality oxide can be grown on a silicon wafer. However, high temperatures ($\sim 1000^\circ$) are required to perform these processes. This is sometimes undesirable, since high temperatures influence the distribution of impurities in the silicon bulk and some devices require a high quality oxide to be grown in the presence of glass substrates, limiting the allowed ambient temperatures. An alternative to thermal oxidation for the growth of thin films is presented in the form of NAOS. An empirical model for NAOS is presented and included in the LS framework.

Silicon dioxide is a very useful masking tool during etching and ion implantation steps for surfaces below it. Through the introduction of LON the ability to grow nanosized patterns on a silicon wafer enabled the generation of nanosized devices, such

as junctionless transistors. A model for the surface deformation after the application of a negatively-charged AFM needle in intermittent contact and non-contact modes has been presented. The AFM needle is modeled as one or more charged dots. A MC technique is utilized in order to generate a particle distribution which reflects the surface charge density resulting from the introduced electric field. The ray tracing technique is then used to accelerate these particles to the LS surface, where a pattern is generated and the expected resulting topography is produced. Models for nanodots and nanowires are introduced to the LS framework. The model is able to handle a hemispherical needle tip by modeling it using a single dot charge or a rough needle tip, using multiple dot charges which are placed such that they mimic the applied electric field. An interesting extension of this model would be the introduction of AFM needle arrays, which are commonly used in order to increase the process throughput. The effects of the neighboring AFM needles could be analyzed along with a suggestion regarding the minimum distance between AFM needles placed in an array so that the desired pattern is unaffected.

Two other processes, which have garnered some attention recently have also been implemented within the LS framework. Spray pyrolysis deposition, which is a cost effective method for the deposition of thin material films on a silicon substrate has been introduced. The model examines the changing topography, when multiple droplets undergo trajectories dictated by the applied forces, finally striking the surface for deposition. In addition, a model similar to CVD deposition is suggested, when the droplets can be seen as a flux and not as individual particles and when they evaporate near the surface but prior to fully contacting the wafer in liquid form. Three-dimensional BiCS based memories are speculated to be the next step towards increasing memory capacity without technology node reduction, since the currently used NAND gate cannot be miniaturized below the 10nm node. The BiCS concept is the utilization of vertical storage so that area can be preserved and increasing memory capacity can be made much more cost effective. The main issue concerning BiCS is the difficulty in fabricating such complex structures, mainly the etching of multiple Si and SiO₂ layers. Sixteen interchanging layers of Si and SiO₂ must be etched through a hole with a diameter of approximately 50nm, if the technology is to be cost effective. A model for the etching of silicon and silicon dioxide has been implemented, taking into account the effects of the stacked structure.

Many implemented processes require long simulation times, especially those using a MC particle distribution and ray tracing techniques. Some simulations, such as AFM lithography with a rough needle tip, cannot be performed with an explicit particle distribution but rather rejection sampling must be used. With increasing aspect ratios and modeling requirements, parallelization becomes essential. The LS code implements an OpenMP framework for parallelization on shared memory machines. Introducing the message passing interface (MPI) to the simulator could allow for smaller simulation times and a greater precision, both with a finer mesh and with a larger number of MC particles in the simulation domain.

Appendix A.

Droplet Transport Equations for Spray Pyrolysis Modeling

A.1. Transport under a Velocity-Dependent Acceleration

This section is devoted to describe the derivation of the equations of motion (5.3)-(5.12) for a droplet experiencing a force in the direction of its motion such as gravity as well as forces working against its motion such as the thermophoretic force and the velocity-dependent Stokes force. For now, it is assumed that there is no influence from the electric force on the droplet motion. The first step is to equate all forces acting on the droplet

$$F_{tot} = F_g + (F_{th}) + F_S, \quad (\text{A.1})$$

where F_g is the force due to gravity, F_S is the Stokes force, and the thermophoretic force F_{th} is in brackets, because it is only included, when the droplet reaches the heat zone, and at that point, the radius must be modified according to its evaporation. However, for the following derivations, a constant radius will be assumed. Therefore, when the thermophoretic force is to be included, a smaller radius r_d is carried through the equations. The forces can be converted to droplet acceleration using

$$a(t)_{tot} = a(t)_g + (a(t)_{th}) + a(t)_S, \quad (\text{A.2})$$

where $a(t)_g$, $a(t)_{th}$, and $a(t)_S$ are the droplet accelerations due to gravity, the thermophoretic force, and the Stokes force, respectively. Since $F = m \cdot a$, then

$$a(t) = g + \left(\frac{F_{th}}{m} \right) + \frac{F_S}{m} \quad (\text{A.3})$$

and the droplet mass m is given by

$$m = \frac{4\pi}{3} \rho_d r_d^3. \quad (\text{A.4})$$

The explicit equation for the droplet acceleration can be derived by substituting the relevant forces and the droplet mass m into (A.3)

$$a(t) = \left[g + \left(-\frac{27 \eta_a^2 \kappa_a \nabla T}{4 \rho_a \rho_d T (2\kappa_a + \kappa_d) r^2} \right) \right] - \frac{9 \eta_a}{2 \rho_d r^2} v(t), \quad (\text{A.5})$$

where the meaning and values for the droplet and ambient parameters in (A.5) can be found in Table 6.1. In order to simplify the derivation, all constant values will be grouped together and only two constants will remain in the form of the independent constant a and constant b , which relates the velocity dependence of the acceleration

$$a = g + \left(-\frac{27 \eta_a^2 \kappa_a \nabla T}{4 \rho_a \rho_d T (2\kappa_a + \kappa_d) r^2} \right), \quad b = \frac{9 \eta_a}{2 \rho_d r^2} v(t), \quad (\text{A.6})$$

allowing for (A.5) to be rewritten as

$$a(t) = a - b v(t), \quad (\text{A.7})$$

The solution to (A.7) is found by first noting that it is a differential equation

$$\frac{dv(t)}{dt} = a - b v(t), \quad (\text{A.8})$$

which can be re-written in the form

$$\frac{dv(t)}{dt} + b v(t) - a = 0 \quad (\text{A.9})$$

and converted into Euler's characteristic equation

$$r + b = 0. \quad (\text{A.10})$$

This characteristic equation only has one root, $r = -b$, meaning the velocity can be solved by writing

$$v(t) = A e^{-bt} + B, \quad (\text{A.11})$$

where A and B are constants. In order to find A and B , two assumptions must be made: the initial velocity $v(0) = v_0$ is known and at some time t , the velocity will reach a terminal velocity due to the equivalent and opposite forces acting on the droplet, meaning $\frac{dv(t)}{dt}_{t=\infty} = 0$. Therefore, when t approaches infinity, $v(t)$ from (A.11) approaches B , meaning that B is the terminal velocity v_∞ . This can be substituted into (A.7) to obtain

$$0 = a - b B, \quad \text{then } B = \frac{a}{b}. \quad (\text{A.12})$$

Now that B and $v(0)$ are known, they can be substituted into (A.11) to find A

$$v_0 = A + \frac{a}{b}, \quad \text{then } A = v_0 - \frac{a}{b}, \quad (\text{A.13})$$

giving the final description for the velocity of the droplet at any time t

$$v(t) = v_0 e^{-bt} - \frac{a}{b} e^{-bt} + \frac{a}{b}. \quad (\text{A.14})$$

In order to find the displacement of the droplet under the given forces, (A.14) can be integrated from $t = 0$, when the initial displacement d_0 is set to 0

$$d(t) = \int_0^t v(t) dt = \int_0^t \left(v_0 e^{-bt} - \frac{a}{b} e^{-bt} + \frac{a}{b} \right) dt. \quad (\text{A.15})$$

resulting in

$$d(t) = \left[-\frac{v_0}{b} e^{-bt} + \frac{a}{b^2} e^{-bt} + \frac{a}{b} t \right]_0^t. \quad (\text{A.16})$$

The displacement is then given by

$$d(t) = \frac{a}{b} t + \frac{a}{b^2} e^{-bt} - \frac{v_0}{b} e^{-bt} - \left(-\frac{v_0}{b} + \frac{a}{b^2} \right) \quad (\text{A.17})$$

or

$$d(t) = \frac{1}{b} \left(v_0 - \frac{a}{b} \right) (1 - e^{-bt}) + \frac{a}{b} t. \quad (\text{A.18})$$

The time t is needed in order to calculate the droplet displacement. As the droplet travels through the ambient, it is much easier to calculate the time required for the droplet to reach the wafer followed by the calculation of the radial direction displacement. This would make simulations much quicker than a discretization of the time t in order to follow the droplet trajectory. The time is found by inverting (A.18)

$$t = \frac{a W \left[\frac{(a - b v_0) \cdot e^{1 - \frac{b(v_0 + b d(t))}{a}}}{a} \right] - a + b v_0 + b^2 d(t)}{a b}, \quad (\text{A.19})$$

where $W[\cdot]$ is the Lambert-W function which is solved iteratively and is defined by

$$z = W(z) e^{W(z)}. \quad (\text{A.20})$$

A.2. Transport under a Velocity- and Displacement-Dependent Acceleration

When the acceleration of a droplet also depends on the droplet's position in a simulation environment, or the displacement from its original position, such as is the case with the application of an electric force to a droplet's transport, the total force experienced by a droplet becomes

$$F_{tot} = F_g + (F_{th}) + F_S + F_e, \quad (\text{A.21})$$

where F_e is the electric force and the acceleration becomes

$$a(t)_{tot} = a(t)_g + (a(t)_{th}) + a(t)_S + a(t)_e. \quad (\text{A.22})$$

Acceleration due to the applied electric field is modeled as a linear displacement-dependent acceleration from (5.28)

$$c = \frac{6}{\rho_d} \sqrt{\frac{\gamma \epsilon_0}{r_d^3}} \cdot \frac{\Phi_0}{H} \cdot \frac{K_V}{\log(4H/R)} c_e, \quad (\text{A.23})$$

while acceleration due to gravity and the Stokes component of the acceleration remain the same from Section A.1. Therefore, the following equation must be solved to find the droplet displacement after time t

$$a(t) = a - b v(t) + c d(t). \quad (\text{A.24})$$

The equation can be re-written into a standard quadratic form, which is easier to solve

$$a(t) + b v(t) - c d(t) - a = 0. \quad (\text{A.25})$$

Noting that $a(t) = \frac{d^2 d(t)}{dt^2}$, $v(t) = \frac{dd(t)}{dt}$, and $d(t)$ is the displacement.

$$\frac{dd^2(t)}{dt^2} + b \frac{dv(t)}{dt} - c d(t) - a = 0. \quad (\text{A.26})$$

Using the Laplace method for solving differential equations, the characteristic equation, (A.26) can be re-written using s to depict a derivation step and r_i to depict the roots of equations. Assuming the initial velocity v_0 and initial displacement d_0 , (A.26) becomes

$$(s^2 d(t) - s d_0 - v_0) + b(s d(t) - d_0) - c d(t) - \frac{a}{s} = 0. \quad (\text{A.27})$$

Multiplying by s gives

$$s^3 d(t) - s^2 d_0 - s v_0 + s^2 b d(t) - s b d_0 - s c d(t) - a = 0. \quad (\text{A.28})$$

Isolating for $d(t)$ gives

$$d(t) = \frac{s^2 d_0 + s(v_0 + b d_0) + a}{s(s^2 + s b - c)}, \quad (\text{A.29})$$

which is then split according to the numerator's power of s using partial fractional decomposition

$$d(t) = \underbrace{\frac{s d_0}{(s^2 + s b - c)}}_{\text{System 1}} + \underbrace{\frac{v_0 + b d_0}{(s^2 + s b - c)}}_{\text{System 2}} + \underbrace{\frac{a}{s(s^2 + s b - c)}}_{\text{System 3}}. \quad (\text{A.30})$$

The roots of the equation can be found by finding s values for which (A.30) is invalid, or infinity. These roots are

$$r_1 = \frac{-b + \sqrt{b^2 + 4c}}{2}, \quad r_2 = \frac{-b - \sqrt{b^2 + 4c}}{2}, \quad r_3 = 0. \quad (\text{A.31})$$

In order to find the final equation for the displacement $d(t)$, a solution to each system in (A.30) must be found and added together

- **System 1**

System 1 is set up such that the two roots are separated

$$\frac{s d_0}{(s^2 + s b - c)} = \frac{A_1}{(s - r_1)} + \frac{B_1}{(s - r_2)}, \quad (\text{A.32})$$

where A_1 and B_1 are parameters to solve the displacement due to System 1

$$d(t)_1 = A_1 e^{(-r_1 t)} + B_1 e^{(-r_2 t)}. \quad (\text{A.33})$$

A_1 and B_1 are found using (A.32)

$$A_1 = d_0 \left(1 - \frac{r_2}{r_2 - r_1} \right), \quad \text{and} \quad B_1 = d_0 \frac{r_2}{r_2 - r_1}. \quad (\text{A.34})$$

- **System 2**

Similar to System 1, System 2 is set up, separating the effects from the two roots

$$\frac{v_0 + b d_0}{(s^2 + s b - c)} = \frac{A_2}{(s - r_1)} + \frac{B_2}{(s - r_2)}, \quad (\text{A.35})$$

where A_2 and B_2 are parameters to solve the displacement due to System 2

$$d(t)_2 = A_2 e^{(-r_1 t)} + B_2 e^{(-r_2 t)}. \quad (\text{A.36})$$

A_2 and B_2 are found using (A.35)

$$A_2 = -\frac{v_0 + b d_0}{r_2 - r_1}, \quad \text{and} \quad B_2 = \frac{v_0 + b d_0}{r_2 - r_1}. \quad (\text{A.37})$$

- **System 3**

System 3 has an additional root involvement from the presence of s in the denominator, so the system is set up as

$$\frac{a}{s(s^2 + s b - c)} = \frac{A_3}{(s - r_1)} + \frac{B_3}{(s - r_2)} + \frac{C_3}{s}, \quad (\text{A.38})$$

where A_3 , B_3 , and C_3 are parameters to solve the displacement due to System 3

$$d(t)_3 = A_3 e^{(-r_1 t)} + B_3 e^{(-r_2 t)} + C_3. \quad (\text{A.39})$$

A_3 , B_3 , and C_3 are found using (A.38)

$$A_3 = \frac{a}{r_1 (r_1 - r_2)}, \quad B_3 = \frac{a}{r_2 (r_2 - r_1)}, \quad \text{and} \quad C_3 = \frac{a}{r_1 r_2}. \quad (\text{A.40})$$

After combining all three systems, the equation which governs the displacement at time t due to velocity and displacement-dependent acceleration is given by

$$d(t) = (A_1 + A_2 + A_3) e^{-r_1 t} + (B_1 + B_2 + B_3) e^{-r_2 t} + C_3. \quad (\text{A.41})$$

It should be noted that, if the initial displacement is set to 0, then $A_1 = B_1 = 0$. Similarly, if the initial velocity is also set to 0, then $A_2 = B_2 = 0$, significantly reducing the complexity of the problem.

Appendix B.

Generating a Distribution for the Droplet Radius

The random distribution for the droplet radius for the ESD spray pyrolysis model in (6.1) is derived in this section. The volume fraction is evenly distributed along the droplets whose radii range from $r_{min} = 2.5\mu m$ to $r_{max} = 55\mu m$. Therefore, the first step is to relate the radius distribution linearly to a value $x \in [0, 1]$ so that as x goes from 0 to 1, r_d goes from r_{min} to r_{max} :

$$r_d(x) = (r_{max} - r_{min})x + r_{min}, \quad \text{where } x \in [0, 1]. \quad (\text{B.1})$$

Next, the assertion is made that x represents the evenly distributed volume number fraction, or normalized volume $\xi = x$. Using the equation for the volume of a sphere, the relationship between volume and radius is established as

$$V_{sphere} = \frac{4\pi}{3}r_d^3. \quad (\text{B.2})$$

Therefore, when the volume is evenly distributed, the effect on the radius will be $\xi_V \propto \frac{1}{r_d^3}$. Initially, it might be counter-intuitive to note the inverse relationship since $V \propto r^3$. However, when a volume of $V = 100m^3$ is distributed for a radius $r_1 = 10m$, then

$$100 = N(r = 10) \cdot \frac{4\pi}{3}(10)^3, \quad (\text{B.3})$$

where N is the number fraction, resulting in $N = 0.0238$. When the same volume is distributed for droplets of a radius $r_2 = 20m$, then the calculation above leads to the number fraction $N(r = 20) = 0.00298$, which is 8 times less, or $\left(\frac{r_1}{r_2}\right)^3$ times less.

Now we know that the radius distribution should follow the equation

$$r_\xi = \frac{C}{r_d^3}, \quad (\text{B.4})$$

where C is a normalization constant which must be found, r_ξ is the randomly distributed radius, and r_d is the radius relating r_{min} and r_{max} to an even volume distribution $\xi_V \in [0, 1]$ from (B.1)

$$r_\xi = \frac{C}{[(r_{max} - r_{min}) \xi_V + r_{min}]^3}. \quad (\text{B.5})$$

Inverting (B.5) to solve for ξ_V allows to find the CPD function $\Phi(r_\xi)$

$$\Phi(r_\xi) = \xi_V = \frac{1}{r_{max} - r_{min}} \left[\left(\frac{C}{r_\xi} \right)^{1/3} - r_{min} \right]. \quad (\text{B.6})$$

The derivative of (B.6) gives the PDF

$$f(r_\xi) = \frac{d\Phi(r_\xi)}{dr_\xi} = -\frac{C^{1/3}}{3} \cdot \frac{1}{r_{max} - r_{min}} \cdot r_\xi^{-4/3}, \quad (\text{B.7})$$

where it can be noted that the last r_{min} term from (B.6) has disappeared. The only non-constant term in (B.7) is $r_\xi^{-4/3}$, therefore a replacement constant, which will be the new normalization constant is introduced for simplicity

$$A \equiv -\frac{C^{1/3}}{3} \cdot \frac{1}{r_{max} - r_{min}} \quad (\text{B.8})$$

and (B.7) can be rewritten to

$$f(r_\xi) = A \cdot r_\xi^{-4/3}. \quad (\text{B.9})$$

Using the PDF from (B.9), we can now proceed to find the normalized distribution r_ξ , but first the normalization constant A must be found by integrating (B.9) with respect to r_ξ from r_{min} to r_{max} and equating the integral to 1

$$\int_{r_{min}}^{r_{max}} f(r_\xi) dr_\xi = \int_{r_{min}}^{r_{max}} A \cdot r_\xi^{-4/3} dr_\xi = 1, \quad (\text{B.10})$$

which can be solved to

$$-3A \left[\left(\frac{1}{r_{max}} \right)^{1/3} - \left(\frac{1}{r_{min}} \right)^{1/3} \right] = 1, \quad (\text{B.11})$$

giving the normalization constant A

$$A = -\frac{1}{3 \left[r_{max}^{-1/3} - r_{min}^{-1/3} \right]} \quad (\text{B.12})$$

and the normalized PDF

$$f(r_d) = -\frac{1}{3[r_{max}^{-1/3} - r_{min}^{-1/3}]} \cdot r_d^{-4/3}. \quad (\text{B.13})$$

Now one can integrate the normalized PDF from r_{min} to r_ξ to find the CPD

$$\int_{r_{min}}^{r_\xi} f(r) dr = \frac{r_\xi^{-1/3} - r_{min}^{-1/3}}{r_{max}^{-1/3} - r_{min}^{-1/3}} = \xi_V \quad (\text{B.14})$$

and invert the CPD to find the quantile function and solve for r_ξ

$$r_\xi = \left\{ \xi_V \cdot \left[(r_{max})^{-1/3} - (r_{min})^{-1/3} \right] + (r_{min})^{-1/3} \right\}^{-3}, \quad (\text{B.15})$$

which gives the equation for the radius distribution r_ξ between r_{min} and r_{max} when the volume number fraction ξ_V is evenly distributed and $\xi_V \in [0, 1]$.

Bibliography

- [1] C. Albonetti, J. Martínez, N. S. Losilla, P. Greco, M. Cavallini, F. Borgatti, M. Montecchi, L. Pasquali, R. García, and F. Biscarini. Parallel-local anodic oxidation of silicon surfaces by soft stamps. *Nanotechnology*, 19(43):435303(9), 2008.
- [2] W. Arden, M. Brillouet, P. Coge, P. Graef, B. Huizing, and R. Mahnkopf. More-than-Moore white paper. Technical report, International Technical Roadmap for Semiconductors, 2010.
<http://www.itrs.net/Links/2010ITRS/IRC-ITRS-MtM-v2%203.pdf>.
- [3] T. K. Asuha, O. Maida, M. Inoue, M. Takahashi, Y. Todokoro, and H. Kobayashi. Ultrathin silicon dioxide layers with a low leakage current density formed by chemical oxidation of Si. *Applied Physics Letters*, 81(18):3410–3412, 2002.
- [4] P. Avouris, T. Hertel, and R. Martel. Atomic force microscope tip-induced local oxidation of silicon: kinetics, mechanism, and nanofabrication. *Applied Physics Letters*, 71(2):285–287, 1997.
- [5] P. Avouris, Y. Lin, F. Xia, T. Mueller, D. Farmer, C. Dimitrakopoulos, and A. Grill. Graphene-based fast electronics and optoelectronics. In *Device Research Conference (DRC)*, pages 205–206, 2010.
- [6] P. Avouris, R. Martel, T. Hertel, and R. Sandstrom. AFM-tip-induced and current-induced local oxidation of silicon and metals. *Applied Physics A: Materials Science & Processing*, 66(1):S659–S667, 1998.
- [7] C. Bai. *Scanning tunneling microscopy and its application*. Scientific and Technical Publishers, 1995.
- [8] A. Bardea and R. Naaman. Magnetolithography: From the bottom-up route to high throughput. *Advances in Imaging and Electron Physics*, 164:1–27, 2010.
- [9] D. Beckel, A. Dubach, A. Studart, and L. Gauckler. Spray pyrolysis of $\text{La}_{0.6}\text{Sr}_{0.4}\text{Co}_{0.2}\text{Fe}_{0.8}\text{O}_{3-\delta}$ thin film cathodes. *Journal of Electroceramics*, 16(3):221–228, 2006.

- [10] R. J. Belen, S. Gomez, D. Cooperberg, M. Kiehlbauch, and E. S. Aydil. Feature-scale model of Si etching in SF_6/O_2 plasma and comparison with experiments. *Journal of Vacuum Science & Technology A: Vacuum, Surfaces, and Films*, 23(2):1430–1439, 2005.
- [11] R. J. Belen, S. Gomez, M. Kiehlbauch, and E. S. Aydil. Feature scale model of Si etching in $\text{SF}_6/\text{O}_2/\text{HBr}$ plasma and comparison with experiments. *Journal of Vacuum Science & Technology A: Vacuum, Surfaces, and Films*, 24(2):350–361, 2006.
- [12] G. Binnig, C. F. Quate, and C. Gerber. Atomic force microscope. *Physical Review Letters*, 56(9):930–933, 1986.
- [13] G. Binnig and H. Rohrer. EU patent number 0027517: Scanning apparatus for surface analysis using vacuum-tunnel effect at cryogenic temperatures. (issued 29 April 1981).
- [14] G. Binnig and H. Rohrer. Scanning tunneling microscopy. *Surface Science*, 126(1–3):236–244, 1983.
- [15] G. Binnig and H. Rohrer. Scanning tunneling microscopy – from birth to adolescence (Nobel lecture). *Angewandte Chemie International Edition in English*, 26(7):606–614, 1987.
- [16] G. Binnig, H. Rohrer, C. Gerber, and E. Weibel. Surface studies by scanning tunneling microscopy. *Physical Review Letters*, 49(1):57–61, 1982.
- [17] G. Binnig, H. Rohrer, C. Gerber, and E. Weibel. 7×7 Reconstruction on Si(111) resolved in real space. *Physical Review Letters*, 50(2):120–123, 1983.
- [18] J. Bjorkholm. Euv lithography - the successor to optical lithography. *Intel Technology Journal*, 3:98, 1998.
<http://download.intel.com/technology/itj/q31998/pdf/euv.pdf>.
- [19] G. Blandenet, M. Court, and Y. Lagarde. Thin layers deposited by the pyrosol process. *Thin Solid Films*, 77(1–3):81–90, 1981.
- [20] A. Bongiorno and A. Pasquarello. Atomic-scale modelling of kinetic processes occurring during silicon oxidation. *Journal of Physics: Condensed Matter*, 17(21):S2051–S2063, 2005.
- [21] O. Buiiu, G. Kennedy, M. Gartner, and S. Taylor. Structural analysis of silicon dioxide and silicon oxynitride films produced using an oxygen plasma. *IEEE Transactions on Plasma Science*, 26(6):1700–1712, 1998.
- [22] D. A. P. Bulla and N. I. Morimoto. Deposition of thick TEOS PECVD silicon oxide layers for integrated optical waveguide applications. *Thin Solid Films*, 334(1–2):60–64, 1998.

- [23] D. Bullen and C. Liu. Electrostatically actuated dip pen nanolithography probe arrays. *Sensors and Actuators A: Physical*, 125(2):504–511, 2006.
- [24] J. H. Burnett, S. G. Kaplan, E. L. Shirley, P. J. Tompkins, and J. E. Webb. High-index materials for 193 nm immersion lithography. In *Proceedings of SPIE 5754, Optical Microlithography XVIII*, pages 611–621, 2005.
- [25] M. Burzo, P. Komarov, and P. Raad. Thermal transport properties of gold-covered thin-film silicon dioxide. *IEEE Transactions on Components and Packaging Technologies*, 26(1):80–88, 2003.
- [26] N. Cabrera and N. F. Mott. Theory of the oxidation of metals. *Reports on Progress in Physics*, 12:163–184, 1949.
- [27] T. S. Cale and G. B. Raupp. A unified line-of-sight model of deposition in rectangular trenches. *Journal of Vacuum Science & Technology B: Microelectronics and Nanometer Structures*, 8(6):1242–1248, 1990.
- [28] M. Calleja and R. García. Nano-oxidation of silicon surfaces by noncontact atomic-force microscopy: size dependence on voltage and pulse duration. *Applied Physics Letters*, 76(23):3427–3429, 2000.
- [29] R. R. Chamberlin and J. S. Skarman. Chemical spray deposition process for inorganic films. *Journal of the Electrochemical Society*, 113(1):86–89, 1966.
- [30] S. Y. Chou, P. R. Krauss, and P. J. Renstrom. Imprint lithography with 25-nanometer resolution. *Science*, 272(5258):85–87, 1996.
- [31] S. Y. Chou, P. R. Krauss, and P. J. Renstrom. Nanoimprint lithography. *Journal of Vacuum Science & Technology B: Microelectronics and Nanometer Structures*, 14(6):4129–4133, 1996.
- [32] K. Choy and B. Su. Growth behavior and microstructure of CdS thin films deposited by an electrostatic spray assisted vapor deposition (ESAVD) process. *Thin Solid Films*, 388(1–2):9–14, 2001.
- [33] M.-C. Chuang and J. W. Coburn. Molecular-beam study of gas-surface chemistry in the ion-assisted etching of silicon with atomic and molecular hydrogen and chlorine. *Journal of Vacuum Science & Technology*, 8(3):1969–1976, 1990.
- [34] C. R. Cleavelin, S. Pas, E. M. Vogel, and J. J. Wortman. *Oxidation*, chapter 7, pages 163–183. Marcel Dekker Inc., 2000.
- [35] J.-P. Colinge, C.-W. Lee, A. Afzalian, N. D. Akhavan, R. Yan, I. Ferain, P. Razavi, B. O’Neill, A. Blake, M. White, A.-M. Kelleher, B. McCarthy, and R. Murphy. Nanowire transistors without junctions. *Nature Nanotechnology*, 5(3):225–229, 2010.

- [36] E. B. Cooper, S. R. Manalis, H. Fang, H. Dai, K. Matsumoto, S. C. Minne, T. Hunt, and C. F. Quate. Terabit-per-square-inch data storage with the atomic force microscope. *Applied Physics Letters*, 75(22):3566–3568, 1999.
- [37] H. Cui, Y. Sun, G. Z. Yang, G. W. Yang, and C. X. Wang. Size-dependent oxidation behavior for the anomalous initial thermal oxidation process of Si. *Applied Physics Letters*, 94(8):083108–083108–3, 2009.
- [38] J. Dagata, J. Schneir, H. Harary, C. Evans, M. Postek, and J. Bennett. Modification of hydrogen-passivated silicon by a scanning tunneling microscope operating in air. *Applied Physics Letters*, 56(20):2001–2003, 1990.
- [39] J. A. Dagata, F. Perez-Murano, G. Abadal, K. Morimoto, T. Inoue, J. Itoh, and H. Yokoyama. Predictive model for scanned probe oxidation kinetics. *Applied Physics Letters*, 76(19):2710–2712, 2000.
- [40] H. C. Day and D. R. Allee. Selective area oxidation of silicon with a scanning force microscope. *Applied Physics Letters*, 62(21):2691–2693, 1993.
- [41] R. M. C. de Almeida, S. Gonçalves, I. J. R. Baumvol, and F. C. Stedile. Dynamics of thermal growth of silicon oxide films on Si. *Physical Review B*, 61(19):12992–12999, 2000.
- [42] B. E. Deal and A. S. Grove. General relationship for the thermal oxidation of silicon. *Journal of Applied Physics*, 36(12):3770–3778, 1965.
- [43] A. A. Dehzangi, A. A. M. Abdullah, F. F. Larki, S. S. D. Hutagalung, E. E. B. Saion, M. M. N. Hamidon, J. J. Hassan, and Y. Y. Gharayebi. Electrical property comparison and charge transmission in p-type double gate and single gate junctionless accumulation transistor fabricated by AFM nanolithography. *Nanoscale Research letters*, 7(1):381, 2012.
- [44] M. Despont, J. Brugger, U. Drechsler, U. Drig, W. Hberle, M. Lutwyche, H. Rothuizen, R. Stutz, R. Widmer, G. Binnig, H. Rohrer, and P. Vettiger. VLSI-NEMS chip for parallel AFM data storage. *Sensors and Actuators A: Physical*, 80(2):100–107, 2000.
- [45] S. Djurkovic, C. Clemons, D. Golovaty, and G. Young. Effects of the electric field shape on nano-scale oxidation. *Surface Science*, 601(23):5340–5358, 2007.
- [46] E. Dubois and J.-L. Bubbendorff. Nanometer scale lithography on silicon, titanium and PMMA resist using scanning probe microscopy. *Solid-State Electronics*, 43(6):1085–1089, 1999.
- [47] B. El-Kareh. *Fundamentals of Semiconductor Processing Technologies*. Kluwer Academic Publishers, 1995.
- [48] J.-J. Eltgen. US patent number 5644987: Process and apparatus for printing using a magnetic toner which is electrostatically charged. (issued 08 August 1997).

- [49] B. Engquist and S. Osher. Stable and entropy satisfying approximations for transonic flow calculations. *Mathematics of Computation*, 34(149):45–75, 1980.
- [50] O. Ertl. *Numerical Methods for Topography Simulation*. Dissertation, Technischen Universität Wien, Fakultät für Elektrotechnik und Informationstechnik, 2010.
<http://www.iue.tuwien.ac.at/phd/ertl/>.
- [51] O. Ertl and S. Selberherr. A fast level set framework for large three-dimensional topography simulations. *Computer Physics Communications*, 180(8):1242–1250, 2009.
- [52] F.-R. F. Fan and A. J. Bard. Electrochemical detection of single molecules. *Science*, 267(5199):871–874, 1995.
- [53] T.-H. Fang. Mechanisms of nanooxidation of Si(100) from atomic force microscopy. *Microelectronics Journal*, 35(9):701–707, 2004.
- [54] P. Fay, R. T. Brockenbrough, G. Abeln, P. Scott, S. Agarwala, I. Adesida, and J. W. Lyding. Scanning tunneling microscope stimulated oxidation of silicon (100) surfaces. *Journal of Applied Physics*, 75(11):7545–7549, 1994.
- [55] P. A. Fontaine, E. Dubois, and D. Stievenard. Characterization of scanning tunneling microscopy and atomic force microscopy-based techniques for nanolithography on hydrogen-passivated silicon. *Journal of Applied Physics*, 84(4):1776–1781, 1998.
- [56] R. Gallage, A. Matsuo, T. Watanabe, N. Matsushita, and M. Yoshimura. Fabrication of transparent ceria films by spray deposition without post firing. *Journal of Electroceramics*, 22(1):33–39, 2009.
- [57] Y. Gan, H. Wong, and W. Lee. A novel atomic force microscopy based lithography system for automated patterning via anodic oxidation. *Composites Part B: Engineering*, 42(3):456–461, 2011.
- [58] A. Gañán-Calvo, J. Lasheras, J. Dávila, and A. Barrero. The electrostatic spray emitted from an electrified conical meniscus. *Journal of Aerosol Science*, 25(6):1121–1142, 1994.
- [59] R. García. Keynote speech: Bridging nano and macro worlds with water miniscii: attomol chemistry and nanofabrication by local oxidation nanolithography. *LITHO*, 2004.
http://www.imm.cnm.csic.es/spm/Articulos/Garcia_Litho2004.pdf.
- [60] R. García, M. Calleja, and F. Perez-Murano. Local oxidation of silicon surfaces by dynamic force microscopy: Nanofabrication and water bridge formation. *Applied Physics Letters*, 72(18):2295–2297, 1998.
- [61] R. García, R. V. Martínez, and J. Martínez. Nano-chemistry and scanning probe nanolithographies. *Chemical Society Review*, 35(1):29–38, 2006.

- [62] A. García-Martin and R. García. Formation of nanoscale liquid menisci in electric fields. *Applied Physics Letters*, 88(12):123115–123115–3, 2006.
- [63] U. Gasser, M. Sigrist, S. Gustavsson, K. Ensslin, and T. Ihn. *Tip-Based Nanofabrication: Fundamentals and Applications*, chapter 3: Double Layer Local Anodic Oxidation Using Atomic Force Microscopy, pages 91–128. Springer, 1st edition, 2011.
- [64] M. Giorgio, B. Elise, K. Anton, and S. Steinhauer. Private communication with members of the molecular diagnostics, health and environment group at the Austrian Institute of Technology (AIT)., 2012.
- [65] A. E. Gordon, R. T. Fayfield, D. D. Litfin, and T. K. Higman. Mechanisms of surface anodization produced by scanning probe microscopes. *Journal of Vacuum Science & Technology B: Microelectronics and Nanometer Structures*, 13(6):2805–2808, 1995.
- [66] S. Gottlieb and C. W. Shu. Total variation diminishing Runge-Kutta schemes. *Mathematics of Computation*, 67(221):73–85, 1998.
- [67] L. Gross, F. Mohn, N. Moll, B. Schuler, A. Criado, E. Guitin, D. Pea, A. Gourdon, and G. Meyer. Bond-order discrimination by atomic force microscopy. *Science*, 337(6100):1326–1329, 2012.
- [68] R. Guckenberger, M. Heim, G. Cevc, H. F. Knapp, W. Wiegrabe, and A. Hillebrand. Scanning tunneling microscopy of insulators and biological specimens based on lateral conductivity of ultrathin water films. *Science*, 266(5190):1538–1540, 1994.
- [69] L. J. Guo. Recent progress in nanoimprint technology and its applications. *Journal of Physics D: Applied Physics*, 37(11):R123–R141, 2004.
- [70] B. Haavind and J. Montgomery. SPIE: AMD, IBM tip first ”full field” EUV chip. Solid State Technology: Insights for Electronics Manufacturing, 2008. <http://www.electroiq.com/articles/mlw/2008/02/spie-amd-ibm-tip-first-full-field-euv-chip.html>.
- [71] H. F. Hamann, M. O’Boyle, Y. C. Martin, M. Rooks, and H. K. Wickramasinghe. Ultra-high-density phase-change storage and memory. *Nature Materials*, 5(5):383–387, 2006.
- [72] E. Harari. Plenary: Flash memory – the great disruptor! In *IEEE International Solid-State Circuits Conference (ISSCC) Digest of Technical Papers*, pages 10–15, 2012.
- [73] T. Hattori, Y. Ejiri, K. Saito, and M. Yasutake. Fabrication of nanometer-scale structures using atomic force microscope with conducting probe. *Journal of Vacuum Science & Technology A: Vacuum, Surfaces, and Films*, 12(4):2586–2590, 1994.

- [74] R. Hayes, N. Borisenko, M. K. Tam, P. C. Howlett, F. Endres, and R. Atkin. Double layer structure of ionic liquids at the Au(111) electrode interface: an atomic force microscopy investigation. *The Journal of Physical Chemistry C*, 115(14):6855–6863, 2011.
- [75] A. Hemeryck, N. Richard, A. Estève, and M. D. Rouhani. Diffusion of oxygen atom in the topmost layer of the Si(100) surface: Structures and oxidation kinetics. *Surface Science*, 601(11):2339–2343, 2007.
- [76] C. D. Hendricks Jr. Charged droplet experiments. *Journal of Colloid Science*, 17(3):249–259, 1962.
- [77] M. D. Henry. *ICP Etching of silicon for micro and nanoscale devices*. Ph.d. dissertation, California Institute of Technology, 2010.
<http://thesis.library.caltech.edu/5846/2/MDH-Thesis-Rev1.pdf>.
- [78] D. W. Hess. Plasma-assisted oxidation, anodization, and nitridation of silicon. *IBM Journal of Research and Development*, 43(1.2):127–145, 1999.
- [79] Y. Hirai, S. Yoshida, and N. Takagi. Defect analysis in thermal nanoimprint lithography. *Journal of Vacuum Science & Technology B: Microelectronics and Nanometer Structures*, 21(6):2765–2770, 2003.
- [80] C. Hollauer. *Modeling of Thermal Oxidation and Stress Effects*. Dissertation, Technischen Universität Wien, Fakultät für Elektrotechnik und Informationstechnik, 2007.
<http://www.iue.tuwien.ac.at/phd/hollauer/>.
- [81] H. Holterman. *Kinetics and Evaporation of Water Drops in Air*. IMAG, Wageningen (Netherlands), 2003.
- [82] S. Hong and C. A. Mirkin. A nanoplotter with both parallel and serial writing capabilities. *Science*, 288(5472):1808–1811, 2000.
- [83] B. Houston, M. B. Nielsen, C. Batty, O. Nilsson, and K. Museth. Hierarchical RLE level set: A compact and versatile deformable surface representation. *ACM Transactions on Graphics*, 25(1):151–175, 2006.
- [84] J. Huang, C.-L. Tsai, and A. A. Tseng. The influence of the bias type, doping condition and pattern geometry on AFM tip-induced local oxidation. *Journal of the Chinese Institute of Engineers*, 33(1):55–61, 2010.
- [85] S. Hutagalung and K. Lew. Electrical characteristics of silicon nanowire transistor fabricated by AFM lithography. In *IEEE International Conference on Semiconductor Electronics (ICSE)*, pages 358–362, 2010.
- [86] T. Ichikawa, D. Ichinose, K. Kawabata, and N. Tamaoki. Topography simulation of BiCS memory hole etching modeled by elementary experiments of SiO₂ and Si etching. In *International Conference on Simulation of Semiconductor Processes and Devices (SISPAD)*, pages 45–48, 2010.

- [87] N. Ikarashi, K. Watanabe, and Y. Miyamoto. High-resolution transmission electron microscopy of an atomic structure at a Si(001) oxidation front. *Physical Review B*, 62(23):15989–15995, 2000.
- [88] S. Imai, M. Takahashi, and H. K. Asuha. Nitric acid oxidation of silicon at $\sim 120^\circ\text{C}$ to form 3.5-nm SiO_2/Si structure with good electrical characteristics. *Applied Physics Letters*, 85(17):3783–3785, 2004.
- [89] S. Imai, M. Takahashi B., K. Matsuba B., Asuha B., Y. Ishikawa B., and H. Kobayashi B. Formation and electrical characteristics of silicon dioxide layers by use of nitric acid oxidation method. *Acta Physica Slovaca*, 55(3):305–313, 2005.
- [90] K. Imamura, O. Maida, K. Hattori, M. Takahashi, and H. Kobayashi. Low temperature formation of SiO_2/Si structure by nitric acid vapor. *Journal of Applied Physics*, 100(11):114910–114910–4, 2006.
- [91] Institute for Microelectronics, Technischen Universität Wien: PROMIS. <http://www.iue.tuwien.ac.at/index.php?id=promis>.
- [92] A. M. Ionescu. Electronic devices: Nanowire transistors made easy. *Nature Nanotechnology*, 5(3):178–179, 2010.
- [93] I. Ionica, L. Monts, S. Ferraton, J. Zimmermann, L. Saminadayar, and V. Bouchiat. Field effect and coulomb blockade in silicon on insulator nanostructures fabricated by atomic force microscope. *Solid-State Electronics*, 49(9):1497–1503, 2005.
- [94] J. Jang, H.-S. Kim, W. Cho, H. Cho, J. Kim, S. I. Shim, Y. Jang, J.-H. Jeong, B.-K. Son, D. W. Kim, Kihyun, J.-J. Shim, J. S. Lim, K.-H. Kim, S. Y. Yi, J.-Y. Lim, D. Chung, H.-C. Moon, S. Hwang, J.-W. Lee, Y.-H. Son, U.-I. Chung, and W.-S. Lee. Vertical cell array using TCAT (Terabit Cell Array Transistor) technology for ultra high density NAND flash memory. In *2009 Symposium on VLSI Technology*, pages 192–193, 2009.
- [95] M. Johannes, D. Cole, and R. Clark. Three-dimensional design and replication of silicon oxide nanostructures using an atomic force microscope. *Nanotechnology*, 18(34):345304–7, 2007.
- [96] A. R. Jones and K. C. Thong. The production of charged monodisperse fuel droplets by electrical dispersion. *Journal of Physics D: Applied Physics*, 4(8):1159–1168, 1971.
- [97] R. Katsumata, M. Kito, Y. Fukuzumi, M. Kido, H. Tanaka, Y. Komori, M. Ishiduki, J. Matsunami, T. Fujiwara, Y. Nagata, L. Zhang, Y. Iwata, R. Kirisawa, H. Aochi, and A. Nitayama. Pipe-shaped BiCS flash memory with 16 stacked layers and multi-level-cell operation for ultra high density storage devices. In *Proceedings of the 2009 Symposium on VLSI Technology*, pages 136–137, 2009.

- [98] L. E. Katz and L. C. Kimerling. Defect formation during high pressure, low temperature steam oxidation of silicon. *Journal of the Electrochemical Society*, 125(10):1680–1683, 1978.
- [99] A. J. Kelly. Charge injection electrostatic atomizer modeling. *Aerosol Science and Technology*, 12(3):526–537, 1990.
- [100] J. Kim, A. Hong, S. M. Kim, E. Song, J. H. Park, J. Han, S. Choi, D. Jang, J. T. Moon, and K. Wang. Novel vertical-stacked-array-transistor (VSAT) for ultra-high-density and cost-effective NAND flash memory devices and SSD (solid state drive). In *Proceedings of the 2009 Symposium on VLSI Technology*, pages 186–187, 2009.
- [101] J. Kim, A. J. Hong, S. M. Kim, K.-S. Shin, E. B. Song, Y. Hwang, F. Xiu, K. Galatsis, C. O. Chui, R. N. Candler, S. Choi, J.-T. Moon, and K. L. Wang. A stacked memory device on logic 3D technology for ultra-high-density data storage. *Nanotechnology*, 22(25):254006–7, 2011.
- [102] W. Kim, S. Choi, J. Sung, T. Lee, C. Park, H. Ko, J. Jung, I. Yoo, and Y. Park. Multi-layered vertical gate NAND flash overcoming stacking limit for terabit density storage. In *Proceedings of the 2009 Symposium on VLSI Technology*, pages 188–189, 2009.
- [103] H. Kobayashi, K. Imamura, W.-B. Kim, S.-S. Im, and Asuha. Nitric acid oxidation of Si (NAOS) method for low temperature fabrication of SiO₂/Si and SiO₂/SiC structures. *Applied Surface Science*, 256(19):5744–5756, 2010.
- [104] H. Kobayashi, T. Matsumoto, and S. Imai. Nitric acid oxidation method to form a gate oxide layer in sub-micrometer TFT. *ECS Meeting Abstracts*, 22(4), 2011.
- [105] H. Kobayashi Asuha, O. Maida, M. Takahashi, and H. Iwasa. Nitric acid oxidation of Si to form ultrathin silicon dioxide layers with a low leakage current density. *Journal of Applied Physics*, 94(11):7328–7335, 2003.
- [106] H. Koo, S. Hong, S. Ju, I. Seo, and Y. Kang. PbO-B₂O₃-SiO₂ glass powders with spherical shape prepared by spray pyrolysis. *Journal of Non-Crystalline Solids*, 352(30–31):3270–3274, 2006.
- [107] G. Korotcenkov, V. Brinzari, J. Schwank, M. DiBattista, and A. Vasiliev. Peculiarities of SnO₂ thin film deposition by spray pyrolysis for gas sensor application. *Sensors and Actuators B: Chemical*, 77(1–2):244–252, 2001.
- [108] N. Kramer, J. Jorritsma, H. Birk, and C. Schonenberger. Nanometer lithography on silicon and hydrogenated amorphous silicon with low energy electrons. *Journal of Vacuum Science & Technology B: Microelectronics and Nanometer Structures*, 13(3):805–811, 1995.

- [109] N. Kramer, M. van den Berg, and C. Schoenenberger. Scanning tunnelling microscope-induced oxidation of hydrogen passivated silicon surfaces. *Thin Solid Films*, 281–282(0):637–639, 1996.
- [110] C. Krzeminski, G. Larrieu, J. Penaud, E. Lampin, and E. Dubois. Silicon dry oxidation kinetics at low temperature in the nanometric range: Modeling and experiment. *Journal of Applied Physics*, 101(6):064908–8, 2011.
- [111] Y. Kubota. Submicrometer ultralow-power TFT with 1.8 nm NAOS SiO₂/20nm CVD SiO₂ gate stack structure. *IEEE Transactions on Electron Devices*, 58(4):1134–1140, 2011.
- [112] Y. Kubota, T. Matsumoto, H. Tsuji, N. Suzuki, S. Imai, and H. Kobayashi. 1.5-V-operation ultralow power circuit of Poly-Si TFTs fabricated using the NAOS method. *IEEE Transactions on Electron Devices*, 59(2):385–392, 2012.
- [113] A. La Magna and G. Garozzo. Factors affecting profile evolution in plasma etching of SiO₂ modeling and experimental verification. *Journal of The Electrochemical Society*, 150(10):F178–F185, 2003.
- [114] A. La Storia, D. Ercolini, F. Marinello, R. D. Pasqua, F. Villani, and G. Mauriello. Atomic force microscopy analysis shows surface structure changes in carvacrol-treated bacterial cells. *Research in Microbiology*, 162(2):164–172, 2011.
- [115] S. Lai. Non-volatile memory technologies: The quest for ever lower cost. In *Proceedings of the IEEE International Electron Devices Meeting (IEDM)*, pages 1–6, 2008.
- [116] T. Lane. Atomic force microscopy. *Journal of the Advanced Undergraduate Physics Laboratory Investigation*, pages 1–6, 2012.
<http://opus.ipfw.edu/jaupli/vol0/iss0/2>.
- [117] F. Larki, S. D. Hutagalung, A. Dehzeni, E. B. Saion, A. Abedini, A. M. Abdullah, M. N. Hamidon, and J. Hassan. Electronic transport properties of junctionless lateral gate silicon nanowire transistor fabricated by atomic force microscope nanolithography. *Microelectronics and Solid State Electronics*, 1:15–20, 2012.
- [118] C. Larriba-Andaluz and J. F. de la Mora. Electrospraying insulating liquids via charged nanodrop injection from the taylor cone of an ionic liquid. *Physics of Fluids*, 22(7):072002–7, 2010.
- [119] A. Lefebvre. *Atomization and sprays*. Hemisphere Publishing Corporation, 1989.
- [120] B. Legrand and D. Stievenard. Nanooxidation of silicon with an atomic force microscope: A pulsed voltage technique. *Applied Physics Letters*, 74(26):4049–4051, 1999.
- [121] I. W. Lenggoro. An experimental and modeling investigation of particle production by spray pyrolysis using a laminar flow aerosol reactor. *Journal of Materials Research*, 15(3):733–743, 2000.

- [122] E. A. Lewis and E. A. Irene. The effect of surface orientation on silicon oxidation kinetics. *Journal of the Electrochemical Society*, 134(9):2332–2339, 1987.
- [123] L. Ley, T. Teuschler, K. Mahr, S. Miyazaki, and M. Hundhausen. Kinetics of field-induced oxidation of hydrogen-terminated si (111). *Journal of Vacuum Science & Technology B: Microelectronics and Nanometer Structures*, 14(4):2845–2849, 1996.
- [124] L. N. Lie, R. R. Razouk, and B. E. Deal. Selective oxidation of silicon in high pressure steam. *Journal of the Electrochemical Society*, 125(11):1824–1829, 1981.
- [125] L. N. Lie, R. R. Razouk, and B. E. Deal. High pressure oxidation of silicon in dry oxygen. *Journal of the Electrochemical Society*, 129(12):2828–2834, 1982.
- [126] J. R. Ligenza. Effect of crystal orientation on oxidation rates of silicon in high pressure steam. *The Journal of Physical Chemistry*, 65(11):2011–2014, 1961.
- [127] J. E. Lilienfeld. US patent number 1745175: Method and apparatus for controlling electric current. (issued 28 January 1930).
- [128] J. E. Lilienfeld. US patent number 1900018: Device for controlling electric current. (issued 07 March 1933).
- [129] N. S. Losilla, J. Martínez, and R. Garca. Large area nanoscale patterning of silicon surfaces by parallel local oxidation. *Nanotechnology*, 20(47):475304–5, 2009.
- [130] C.-Y. Lu, H. T. Lue, and Y. C. Chen. State-of-the-art flash memory devices and post-flash emerging memories. *Science China Information Sciences*, 54(5):1039–1060, 2011.
- [131] C.-Y. Lu and J. Sung. Reverse short-channel effects on threshold voltage in submicrometer salicide devices. *IEEE Electron Device Letters*, 10(10):446–448, 1989.
- [132] A. Ludsteck, J. Schulze, I. Eisele, W. Dietl, and Z. Nenyai. Growth model for thin oxides and oxide optimization. *Journal of Applied Physics*, 95(5):2827–2831, 2004.
- [133] M. Luna, J. Colchero, and A. M. Baro. Intermittent contact scanning force microscopy: The role of the liquid necks. *Applied Physics Letters*, 72(26):3461–3463, 1998.
- [134] J. Lyding. UHV STM nanofabrication: progress, technology spin-offs, and challenges. *Proceedings of the IEEE*, 85(4):589–600, 1997.
- [135] S. F. Lyuksyutov, P. B. Paramonov, I. Dolog, and R. M. Ralich. Peculiarities of an anomalous electronic current during atomic force microscopy assisted nanolithography onn-type silicon. *Nanotechnology*, 14(7):716–721, 2003.

- [136] W. Ma, C. Yang, X. Gong, K. Lee, and A. Heeger. Thermally stable, efficient polymer solar cells with nanoscale control of the interpenetrating network morphology. *Advanced Functional Materials*, 15(10):1617–1622, 2005.
- [137] S. Major, A. Banerjee, and K. Chopra. Highly transparent and conducting indium-doped zinc oxide films by spray pyrolysis. *Thin Solid Films*, 108(3):333–340, 1983.
- [138] J. Manificier, J. Fillard, and J. Bind. Deposition of $\text{In}_2\text{O}_3/\text{SnO}_2$ layers on glass substrates using a spraying method. *Thin Solid Films*, 77(1-3):67 – 80, 1981.
- [139] G. Marsaglia and T. A. Bray. A convenient method for generating normal variables. *Society for Industrial and Applied Mathematics (SIAM) Review*, 6(3):260–264, 1964.
- [140] R. V. Martínez, N. S. Losilla, J. Martínez, Y. Huttel, and R. García. Patterning polymeric structures with 2 nm resolution at 3 nm half pitch in ambient conditions. *Nano Letters*, 7(7):1846–1850, 2007.
- [141] R. V. Martínez, J. Martínez, and R. García. Silicon nanowire circuits fabricated by AFM oxidation nanolithography. *Nanotechnology*, 21(24):245301–5, 2010.
- [142] H. Z. Massoud and J. D. Plummer. Analytical relationship for the oxidation of silicon in dry oxygen in the thin-film regime. *Journal of Applied Physics*, 62(8):3416–3423, 1987.
- [143] H. Z. Massoud, J. D. Plummer, and E. A. Irene. Thermal oxidation of silicon in dry oxygen: Accurate determination of the kinetic rate constants. *Journal of The Electrochemical Society*, 132(7):1745–1757, 1985.
- [144] H. Z. Massoud, J. D. Plummer, and E. A. Irene. Thermal oxidation of silicon in dry oxygen: Growth - rate enhancement in the thin regime II. Physical mechanisms. *Journal of The Electrochemical Society*, 132(11):2693–2700, 1985.
- [145] F. Masuoka. US patent number 4437172: Semiconductor memory device (issued 13 March 1984).
- [146] F. Masuoka and K. Ochiai. US patent number 4710897: Semiconductor memory device comprising six-transistor memory cells (issued 01 December 1987).
- [147] T. Matsumoto, Y. Kubota, M. Yamada, H. Tsuji, T. Shimatani, Y. Hirayama, S. Terakawa, S. Imai, and H. Kobayashi. Ultralow-power TFT with gate oxide fabricated by nitric acid oxidation method. *IEEE Electron Device Letters*, 31(8):821–823, 2010.
- [148] C. Mellor. The 3D die stack tack: Toshiba builds towering column of flash. The Register online, 2012.
http://www.theregister.co.uk/2012/10/15/toshiba_3d_solid_state/.

- [149] G. Mesa, E. Dobado-Fuentes, and J. J. Saenz. Image charge method for electrostatic calculations in field-emission diodes. *Journal of Applied Physics*, 79(1):39–44, 1996.
- [150] G. L. Messing, S.-C. Zhang, and G. V. Jayanthi. Ceramic powder synthesis by spray pyrolysis. *Journal of the American Ceramic Society*, 76(11):2707–2726, 1993.
- [151] A. Misaka and K. Harafuji. Simulation study of micro-loading phenomena in silicon dioxide hole etching. *IEEE Transactions on Electron Devices*, 44(5):751–760, 1997.
- [152] S. Mizushima, S. Imai, Asuha, M. Tanaka, and H. Kobayashi. Nitric acid method for fabrication of gate oxides in TFT. *Applied Surface Science*, 254(12):3685–3689, 2008.
- [153] J. B. Mooney and S. B. Radding. Spray pyrolysis processing. *Annual Review of Materials Science*, 12(1):81–101, 1982.
- [154] G. Moore. Cramming more components onto integrated circuits. *Electronics*, 38(8):114–117, 1965.
- [155] J. L. Moruzzi, A. Kiermasz, and W. Eccleston. Plasma oxidation of silicon. *Plasma Physics*, 24(6):605–614, 1982.
- [156] G. Mutinati, E. Brunet, S. Steinhauer, A. Köck, J. Teva, J. Kraft, J. Siegert, F. Schrank, and E. Bertagnoli. CMOS-integrable ultrathin SnO₂ layer for smart gas sensor devices. *Procedia Engineering*, 47, 2012.
- [157] A. Nakaruk and C. Sorrell. Conceptual model for spray pyrolysis mechanism: fabrication and annealing of titania thin films. *Journal of Coatings Technology and Research*, 7(5):665–676, 2010.
- [158] M. R. Namin and B. H. Blott. Superconducting Bi-Sr-Ca-Cu-O films prepared by DC magnetron sputtering on new polycrystalline substrates. *Superconductor Science and Technology*, 4(3):110–113, 1991.
- [159] M. Navi and S. T. Dunham. A viscous compressible model for stress generation/relaxation in SiO₂. *Journal of the Electrochemical Society*, 144(1):367–371, 1997.
- [160] K.-O. Ng and D. Vanderbilt. Structure and oxidation kinetics of the Si(100)-SiO₂ interface. *Physical Review B*, 59(15):10132–10137, 1999.
- [161] S. H. Ng, J. Wang, D. Wexler, S. Y. Chew, and H. K. Liu. Amorphous carbon-coated silicon nanocomposites: a low-temperature synthesis via spray pyrolysis and their application as high-capacity anodes for lithium-ion batteries. *The Journal of Physical Chemistry C*, 111(29):11131–11138, 2007.

- [162] A. Notargiacomo and A. Tseng. Assembling uniform oxide lines and layers by overlapping dots and lines using AFM local oxidation. In *IEEE Conference on Nanotechnology*, pages 907–910, 2009.
- [163] J. Ohshima. State-of-the-art flash memory technology, looking into the future. In *Presented at the GSA/Sematech Memory Conference*, 2012.
- [164] A. Orians, C. Clemons, D. Golovaty, and G. Young. One-dimensional dynamics of nano-scale oxidation. *Surface Science*, 600(16):3297–3312, 2006.
- [165] S. Osher and J. A. Sethian. Fronts propagating with curvature-dependent speed: Algorithms based on hamilton-jacobi formulations. *Journal of Computational Physics*, 79(1):12–49, 1988.
- [166] B. Päivänranta, A. Langner, E. Kirk, C. David, and Y. Ekinici. Sub-10 nm patterning using EUV interference lithography. *Nanotechnology*, 22(37):375302–7, 2011.
- [167] A. Pantazi, A. Sebastian, T. A. Antonakopoulos, P. B andchtold, A. R. Bonaccio, J. Bonan, G. Cherubini, M. Despont, R. A. DiPietro, U. Drechsler, U. D andrig, B. Gotsmann, W. H andberle, C. Hagleitner, J. L. Hedrick, D. Jubin, A. Knoll, M. A. Lantz, J. Pentarakis, H. Pozidis, R. C. Pratt, H. Rothuizen, R. Stutz, M. Varsamou, D. Wiesmann, and E. Eleftheriou. Probe-based ultrahigh-density storage technology. *IBM Journal of Research and Development*, 52(4.5):493–511, 2008.
- [168] F. Paraguay D., W. Estrada L., D. Acosta N., E. Andrade, and M. Miki-Yoshida. Growth, structure and optical characterization of high quality ZnO thin films obtained by spray pyrolysis. *Thin Solid Films*, 350(1–2):192–202, 1999.
- [169] A. Pasquarello, M. S. Hybertsen, and R. Car. Atomic dynamics during silicon oxidation. In Y. J. Chabal, editor, *Fundamental Aspects of Silicon Oxidation*, volume 46 of *Springer Series in Materials Science*, pages 107–125. Springer Berlin Heidelberg, 2001.
- [170] L. Pauling. The nature of silicon-oxygen bonds. *American Mineralogist*, 65:321–323, 1980.
- [171] D. Perednis. *Thin Film Deposition by Spray Pyrolysis and the Application in Solid Oxide Fuel Cells*. Dissertation, Swiss Federal Institute of Technology Zurich - Eidgenössische Technische Hochschule (ETH) Zürich, 2003.
<http://e-collection.library.ethz.ch/eserv/eth:26881/eth-26881-02.pdf>.
- [172] D. Perednis and L. J. Gauckler. Solid oxide fuel cells with electrolytes prepared via spray pyrolysis. *Solid State Ionics*, 166(3-4):229–239, 2004.
- [173] R. Perez. Discriminating chemical bonds. *Science*, 337(6100):1305–1306, 2012.
- [174] R. D. Piner, J. Zhu, F. Xu, S. Hong, and C. A. Mirkin. "Dip-pen" nanolithography. *Science*, 283(5402):661–663, 1999.

- [175] J. D. Plummer, M. D. Deal, and P. B. Griffin. *Silicon VLSI Technology - Fundamentals, Practice and Modeling*. Prentice Hall Electronics and VLSI Series. Prentice-Hall Inc., Upper Saddle River, NJ, 2000.
- [176] W. H. Press. *Numerical Recipes: The Art of Scientific Computing*. Cambridge University Press, 3rd edition, 2007.
- [177] M. Quirk and J. Serda. *Semiconductor Manufacturing Technology*. Prentice-Hall Inc., Upper Saddle River, NJ, 2001.
- [178] M. Radi. *Three-Dimensional Simulation of Thermal Oxidation*. Dissertation, Technischen Universität Wien, Institute for Microelectronics, 1998. <http://www.iue.tuwien.ac.at/phd/radi/>.
- [179] R. R. Razouk, L. N. Lie, and B. Deal. Kinetics of high pressure oxidation of silicon in pyrogenic steam. *Journal of the Electrochemical Society*, 128(10):2214–2220, 1981.
- [180] S. Rozati and T. Ganj. Transparent conductive Sn-doped indium oxide thin films deposited by spray pyrolysis technique. *Renewable Energy*, 29(10):1671–1676, 2004.
- [181] J. Ruzyllo¹, G. T. Duranko¹, and A. M. Hoff¹. Preoxidation UV treatment of silicon wafers. *Journal of the Electrochemical Society*, 134(8):2052–2055, 1987.
- [182] K. Sakai. High-index immersion lithography. *Recent Advances in Nanofabrication Techniques and Applications*, pages 397–416, 2004. <http://cdn.intechweb.org/pdfs/24508.pdf>.
- [183] W. Sears and M. A. Gee. Mechanics of film formation during the spray pyrolysis of tin oxide. *Thin Solid Films*, 165(1):265–277, 1988.
- [184] M. Serra-García, F. Pérez-Murano, and A. San Paulo. Nonlinear detection mechanism in quantitative atomic force microscopy characterization of high-frequency nanoelectromechanical systems. *Physical Review B*, 85(3):035433–9, 2012.
- [185] J. A. Sethian. *Level Set Methods and Fast Marching Methods*. Cambridge University Press, 2nd edition, 1999.
- [186] T. Shimura, E. Mishima, H. Watanabe, K. Yasutake, M. Umeno, K. Tatsumura, T. Watanabe, I. Ohdomari, K. Yamada, S. Kamiyama, Y. Akasaka, Y. Nara, and K. Nakamura. Ordered structure in the thermal oxide layer on silicon substrates. *ECS Transactions*, 1(1):39–48, 2005.
- [187] W. Siefert. Properties of thin In₂O₃ and SnO₂ films prepared by corona spray pyrolysis, and a discussion of the spray pyrolysis process. *Thin Solid Films*, 120(4):275–282, 1984.
- [188] Silvaco, Inc.: ATHENA Process Simulation Framework. http://www.silvaco.com/products/process_simulation/athena.html.

- [189] Silvaco, Inc.: VICTORY Process 3D Process Simulator.
http://www.silvaco.com/products/vwf/athena/victory/victory_br.html.
- [190] P. Smeys. *Geometry and Stress Effects in Scaled Integrated Circuit Isolation Technologies*. Ph.d. dissertation, Stanford University, 1996.
<http://searchworks.stanford.edu/view/3371223>.
- [191] E. S. Snow and P. M. Campbell. Fabrication of Si nanostructures with an atomic force microscope. *Applied Physics Letters*, 64(15):1932–1934, 1994.
- [192] E. S. Snow, G. G. Jernigan, and P. M. Campbell. The kinetics and mechanism of scanned probe oxidation of Si. *Applied Physics Letters*, 76(13):1782–1784, 2000.
- [193] Spraying Systems Co., Volume median diameter versus air pressure at constant liquid pressures. Data Sheet No. 36892-8M.
- [194] S. N. Srivastava, K. C. Thompson, E. L. Antonsen, H. Qiu, J. B. Spencer, D. Papke, and D. N. Ruzic. Lifetime measurements on collector optics from Xe and Sn extreme ultraviolet sources. *Journal of Applied Physics*, 102(2):023301–6, 2007.
- [195] Stanford University: SUPREM-IV.
<http://www-tcad.stanford.edu/tcad/programs/suprem4.html>.
- [196] Stanford University: SUPREM-IV.GS Two Dimensional Process Simulation for Silicon and Gallium Arsenide, 1993.
<http://www-tcad.stanford.edu/tcad/pubs/Suprem-IV.GS.pdf>.
- [197] D. Stiévenard, P. Fontaine, and E. Dubois. Nanooxidation using a scanning probe microscope: an analytical model based on field induced oxidation. *Applied Physics Letters*, 70(24):3272–3274, 1997.
- [198] D. Stiévenard and B. Legrand. Silicon surface nano-oxidation using scanning probe microscopy. *Progress in Surface Science*, 81(2–3):112–140, 2006.
- [199] A. M. Stoneham, M. A. Szymanski, and A. L. Shluger. Atomic and ionic processes of silicon oxidation. *Physical Review B*, 63(24):241304–4, 2001.
- [200] H. Sugimura, T. Uchida, N. Kitamura, and H. Masuhara. Scanning tunneling microscope tip-induced anodization for nanofabrication of titanium. *The Journal of Physical Chemistry*, 98(16):4352–4357, 1994.
- [201] H. Sugimura, T. Uchida, N. Kitamura, and H. Masuhara. Scanning tunneling microscope tip-induced anodization of titanium: Characterization of the modified surface and application to the metal resist process for nanolithography. *Journal of Vacuum Science & Technology B: Microelectronics and Nanometer Structures*, 12(5):2884–2888, 1994.

- [202] A. G. Sutjipto, A. R. Muhida, and S. Mridha. Novel nanofabrication process of oxide patterns using AFM in low operating temperature: a promising lithographic tool for future molecular electronics. In *Proceedings of the International Conference on Electrical Engineering and Informatics*, pages 238–239, 2007.
- [203] V. Suvorov, A. Hössinger, Z. Djurić, and N. Ljepojevic. A novel approach to three-dimensional semiconductor process simulation: Application to thermal oxidation. *Journal of Computational Electronics*, 5(4):291–295, 2006.
- [204] Synopsys, Inc.: Sentaurus Process.
<http://www.synopsys.com/Tools/TCAD/ProcessSimulation/Pages/SentaurusProcess.aspx>.
- [205] Synopsys, Inc.: Taurus TSUPREM-IV.
<http://www.synopsys.com/Tools/TCAD/ProcessSimulation/Pages/TaurusTSupreme4.aspx>.
- [206] H. Tanaka, M. Kido, K. Yahashi, M. Oomura, R. Katsumata, M. Kito, Y. Fukuzumi, M. Sato, Y. Nagata, Y. Matsuoka, Y. Iwata, H. Aochi, and A. Nitayama. Bit cost scalable technology with punch and plug process for ultra high density flash memory. In *IEEE Symposium on VLSI Technology*, pages 14–15, 2007.
- [207] Q. Tang, S. Shi, and L. Zhou. Nanofabrication with atomic force microscopy. *Journal of Nanoscience and Nanotechnology*, 4(8):948–963, 2004.
- [208] K. Tatsumura, T. Watanabe, D. Yamasaki, T. Shimura, M. Umeno, and I. Ohdomari. Residual order within thermally grown amorphous SiO₂ on crystalline silicon. *Physical Review B*, 69(8):085212–5, 2004.
- [209] M. Tello and R. García. Nano-oxidation of silicon surfaces: Comparison of non-contact and contact atomic-force microscopy methods. *Applied Physics Letters*, 79(3):424–426, 2001.
- [210] T. Teuschler, K. Mahr, S. Miyazaki, M. Hundhausen, and L. Ley. Nanometer-scale field-induced oxidation of Si(111):H by a conducting-probe scanning force microscope: Doping dependence and kinetics. *Applied Physics Letters*, 67(21):3144–3146, 1995.
- [211] A. Tischner, T. Maier, C. Stepper, and A. Köck. Ultrathin SnO₂ gas sensors fabricated by spray pyrolysis for the detection of humidity and carbon monoxide. *Sensors and Actuators B: Chemical*, 134(2):796–802, 2008.
- [212] A. A. Tseng. Advancements and challenges in development of atomic force microscopy for nanofabrication. *Nano Today*, 6(5):493–509, 2011.

- [213] A. A. Tseng, T. Lee, A. Notargiacomo, and T. P. Chen. Formation of uniform nanoscale oxide layers assembled by overlapping oxide lines using atomic force microscopy. *Journal of Micro/Nanolithography, MEMS, and MOEMS*, 8(4):043050–8, 2009.
- [214] Y. Tu and J. Tersoff. Microscopic dynamics of silicon oxidation. *Physical Review Letters*, 89(8):086102–4, 2002.
- [215] D. Veberic. Having Fun with Lambert W(x) Function. *ArXiv e-prints*, 2010. <http://adsabs.harvard.edu/abs/2010arXiv1003.1628V>.
- [216] J. C. Vigi   and J. Spitz. Chemical vapor deposition at low temperatures. *Journal of The Electrochemical Society*, 122(4):585–588, 1975.
- [217] S. A. Vitale, H. Chae, and H. H. Sawin. Silicon etching yields in F₂, Cl₂, Br₂, and HBr high density plasmas. *Journal of Vacuum Science & Technology A: Vacuum, Surfaces, and Films*, 19(5):2197–2206, 2001.
- [218] W. L. Warren, K. Vanheusden, J. R. Schwank, D. M. Fleetwood, P. S. Winokur, and R. A. B. Devine. Mechanism for anneal-induced interfacial charging in SiO₂ thin films on Si. *Applied Physics Letters*, 68(21):2993–2995, 1996.
- [219] H. Watanabe, N. Miyata, and M. Ichikawa. Layer-by-layer oxidation of Si(001) surfaces. In Y. J. Chabal, editor, *Fundamental Aspects of Silicon Oxidation*, volume 46 of *Springer Series in Materials Science*, pages 89–105. Springer Berlin Heidelberg, 2001.
- [220] T. Watanabe and I. Ohdomari. A new kinetic equation for thermal oxidation of silicon replacing the Deal-Grove equation. *ECS Transactions*, 6(3):465–481, 2007.
- [221] T. Watanabe, K. Tatsumura, and I. Ohdomari. New linear-parabolic rate equation for thermal oxidation of silicon. *Physical Review Letters*, 96(19):196102–4, 2006.
- [222] S. B. Weber, H. L. Lein, T. Grande, and M.-A. Einarsrud. Deposition mechanisms of thick lanthanum zirconate coatings by spray pyrolysis. *Journal of the American Ceramic Society*, 94(12):4256–4262, 2011.
- [223] J. Welker and F. J. Giessibl. Revealing the angular symmetry of chemical bonds by atomic force microscopy. *Science*, 336(6080):444–449, 2012.
- [224] L. Weng, L. Zhang, Y. Chen, and L. Rokhinson. AFM local oxidation nanolithography of graphene. *Bulletin of the American Physical Society*, 54:1–3, 2009.

- [225] S. Whang, K. Lee, D. Shin, B. Kim, M. Kim, J. Bin, J. Han, S. Kim, B. Lee, Y. Jung, S. Cho, C. Shin, H. Yoo, S. Choi, K. Hong, S. Aritome, S. Park, and S. Hong. Novel 3-dimensional dual control-gate with surrounding floating-gate (DC-SF) NAND flash cell for 1Tb file storage application. In *IEEE International Electron Devices Meeting (IEDM)*, pages 29–7, 2010.
- [226] R. T. Whitaker. A level-set approach to 3D reconstruction from range data. *International Journal of Computer Vision*, 29(3):203–231, 1998.
- [227] R. Wiesendanger. *Scanning probe microscopy and spectroscopy: Methods and applications*. Cambridge University Press, 1994.
- [228] O. Wilhelm. *Electrohydrodynamic spraying – Transport, Mass and Heat Transfer of Charged Droplets and Their Application to the Deposition of Thin Functional Films*. Dissertation, Swiss Federal Institute of Technology Zurich - Eidgenössische Technische Hochschule (ETH) Zürich, 2004.
<http://fex-dev2.ethz.ch/eserv/eth:27191/eth-27191-02.pdf>.
- [229] D. R. Wolters and A. T. A. Z. Duijnhoven. Silicon oxidation and fixed oxide charge. *Journal of the Electrochemical Society*, 139(1):241–249, 1992.
- [230] Y. Xia and G. Whitesides. Soft lithography. *Angewandte Chemie International Edition*, 37(1):550–575, 1998.
- [231] M. Yasutake, Y. Ejiri, and T. Hattori. Modification of silicon surface using atomic force microscope with conducting probe. *Japanese Journal of Applied Physics Letters B*, 32:L1021–L1023, 1993.
- [232] H. Yu, Y. Sun, N. Singh, G.-Q. Lo, and D.-L. Kwong. Perspective of flash memory realized on vertical Si nanowires. *Microelectronics Reliability*, 52(4):651–661, 2012.
- [233] M. Zhang, D. Bullen, S.-W. Chung, S. Hong, K. S. Ryu, Z. Fan, C. A. Mirkin, and C. Liu. A MEMS nanoplotter with high-density parallel dip-pen nanolithography probe arrays. *Nanotechnology*, 13(2):212–217, 2002.
- [234] Q. Zhong, D. Inniss, K. Kjoller, and V. Elings. Fractured polymer/silica fiber surface studied by tapping mode atomic force microscopy. *Surface Science Letters*, 290(1-2):L688–L692, 1993.
- [235] J. Zou, D. Bullen, X. Wang, C. Liu, and C. A. Mirkin. Conductivity-based contact sensing for probe arrays in dip-pen nanolithography. *Applied Physics Letters*, 83(3):581–583, 2003.

List of Publications

- [1] L. Filipovic and S. Selberherr. Electric field based simulations of local oxidation nanolithography using atomic force microscopy in a level set environment. In *Proceedings of the International Symposium on Microelectronics Technology and Devices (SBMicro)*, pages 265–272, Brasilia, Brazil, 2012.
- [2] L. Filipovic and S. Selberherr. Simulations of local oxidation nanolithography by AFM based on the generated electric field. In *International Conference on Simulation of Semiconductor Processes and Devices (SISPAD)*, pages 189–192, Denver, CO, USA, 2012.
- [3] L. Filipovic and S. Selberherr. Simulation of silicon nanopatterning using nc-AFM. In *International Conference on non-contact Atomic Force Microscopy*, page 108, Cesky Krumlov, Czech Republic, 2012.
- [4] J. Weinbub, K. Rupp, L. Filipovic, A. Makarov, and S. Selberherr. Towards a free open source process and device simulation framework. In *15th International Workshop on Computational Electronics (IWCE)*, pages 1–4, Madison, USA, 2012.
- [5] L. Filipovic and S. Selberherr. A two-dimensional Lorentzian distribution for an Atomic Force Microscopy simulator. In K. K. Sabelfeld and I. Dimov, editors, *Monte Carlo Methods and Applications*, DeGruyter Proceedings in Mathematics, pages 97–104. Walter de Gruyter, 2012.
- [6] L. Filipovic and S. Selberherr. A Monte Carlo simulator for non-contact mode atomic force microscopy. In I. Lirkov, S. Margenov, and J. Waśniewski, editors, *Large-Scale Scientific Computing*, volume 7116 of *Lecture Notes in Computer Science*, pages 447–454. Springer Berlin Heidelberg, 2012.
- [7] L. Filipovic and S. Selberherr. A level set simulator for nanooxidation using non-contact atomic force microscopy. In *International Conference on Simulation of Semiconductor Processes and Devices (SISPAD)*, pages 307–310, Osaka, Japan, 2011.
- [8] L. Filipovic and S. Selberherr. A two-dimensional Lorentzian distribution for an atomic force microscopy simulator. In *Abstracts IMACS Seminar on Monte Carlo Methods (MCM)*, page 30, Borovets, Bulgaria, 2011.

- [9] L. Filipovic and S. Selberherr. A Monte Carlo simulator for non-contact mode atomic force microscopy. In *International Conference on Large-Scale Scientific Computations (LSSC)*, pages 42–43, Sozopol, Bulgaria, 2011.
- [10] L. Filipovic, H. Ceric, J. Cervenka, and S. Selberherr. A simulator for local anodic oxidation of silicon surfaces. In *24th Canadian Conference on Electrical and Computer Engineering*, pages 695–698, Niagara Falls, Canada, 2011.
- [11] L. Filipovic, O. Ertl, and S. Selberherr. Parallelization strategy for hierarchical run length encoded data structures. In *Proceeding of Parallel and Distributed Computing and Networks*, pages 131–138, Innsbruck, Austria, 2011.
- [12] O. Ertl, L. Filipovic and, and S. Selberherr. Three-dimensional simulation of focused ion beam processing using the level set method. In *International Conference on Simulation of Semiconductor Processes and Devices (SISPAD)*, pages 49–52, Bologna, Italy, 2010.
- [13] L. Filipovic and L. MacEachern. A 10-bit low-power SAR ADC with a tunable series attenuation capacitor. In *International Conference on Microelectronics (ICM)*, pages 399–402, Sharjah, UAE, 2008.

Curriculum Vitae

Date of birth February 12th, 1983
Place of birth Sarajevo, Yugoslavia
Citizenship Canada

Sept. 2001 – June 2006

Carleton University, Ottawa ON, Canada
Bachelor's of Engineering (with practical component)
Concentration: VLSI with CMOS design of analog circuits

May 2003 – Dec. 2003 and Sept. 2004 – Aug. 2005

Employed at Dy4 Systems (later Curtiss-Wright Embedded Computing)
Practical component of the Bachelor of Engineering degree

Sept. 2006 – June. 2009

Carleton University, Ottawa ON, Canada
Graduate program in applied sciences at the Department of Electronics
National Science and Engineering Research Council of Canada (NSERC) grant
Masters's Thesis: "Low Power 10-bit Analog to Digital Converter"

Sept. 2006 – June. 2009

Carleton University, Ottawa ON, Canada
Teaching and Laboratory Assistant at the Department of Electronics

since January 2010

Vienna University of Technology, Austria
PhD program at the Institute for Microelectronics